Ghent University
Faculty of Engineering
Department of Electrical Energy, Systems and Automation (EESA)
Electrical Energy Laboratory (EELAB)

Modification of Magnetic Properties of Non Oriented Electrical Steels by the Production of Electromagnetic Devices

Wijziging van de Magnetische Eigenschappen van Niet-georiënteerde Elektrische Staalsoorten door de Productie van Elektromagnetische Toestellen

---

Alexandre Pulnikov

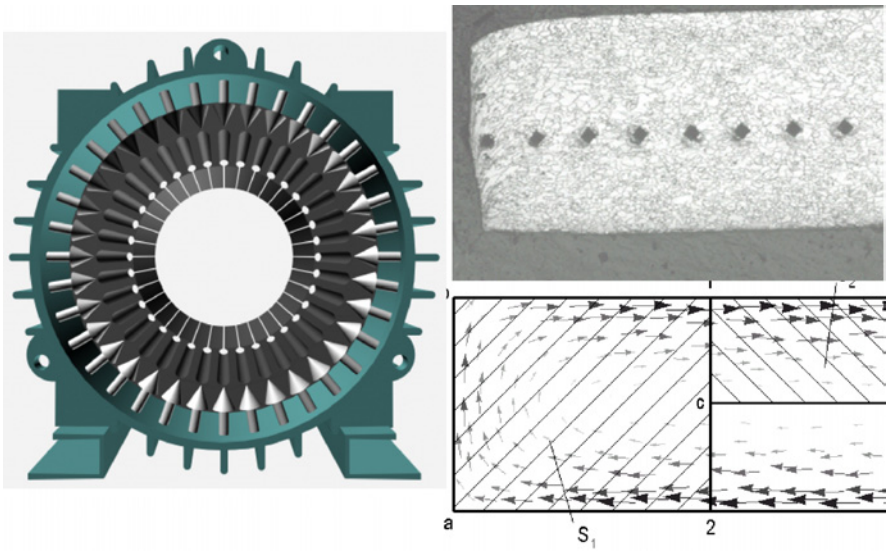

Proefschrift tot het bekomen van de graad van
Doctor in de Toegepaste Wetenschappen:
Werktuigkunde-Elektrotechniek
Academiejaar 2003-2004

Promoters:

Prof. J. MELKEBEEK,
Prof. L. DUPRÉ

Ghent University
Faculty of Engineering
Department of Electrical Energy, Systems and Automation (EESA)
Electrical Energy Laboratory (EELAB)

Sint-Pietersnieuwstraat 41,
B-9000 Gent, Belgie

Acknowledgement

First of all I would like to thank my promoters **Prof. J. Melkebeek** and **Prof. L. Dupré** for providing me an environment for accomplishing this work. I have learnt a lot from discussions we had. I am especially grateful for their guidance during my work and for their thorough review of this thesis.

I would like to thank **Dr. A. Belhadj**, **Dr. P. Baudouin** and **Dr. R. Petrov** for the knowledge they shared with me on metallurgical aspects of electrical steels. I express my gratitude to **Dr. P. Baudouin** for his help with the microhardness measurements. I am also grateful to **Dr. R. Petrov** from the Department of Metallurgy and Materials Science for the strain-stress measurements and for the help with a literature. I would like to thank **ir. R. Decocker** for his help with the magnetostriction measurements.

I am grateful to my former colleagues **Dr. M. De Wulf** and **Dr. D. Makaveev** for discussions we had on the general issues of the magnetic measurements. A LabView software developed by **Dr. M. De Wulf** for the control of the single sheet testers was used as a basement for my own software.

I would like to thank **ir. V. Permiakov** for his help with the magnetic measurements and for the discussions we had.

I would like to thank **ir. G. Langelaan** from the Department of Metallurgy and Materials Science, Katholieke Universiteit Leuven for the measurements of the residual stresses.

I would like to thank **Dr. H. Wisselink** from NIMR, University of Twente for the 2D simulations of mechanical cutting, he conducted on his finite element software. I am also grateful to **Prof. B. Verhegghe** for his suggestions and comments on the simulations of cutting.

I would like to thank **Dr. J. Gyselinck** from the University of Liege for his valuable contribution into the electromagnetic finite element computations presented in this thesis. Most of these computations were performed using GetDP (www.geuz.org/getdp/) freely distributed finite element software and GMSH (www.geuz.org/gmsh/) mesh generator.

I would like to thank our technicians **C. Vervust**, **F. De Boever** and **T. Boone** for the construction of the measurement setups. Their practical ideas regarding the designs of the setups were very helpful. I am also grateful for the high quality and high precision they achieved during the construction of the setups.

I would like to thank my father **Dr. A. Pulnikov** for shearing his knowledge on the production aspects of electrical machines as well as for providing me some technical data on induction motors.

Важной составляющей любого исследования являются понимание и поддержка близких. В этом смысле косвенное участие порой бывает весомей участия прямого. Поэтому мне хотелось бы поблагодарить свою супругу Любу, а также родителей и младшего брата за создание комфортной атмосферы. Благодаря вам я не знал ни усталости, ни разочарования.

List of symbols

General notation:

1. Scalars: A, A.
2. Vectors: $\overline{A}$, (A).
3. Matrices: $\overline{\overline{A}}$, [A].

Symbols.

Symbol	Definition
$\overline{A}$	Vector magnetic potential, Wb/m
$\overline{B}$	Magnetic flux density, T
e	Electromotive force, V
$\overline{E}$	Electric field, V/m
f	Frequency, Hz
F	Force, N
$\overline{H}$	Magnetic field, A/m
I, i	Electric current, A
$\overline{J}$	Electric current density, A/m^2
L	Inductance, H
M	Magnetization, A/m
P	Losses, W/kg
R	Resistance, Ω (Chapter 5) Magnetic reluctance, 1/H (Chapter 9)
S	Cross-sectional area of the sample, m^2
t	Time, s
T	Mechanical torque, Nm (Chapter 1) Time period, s
U, u	Displacement, m (Chapter 3)
v	Voltage, V
w	Number of turns of the winding
W	Energy, J Energy loss, J/m^3 (Chapter 7)
ε	True strain
λ	Magnetostriction
λ_{100}	Spontaneous deformation of the steel crystal when completely magnetized in [100] crystallographic direction
λ_{111}	Spontaneous deformation of the steel crystal when completely magnetized in [111] crystallographic direction
μ	Magnetic permeability, H/m

ε	Permittivity, F/m
ρ	Electric resistivity, Ωm
σ	True stress, Pa Electric conductivity, 1/Ωm (Chapter 4, 8)
Φ	Magnetic flux, Wb
ϕ	Scalar magnetic potential, V
χ	Magnetic susceptibility, H/m

Abbreviations.

e.m.f.	Electromotive force
m.m.f.	Magnetomotive force
RD	Rolling direction
RSST	Rotational single sheet tester
SST	Single sheet tester
TD	Transverse direction

Content

Introduction

This work deals with the effect of mechanical deformation on the magnetic properties of non-oriented electrical steels. Non-oriented electrical steel is probably the most used class of magnetic materials. It is well known that a detailed description of the magnetic behaviour of electrical steels is crucial for the accurate simulation of electromagnetic devices and consequently an accurate prediction of their performances. The latter is necessary during the design stage of the device.

Therefore a lot of efforts were recently made for the elaboration of adequate material models at the Electric Energy Laboratory, University Ghent, and other research groups throughout the world.

Although non-oriented electrical steels deserve careful treatment, in order to reduce the production cost of an electromagnetic device, the materials are subjected to various mechanical deformations during production and shaping of the laminations and assembling of the core. These machine production processes often result in a deterioration of the magnetic material quality. The purpose of the current investigation is to provide information on these production effects and to develop a numerical procedure that could be introduced in the numerical analysis of electromagnetic devices.

In Chapter 1, the principles of ferromagnetism are discussed. The basics of the magnetic domain theory along with the conventional approach to the investigation of the effect of elastic stresses are presented.

In Chapter 2 a basic description of defects encountered in non-oriented electrical steels is given. The dislocation theory is reviewed and some general mechanical properties of non-oriented electrical steels are analyzed.

The numerical and experimental investigation of the mechanical deformations in electrical steels is carried out in Chapter 3. Of course, it is not possible to cover all the multitude of the electromagnetic devices in the frame of one study. So, in this work we concentrate on the low-power induction machines as they are widely used and also quite sensitive to the effects of machine construction. The influence of the different cutting parameters on the plastic deformation of the sheet was investigated numerically. The numerical investigation is confirmed by micro hardness measurements.

The investigation of the effect of the mechanical stresses on the magnetic properties requires special equipment. The measurement setups, constructed in the frame of this work clearly differ from the conventional structures. Therefore in Chapter 4 a detailed analysis of the parameters of the constructed setups was conducted. The general approaches used in the measurement of the magnetic quantities were described in the same chapter.

Throughout the study, described in this thesis, we will impose a sinusoidal magnetic flux density in the samples under investigation. Maintaining the specified induction shape requires some additional measures as described in Chapter 5.

In Chapter 6 a multidirectional experimental investigation of the effect of applied mechanical stresses on the magnetic properties of electrical steels is carried out. It is shown that the elastic stresses result in a considerable anisotropy of the magnetic properties. It is also demonstrated that an applied plastic deformation leads to a deterioration of the magnetic properties in all the directions in the plane of the sheet. The plastic deformation leads to the nucleation of residual stresses. A short study on this matter is proposed.

In Chapter 7 the relation between the magnetic properties under applied tension on one hand and under applied compression on the other hand was determined. The link with magnetostriction properties under applied elastic stress was shown both theoretically and experimentally. It is shown that different approaches can be considered during magnetostriction measurements under applied elastic stress.

In Chapter 8 the experimental investigation of the effect of mechanical cutting on the magnetic properties of non-oriented electrical steel is carried out. The measurements were performed at 3 Hz using the needle-probe method.

In Chapter 9 a simple numerical model for an low power induction machine was developed that accounts for the effect of elastic stresses as well as the effect of punching at the edges of the laminations. In order to demonstrate the performance of the model a low power induction machine was simulated. A general correspondence with experimental results reported in the literature was achieved. The developed approach can be extended to other geometries or other types of machines. However some of the assumptions relevant to the low power induction machine can be inapplicable to other devices.

In this work finite element methods were used as a tool for complex mechanical and magnetic problems. As only standard numerical approaches were used, we refer to elaborated and comprehensive descriptions of the finite element approach, available in e.g. [Chari][Salon][Gyselinck].

Chapter 1. Ferromagnetism.

Introduction.

When considering magnetization processes in materials at a certain instant, it is observed that the material behavior does not only depend on the magnetic excitation at that instant but also on the magnetic excitation before. The material shows memory effects, also called hysteresis effects. Many applications, from electric machines to transformers and permanent magnetics, from various types of electronic devices to magnetic recording, rely heavily on particular aspects of hysteresis. Hysteresis loops may take many different shapes and it is important to list a few parameters that give some prime characterization of loop properties. Two quantities of particular importance in this respect are the remanence magnetization or remanence M_r and the coercive field H_c.

The remanence presents the magnetization obtained after applying a large field to the specimen and then removing it. It is the natural quantity expressing the fact that a ferromagnet can be spontaneously magnetized, even in the absence of external actions. The coercive field is the field needed to bring the magnetization from the remanence to zero. The coercive field measures the order of magnitude of the fields that must be applied to a material in order to reverse its magnetization. Materials can be classified according to the values taken by these two parameters. It is common to subdivide materials into soft and hard magnetic materials. Soft magnetic materials are materials that are easy to magnetize, destined to applications where a low coercive field is a prime requirement. Hard magnetic materials are materials that are stable in a sense that they are a source of magnetic field, insensitive to external actions. In this work we will consider only soft magnetic materials. The emergence of the macroscopic hysteresis behaviour is intimately related to the existence of magnetic domains. It is only over scales larger than the domain size that the macroscopic hysteresis properties of a material become manifest. Magnetic hysteresis characteristics must be interpreted as an average behavior of a material volume where many magnetic domains are present. On the scale of magnetic domains, the magnetic state of the material is defined by the magnetic domain structure and many domain structures may exist for the same value of magnetic field and average magnetization. Indeed, in a macroscopic magnetic system, there is always a substantial amount of disorder: presence of grains in polycrystals, dislocations and lattice deformations, fluctuations of composition, presence of inclusions, precipitates… These sources of disorder are coupled to the magnetization in the material through exchange, anisotropy and magnetostatic interactions. This will be explained in more detail in this introductory chapter.

In most cases the properties of the magnetic materials greatly affect the characteristics of the electromagnetic devices. Therefore their improvement is not possible without better understanding of the “customs” and “habits” of the magnetic materials.

In the current chapter basic mechanisms of the ferromagnetism are considered and the interrelation between these mechanisms is discussed. The purpose of this chapter is to provide a theoretical basis for the conducted investigation.
We will begin with the fundamentals of electromagnetism described in the equations of Maxwell.

Section 1.1. Maxwell's equations and constitutive laws

Macroscopic electromagnetic phenomena are often described by the following vector fields, which can be space and time dependent:

- $\overline{E}$: electrical field [V/m]
- $\overline{D}$: electric flux density [C/m^2]
- $\overline{H}$: magnetic field [A/m]
- $\overline{B}$: magnetic flux density [T]

Notice that these four vector fields are not independent. They are interconnected by:

(a) the *Maxwell's equations* given by:

$$\nabla \times \overline{E} = -\frac{\partial \overline{B}}{\partial t} \quad (Faraday's \quad law) \tag{1.1.1}$$

$$\nabla \times \overline{H} = \overline{J} + \frac{\partial \overline{D}}{\partial t} \quad (Ampere's \quad law) \tag{1.1.2}$$

$$\nabla \cdot \overline{D} = \rho \quad (electric \quad Gauss \quad law) \tag{1.1.3}$$

$$\nabla \cdot \overline{B} = 0 \quad (magnetic \quad Gauss \quad law) \tag{1.1.4}$$

where $\overline{J}$ is the current density vector [A/m^2] while ρ [C/m^3] equals the charge density.

(b) the *constitutive laws* which are given in the most general way by $\overline{D} = \overline{D}(\overline{E}, \overline{E}_{past})$, $\overline{B} = \overline{B}(\overline{H}, \overline{H}_{past})$ and $\overline{J} = \overline{J}(\overline{E}, \overline{E}_{past})$.
In the case of lossless materials the dependence of the history of the vector fields $\overline{E}$ and $\overline{H}$, denoted by the index 'past', is absent. In case of linear, homogeneous and isotropic material the constitutive laws reduces to

$$\overline{B} = \mu \overline{H} = \mu_0 \mu_r \overline{H} \tag{1.1.5}$$

$$\overline{D} = \varepsilon \overline{E} = \varepsilon_0 \varepsilon_r \overline{E} \tag{1.1.6}$$

$$\overline{J} = \sigma \overline{E} \tag{1.1.7}$$

with μ and ε the permeability and permittivity of the material. μ_r and ε_r are the relative permeability and relative permittivity of the material (relative to air).

Notice that in this work we will only consider quasistatic magnetic systems. For these systems $\partial \overline{D} / \partial t$ is negligible. Consequently the relevant Maxwell's equations become

$$\nabla \times \overline{E} = -\frac{\partial \overline{B}}{\partial t} \quad or \quad \oint_L \overline{E} \cdot d\overline{l} = -\frac{d}{dt} \int_S \overline{B} \cdot \overline{n} ds = -\frac{d\Phi}{dt} \tag{1.1.8}$$

$$\nabla \times \bar{H} = \bar{J} \quad or \quad \oint_L \bar{H} \cdot d\bar{l} = \int_S \bar{J} \cdot \bar{n} ds = I_{tot} \tag{1.1.9}$$

$$\nabla \cdot \bar{B} = 0 \quad or \quad \Phi = \oint_S \bar{B} \cdot \bar{n} ds = 0 \tag{1.1.10}$$

The integral forms directly follows from Stokes theorem or the divergence theorem.
Equation (1.1.8) states that the time variation of the magnetic flux Φ through the surface S bounded by the specified contour L induces the electromagnetic force (e.m.f.) in this contour. Similarly, equation (1.1.9) states that the electric current I_{tot} through the surface S bounded by the specified contour L induces the magnetomotive force (m.m.f.) in this contour. The last equation shows that the total magnetic flux Φ through a closed surface S always equals zero.

In air (μ_r=1, ε_r=1) the Maxwell's equations for quasistatic magnetic systems are

$$\nabla \times \bar{E} = -\frac{\partial \bar{B}}{\partial t} \tag{1.1.11}$$

$$\nabla \times \frac{\bar{B}}{\mu_0} = \bar{J} \tag{1.1.12}$$

$$\nabla \cdot \bar{B} = 0 \tag{1.1.13}$$

It is well known that Maxwell's equations valid in materials can be reconstructed from (1.1.11), (1.1.12) and (1.1.13). Here materials are replaced by microcurrents as described in the next section.

Section 1.2. Magnetic moments and magnetization.

In magnetic materials two types of magnetic fields are present: the applied magnetic field due to external electrical currents and the magnetization of the material due to electrical microcurrents.
Ampere made the hypothesis that in ferromagnetic media microscopic circulating currents can be associated with the atoms present in the material. It was confirmed by the later investigations conducted by Reserford. The electronic motion inside an atom, according to the spin angular momentum, produces a microscopic current $\vec{j}_{micro}$ responsible for the generation of a local magnetic field $\bar{m}$. According to (1.1.12) we have

$$\bar{j}_{micro} = \nabla \times \bar{m} \tag{1.2.1}$$

The vector $\bar{m}$ defines the atomic magnetic moment. The density of the atomic magnetic moments is called the magnetization in point $\bar{r}$ of the body:

$$\bar{M} = \lim_{\Delta V \to 0} \sum_i \frac{\bar{m}_i}{\Delta V} \tag{1.2.2},$$

where index *i* refers to the atomic magnetic moments present in the small volume ΔV enclosing point $\bar{r}$.
Starting from the magnetization $\bar{M}$ we may introduce an equivalent magnetization current $\bar{J}_M$ for the considered volume of the ferromagnetic body (Fig. 1.2.1):

$$\overline{J}_M = \nabla \times \overline{M} \qquad (1.2.3),$$

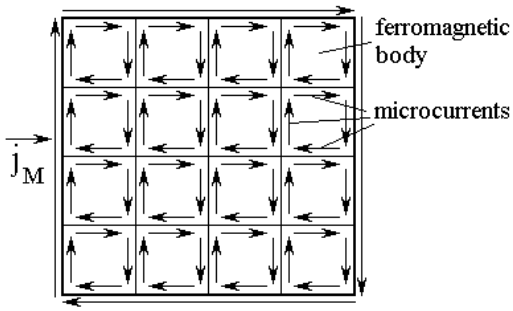

Fig. 1.2.1. Definition of the equivalent magnetization current.

The field $\overline{H}$ created by the external sources and the internal field $\overline{M}$ due to the magnetic moments are considered separately. Since both internal and external fields contribute to the magnetic flux density $\overline{B}$ the following relation can be established:

$$\overline{M} + \overline{H} = \frac{1}{\mu_0}\overline{B}_{\text{int}} + \frac{1}{\mu_0}\overline{B}_{ext} = \frac{1}{\mu_0}\overline{B} \qquad (1.2.4)$$

Considering (1.1.12) from both contributions we obtain

$$\nabla \times (\frac{\overline{B}_{\text{int}}}{\mu_0} + \frac{\overline{B}_{ext}}{\mu_0}) = \overline{J} + \overline{J}_M \qquad (1.2.5)$$

which finaly results in the general Ampere's law:

$$\nabla \times \overline{H} = \overline{J} \qquad (1.2.6)$$

It is well known that the magnetization $\overline{M}$ depends on the applied external magnetic field $\overline{H}$. This dependence is described by the constitutive law of the material. Here, the following material constants μ and χ are introduced:

$$\overline{B} = \mu_0(\overline{H} + \overline{M}) = \mu\overline{H} = \mu_0(1+\chi)\overline{H} \qquad (1.2.7)$$

μ is the permeability of the material and χ is its susceptibility. The permeability defines the relation between the magnetic flux density $\overline{B}$ and the external magnetic field $\overline{H}$. In the absence of the magnetic media the permeability is equal to μ_0. The susceptibility in this case is obviously equal to zero.

The term permeability of the ferromagnetic material defines its amplifying capabilities for the magnetic flux density $\overline{B}$ for a constant magnetic field $\overline{H}$.

Section 1.3. Interaction of the magnetic moments with the applied magnetic field.

The interaction energy of the magnetic moment $\overline{m}$ in a local magnetic field $\overline{H}_{loc}$ is defined as:

$$E_H = -\mu_0 \overline{H}_{loc} \cdot \overline{m} \qquad (1.3.1)$$

The local magnetic field $\overline{H}_{loc}$ in this case is the field acting on the moment. This field $\overline{H}_{loc}$ is the sum of the externally applied field (usually created by the macroscopic currents) and the magnetization created by the magnetic moments of the neighboring atoms inside the material.

The potential energy E_H favors the alignment of the magnetic moment along the local field $\overline{H}_{loc}$ as it corresponds to a smaller potential energy due to interaction with the field.

What happens if the magnetic moment is not perfectly aligned with $\overline{H}_{loc}$? It is known from the law of conservation of energy that the energy of the considered body can be changed via motion in the potential field or heat transfer. Let us neglect the heat transfer. Then the infinitesimal change of the energy ∂E_H can be interpreted as the work executed by the mechanical torque on the rotation of the magnetic moment over an angle $\partial\alpha$. The value of the torque can be found as:

$$T = \frac{\partial E_H}{\partial \alpha} = \frac{\partial}{\partial \alpha}\left(-\mu_0 H_{loc} m \cos\alpha\right) = \mu_0 H_{loc} m \sin\alpha \qquad (1.3.2),$$

where α is the angle between the external field and the magnetic moment. The analogous definition of the torque can be found in [Bozorth1993 p. 841].

Relation (1.3.2) can be extended to the macroscopic scale after substitution of m with the magnetization M of the body. It clearly shows that two permanent magnets with coplanar magnetizations in the vicinity of each other and with fixed axes will rotate in order to align their magnetizations.

In this case the energy defined in (1.3.1) is the interaction energy between the circulating currents. So circulating currents tend to align their axes.

In the real devices like electrical machines the excitation windings and the magnetic parts are separated in space. The mechanical behaviour of the motor is defined by the interaction of the physical currents in the conducting system and the magnetization currents (1.2.3) of the magnetic part. The susceptibility of the ferromagnetic material defines the ratio between the magnetization currents and the excitation currents. Since equivalent magnetization currents are usually larger the larger stresses are acting on the carrier of these currents, i.e. on the ferromagnetic body. In other words, the mechanical torque created by the machine is rather acting on the teeth of the magnetic core than on the winding in the slots. Thus the separation of the magnetic and the excitation parts in the electrical machine results in a decrease of the stresses acting on the windings.

Section 1.4. Magnetostatic energy.

Let us consider the case when the external currents are absent ($\overline{J} = \overline{0}$), but the ferromagnetic body with the magnetization $\overline{M}$ is present. Since the external currents are equal to zero, we have

$$\nabla \times \overline{H} = \overline{0} \tag{1.4.1}$$

From equations (1.2.3), (1.2.4) and (1.2.5) it can be derived that

$$\overline{J}_M = \frac{1}{\mu_0} \nabla \times \overline{B} \tag{1.4.2}$$

So the magnetization currents defined in section 1.2 can create the magnetic field beyond the ferromagnetic body. Taking the divergence of equation (1.2.4) and keeping in mind (1.1.13) the following can be obtained:

$$\nabla \cdot \overline{B} = \mu_0 (\nabla \cdot \overline{H} + \nabla \cdot \overline{M}) = 0 \tag{1.4.3}$$

or equivalently

$$\nabla \cdot \overline{H} = -\nabla \cdot \overline{M} = \rho_M \tag{1.4.4}$$

Considering equations (1.4.1.) and (1.4.4.) it can be concluded that the magnetic field $\overline{H}$ under the given conditions ($\overline{J} = \overline{0}$) has the properties of a potential field, i.e. can be written as the gradient of a scalar function. The term ρ_M is often called the free magnetic charges.

The magnetic field can be substituted by the gradient of a scalar magnetic potential ϕ:

$$\overline{H} = -\nabla \cdot \phi \tag{1.4.5}$$

$$\nabla^2 \phi = \Delta \phi = -\rho_M \tag{1.4.6}$$

The solution of this problem for a simple geometry has been obtained using standard finite element software (Fig. 1.4.1).

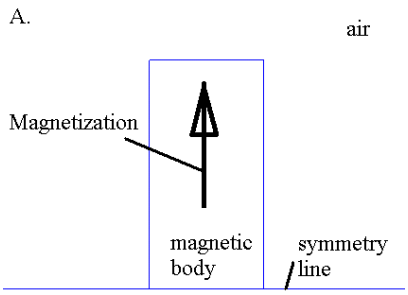

Fig. 1.4.1.A. Solution of the magnetostatic problem with presence of the magnetic media. A – geometry of the problem,

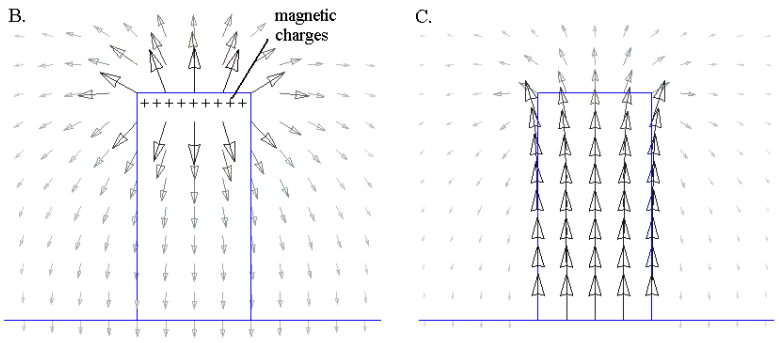

Fig. 1.4.1.B-C. Solution of the magnetostatic problem with presence of the magnetic media. B – magnetic field H-distribution, C – magnetic flux density B-distribution.

It can be seen that inside the magnetic body the magnetic field $\overline{H}$ and the magnetization $\overline{M}$ are pointing in the opposite directions. The top surface of the ferromagnetic body is acting as a positive charge. Since the magnetic field is pointing opposite to the magnetization (Fig. 1.4.1) inside the body it is also called a demagnetizing field.
The magnetic field and the magnetic moments of the ferromagnetic body oppose each other, which leads to the interaction energy introduced in section 1.3.
The energy in the material due to the demagnetizing field $H = -\nabla\phi$ is also called the magnetostatic energy (V_B= volume defined by the body):

$$E_M = \frac{\mu_0}{2}\int_{V_B}(\nabla\phi)^2 dV \qquad (1.4.7)$$

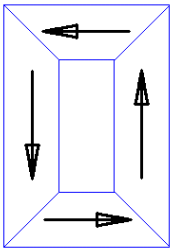

Fig. 1.4.2. The structure without free magnetic charges.

The smaller the demagnetizing field, the smaller is the magnetostatic energy. The demagnetizing field can be avoided by arranging the moments in such a way that no free magnetic charges are present, like the one shown in Fig. 1.4.2.

Section 1.5. Exchange energy.

The configuration of the magnetic moments in the real magnetic material is a result of a competition of a number of factors. In this section we are going to consider two of them, namely the thermal agitation and the exchange energy.
Thermal agitation is dominant at the high temperatures. It destroys any ordering of the magnetic moments and provides a paramagnetic state. If temperature decreases below the Curie point then the thermal agitation also decreases.
Since each atom has a magnetic moment it induces a torque on its neighbor (Section 1.3). It results in their alignment if forces of thermal agitation are sufficiently low. The more atoms are aligned, the stronger is their field, which results in the spontaneous magnetization of the whole volume of the ferromagnetic body. The energy keeping magnetic moments aligned is called exchange energy. The main feature of this energy is that it is isotropic in space.
So it can be said that the Curie point constitutes a boundary between the spontaneous magnetization and the paramagnetic state of the ferromagnetic material.
However the effect of thermal agitation does not vanish immediately after the transition of the material into the ferromagnetic state. Instead it leads to the reduction of the spontaneous magnetization. According to [Bertotti1998 p.137] this reduction becomes negligibly small at temperatures below $0.5T_C$. In our investigation this limit will not be exceeded. Therefore spontaneous magnetization is assumed to be independent of the temperature.

Section 1.6. Magnetic anisotropy.

1.6.1. Crystallographic anisotropy.

Atoms of iron occupy specific positions in the ferromagnetic body thereby producing the metal lattice (Fig. 1.6.1). It was found that there is a certain coupling between the lattice and each magnetic moment. This effect is normally referred as magnetic anisotropy. As it will be shown further this is not the only source of the anisotropy in the iron. In order to avoid possible confusion this mechanism will further be called crystallographic magnetic anisotropy.

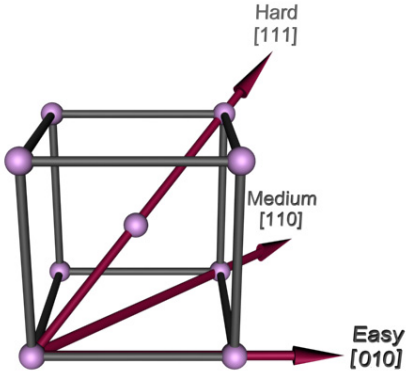

Fig. 1.6.1. Iron lattice.

In the beginning of the last century [Bozorth1993 p.592] different experiments were conducted in order to understand the nature of the magnetic crystalline anisotropy of iron. Experimentally, it was observed that in a structure similar to the lattice cell of iron, but on a much larger scale and with permanent magnets positioned in the place of the atoms of the lattice, the stable orientations of the permanent magnets are obtained parallel to the one of the easy crystallographic axes [100], [010] or [001], see Fig.1.6.1. The physics behind this phenomenon is more complicated than pure interaction of the magnetic moments because of the electrostatic fields created by the atoms of the cell, which affects the spin-orbit coupling of the electrons. In other words, the atomic structure cannot be completely replaced by the permanent magnets as the iron atoms are also involved in formation of the metallic bond. The latter introduces an additional effect on the circulation of the electrons.

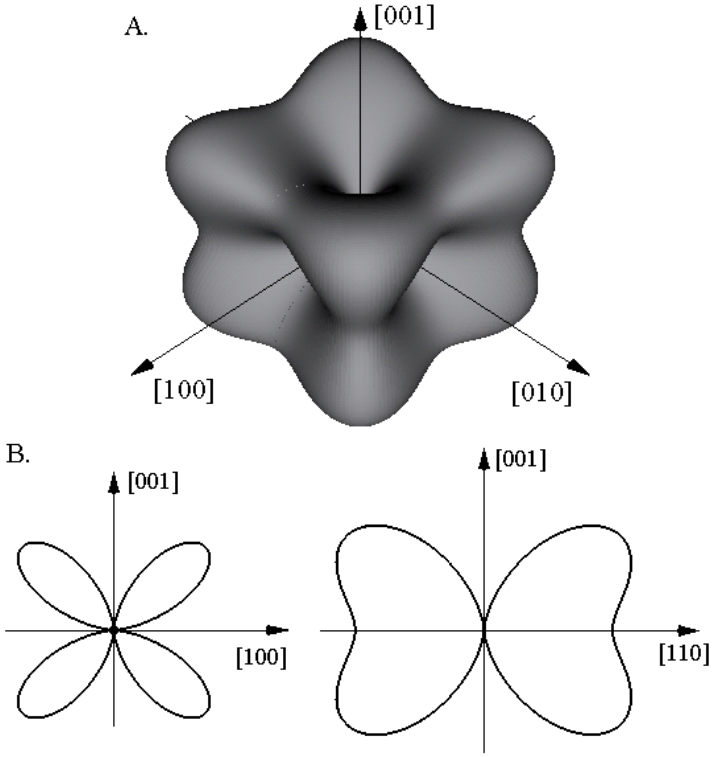

Fig. 1.6.2. Magnetic anisotropy distribution. A. space distribution, B. projections on the crystallographic planes.

Since iron lattice has a cubic symmetry, an analogous symmetry is present in the mathematical description of the iron magnetic crystalline anisotropy in terms of energy:

$$E_K = K_0 + K_1(\cos^2\alpha_1\cos^2\alpha_2 + \cos^2\alpha_2\cos^2\alpha_3 + \cos^2\alpha_1\cos^2\alpha_3) + K_2\cos^2\alpha_1\cos^2\alpha_2\cos^2\alpha_3 \quad (1.6.1),$$

where $\cos\alpha_1, \cos\alpha_2, \cos\alpha_3$ are the direction cosines of the magnetization M with respect to the easy crystallographic axes; K_0, K_1, K_2 are the anisotropy constants. K_0 is the isotropic component attributed to the exchange energy. If exchange energy is considered separately then K_0 can be omitted. The other two constants have the following values for iron: K_1=48000J/m^3, K_2=-5000J/m^3. As the second constant K_2 is one order smaller than the first one (K_1), we will further neglect it. The space distribution of the magnetic crystalline anisotropy energy is shown in Fig. 1.6.2.
Addition of Si affects the interaction between the atoms of iron and the lattice. So the anisotropy (K_1) monotonously decreases with an increase of the Si content [Cahn1987 p.535]. This is important for us as we will be working with the FeSi alloys rather than with a pure iron.

1.6.2. Magnetoelastic anisotropy.

There is another source of magnetic anisotropy. The ferromagnetic materials experience spontaneous deformation owing to the magnetoelastic energy [Langman1990]:

$$E_{me} = -\frac{3}{2}\lambda_{100}\sigma\sum_i \cos^2\alpha_i \cos^2\beta_i - 3\lambda_{111}\sigma\sum_{i\neq j}\cos\alpha_i\cos\alpha_j\cos\beta_i\cos\beta_j \qquad (1.6.2)$$

where λ_{100} and λ_{111} are the magnetostriction constants,

α_i are the direction angles of the magnetization with respect to the crystal axes,
β_i are the direction angles of the stress with respect to the crystal axes.
Here relatively small elastic stresses are considered. Then in the metals there is a linear dependence between the applied elastic stress and the corresponding elastic strain defined via the matrix equations. Therefore the mechanical stress in equation (1.6.2) can be replaced by the equivalent strain. So an elastic deformation of the ferromagnetic body leads to change of the magnetoelastic energy of this body.
This deformation can be spontaneous. When an external magnetic field is applied, the ferromagnetic materials experience spontaneous deformation called magnetostriction. The mechanism of this phenomenon will be discussed in the following chapters.
The spontaneous deformation of the ferromagnetic body occurs when the magnetization changes its orientation with respect to the crystalline axes. Notice that the sign of the magnetoelastic energy depends on whether the system is considered from inside, i.e. loosing its potential energy, or from the outside, i.e. performing the mechanical work. If the system is observed from the outside then the magnetoelastic energy is the work executed by the internal stresses on the deformation of the unit volume. Therefore if spontaneous deformation is investigated, then negative magnetoelastic energy should be used. After necessary mathematical transformations the following equation for the spontaneous deformation of the cubic crystal can be obtained:

$$\varepsilon = \frac{3}{2}\lambda_{100}\left[\sum_i \cos^2\alpha_i \cos^2\beta_i - \frac{1}{3}\right] + 3\lambda_{111}\sum_{i\neq j}\cos\alpha_i\cos\alpha_j\cos\beta_i\cos\beta_j \qquad (1.6.3)$$

In ferromagnetic materials, under normal circumstances, magnetization is always present and so does the deformation of the lattice due to the presence of the magnetic domains. This deformation becomes perceptible if the magnetization changes its orientation in the considered volume of the ferromagnetic body.

Consider deformation and magnetization acting in the [100] direction. From (1.6.3) it can be derived that deformation would be equal to λ_{100}, which provides the physical meaning of the magnetostriction constants. For pure iron λ_{100}=2.07E-5, λ_{111}=-2.12E-5. The mechanical stress can also be applied externally. In this case the magnetoelastic energy is brought inside the ferromagnetic body as a mechanical work executed by the external forces. For the sake of clarity in this chapter the external deformation is assumed to be dominant compared to the magnetostriction. Magnetostriction effects will be neglected further in this chapter. We will return to magnetostriction in Chapter 7.

The anisotropy energy is defined by the sum of the crystallographic anisotropy energy, see Eq. (1.6.1) and the magnetoelastic energy given by (1.6.2).

The magnetoelastic anisotropy is very close to our subject of interest. So, we will study it in more detail.

Case 1.
Consider stress (tensile or compressive) acting in the [100] direction. The distribution of the magnetoelastic energy for different orientations of the magnetization with respect to the crystallographic axes is shown in Fig. 1.6.3.

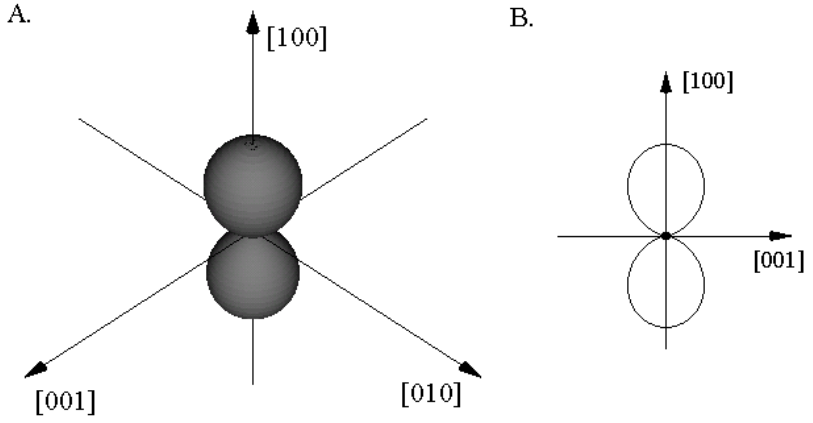

Fig. 1.6.3. Magnetoelastic energy. A. Space distribution. B. Projection on the [100][001] crystallographic plane.

From equation (1.6.2) it can be seen that only the first magnetostriction constant λ_{100} contributes into the magnetoelastic energy. So the energy has a clear axial anisotropy pointing in the direction of the stress.
Superposition of the magnetoelastic energy with other energetic components considered so far results in the effect shown in Fig. 1.6.4 and Fig. 1.6.5. The isotropic component corresponds to the exchange energy. In the present case it has just an auxiliary function, so it was chosen arbitrary.

Conclusions for case 1.

The elastic tensile stress acting along the easy magnetization axis in the iron lattice leads to a reduction of the anisotropy energy in the direction of the stress. The opposite takes place when compressive elastic stress is applied. However the magnetic anisotropy remains unaffected by the elastic stress in the plane oriented perpendicular to the stress.

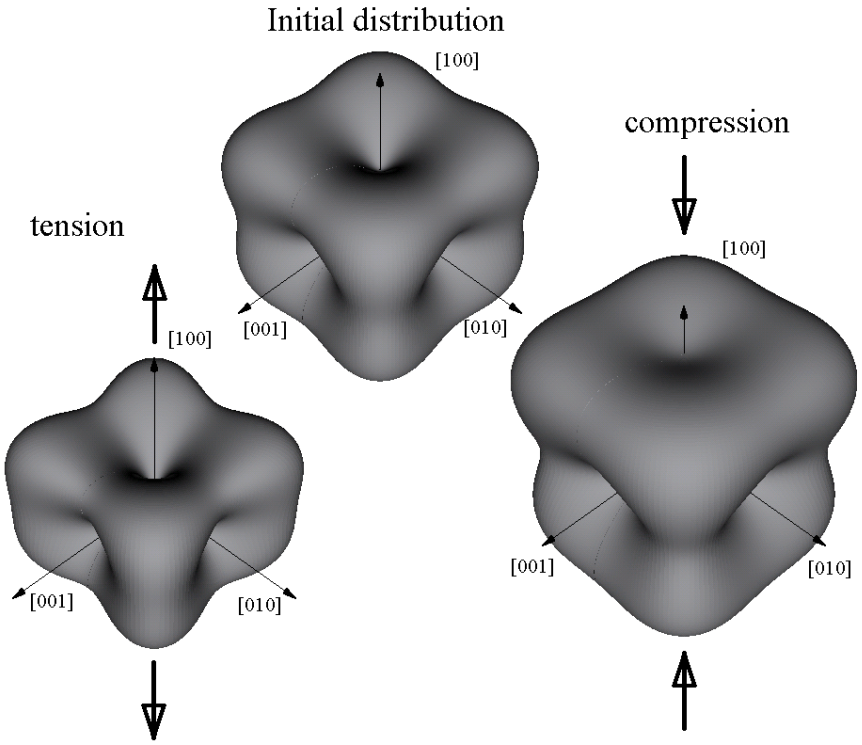

Fig. 1.6.4. Change of the initial anisotropy energy distribution due to the action of 30MPa tension and 30MPa compression in the [100] direction. The pictures show the sum of the crystallographic anisotropy energy and the magnetoelastic energy.

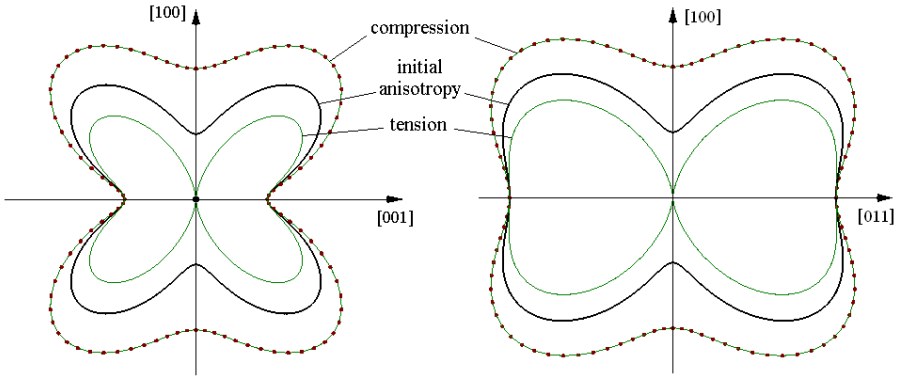

Fig. 1.6.5. Projections of the magnetoelastic energy space distributions under the action of the elastic stresses.

Case 2.

Consider the more complicated case. The stress acting in the [101] crystallographic direction results in the magnetoelastic energy shown in Fig. 1.6.6. This distribution is more complicated due to the action of the second anisotropy constant λ_{111} that has a negative sign. We find that the stress is affecting the most the plane normal to the direction of the stress. Indeed, let's confirm this by a simple calculation. Let $\cos\alpha_1 = \cos\alpha_3 = \cos\beta_1 = \cos\beta_3 = 1/\sqrt{2}$, and $\cos\alpha_2 = \cos\beta_2 = 0$. Then, from (1.6.2), $E_{me} = -\frac{3}{4}\sigma\lambda_{100} - 3\sigma\lambda_{111}\frac{1}{4}$. Taking into account the signs of the magnetostriction constants the value of the magnetoelastic energy is close to zero. If, for instance, $\cos\beta_1 = -1/\sqrt{2}$ then the sign of the second term in the expression of the magnetoelastic energy changes and the modulus of the energy increases. So my statement has been proved.

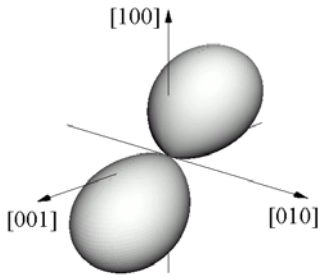

Fig. 1.6.6. Magnetoelastic energy due to the mechanical stress acting in the [101] direction.

The analogous superposition with the magnetoelastic energy was carried out on Fig. 1.6.7. It can be seen that the effect of the stress is perpendicular to its direction.

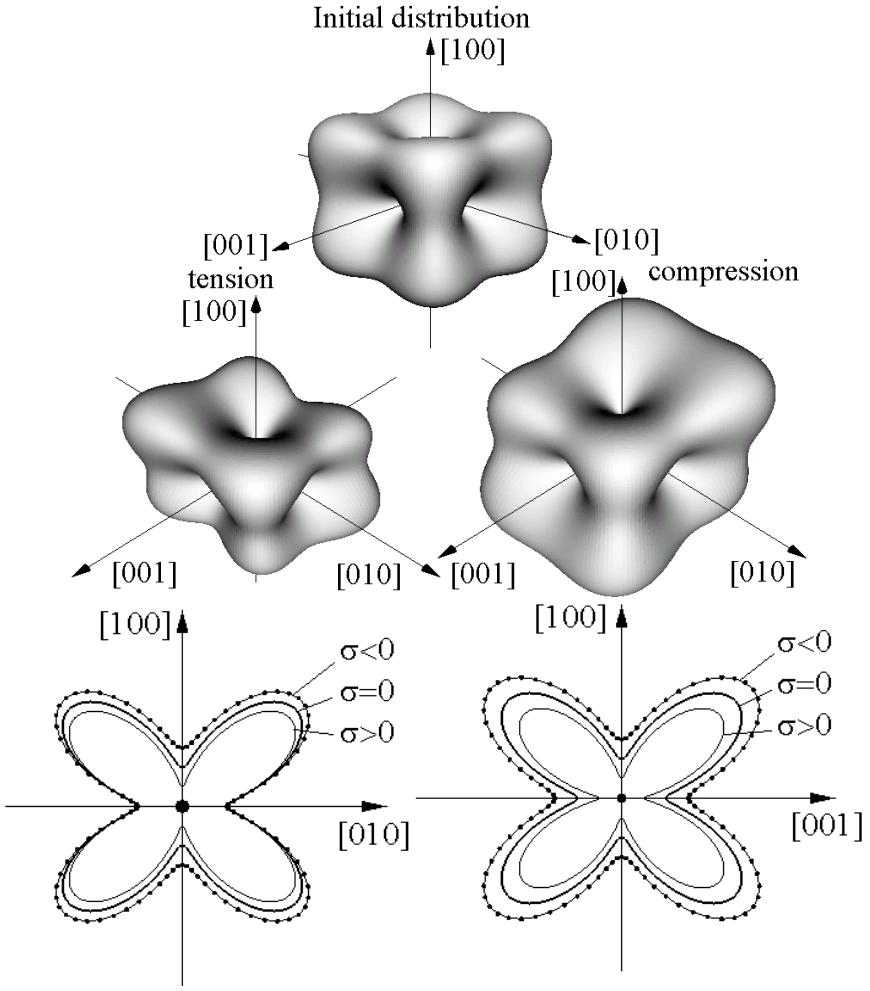

Fig. 1.6.7. Change of the initial magnetoelastic energy distribution due to the action of 15MPa tension and 15MPa compression in the [101] direction. The pictures show the sum of the crystallographic anisotropy energy and the magnetoelastic energy.

Conclusions for case 2.

Tension applied in the medium hard magnetization direction e.g. [101] results in decrease of the sum of the anisotropy and the magnetoelastic energies in the plane perpendicular to it. The opposite occurs for the compression. Thus the effect of the elastic stress depends on its orientation with respect to the crystallographic axes.

Case 3.

Addition of Si is known to have an effect on the magnetostriction constants [Bozorth1993 p. 649]. At a content of around 6.5% the material becomes virtually silent. However for technological reasons Si content normally does not exceed 3.5%.
In order to estimate the effect of the Si on the magnetoelastic energy and corresponding response of the system to the application of the elastic stress, let us consider material containing 3.5% Si. The following values were used for the calculation of the corresponding components of the energy of the system: K_1= 3400J/m^2, λ_{100}=2.6E-5, λ_{111}=-0.35E-5. In order to facilitate a comparison with case 2 the same stress values are used.
Since the anisotropy constant of this material is smaller than the one defined for pure iron and the magnetostriction constant λ_{100} is larger, the response of the system to the elastic stress applied along [100] increases accordingly (Fig. 1.6.8).

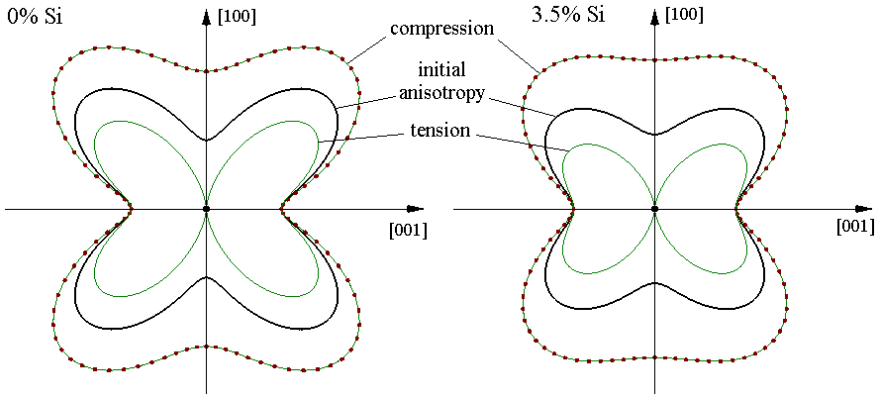

Fig. 1.6.8. Effect of addition of Si on magnetoelastic energy space distributions under the action of the elastic stresses.

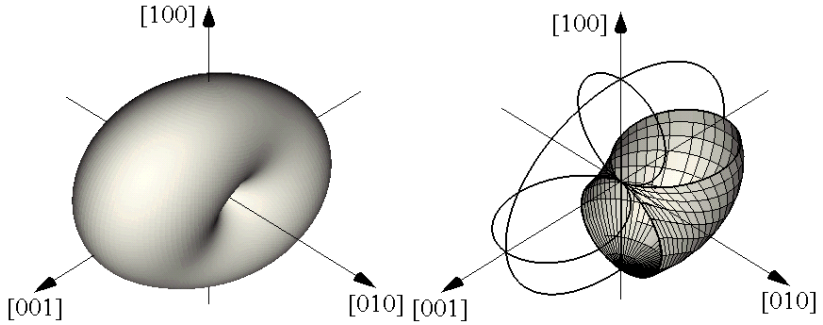

Fig. 1.6.9. Magnetoelastic energy due to the mechanical stress acting in the [101] direction after addition of 3.5% Si.

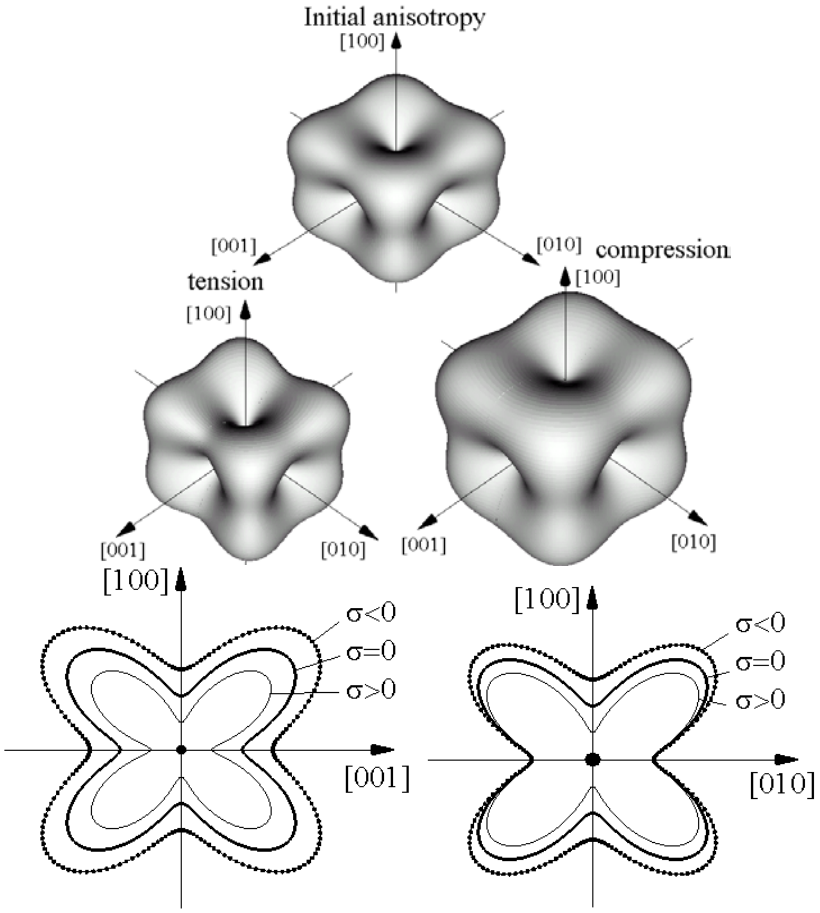

Fig. 1.6.10. Change of the initial energy distribution due to the action of 15MPa tension and 15MPa compression in the [101] direction after addition of 3.5% Si. The pictures show the sum of the crystallographic anisotropy energy and the magnetoelastic energy.

The magnetoelastic energy due to the stress applied along the [101] direction is also changed (Fig.1.6.9) as the absolute value of the second magnetostriction constant is much smaller.

Conclusions for case 3.

After addition of Si a decrease of the sum of the anisotropy and the magnetoelastic energies can be observed in the direction of the tensile stress. The opposite is encountered for the compression. The perpendicular plane is also affected but in a smaller degree compared to pure iron. Thus a response of the sum of the anisotropy and the magnetoelastic energies of the ferromagnetic material to the application of the elastic stress also depends on its chemical composition.

Section 1.7. Magnetic domains and domain walls.

The magnetic domains emerge in the ferromagnetic body as a result of the competition of the different components of the total energy of the system. The interaction energy forces the magnetic moments to align with the externally applied magnetic field. The exchange energy forces the magnetic moments to stay aligned next to each other. The anisotropy energy favors the alignment of the magnetic moments along the easy magnetization axis. Finally, the magnetostatic energy favors the configuration where no free magnetic charges are present. The magnetic domain structure is therefore the optimal energetic compromise which minimizes the sum of the different types of energies. The domain configuration resembles the one shown in Fig. 1.4.2 thereby providing a considerable reduction of the magnetostatic energy. Inside the volume of the magnetic domain the orientation is normally defined by the magnetic anisotropy of the material. A simple domain structure is shown in Fig. 1.7.1.

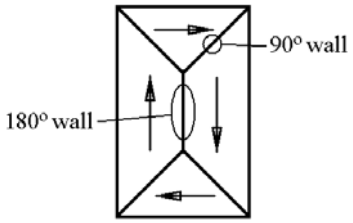

Fig. 1.7.1. A simple domain structure.

Fig. 1.7.2. The structure of the 180^0 domain wall.

The border between the two neighboring domains is called the domain wall. In the magnetic wall there is a distortion of the exchange energy. Therefore the wall takes a few atomic steps in order to smoothen the transition of the magnetic moments from one orientation to another. According to [Bertotti1998 p. 198] the 180^0 domain wall occupies in iron 250 lattice spacings. So generally speaking the domain wall is rather a volume than a surface, but for the materials investigated in this work the domain wall can be considered as a surface due to the relatively large size of the magnetic domains.
Under the action of an applied external magnetic field the domain walls can move in order to provide the corresponding response of the ferromagnetic body. Generally speaking, ferromagnetic materials are the amplifiers of the magnetic field, because the internal field can be few orders larger than the external one. So a relatively large magnetic flux can be obtained at much smaller fields compared to the case where no ferromagnetic materials are used. The first mechanism involved in the amplification is the intrinsic magnetization, which was discussed in the Section 1.2. The second mechanism involves the domain wall motion and defines the efficiency of the

ferromagnetic material as an amplifier. In an ideal material the domains are aligned parallel to the field and domain walls move smoothly. However in real ferromagnetic materials like non-oriented electrical steel, the domains are oriented randomly and the domain walls are often pinned to different types of the lattice irregularities.
Inside the domain wall the energetic equilibrium is, of course, also satisfied. If a certain pressure is imposed on the domain wall due to the action of the applied magnetic field the exchange energy between the neighboring atoms in the wall provides a rigidity. So if the wall is pinned to a certain defect in the lattice it can bow until it becomes energetically favorable to unpin and move to the new location.
This phenomenon is especially pronounced in the case when the material is in the demagnetized state and the applied magnetic field is relatively small. Bowing of the domain walls is an effective process in a sense that it leads to a negligible dissipation of energy in case of a quasi-static excitation. The domain configuration remains unchanged. The bowing of the domain wall is reversible in a sense that once the applied magnetic field is reduced to zero the domain walls tend to straighten back as it decreases the area of the domain walls. Consequently, the original domain configuration is recovered.

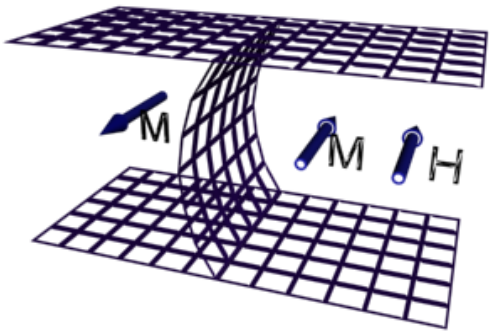

Fig. 1.7.3. Domain wall bowing under the action of the applied magnetic field.

The magnetic behaviour of the material at low fields is governed by the Rayleigh law [Bertotti1998 p. 310]. This law says that at low applied magnetic fields, the magnetization of the ferromagnetic material increases according to a quadratic law. For higher fields, the domains with a favorable orientation irreversibly expand. The ferromagnetic body gains certain magnetostatic energy, which facilitates further domain growth. The investigation of the Rayleigh zone provides important information on pinning.
Inside the volume of a domain the exchange and anisotropy energies are minimal, because the magnetic moments are oriented along each other. In the domain wall this uniformity is distorted (Fig. 1.7.2), which results in an increase of the potential energy. Therefore the energy stored in the domain walls is usually considered separately. This energy is defined by the total area of the magnetic domain walls.

Section 1.8. Hysteresis loop parameters.

When the applied magnetic field varies periodically in time, the sequence of the instantaneous magnetic states of the ferromagnetic body produces a hysteresis loop.

Depending on the value of the applied field it can lead to the considerable modification of the magnetic domain structure. Here we assume that the material is driven into the saturation at the maximum applied magnetic field. In this case the modification of the domain structure involves domain wall motion as well as rotation of the domains.
It is shown in [Bertotti1998 p. 349] that the domain wall movement is more favorable from the energetic point of view. Though it is difficult to tell exactly when one process finishes and another starts it is generally assumed that the rather vertical branches of the hysteresis loop result from the domain wall motion. This assumption is based upon the fact that a considerable change in the magnetization in these branches corresponds to a small change in the applied field. The rather horizontal branches of the loop correspond to a rotation of the domain walls. The smooth region in between corresponds to the transition zone between the two most common magnetization mechanisms.
The quasi-static limit magnetization loop (also called hysteresis loop) has a few distinctive parameters, which can be used in order to estimate the behavior of the magnetic material. We will consider here just two of them – the remanence and the coercive field.

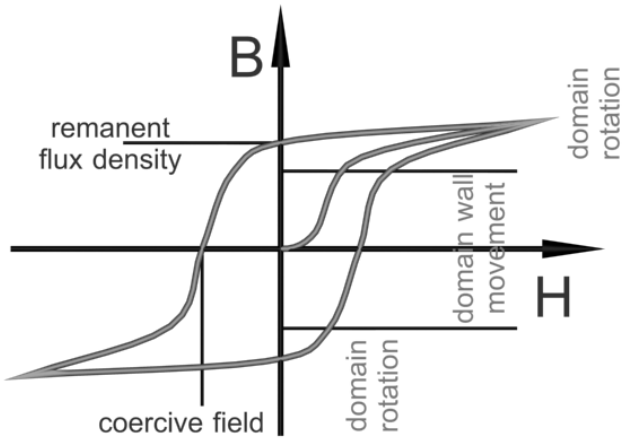

Fig. 1.8.1. Typical hysteresis loop of the ferromagnetic material.

The remanence is the residual magnetization of the ferromagnetic body remaining after the reduction of the applied magnetic field from saturation state to zero. The remanence is linked with the intricate properties of the ferromagnetic body such as the density of the pinning sites and the anisotropy. It can generally be assumed that the remanence induction is stronger in the direction where the anisotropy energy attains the smallest value.
Assuming quasi-static magnetization process, the coercive field is the magnetic field required in order to reduce the magnetization from remanence to zero. Pinning of the domain walls is mainly responsible for the coercive field in the polycrystalline materials we are investigating.
Several type of pinning sites exist: a pinning site can be positioned in one point, can be linear (1D) or a surface (2D). The point pinning sites emerge at the point defects of the iron lattice. The linear defects normally occur at the series of point defects and

dislocation tangles. The surface defects are the surface of the sample and the grain boundaries. The lattice defects will be considered later.
Pinning of the domain walls impedes the domain wall motion. So a ferromagnetic body with a larger amount of the pinning sites requires a larger field in order to achieve a new magnetic state. It therefore affects the slope of the hysteresis loop, which is usually estimated via the magnetic permeability.
The increment of the total magnetic energy of the system is defined as

$$dW_m = \overline{H} \cdot d\overline{B} \qquad (1.8.1)$$

It is necessary to note here that in the case of an unidirectional excitation it is more comfortable to consider the scalar values rather than vectors. This is generally correct because in many types of magnetic characterization techniques, the direction of the magnetic field $\overline{H}$ is constant and known, so it is sufficient to find the component of the magnetic flux density parallel to the magnetic field. There are occasions when there is also a component of induction normal to the applied field. This component however does not contribute to the energy of the system. Therefore transition to scalars is justified from the energetic point of view.
If the ferromagnetic body is positioned in an alternating magnetic field then the dissipated energy per unit volume during one time period T of the applied magnetic field corresponds to the area of the hysteresis loop. This energy is consumed by the ferromagnetic body and constitutes the total loss per cycle per unit volume:

$$W_{total} = \oint HdB = \int_{t}^{t+T} H\frac{dB}{dt}dt \qquad (1.8.2)$$

Notice that in (1.8.2) H denotes the magnetic field at the surface of the magnetic body, while B equals the space average of the magnetic induction over the cross-section perpendicular to the direction of the field. The total magnetic losses can be decomposed into hysteresis losses, classical eddy current losses and excess losses. These three components are of different nature and of different space and time scale. The theory of loss separation permits us to study the mechanisms responsible for each of the components.

The hysteresis component involves the domain wall motion and domain rotation due to the competition of the anisotropy, exchange and magnetostatic energies under the action of the applied magnetic field. This was considered above.

The consequence of the local domain wall motion on the local scale is the existence of local induced electrical currents, also called local eddy currents. The corresponding losses depend on the velocity of the domain walls. They are not dependent on the geometry of the ferromagnetic body. The domain wall velocity is defined by the rate of change of the magnetic flux density in the material. The losses due to the local induced currents can be decreased by a decrease of the domain wall velocity and by an increase of the resistivity of the material.
In the statistical model of losses introduced in [Bertotti1988] the simplest formula for the evaluation of the losses due to the local induced electrical currents, also called excess losses [J/kg], is as follows:

$$W_{exc} = \frac{8}{\delta}\sqrt{\frac{GSV_0}{\rho}}I_p^{3/2}f^{1/2} \qquad (1.8.3),$$

where ρ is the sample resistivity, δ is the material density, *S* is the cross-sectional area of the lamination, *G*=0.1356 is a dimensionless parameter and V_0 is a field parameter related to the local stochastic coercive fields. We recall that in formula (1.8.3) is only valid for materials where the number of active magnetic objects is proportional to the excess field. This is the case for non-oriented electrical steels.
According to this formula the excess losses seem to depend on the cross-section of the body. However in [Bertotti1998 p. 426] it is mentioned that the V_0 is inversely proportional to the cross-sectional area. So the excess losses in non-oriented electrical steels are, indeed, independent of the geometry.

The classical losses emerge due to the eddy currents induced by the global change of the magnetization in the ferromagnetic body. These losses are dependent on the geometry. In certain cases, when the rate of change of the magnetic flux in the sample is very high, a displacement of the flux towards the outer surface of the ferromagnetic body can appear. This leads to a virtual reduction of the cross-section of the ferromagnetic body.
Reduction of the thickness of the sheet is one of the actions to decrease the classical eddy current losses. Another possibility is to increase the resistivity of the ferromagnetic material as will be discussed in the next section.
The decomposition of the total magnetic losses can be easily carried out for simple geometries of the samples normally employed in magnetic measurements. In case of complicated geometries, for instance, those encountered in induction machines, a problem arises with the definition of the classical losses. It requires simulation of the 3D distribution of the eddy currents in the lamination having complex geometry, which complicates the numerical simulation.
If the amplitude of the periodically varying magnetic field gradually increases the tips of the corresponding hysteresis loops describe the magnetization virgin curve. A typical magnetization virgin curve of the ferromagnetic materials is shown in Fig. 1.8.2.

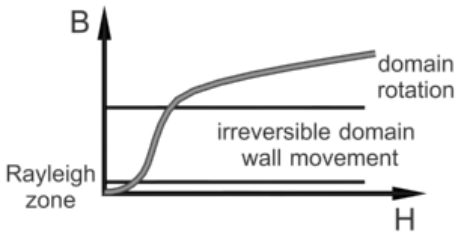

Fig. 1.8.2. Typical magnetization virgin curve of the ferromagnetic material.

Section 1.9. The effect of Si on the magnetic properties.

The magnetic properties of iron deteriorate considerably by the presence of carbon. A smaller deterioration occurs due to the presence of sulphur and oxygen [Bozorth1993 p.84]. So it is important to provide a reduction of the impurities during the production of the electrical steel.
As it was mentioned before, electrical steels are FeSi alloys as Si is often the main ingredient. Addition of the silicon results in a multiple effect on the properties of the steel. It leads to a considerable decrease of the electrical conductivity and a corresponding decrease of the classical and excess eddy current losses. An addition of 3% Si increases the resistivity more than 4 times compared to pure iron. It also

decreases the anisotropy constant, which is beneficial for non-oriented electrical steels as it makes the material less sensitive to the texture.
With respect to the magnetic permeability, the addition of silicon also leads to a positive change. It is shown in [Bozorth1993 p.30] that below 3%Si the maximum permeability of the material remains practically unchanged, but above 3%Si a considerable increase in the maximum permeability was encountered. The maximum value of the permeability was observed around 6.5%Si.
The density of the alloy decreases linearly with the addition of silicon, from 7870kg/m^3 for 0% Si to 7675kg/m^3 for 3% Si. It was also observed that the mechanical properties of FeSi alloys, such as the yield stress, are better compared to those of pure iron [Bozorth1993 p.77].

Section 1.10. Grain-oriented and non-oriented electrical steels.

Electrical steel is a polycrystalline material. It means that these materials consist of a large amount of grains. Grains can be oriented differently with respect to the chosen direction. The statistical distribution of the grains among different directions in the material is called texture. The grain-oriented electrical steels have a so-called Goss texture shown in Fig. 1.10.1. Grain-oriented steels have the best properties in the RD (rolling direction), moderate properties in the TD (transverse direction) and considerably worse properties in the direction that makes a 55^0 angle with the RD as it corresponds to the hard magnetic axis of the iron crystal.

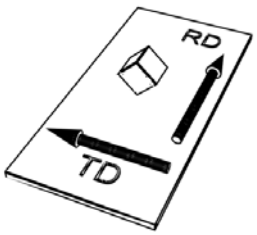

Fig. 1.10.1. Goss texture obtained after the cold-rolling.

Also non-oriented electrical steels are not completely isotropic. A certain difference between the RD and the TD can be noticed [Campos2001] [Landgraf2000]. The difference is usually due to the presence of the texture.
Within each grain the lattice is relatively uniform. As the total energy of the system tends to a minimum, the volume of the grain will be split into magnetic domains. The fact that the domain size is smaller than the size of the grain was confirmed experimentally for grain-oriented electrical steels. Using magnetic force microscopy, experimental confirmation was also obtained for the non-oriented electrical steels as reported in [Baudouin2002 p.96].
So if the size of the grain decreases, a corresponding decrease in the size of the domains can be expected. When an external magnetic field is applied, the domain configuration changes with a certain velocity. The value of the velocity of the domain wall is defined both by the rate of change of the applied field as well as by the distance the domain wall should move in order to provide the appropriate response in the magnetization of the ferromagnetic body. This distance is clearly smaller in material with smaller magnetic

domains. Therefore a decrease in the size of the magnetic grains results in a decrease of the excess losses in the ferromagnetic body [DeWulf2002] [Shimazu1990].
The grain boundary corresponds to 2D defects in the 3D iron lattice. So an increase of the area of the grain boundaries leads to an increase of the pinning of the domain walls in the material. So, for the materials considered in this work, a decrease of the size of the magnetic grains, results in an increase of the coercive field and in an increase of the hysteresis losses in the material.
Consequently, there exists an optimum grain size dependent on the rate of change of the magnetic field. This optimum grain size balances domain wall velocity with pinning. The optimization of the grain size for a sinusoidal field at f=60Hz was conducted for the low carbon steel in [Stephenson1986]. It was found that the optimum grain size is around 100μm. In [Denma2000] it is shown that Si content also has a certain effect on the optimal grain size.
The excess losses are sensitive to dynamic effects unlike the hysteresis losses. So it is generally true that the optimal grain size is smaller for higher frequencies.
In the grain-oriented steels the grain-size is usually larger than 100μm. In order to refine the magnetic domain structure laser scribing is applied [Weidenfeller1996] [Ponnaluri2001].

Conclusion.

In this introductory chapter the important magnetic quantities are introduced and the major relations between the different magnetic phenomena are described by Maxwell's equations and the constitutive laws.

Moreover, we considered in this chapter the energetic state of a material defining the orientation of the magnetic moments under the action of an applied magnetic field. This energetic state is defined by the interaction energy, the exchange energy, the magnetostatic energy, the crystallographic anisotropy energy, and the magnetoelastic energy. We assumed that only the magnetoelastic energy is modified due to the application of the mechanical stress. By considering some numerical examples we illustrated that applying mechanical stresses will lead to the modification of the (local) energetic state of the material resulting in a changement of the arrangements of the magnetic moments and consequently a changement of the magnetic properties of the material.

Chapter 2. The mechanical properties of the electrical steels.

Introduction.

As it was mentioned in the previous chapter, the magnetic properties of the electrical steel are first of all due to the atomic magnetic moments of iron. However the final properties appear to be linked with the orientation of the lattice and also with its purity as it affects pinning of the magnetic domain walls. Therefore, in this chapter some material parameters defining the properties of the lattice are introduced. Moreover, this chapter provides a simplified explanation of what is going on in the steel during plastic deformation.

During the study of electrical steels, a direct observation of the magnetic domains is rarely used due to its technical difficulty. However, having the information on the macroscopic magnetic properties of the material in combination with physical principles, we can have an idea about the magnetization processes inside the material. For instance, we can predict when the domain walls bowing is the dominant process and when the domain wall motion is favored. In material science, a lot of information on the internal magnetic or mechanical processes can also be obtained indirectly, for example, by the identification of the standard stress-strain curve, due to links between this curve and the mentioned internal processes.

It is not the intention of the author to provide a complete description of the processes in the steels. On the contrary, this chapter is an attempt to provide a simplified review of the relevant phenomena which eventually affect the magnetic properties of the non-oriented electrical steels.

Section 2.1. The defects in the metals.

In solid state, metals have a crystal structure, i.e. the atoms are orderly positioned in the lattice (Fig. 1.6.1). In an ideal metal this ordering remains the same in the whole volume of the sample. In that case we have a monocrystal. In real metals some irregularities always take place. The irregularities are divided according to their shape and size into 1D, 2D and 3D defects.

The 1D or point defects are very small and normally do not exceed 2 periods of the lattice. The most common point defect of this type is a vacancy (Fig. 2.1.1), i.e. a place in the lattice which is not occupied by an atom.

When the temperature increases the concentration of the vacancies increases, because atoms situated at the surface of the metal can leave the lattice and their place can be taken by atoms from the inside of the material. Other possible reasons for the nucleation of these defects are plastic deformation and X-Rays. The behavior of the vacancies is tightly linked with a diffusion.

Another known point defect is a interstitial atom. This defect appears when one of the atoms of the lattice leaves its place and stays somewhere in another cell. It also leads to the formation of the vacancy. However concentration of these defects is small since their nucleation requires more energy.

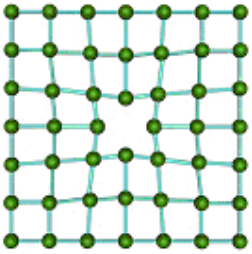

Fig. 2.1.1. Vacancy.

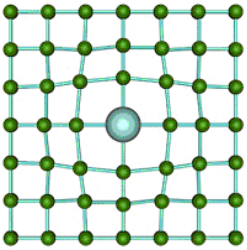

Fig. 2.1.2. Substitutional impurity.

It is well known that there are always some atoms of other chemical elements present in the lattice. They either occupy the place of the main atoms in the lattice, thereby producing a substitutional impurity (Fig. 2.1.2), or embed the cell of the lattice (Fig. 2.1.3). What happens depends on the relative size of the atoms of impurity with respect to the size of the main atoms of the lattice and the distance between the atoms. The nucleation of the interstitial impurity and its movement inside the metal occur without nucleation of the vacancies. So this process consumes less energy compared to the case of a substitutional impurity. Therefore small atoms like C diffuse easier in the metal than the larger atoms like Si.
Point defects result in a distortion of the lattice and the formation of local stress states in all directions.

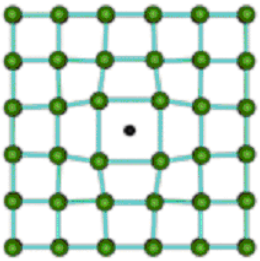

Fig. 2.1.3. Interstitial impurity.

Linear defects can be as long as a length of the grain. In the other two dimensions they are small. Sequences of the point defects relate to the linear defects. But the most common defects of the linear type are the dislocations. Dislocations are linear distortions of the lattice with a shift zone. Two extreme forms of dislocations are shown

on Fig. 2.1.4 and 2.1.5. The structure of the dislocations in the real metal is more complicated. Real dislocations might be the mixed forms of edge and screw dislocation.

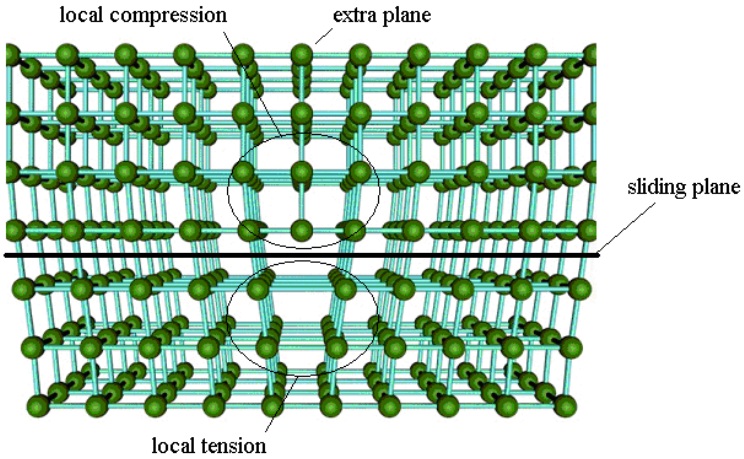

Fig. 2.1.4. Edge dislocation.

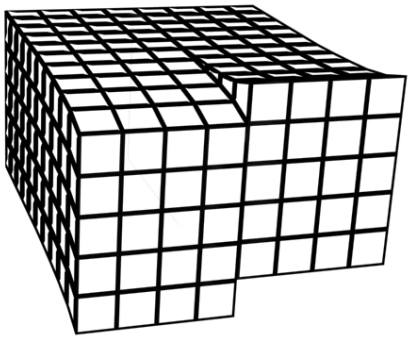

Fig. 2.1.5. Screw dislocation.

A surface along which the shift takes place is called the sliding plane, because it takes less energy for the dislocation to slide along this plane rather than to move in the orthogonal direction. This is common for all the types of dislocations. Another common feature is that the dislocation leads to a complicated local stress state that involves both tension and compression (Fig. 2.1.4).

When liquid metal is cooled down solidification starts simultaneously in a certain number of places called nuclei. In isotropic material, the nuclei are oriented randomly with respect to each other, which reflect on the orientation of the lattice growing around them. The growth stops when lattices with different orientations encounter each other. The volumes with an ordinary lattice orientation are called the grains and the surface separating the grains is denoted as a grain boundary. The grain boundary is a typical 2D defect of polycrystalline materials.
3D defects have sizes considerably larger than a period of the lattice. They consist of cracks, voids and large inclusions of other materials.

The linear and point defects emerge in the crystal lattice already during the crystallization process of the metal. The interaction of the defects produces new irregularities. For instance, a chain of the vacancies can lead to the nucleation of the dislocation. It is shown in [Djachenko1982 p. 28] that it is energetically favorable for the group of the vacancies to make a dislocation than to produce a void.
In electrical steels the dominant lattice defects are the dislocations. The dislocation density is a parameter used in order to estimate the amount of this type of defect in the lattice and defined by the total length of the dislocations in one unit volume of the metal.

Polycrystalline materials in the annealed state have a dislocation density of 10^{10}-10^{13}m^{-2}. The limit dislocation density that can be achieved in the crystal is equal to 10^{16}m^{-2} according to [Djachenko1982 p. 30].

Section 2.2. Elastic and plastic deformation of the lattice. Movement of the dislocations.

2.2.1 Elastic deformation

The elastic properties of the metal are provided by the rigidity of the lattice. The term "elastic" means that the material recovers its initial dimensions when the external force is released.

In the case of linear elastic behaviour, the elastic properties of the metals under the action of uniaxial stress are described by Hooke's law:

$$\sigma = E\frac{\Delta l}{l} \qquad (2.2.1),$$

where E is Young's modulus, Δl is the elongation of the sample and σ is the uniaxial stress.

2.2.2 Plastic deformation

Beyond a certain stress, the deformation of the material becomes irreversible, i.e. it does not recover its initial dimensions after unloading. This stress is denoted as the elastic limit or the yield point. Technically, the yield stress is defined as the stress corresponding to an irreversible strain of 0.2%. It was experimentally discovered [Cahn1987 p. 74] that the elastic limit for metals is few orders smaller than the theoretical estimated value for the considered type of the lattice taking into account the interatomic forces. The difference is due to the fact that in metals under the normal conditions the irreversible deformation is provided by dislocation movements rather than by the rigidity of the lattice. It is energetically favorable for the material to create a local distortion (dislocation) and break the link between the atoms in one row than to break the links between two neighboring layers of atoms in order to shift the lattice on one atomic step. As an example, a schematic representation of the nucleation and movement of the edge dislocation under the action of shear stress is shown in Fig. 2.2.1.

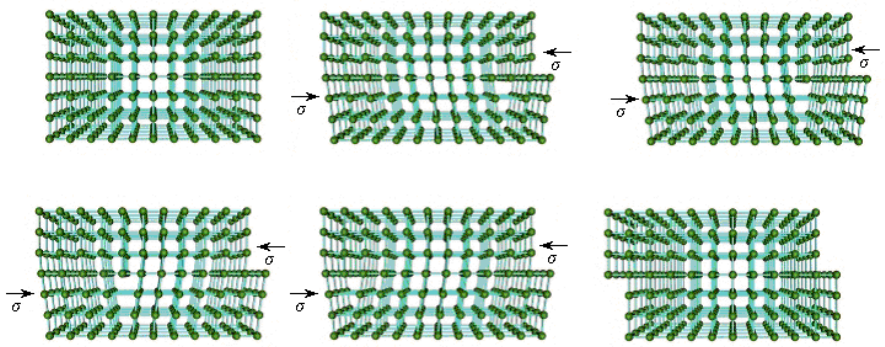

Fig. 2.2.1. Nucleation and movement of the edge dislocation under the action of shear stress.

2.2.3 Stress-strain curve

As in chapter 3, 6 and 7, we study the magnetic properties of SiFe alloys under elastic and plastic deformation, we recall that the mechanical behaviour can be described by a stress-strain curve, as shown in Fig. 2.2.2. Analogous curves were reported in [Hug2002], [Baudouin2002 p. 39] for different grades of non-oriented electrical steels.

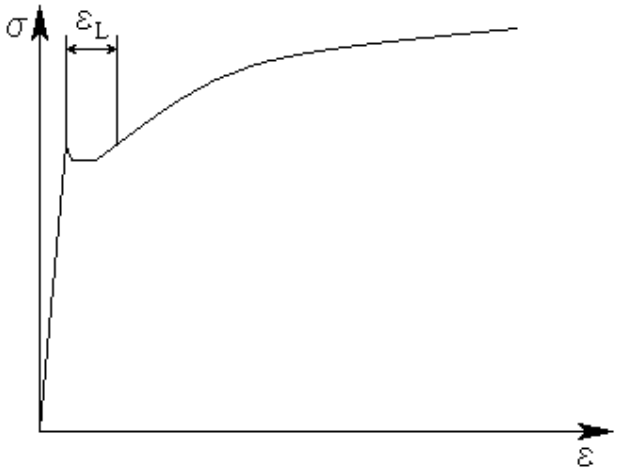

Fig. 2.2.2. Typical stress-strain curve of FeSi alloys showing a non negligible Lüders band (ε_L).

The Lűders band defines the strain range where the plastic deformation becomes unstable, i.e. there is an uncertainty about the strain ε at a given applied stress.

The movement of the dislocations occurs in specific crystallographic planes. According to [Djachenko1982 p. 34] a face centered cubic iron lattice has 12 possible sliding planes. The sliding happens under the action of the shear stress that achieves its maximum in the planes oriented at 45^0 with respect to the direction of the tensile stress. So the dislocation movement begins in the favorably oriented grains. The dislocations cannot easily cross the grain boundaries due to the change of the sliding plane as well as a considerable lattice distortion. However a series of dislocations introduces a certain stress in the neighboring grain, which can lead to the initiation of the plastic deformation there as well. But the efficiency of introducing a certain stress in the neighbouring grain depends on the angle between the sliding planes. Finally the plastic deformation starts spreading from one grain to another. Due to the non-homogeneity of the material in a certain volume this spreading of plastic deformation is going faster.

Section 2.3. Annealing of fully-processed materials

The material absorbs energy during plastic deformation by a growth of the dislocation density. This is the case when shaping the sheets in order to construct the magnetic core of electrical machines and consequently destroy the good magnetic properties of the material. A thermal treatment that results in a recovery of the properties of the material is called annealing. There are two different types of annealing: stress relief annealing and recrystallization annealing.

A stress-relief annealing is normally conducted at the temperatures above 180^0C and below 800^0C. According to [Wu2002] the tangles of the dislocations redistribute and partially annihilate. Annihilation is usually small, so the number of dislocations remains practically unchanged. Another important consequence of the redistribution of the dislocations is a reduction of the residual stresses, since the redistributed dislocation structure is favored from the energetic point of view. However if a cellular structure is present in the grain, things go different. A cellular structure is defined as a dislocation system with a highly non-uniform density within the grain [Cahn1987 p. 142]. The volumes with the highest dislocation density are denoted as the walls of the cells. The cellular structure of the dislocations is more stable and remains practically unaffected by the induced thermal agitation. Though some small changes can be noticed. The walls of the cells get narrow and the size of the cells increases. The dislocations situated inside the cells are attracted by the walls. So the stress-relief annealing is effective only if plastic deformation did not exceed 5-10%.

According to *www.steel-n.com* the stress-relief annealing after punching and shearing for non-oriented electrical steels requires a temperature from 750^0C to 800^0C and an annealing time between 1.5 and 2.5 hours. Another electrical steel producer [AK1 p. 15] suggests annealing at a temperature between 732^0C and 843^0C. The low figure corresponds to the flat laminations of narrow widths. According to [Yanez2002 p. II-13] annealing at 800^0C for 6 hours is sufficient for the complete recrystallization of one of the grades of electrical steel. So the thermal treatment proposed in *www.steel-n.com* and [AK1] actually constitutes an incomplete recrystallization annealing. This is confirmed by the figure presented at [AK1 p. 14].

Section 2.4. Coating of the electrical steels.

Coating is a protective layer that is put on a sheet in order to provide insulation between the laminations of the magnetic core. It also protects the steel from corrosion. The requirements to the coating somewhat confront each other. It should provide good insulation [Lindenmo2000][Loisos2001] and sustain the mechanical contact with a burr but also stay thin in order to avoid reduction of the fill factor of the stacked magnetic core. In order to reduce the wear of the punching set the coating should have a certain lubricating property. We recall that we have organic and non-organic coatings used for electrical steels.

Organic coating has a certain lubricating effect, which is used in order to reduce the wear of the cutting tools during punching. A clear disadvantage of the organic coating is that it can be damaged during the thermal treatment. For instance, the carbon from the coating can easily diffuse in the steel thereby deteriorating its magnetic properties. So stress-relief annealing cannot be done with this type of coating present [AK1].

Non-organic coatings do not have this disadvantage. So if during production the sheet was subjected to plastic deformation it can be recovered by an appropriate thermal treatment. In some cases a controlled oxidation is used in order to provide an insulation of the sheet. However this approach leads to the worsening of the magnetic properties [Bozorth1993 p.84] and remains applicable only for low-power electrical devices owing to the low voltage between the laminations. According to [Nozawa1996 p. 575] the oxides have a smaller coefficient of thermal expansion than the matrix. It helps to develop the isotropic tension in the matrix, which, as we shall see later on, has a positive effect on the magnetic properties of the electrical steels.
The main disadvantage of the non-organic insulation is that it does not provide sufficient lubrication, which increases the wear of the cutting tools.

Chapter 3. Mechanical stresses in electrical machines and transformers due to the construction process.

Introduction.

Electromagnetic energy conversion always requires time dependent magnetic field patterns, which leads to eddy current losses in the magnetic core of the device. In order to decrease these losses the magnetic core is assembled from thin sheets. In some cases, e.g for DC machines, only a static magnetic field is present in a part of the magnetic core. In these cases, there is no need for a laminated structure of the magnetic core. Nevertheless, due to the complexity or other reasons (power electronic supply), the part with a static magnetic field is also constructed using laminated materials.
The desired shape of the sheets is achieved by the separation of material along a specified path. This separation can be performed by one of the following ways:

1) local melting;
2) treating material by chemically aggressive substances, e.g. sulphur acid;
3) applying locally an excessive plastic deformation.

The first type of separation is performed by means of e.g. laser cutting. This type of cutting results in relatively high cutting speeds. When appropriate settings are used, a good quality of the cut edge can be provided. Laser cutting is rather flexible and permits to switch from one geometry to another with minor modification of the facilities. However this method of material separation induces residual thermal stresses. Recently performed X-Ray [Baudouin2002 p. 66] analysis has shown the presence of the residual tensile stresses up to 300MPa at the cut edge, which is definitely a considerable drawback. Another disadvantage of the laser cutting is its high cost. Taking into account the merits and the drawbacks of the method it appears to be more suitable for small series or prototype production.
The second type of material separation is implemented by electro erosion. This method results in a cut, free of any stresses. But the process is slow, which limits its applicability.
Mechanical cutting and water-jetting belong to the third type of material separation methods. Water-jetting provides a good quality of the cut **[**Schoppa2003_2**]**, but due to the need for special equipment and relatively low cutting speed it remains rarely used at the moment. The mechanical cutting constitutes the fastest and the cheapest procedure and therefore the most popular. For this reason we concentrate our attention on this method for material separation. However this method leads to plastic deformation at the edge of the sheet. In Section 3.3 the deformation affected zone is investigated both numerically and experimentally. The 3D effect of punching is evaluated taking into account the complexity of the shape of the sheet.

The laminated magnetic core has to be held together. This is required for the normal operation of electromagnetic devices. If the neighboring laminations of the core start moving with respect to each other, it easily destroys their coatings, which results further in a considerable increase of the eddy-current losses. In large machines, like turbo generators, it can eventually lead to melting of some parts of the magnetic core. Therefore, the magnetic core should be sufficiently “solid” and properly fixed in order to provide the normal operation. As it often happens, the solution of one problem leads to another one. Fixation of the magnetic core leads to the introduction of new mechanical stresses. This problem will be addressed in Section 3.2.

It appears that the most important part of the deformation emerges due to punching of the sheets. Mechanical punching is a fast, relatively simple and cheap way of obtaining the required shape of the sheets. If certain requirements with respect to clearance, positioning and quality of the cutting tools – discussed in the next sections – are met, then this procedure can also provide sufficiently good precision of the final geometry.
The mathematical approach used for the numerical investigation is considered in the Section 3.1.

Section 3.1. Finite element computations in solid mechanics.

In science we often have to deal with problems where the unknown variable is a solution of a partial differential equation defined in a specific part of space. In case of mechanics the unknown is the displacement of a specific point of the medium. Due to the complexity of the shape of the investigated geometries, an analytical solution for most of the structures, appearing in practice, cannot be provided. For this reason, numerical computation methods have become popular.
The most popular method is the finite element method, which is applicable to a broad range of field problems.
In the mechanical computations described in this chapter, as a first approximation, we neglect any heat generation in he body, which corresponds with the quasi-static loading of material. Consequently, the energy of the deformation of the loaded body must correspond to the work executed by the applied external forces.
The deformation energy of the body, with volume V, is defined as:

$$E_{def} = \int_V \frac{1}{2}(\varepsilon)^T(\sigma)dV \qquad (3.1.1)$$

The work executed by the external forces can be computed as:

$$W_{forces} = \int_S (f)^T(u)dS = \int_S (u)^T(f)dS \qquad (3.1.2),$$

where S normally corresponds to the surface of the deformable body. In some cases the load can be applied from inside the body, e.g. in the case of electromagnetic forces. Then $(f)^T(u)$ must be integrated over de volume of the deformable body.
Hooke's law, defined in the previous chapter, was dedicated to the 1D case when only the deformation in the direction of the stress must be described. But, in general, a mechanical load results in a deformation of the body also in the other directions. It requires operation with the stress and strain tensors. For such calculations in two dimensions (xy-plane), a more complex formulation is used:

$$\begin{pmatrix} \sigma_{xx} \\ \sigma_{yy} \\ \sigma_{xy} \end{pmatrix} = \frac{E}{1-\nu^2}\begin{bmatrix} 1 & \nu & 0 \\ \nu & 1 & 0 \\ 0 & 0 & (1-\nu)/2 \end{bmatrix}\begin{pmatrix} \varepsilon_{xx} \\ \varepsilon_{yy} \\ 2\cdot\varepsilon_{xy} \end{pmatrix}, \quad (\sigma) = [D](\varepsilon) \qquad (3.1.3)$$

If deformations are small then the elastic strain vector can be defined as follows:

$$\begin{pmatrix} \varepsilon_{xx} \\ \varepsilon_{yy} \\ 2\cdot\varepsilon_{xy} \end{pmatrix} = \begin{bmatrix} \frac{\partial}{\partial x} & 0 \\ 0 & \frac{\partial}{\partial y} \\ \frac{\partial}{\partial y} & \frac{\partial}{\partial x} \end{bmatrix} \begin{pmatrix} u_x \\ u_y \end{pmatrix}, \qquad (3.1.4)$$

where u_x and u_y are the functions defining the displacement of each point of a deformable body in the xy-plane.

In this work, deformation of materials are calculated by finite element procedures. Here the deformation (u_x,u_y) at each point as a result of external forces or enforced displacement at boundaries are obtained by achieving an equality between the deformation energy of the body (3.1.1) and the work performed by the external forces (3.1.2).

Section 3.2. The elastic stresses in electrical steels

3.2.1. Stresses due to assembling and fixation of the magnetic core.

The magnetic core is gripped in the frame in order to avoid a displacement of the laminations and in order to decrease vibrations of the stack during operation of the device. The mechanical stresses introduced due to this type of assembling are of elastic nature.

In transformers and large electrical machines, the core is normally compressed in the direction perpendicular to the plane of the sheets by means of bolts and special non-magnetic metal plates (Fig. 3.2.1). This compression results in an increase of the friction force between the laminations and keeps the core solid. The value of applied compression is chosen according to the length of the core, i.e. the longer it is, the larger the applied compression. Different producers use different compressions. An inquiry performed in Russia has shown that compressions higher than 9MPa are not applied in practice.
In a laminated core the load applied to the surface of the core can be assumed uniformly distributed in the cross-section after a few laminations.

The stator sheets of low power induction motors are normally compressed in the frame of the motor (Fig. 3.2.2) when the frame is hot. After cooling down of the frame the stator core is subjected to a uniform radial deformation. This method of fixation is simple and technological, but it leads to complicated stress patterns in the yoke of the stator (Fig. 3.2.3, 3.2.4, 3.2.5). In the example, the outer diameter of the sheet is equal to 140 mm. A uniform normal displacement towards the center of the sheet, equal to 20 μm, is applied to the outer boundary, which results in mechanical stress reaching 163MPa in certain areas of the sheet. The highest stress is situated just above the slot. The teeth of the sheet remain almost unaffected by these stresses. The stator sheets are subject mainly to compression (Fig. 3.2.5). Since the problem is linear, it is sufficient to

perform calculations for one deformation only. For another case it is possible to scale the numerical values, because distribution of the stresses and strains remains the same.

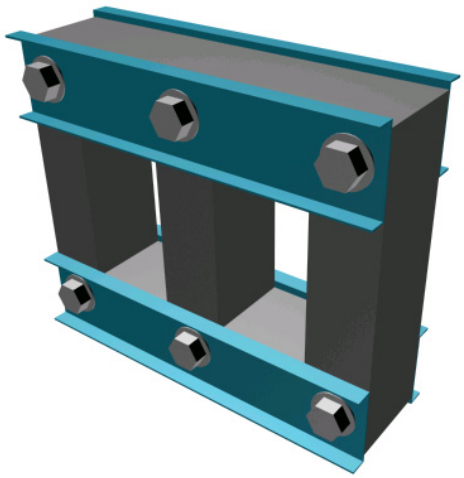

Fig. 3.2.1. Compression of the magnetic core in transformers and high power electrical machines.

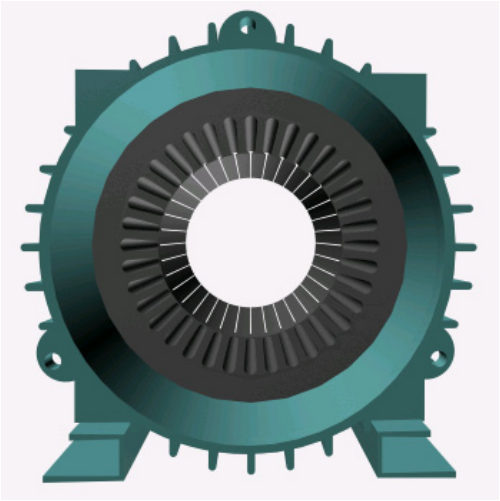

Fig. 3.2.2. Compression of the stator in the low power induction machines.

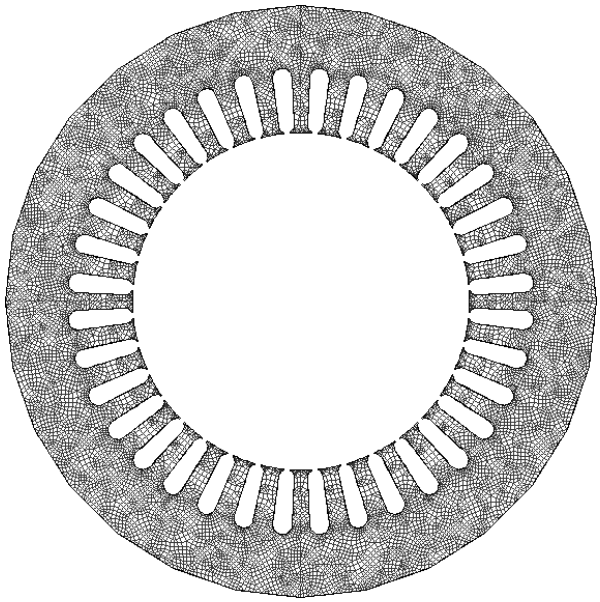

Fig. 3.2.3. Quadrilateral finite element mesh with 16911 nodes and 15289 elements.

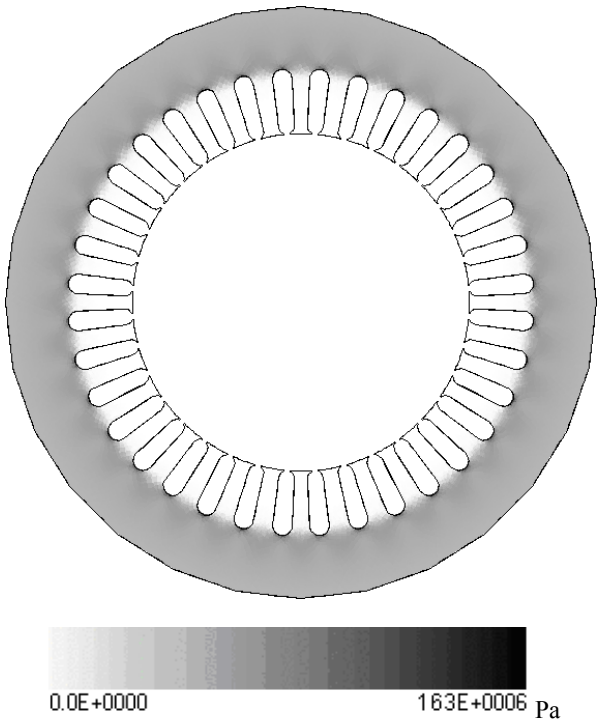

Fig. 3.2.4. Stress distribution in Pa in the stator sheet obtained by FE computations.

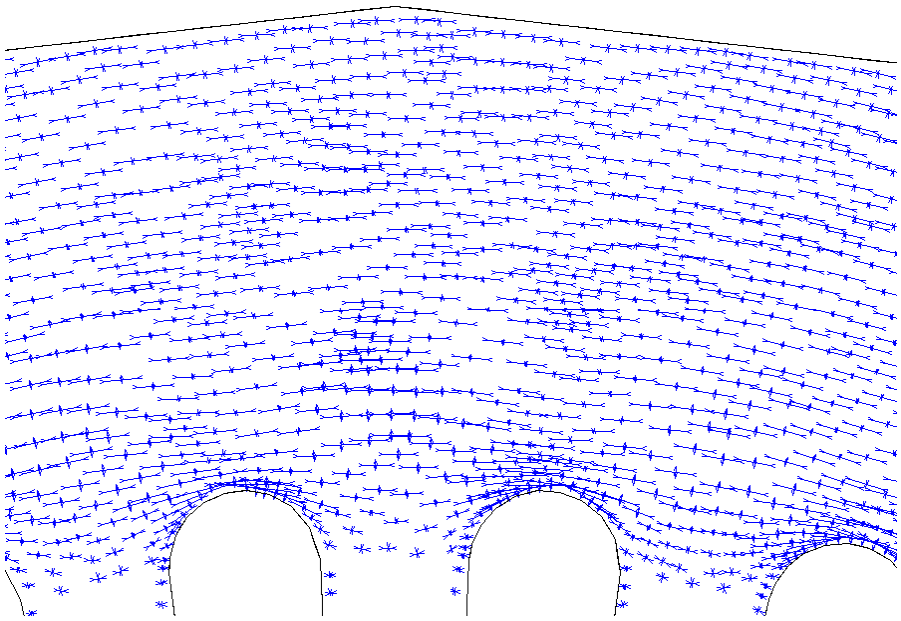

Fig. 3.2.5. Strain distribution in the stator sheet (the arrows define the principal strains) obtained by FE computations.

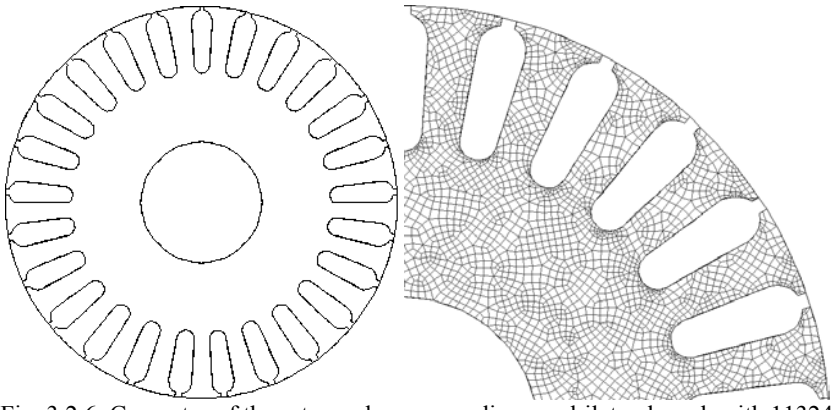

Fig. 3.2.6. Geometry of the rotor and corresponding quadrilateral mesh with 11324 nodes and 10186 elements.

A similar situation is present in the rotor (Fig. 3.2.6). The outside diameter of the rotor is equal to 80 mm. The rotor core is compressed on the shaft which imposes a uniform deformation to the internal surface of the core. A uniform radial displacement equal to 10 μm was applied to the internal surface of the rotor. The simulation shows that the stress (Fig. 3.2.7) is also mainly concentrated in the yoke of the core. The only difference with the stator is that the stress is concentrated at the inner part of the sheets.

Like in the previous case the stress in the teeth is negligible. However the strain distribution (Fig. 3.2.8) indicates that the core of the rotor is affected both by tension and compression.

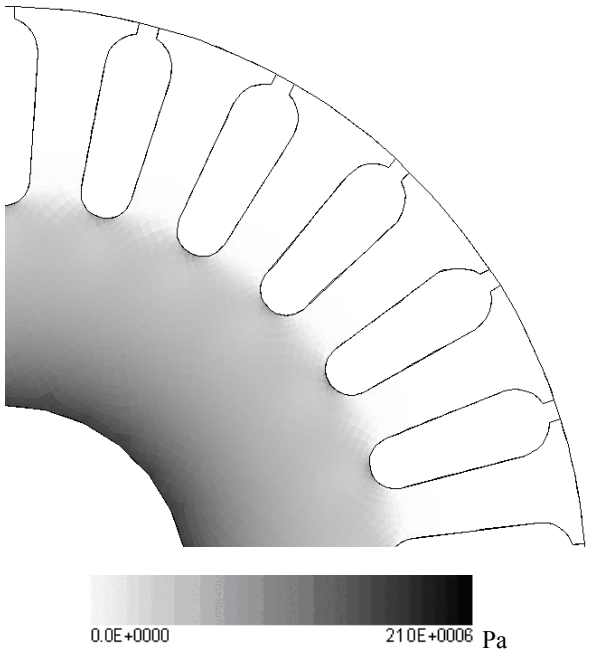

Fig. 3.2.7. Stress distribution in Pa in the rotor sheet obtained by FE computations.

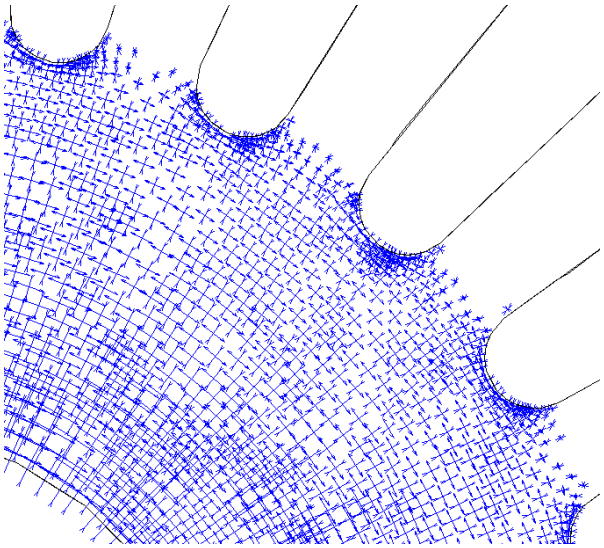

Fig. 3.2.8. Strain distribution in the rotor sheet (the arrows define the principal strains) obtained by FE computations.

3.2.2. Stresses due to bending.

During production of the sheets certain bending can take place [Godec1977]. The inner surface of the sheet with respect to the bending radius is subjected to compression (Fig. 3.2.2.1) and the outer one is subjected to tension.
The maximum strain and the corresponding stress can be obtained using the simple relation:

$$\varepsilon = \frac{1}{\frac{2R}{t}+1},\ \sigma = E\varepsilon \qquad (3.2.2.1)$$

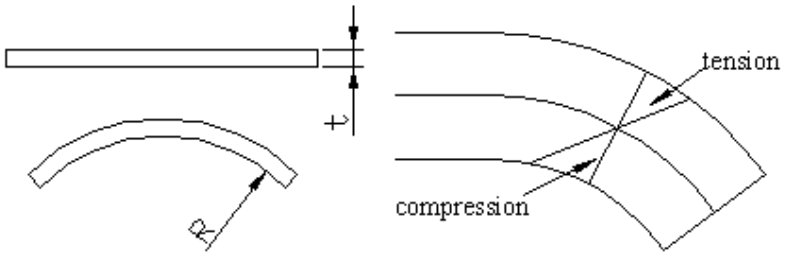

Fig. 3.2.2.1. Bending of the sheet.

An excessive bending can result in a plastic deformation, which normally should be avoided. For instance, for the elastic limit of 350MPa and thickness of 0.65mm the minimal bending radius is equal to 0.186m. It is shown in [Godec1977] that the violation of this simple requirement can lead to a permanent deterioration of the magnetic properties.
The study presented in [Hubert2003] deals with the influence of the micro-plasticity on the magnetic properties. It is shown that approaching the yield stress closer than 12% can result in an irreversible degradation of the magnetic properties of non-oriented electrical steel. The suggested reason is the presence of internal stresses. So the practical limit for the bending radius is generally defined by (3.2.2.1) using 80 % of the elastic stress limit. Otherwise the original magnetic properties cannot be guaranteed.
Bending of the sheet can happen at some of the production stages following slitting [Godec1977] especially for grain-oriented electrical steels.

Section 3.3. Effect of mechanical cutting.

The term mechanical cutting is a common reference to guillotining and punching. Punching is a particular case of guillotining (Fig. 3.3.1), i.e. when cutting is conducted without rake angle (α in Fig. 3.3.1).

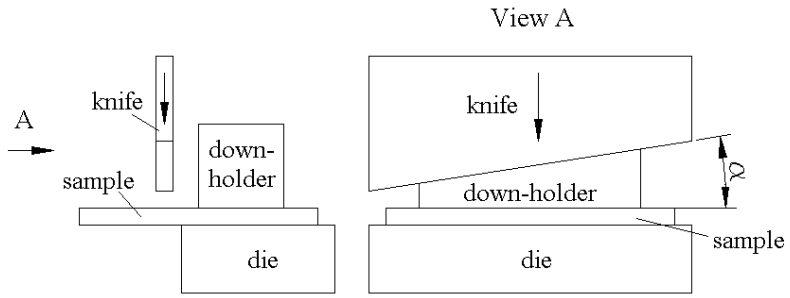

Fig. 3.3.1. Schematic representation of guillotining.

During guillotining the sheet has to conform to the inclination of the knife [Wisselink2000 p. 4]. Therefore the shearing deformation is accompanied by a complicated bending deformation pattern. It leads to shape defects such as bowing and twisting of the sheets. This is especially pronounced when the sheets are narrow and the cut is performed along the longest side.
The typical force-displacement curves for punching and guillotining are shown in Fig. 3.3.2. The force-displacement curve obtained for punching is has a similar shape as the stress-strain curve obtained in the tensile test. The maximum of the stress-strain curve is called the necking, because the total load is decreasing while the true stress in the material can be increasing.

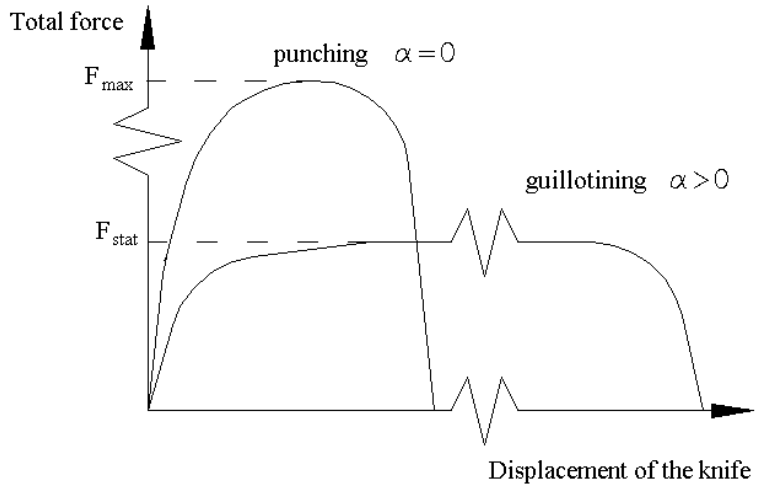

Fig. 3.3.2. Typical force-displacement curves [Wisselink2000 ch. 1]

In guillotining the shearing takes place locally. The maximum force in guillotining decreases with the rake angle. However the displacement of the knife increases accordingly.
The area confined by the curves in Fig. 3.3.2 and the horizontal axis defines the energy absorbed by the material on the plastic deformation. The shape defects emerging after guillotining confirm a larger consumption of energy with an increase of the rake angle.

As the magnetic properties are deteriorated by the plastic deformation the punching is preferable to guillotining.
The complexity of the plastic deformation encountered during guillotining is considered in great detail in [Wisselink2000 ch. 7].
The main zones on the edge of the cut sheet are shown in Fig. 3.3.3. Certain bending of the sheet over the edge of the die leads to the formation of the roll-over (Fig. 3.3.3). A part of the edge that was in contact with a cutting tool is called the shearing zone. After certain penetration of the knife a ductile fracture appears. Mechanical cutting often leads to the formation of a burr, which is one of the parameters commonly used for the definition of the quality of the cut. The height of the burr increases with the clearance. This is confirmed both numerically and experimentally in [Brokken1999 p. 60] for conventional steels. The experimental confirmation of this effect for electrical steels can be found in [Baudouin2002 p. 22].

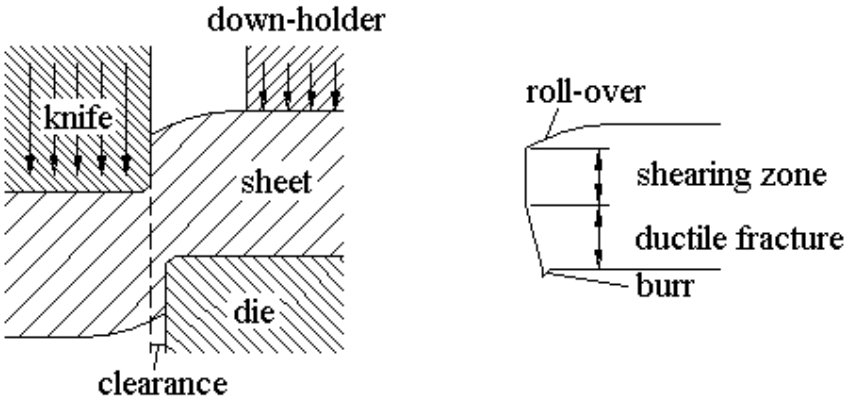

Fig. 3.3.3. The typical shape of the sheet obtained using punching.

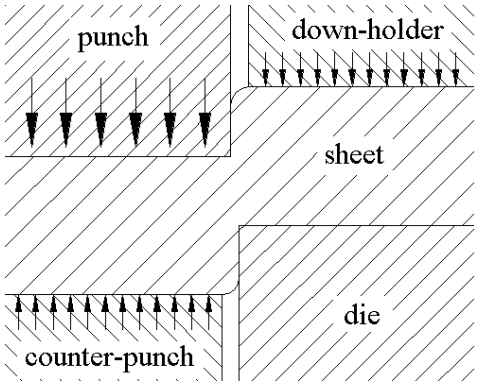

Fig. 3.3.4. Fine-blanking.

The size of the sheared zone, on the contrary, decreases with the clearance [Brokken1999 p. 60]. It is also shown there that the roll-over increases with the clearance. Analogous results obtained both experimentally and numerically are presented in [Wisselink2000 p. 100-101].

A more advanced punching system contains a counterpunch underneath the punch [Brokken1999 p. 3]. The counterpunch induces a hydrostatic pressure on the sheet. A superimposed hydrostatic pressure significantly increases the strain at fracture [Wisselink2000 p. 23]. Apart from that it is shown in [Wisselink2000 p. 91-97] that the maximum strain at 50% penetration of the punch decreases almost 2 times if the sheet is clamped on both sides compared to a conventional set-up. The same difference was observed in damage. Under these circumstances the ductile fracture can be delayed in terms of the knife displacement or even completely eliminated. The shearing zone obviously increases. It results in a shinier cut compared to conventional punching. Therefore this process is often called the fine-blanking.
With respect to the shape quality, the fine-blanking procedure is more favorable. But due to the need for significantly more sophisticated equipment fine-blanking is also more expensive. So up to now conventional punching remains the dominant procedure for the production of the sheets of electrical machines and transformers.
A slitting or a circular guillotining [Carlberg1971] is sometimes used for the mechanical separation of sheets of grain-oriented electrical steels. A comparison of the effect of slitting and guillotining is presented in [Wisselink2000 p. 90].
In the subsections below the numerical investigation of punching is described considering V850-65 non-oriented electrical steel.

3.3.1 Numerical investigation of the mechanical cutting.

V850-65 non-oriented electrical steel is studied (Fig. 3.3.1.1) throughout this subsection.

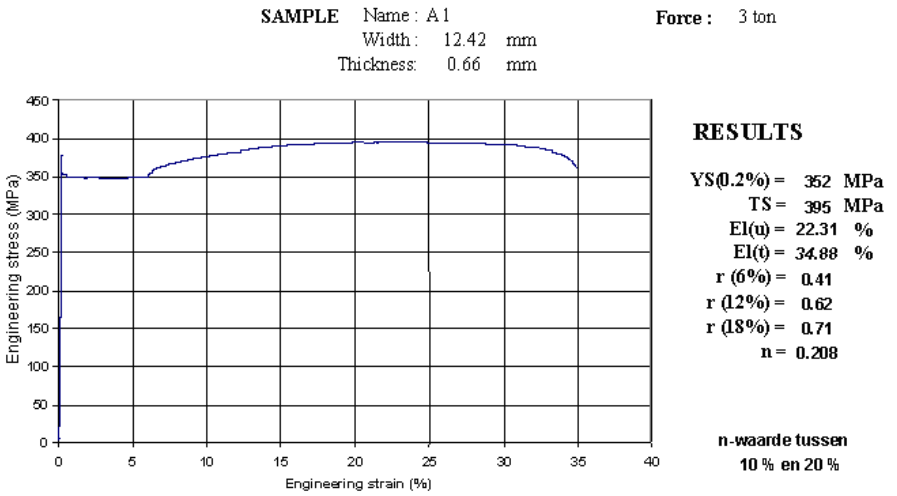

Fig. 3.3.1.1. The stress-strain characteristic of the V850-65 non-oriented electrical steel.

3.3.1.1. 2D simulation of the mechanical cutting.

The 2D simulations were done using the software developed by Dr. H. Wisselink in the frame of his PhD [Wisselink2000]. The first aim of this numerical investigation is to estimate the deformation affected zone. Secondly, the influence of the cutting

parameters on the size of the deformation affected zone is studied. Since large strains occur locally, a huge deformation of specific finite elements can deteriorate the general quality of the finite element mesh if the nodes are attached to the material points. In order to avoid this, remeshing is performed. The nodes of the old mesh are shifted to more favorable positions. The old data on the local mechanical state are transferred to the new mesh. In this way a relatively good quality of the mesh can be maintained and the drastic local deformation can be properly taken into account. Another important feature of the software is that it allows modification of the parameters of cutting such as the friction between the sample and the cutting tools as well as the quality of the knife and the die. The clearance can also be modified.

A clear advantage of the numerical investigation is that it allows a clear estimation of the influence of specific parameters. In practice even the quality of the knife cannot be guaranteed. Notice that the finite element approach implies that the processes in the material can be described by continuous functions, which is not completely correct taking into account the properties of the polycrystalline materials discussed in Chapter 2. In the computations below the von Mises material model was used and dynamic effects were not included. For more details on the features incorporated in the numerical simulation, we refer to [Wisselink2000 ch. 4, 5, 6, 7].

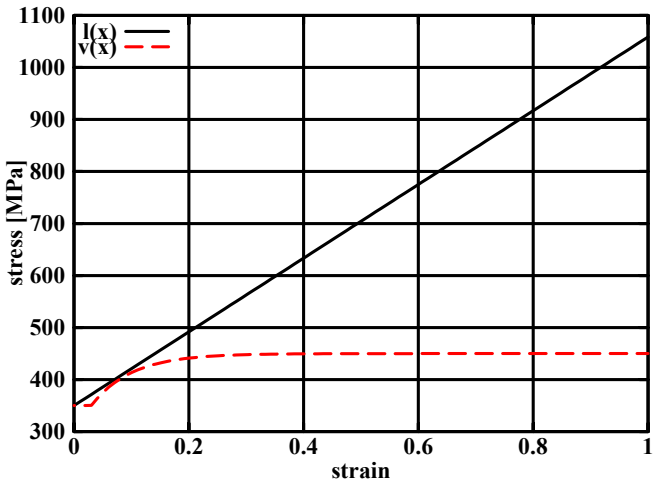

Fig. 3.3.1.1.1. Hardening curves used in the simulations – linear and Voce.

A comparison of the simulations carried out for different curvatures of the edges of the cutting tools is provided in Fig. 3.3.1.1.2 and Fig. 3.3.1.1.3. A 50% displacement was assigned to the punch. It can be seen that the total maximum deformation in case of a blunter tool (ε_{max}=4.623 versus ε_{max}=6.905, see Fig. 3.3.1.1.2) is 50 % smaller. It leads to an uncertainty of the crack, which finally results in a formation of a larger burr. However no considerable difference in the deformation affected zone is observed. The blunter tool is normally a result of wear.

The effect of wear on the burr is experimentally confirmed in [Carlberg1971].

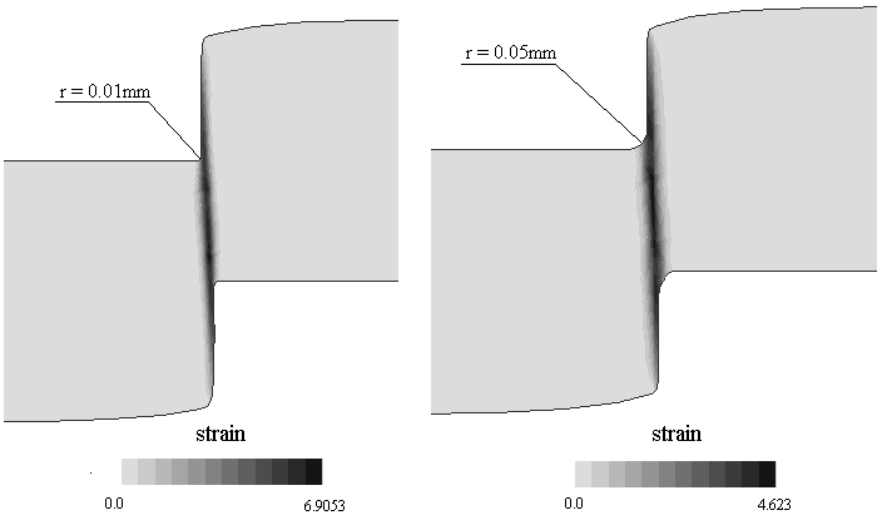

Fig. 3.3.1.1.2. The effect of the quality of the cutting tools on the plastic deformation of the sheet for the Voce material model.

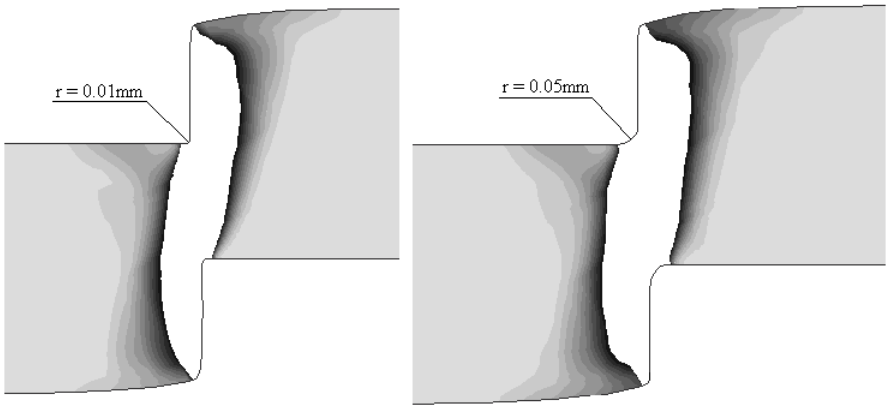

Fig. 3.3.1.1.3. The plastic deformation affected zone (white zone equals zone where $\varepsilon>0.001$) obtained at the different qualities of the edge of the cutting tools for the Voce material model.

If the quality of the cutting tools is low then the required punch force for the specific punch displacement is larger (Fig. 3.3.1.1.4).

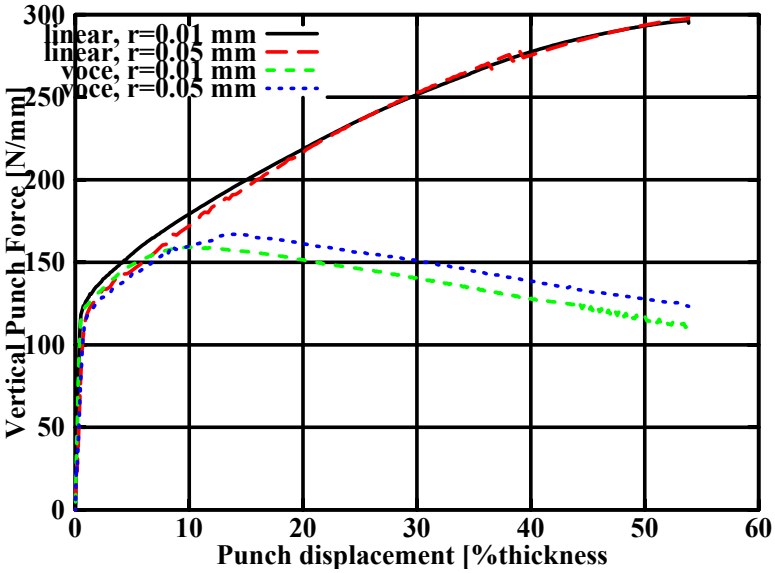

Fig. 3.3.1.1.4. The effect of the different curvatures of the cutting tools on the vertical punch force.

The effect of the clearance is clearly demonstrated in Fig. 3.3.1.1.5. An increase of the clearance leads to a larger roll-over and smaller strains. The strain gradient in the sheet decreases. Like in the previous case it leads to an uncertainty of the crack, so a larger burr can be expected compared to a smaller clearance. The deformation affected zone slightly increases with the increase of the clearance (Fig. 3.3.1.1.6).

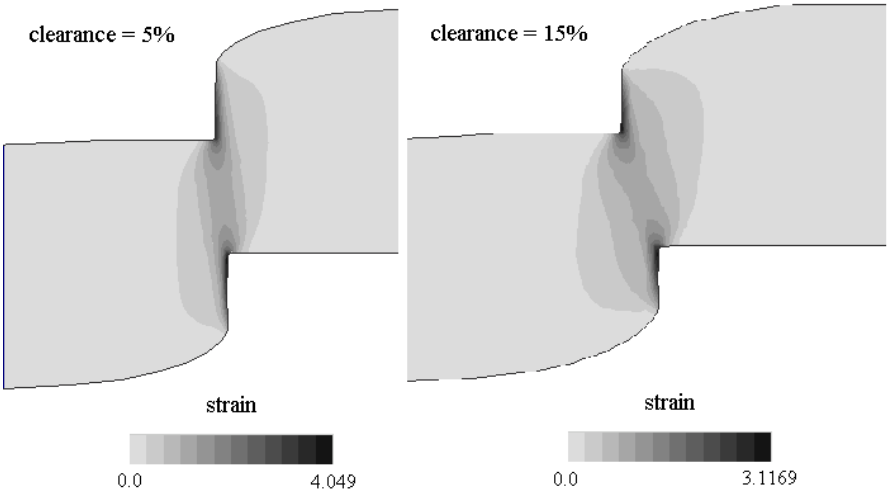

Fig. 3.3.1.1.5. The effect of the clearance on the plastic deformation of the sheet for the linear material model.

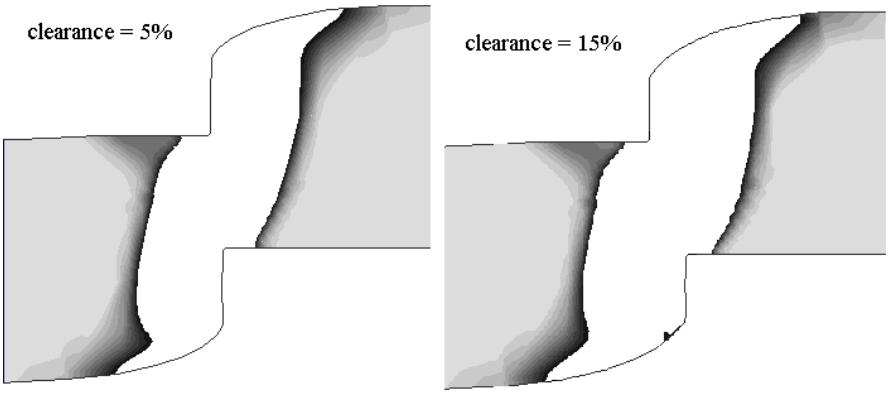

Fig. 3.3.1.1.6. The plastic deformation affected zone (white zone equals zone where ε>0.001) obtained at the different clearances for the linear material model.

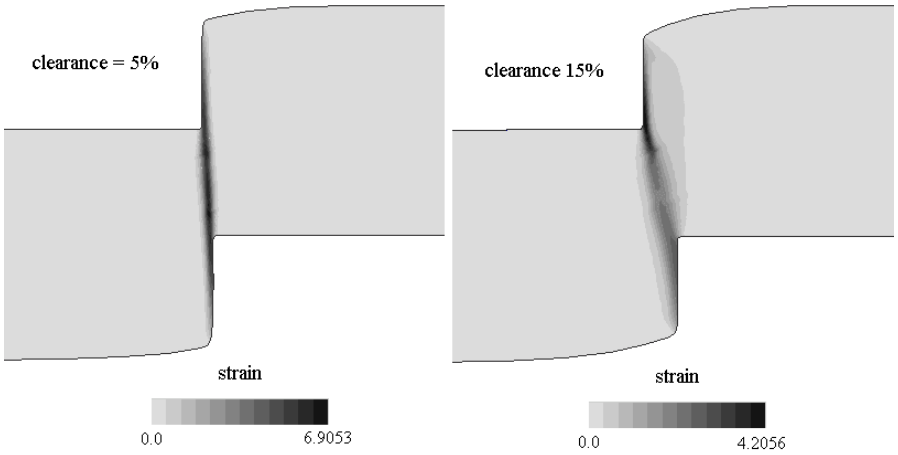

Fig. 3.3.1.1.7. The effect of the clearance on the plastic deformation of the sheet for the Voce material model.

When the Voce material model is used the increase of the roll-over becomes even more pronounced (Fig. 3.3.1.1.7).

Although a smaller clearance generally provides a better cut, it requires a larger force from the punching facility (Fig. 3.3.1.1.8). The increase of the vertical punch force with a reduction of the clearance is in accordance with the results presented in [Brokken1999 p. 55].

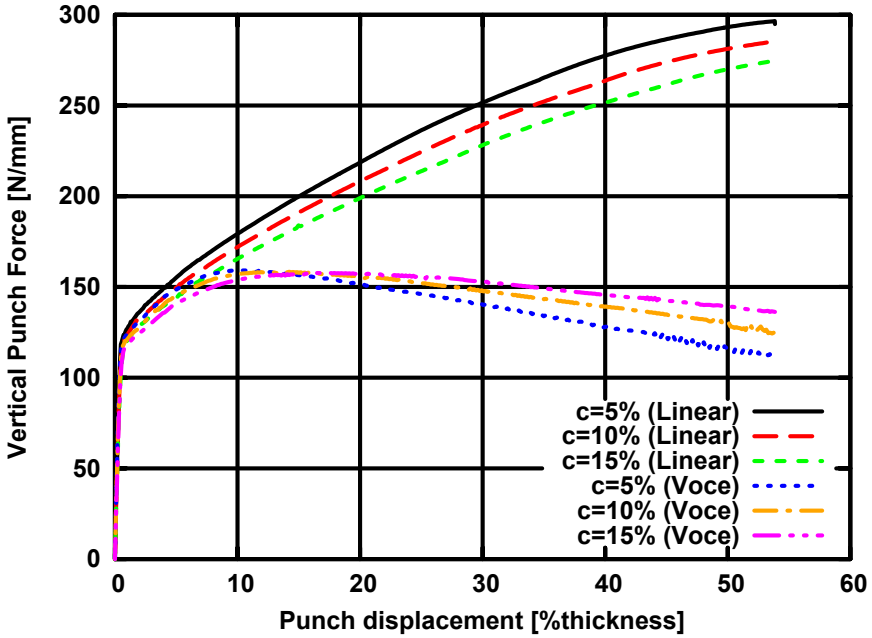

Fig. 3.3.1.1.8. The effect of the different clearances on the vertical punch force.

As was mentioned in Section 2.3, sheets of electrical steel can have a coating on their surface. In order to evaluate the influence of the coating on the punching process, simulations were carried out with a modified friction factor for the contact surfaces.

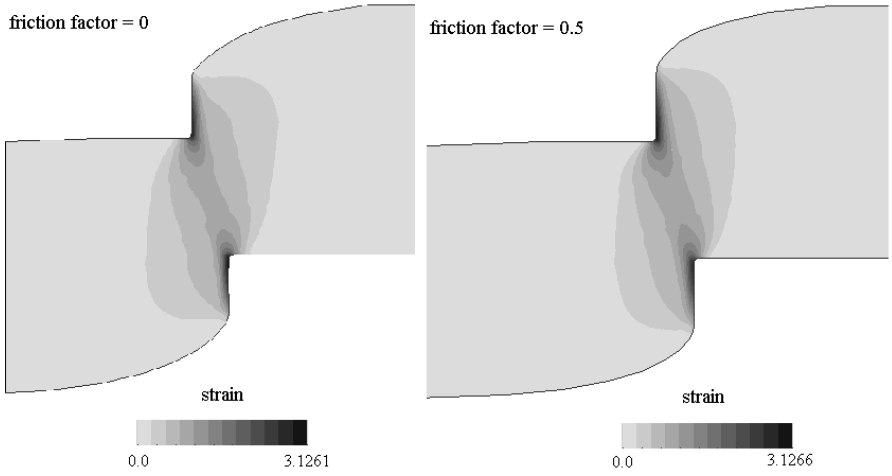

Fig. 3.3.1.1.9. The effect of the friction between the sample and the cutting tools on the plastic deformation of the sheet for the linear material model.

It can be seen from Fig. 3.3.1.1.9 that a smaller friction results in a small increase of roll-over and a smaller shearing area. But the maximum strain (Fig. 3.3.1.1.9) as well as the strain gradient remain the same. Consequently a similar certainty about the crack path is obtained. So the height of the burr can be assumed to be independent of the presence of coating.

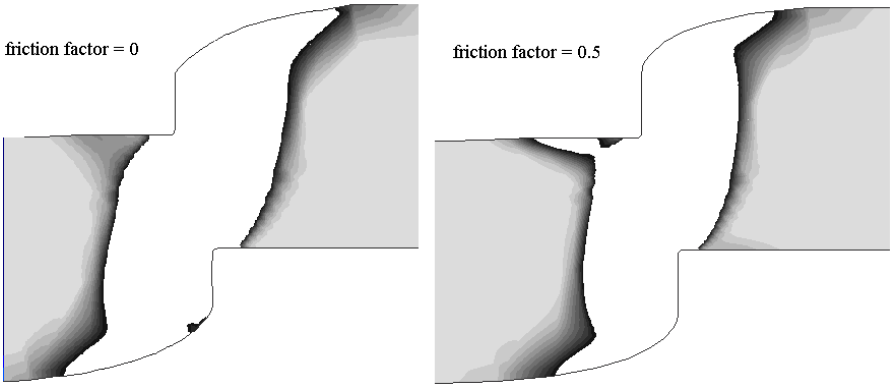

Fig. 3.3.1.1.10. The plastic deformation affected zone (white zone equals zone where ε>0.001) obtained at the different friction factors for the linear material model.

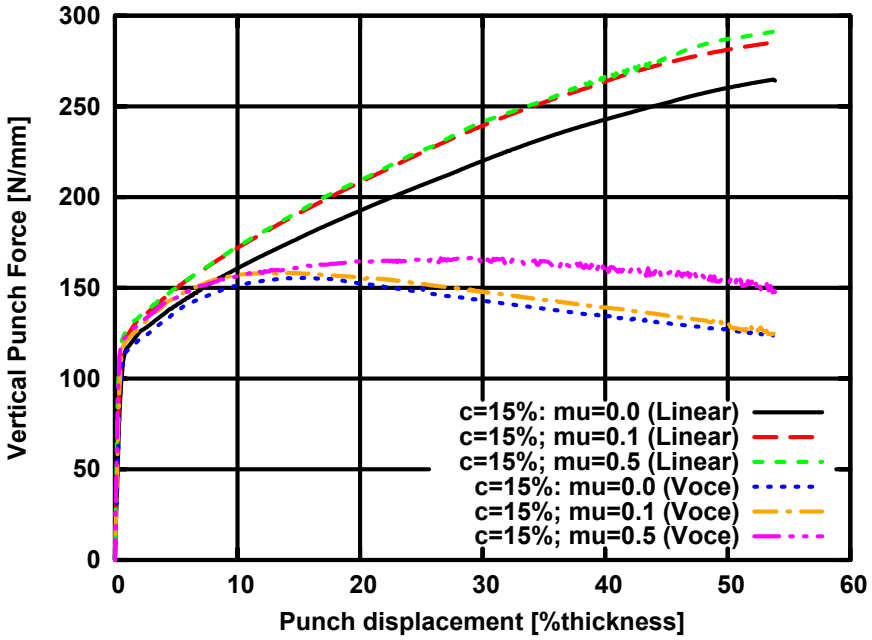

Fig. 3.3.1.1.11. The effect of the different friction coefficients for the contact between the sample and the cutting tools.

The presence of coating (friction factor = 0) results in a certain increase of the deformation affected zone (Fig. 3.3.1.1.10). However coating also leads to a smaller punch force (Fig. 3.3.1.1.11), which is beneficial for the cutting facility. These results are obtained on both material models. Reduced friction helps to decrease the wear of the cutting tools. Better quality of the cutting tools assures a smaller burr. So it can be concluded that the presence of organic coating or any other lubricant is generally favorable both for the tool and eventually also for the quality of the cut.
The use of the two material models allows to draw conclusions for a wide range of electrical steels. In some occasions ultra-low carbon steel is used in practical applications. This material has a better ductility due to the absence of silicon. So the mechanical properties of this steel are closer to the linear model used above. Such steel will have larger roll-over compared to steel with a medium silicon content.
Also the ductile fracture zone increases with the silicon content due to the higher strain gradient (see Fig. 3.3.1.1.5 versus Fig. 3.3.1.1.7).
The punch force multiplied by the punch displacement constitutes the mechanical work executed on the sheet. This work is accumulated via plastic deformation of the sheet. Since the punch force is not constant the performed work has to be defined as the surface below the corresponding curve. It can be seen from Fig. 3.3.1.1.4, 3.3.1.1.8 and 3.3.1.1.11 that the area between the punch force curve and the horizontal axis remains practically constant. Analogous data was collected elsewhere via experiments [Brokken1999 p. 55] and numerical computations [Brokken1999 p. 58]. Thus the mechanical energy absorbed during punching remains practically constant, which means that the deformation affected zone should not experience much changes. The punching parameters affect the strain gradient.
The plastic deformation affected zone can be assumed to be less than 50% of the thickness of the sheet, which can be seen in Fig. 3.3.1.1.10 where a blank region corresponds to a strain exceeding 0.1%.
We can conclude that if punching parameters are varying within certain limits there may be a change in the size of burr, but there should be a correspondence between the deformation affected zones.
The conducted simulations are valid for low punching speeds. At higher speeds viscous and thermal effects take place. The investigation conducted in [Brokken1999 p. 62] shows a certain increase of the punching force. However taking into account the fact that some of the energy is converted into heat [Brokken1999 p. 63], the increase in the energy absorbed via the plastic deformation should be smaller. Eventually, a slight increase in the size of the deformation affected zone can be expected due to the dynamic effects.

3.3.1.2. 3D simulation of the mechanical cutting.

In order to see if the complexity of the real geometry introduces any additional effect on the deformation affected zone the mechanical cutting was simulated in the Warp3D free software (so far available on ftp://cern49.ce.uiuc.edu/dist/) permitting 3D mechanical computations. This software does not allow remeshing although there are some special tools included for handling the large strains. For this reason the simulation was conducted until initiation of the crack. The information on the possibilities of the software can be found on the Web[1]. Once the crack begins, the supplied mechanical

[1] http://cern49.ce.uiuc.edu/cfm/warp3d.html

energy is absorbed by the growth of the crack. So no considerable change in the size of the deformation affected zone can be expected.
A uniform rigid contact was assumed between the sample and the punch as well as between the sample and the die. So the nodes of the mesh lying on the die were fixed, while the specified displacement was assigned to the nodes in contact with a punch. This is some sort of idealization. However the 2D simulation revealed that the friction between the sample and the cutting tools has little effect on the deformation affected zone. So assigning the displacement instead of a proper simulation of the contact is acceptable in this particular case of mechanical cutting.
Another idealization here is that the cutting tools are assumed to have no curvature at the edge. As the previous 2D simulations showed, this will correspond to a smaller deformation affected zone. The main reason for this is that taking into account all these details would require a huge mesh.
Use of cohesive elements for the simulation of the crack is an alternative to methods like elimination of the elements in the mesh. The detailed description of cohesive elements can be found in [Roychowdhury2002] as well as in the Warp3D manual available on ftp://cern49.ce.uiuc.edu/dist/. The use of the cohesive elements is preferable for the simulation of the crack when the rest of the mesh is rough like in our case. The cohesive elements incorporate a mathematical apparatus for the simulation of the smooth crack opening. The initial thickness of the cohesive elements is zero, which is in accordance with the continuum condition of the body prior to the nucleation of the crack. A maximum traction of 410MPa was assigned to the elements. When the peak stress exceeds this value a progressive decay of the tension and shear stresses across the adjacent surfaces of the cohesive element is initiated.
The positioning of the cohesive elements requires knowledge of the path where the crack is most likely to occur. In case of mechanical cutting the destruction of material is most likely along the line connecting the opposite edges of the cutting tools, which is confirmed by more accurate 2D simulations of the crack propagation presented in [Brokken1999 p. 59].

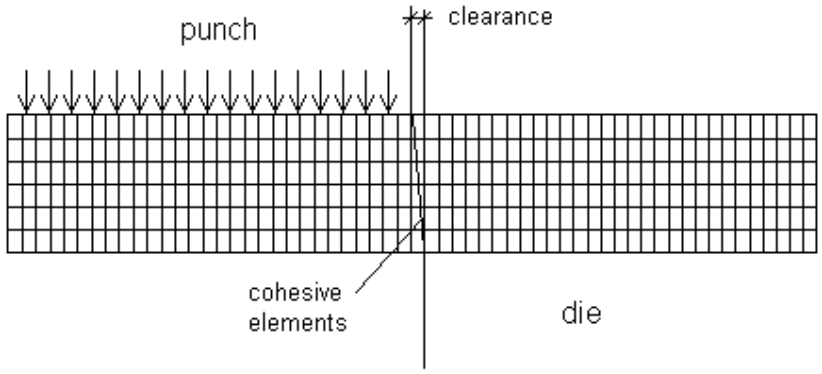

Fig. 3.3.1.2.1. Positioning of the cohesive elements in the mesh.

The mesh of the problem of the tooth tip is presented in Fig. 3.3.1.2.2. The whole mesh as well as the stress distribution at the moment when the crack begins are presented in Fig. 3.3.1.2.3. A linear Von Mises material model (linear hardening – l(x) in Fig. 3.3.1.1.1) was used for the bulk material of the sheet.

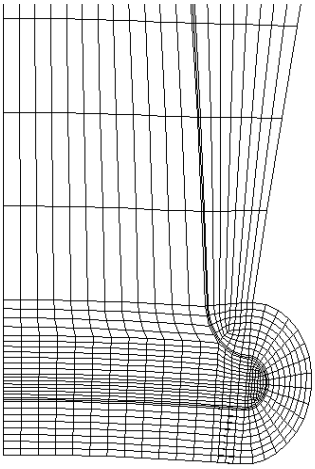

Fig. 3.3.1.2.2. Mesh of the tooth tip.

A considerable distortion of the shape of the elements in the shearing zone can be seen in Fig. 3.3.1.2.3. This is the reason why the fracture initiates that early in terms of the punch displacement. However it is worth noting that the initiation of the crack happens practically at the same displacement of the punch within the complete cutting line, which indicates similarity of the strain. A slight delay was observed only at the corner of the tooth tip.

It can be deduced that the deformation affected zone is also very much the same. The latter is clearly demonstrated in Fig. 3.3.1.2.3. The deformation affected zone appears to be the same along the tooth as well as in the tooth tip. The value of the deformation affected zone is quite close to the results obtained in the 2D simulations. The observed deviation is mainly due to the coarser 3D mesh.

In the actual punching facilities punching of the laminations of electrical machines is performed stepwise. At first the hole in the stator sheet is punched and then the slots. It considerably facilitates the punching conditions and assures a uniform separation of the material. So if a close uniformity with respect to the deformation affected zone was observed in this simulation then yet smaller discrepancy should be present in the real laminations.

The conducted 3D simulations allow to conclude that the punching of a geometry as complex as the teeth of the sheet of electrical machine does not lead to 3D effects. Indeed, the main remark out of these 3D simulations is that the results obtained in the 2D simulations can be extended to the real geometries.

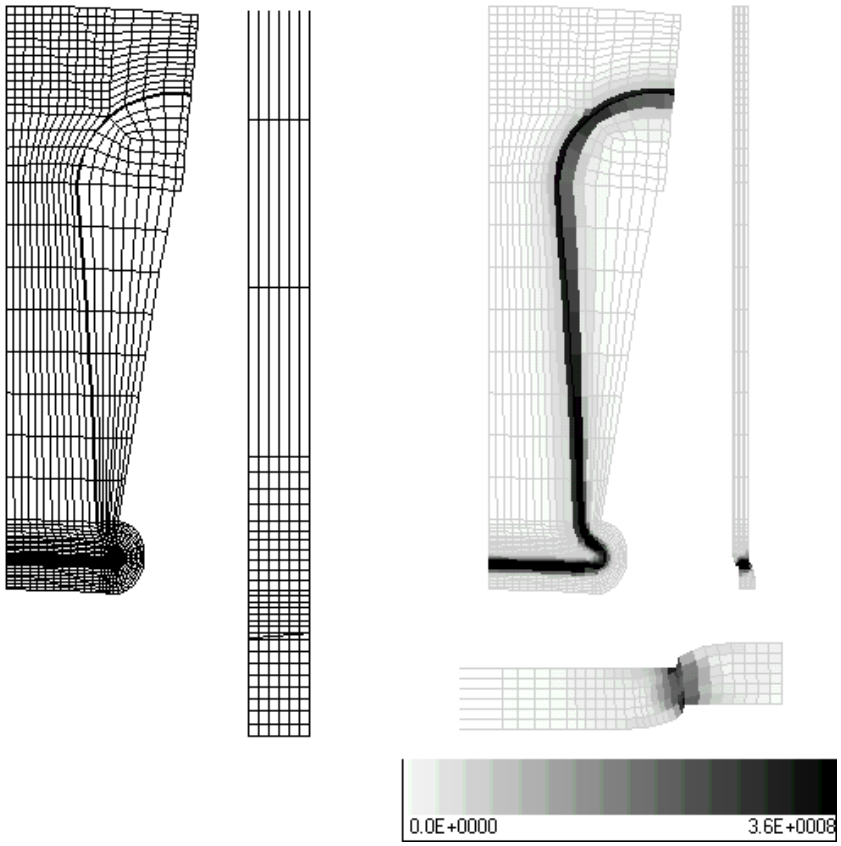

Fig. 3.3.1.2.3. Punching of the stator tooth. Mesh and the stress distribution when the crack starts.

3.3.2. Experimental investigation of mechanical cutting.

The most popular and relatively easy method consists of a direct measurement of the mechanical properties in the cross-section of the sample. It is also called the microhardness measurement.
A plastic deformation results in the change of hardness of the material. Therefore by measuring locally the hardness, it is possible to define the area deformed plastically.
The measurements are carried out as follows. A diamond with a certain weight atop is slowly moved down on the surface of the sample, which results in a small print. The size of the print is directly related to the hardness of material in the region around the print as well as by the weight applied to the diamond. Positioning of the diamond is performed with an accuracy higher than 0,1μm. The size of the print is measured by means of a microscope. A clear advantage of this method is that mechanical properties of the material can be measured very locally.
This type of measurement has some drawbacks as well. Any scratches present on the investigated surface of the sample affect the accuracy of the measurement. Therefore the

surface of the sample has to be carefully polished and treated by chemically active substances.

The presence or even the vicinity of inclusions often leads to a smaller print size. The vicinity of void has an opposite effect. The presence of impurity in the background of the print hinders the accurate measurement of its size. There are two ways to avoid this disadvantage. Either a bigger weight should be applied to the diamond or a higher number of prints should be made. When a larger weight is used, the measurements become less sensitive to the local nonuniformity. On the other hand, the higher number of prints permits to do a simple averaging of the results for every group of two-three prints. The diamond deforms the material plastically, so the print itself results in a change of hardness around the print. In order to diminish the effect of the current print on the successive ones it is recommended to choose the distance between the prints at least 3 times higher than the size of the print itself. The size of the print is defined by the weight applied to the diamond, i.e. the larger this weight the bigger is the print. Thus, application of larger weights leads to a smaller space discretization of the measurements.

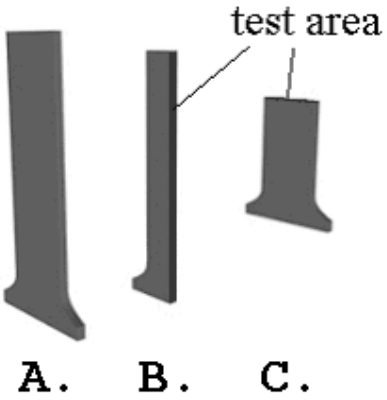

Fig. 3.3.2.1. Position of the cuts. A – sample, B – longitudinal cross-section, C – transverse cross-section

In order to confirm the existence of a plastic deformation distribution in the stator teeth of an induction motor a few standard cuts were made. Two cuts were made in the longitudinal direction of the tooth, two additional cuts were performed in the transverse direction of the tooth (Fig. 3.3.2.1). Preparation of the samples was carried out without introduction of additional plastic deformation. The test area was polished.

The cross-sections of the samples are depicted in Figs. 3.3.2.2 and 3.3.2.3. A considerable deviation in the size of the deformation affected zone was encountered for the transverse cross-sections of the teeth (Fig. 3.3.2.4, 3.3.2.5). The possible reasons could be the non-uniform clearance and/or the non-uniform mechanical contact between the sheet and cutting tools.

The average size of the deformation affected zone for every transverse cross-section is 0.6mm, which is nearly the same as for the longitudinal cross-section (Fig. 3.3.2.6, 3.3.2.7). It means that the effect of punching is practically the same in all the directions and can be assumed to be independent of the shape of the cut piece.

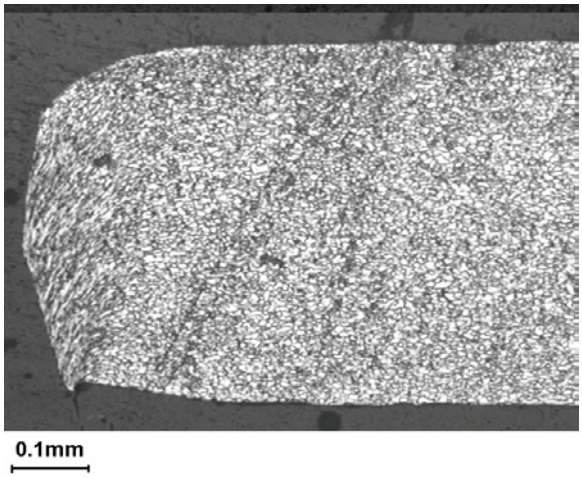

Fig. 3.3.2.2. Longitudinal cross-section of the tooth.

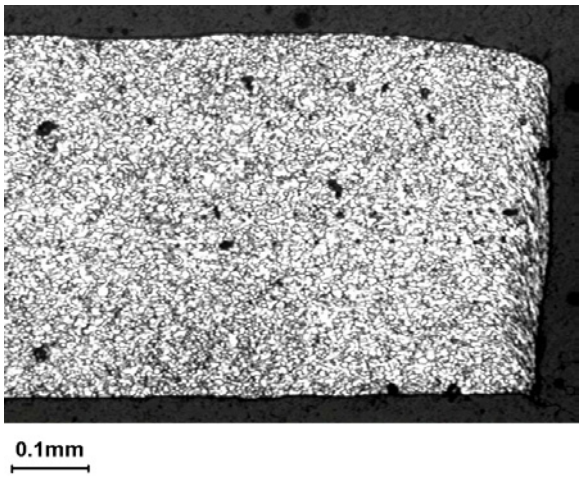

Fig. 3.3.2.3. Transverse cross-section of the tooth.

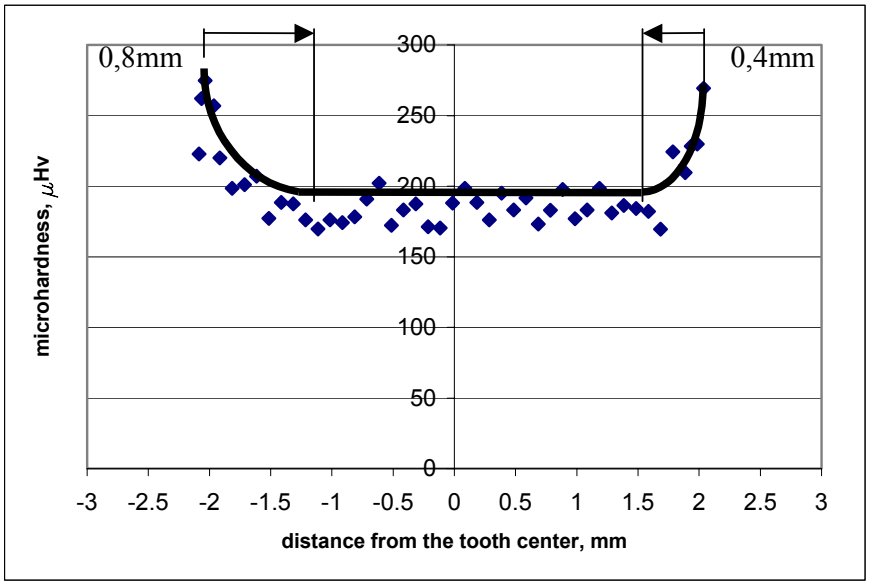

Fig . 3.3.2.4. Microhardness measurements in the transverse cross-section of tooth 1.

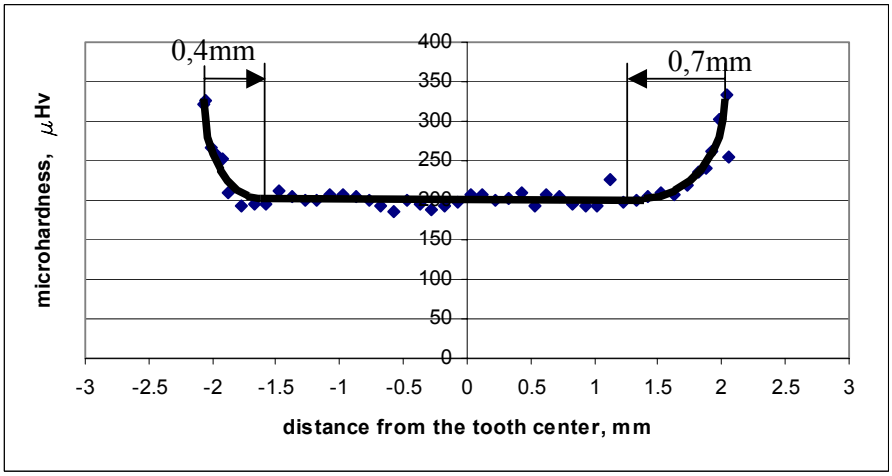

Fig. 3.3.2.5. Microhardness measurements in the transverse cross-section of tooth 2.

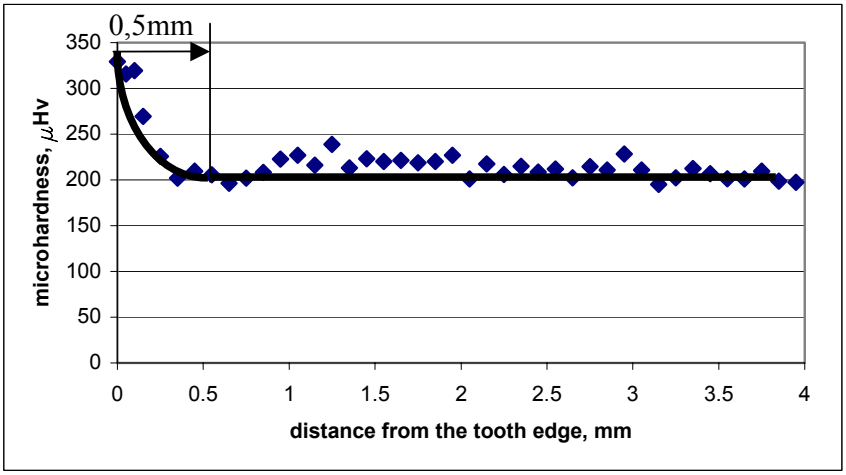

Fig. 3.3.2.6. Microhardness measurements in the longitudinal cross-section of the tooth 1.

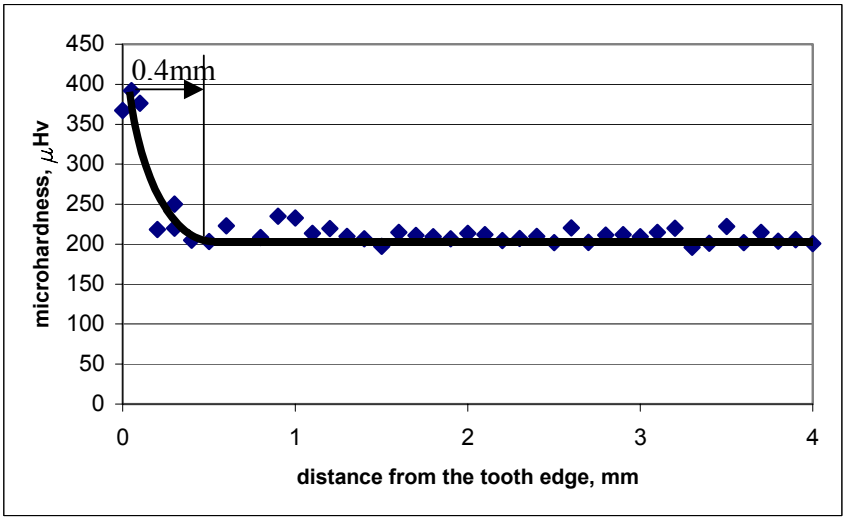

Fig. 3.3.2.7. Microhardness measurements in the longitudinal cross-section of the tooth 2.

A certain difference in the profile of the cut can be seen between the longitudinal (Fig. 3.3.2.2) and the transverse (Fig. 3.3.2.3) cross-sections of the teeth of the stator sheet. The size of the ductile fracture zone in the horizontal direction in Fig 3.3.2.2 is clearly larger than in Fig. 3.3.2.3, which means a considerable difference in the clearances. The difference in the height of the burr indicates the difference in the quality of the cutting tools.

In order to obtain some additional data one more stator sheet was investigated. One of the teeth was cut in the transverse direction (Fig. 3.3.2.8). The left profile of the tooth clearly has a larger roll-over. So the clearance during punching was apparently larger at the left edge of the tooth. The presence of the small tilt angle at the burr indicates that the down-holder was either not used or used inefficiently during punching, because the tilt angle appears due to the bending of the sheet. Bending of narrow sheets like in teeth of the electrical machines is reported in [Carlberg1971].

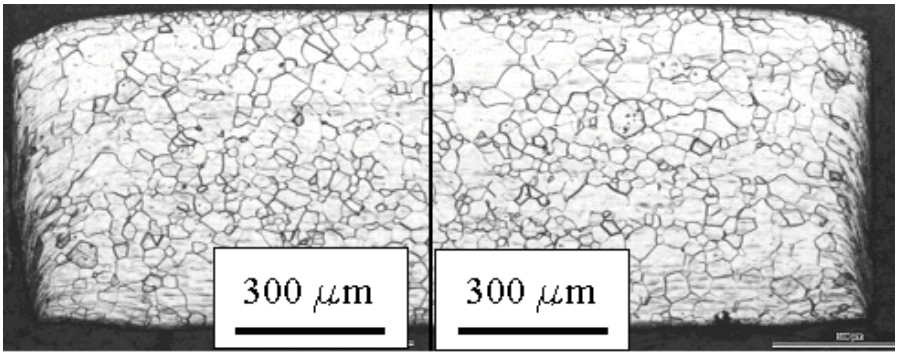

Fig. 3.3.2.8. Transverse cross-sections of the stator tooth of the electrical machine.

It is likely that the bending of the sheet in the transverse direction is responsible for the increase of the deformation affected zone (Fig. 3.3.2.9). The scattering of the results in Fig. 3.3.2.9 is due to the low load (5gr) applied to the diamond. The purpose of the use of a low load was to increase the discretization of the measurements. It leads to the decreased size of the print, which adversely affects the accuracy of the measurements. On the other hand, the results presented in [Castelnau] clearly show that the dislocation density can differ more than 5 times between different grains. This can result in a difference in hardness. Anyway, a certain overestimation of the size of the deformation affected zone is possible if low load is applied to the diamond during the microhardness measurements.

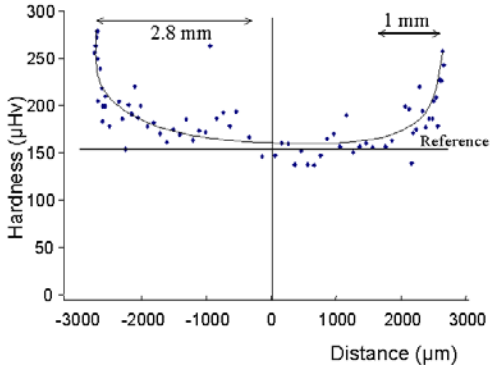

Fig. 3.3.2.9. Microhardness measurements conducted on the tooth shown in Fig. 3.3.2.8.

A scattering of the results is observed due to the difference in the cutting conditions. However in average they converge with the microhardness measurements carried out

elsewhere [Ossart2000]. In [Ossart2000] the size of the deformation affected zone was estimated to be 1mm large with a very low variation of the microhardness between 0.5 and 1mm. The low microhardness variation observed in [Ossart2000] was identified as a low strain state. In principle it is possible to define the relation between microhardness and strain in case if strain is applied (e.g. when rolling). However, as in the procedure described in [Ossart2000] stress was applied, for the material considered in this thesis we could not identify the relation between microhardness and the strain, due to the considerable Lüders band present, which was discussed in Section 2.2 and experimentally confirmed in Fig. 3.3.1.1.

Considering the microhardness measurements, we assume for now that the size of the deformation affected zone in 0.5mm and 0.65mm thick sheets is confined by 0.6-0.7 mm.

No considerable difference in the microhardness distribution is observed between the longitudinal and the transverse cross-sections of the teeth of the stator lamination, which is in agreement with the computational results presented in Section 3.3.1.2. So the complexity of the shape of the sheet can be considered irrelevant to the local effect of punching.

In the current investigation mechanical cutting of the samples was done using the guillotining machine at EELAB. Some cross-sections of these samples are shown in Fig. 3.3.2.8. No considerable difference was encountered compared to the profiles of the sheets used in electrical machines (Fig. 3.3.2.3). This similarity was confirmed by the microhardness measurements (Fig. 3.3.2.6 vs. 3.3.2.9). So the results collected on the samples cut in EELAB can be extended to real cases.

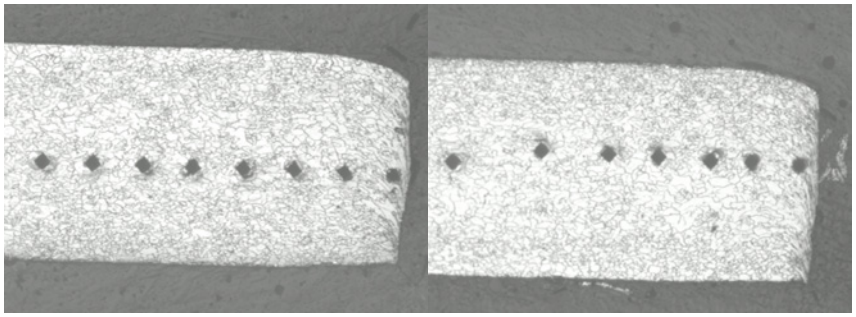

Fig. 3.3.2.8. The cross-sections of the sheets of V850-65 non-oriented electrical steel cut in EELAB laboratory.

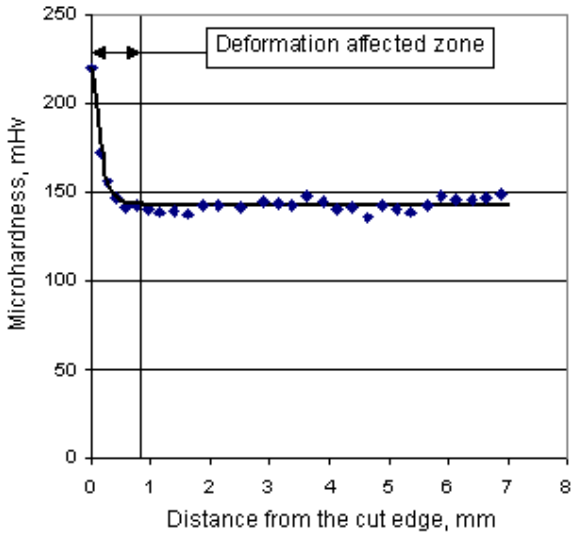

Fig. 3.3.2.9. The microhardness measurements performed on the cross-sections of the sheets of V850-65 non-oriented electrical steel cut in EELAB laboratory.

Conclusions

The laminations of the magnetic cores of electromagnetic devices are affected both by elastic and plastic deformation. In case of low power electrical machines the yoke is mainly subjected to elastic deformation, whereas the plastic deformation is concentrated at the edges of the sheet. In case of high power electrical machines, the whole sheet is subjected to elastic compression applied in the axial direction of the machine and to plastic deformation at the edges of the sheets.

The size of the deformation affected zone due to punching approximately corresponds to the thickness of the sheet. According to computations the deformation affected zone is smaller than the affected zone identified experimentally via microhardness.

The uncertainty of the profile of the sheet in the electrical machines has to be pointed out. The size of the burr can be different depending on the quality of the cutting tools and the clearance used during cutting. It is not the purpose of the current investigation to define the optimal cutting mode. Due to the complexity of the geometry of the magnetic core of the machine there seems to be quite a few options, e.g. the positioning of the cutting tools defining the clearance, for optimizing the cutting. However it is at least important to know the degree of the distortion of the shape of the cut edge of the sheet, which will be elaborated further in Chapter 9.

Chapter 4. The measurement setups.

Introduction.

Magnetic measurements are carried out in order to find magnetic material characteristics described by the relation between the magnetic field H and the magnetic induction B. These characteristics allow us to simulate electromagnetic devices in order to predict their performance. We consider only measurement techniques where the magnetic field H and the magnetic induction B directly follow from integral characteristics such as the magnetic flux in a cross-section or the magnetic energy in a well-defined volume. The basics of the measurements are considered in the first two sections.

In this chapter, the design of measurement structures are discussed which allow relatively easy transition from the integral to the local magnetic quantities. The constructed magnetic measurement structures are presented in the third section of the chapter. Both advantages and limitations of the measurement setups are discussed.

Section 4.1. The measurement of the flux density.

4.1.1. B measurement via the induced voltage in a pickup coil

Consider a rectangular sample of ferromagnetic material uniformly magnetized along one of its symmetry lines as shown in Fig. 4.1.1. The sample is subjected to a time dependent magnetic field H. The flux density can be derived from the voltage $V_{sec}(t)$ induced in the measurement winding by the time varying total magnetic flux:

$$V_{\sec}(t) = w \cdot \frac{d\Phi}{dt} = wS \cdot \frac{dB_{av}}{dt} \tag{4.1.1}$$

$$B_{av}(t) = \frac{1}{wS}\int_0^t V_{\sec}(t)dt = \frac{1}{wS}\sum_{i=1}^{T/\Delta t} V_{\sec_i}\Delta t \tag{4.1.2}$$

where w is the number of turns of the measurement winding, S is the magnetic cross-section of the measuring winding, T is the period of the secondary voltage, $B_{av}(t)$ is the average flux density in the cross-section S and Δt is a sampling period.

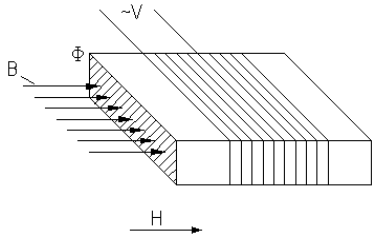

Fig. 4.1.1. Excitation of the rectangular sample.

4.1.2. B measurement via needle probes

4.1.2.1 Some introductory computations

Due to the electrical conductivity of the material, the time varying magnetic flux in the sample induces eddy currents according to Faraday's law (1.1.1). Due to the presence of electrical currents, the distribution of the magnetic field H and the flux density B becomes non-uniform in the sample according to Ampere's law (Fig. 4.1.2).

Before describing the techniques for the local measurement of the flux density in the sample, we briefly discuss the electromagnetic phenomena in the sample to be investigated.

The numerical results presented below are obtained by FE software. In the 2D FE analysis we investigate the electromagnetic phenomena in the plane perpendicular to the magnetic flux. In the FE model the external current and the eddy currents are lying in the plane of interest and the magnetic field is oriented perpendicularly (Fig. 4.1.2A).

The formulation is presented below. From Ampere's law it follows that

$$\begin{aligned} \nabla \times \bar{H} &= \bar{J}_{total} = \bar{J}_{external} + \bar{J}_{eddy} \\ \nabla \times H_z \bar{1}_z &= \bar{J}_{total\,x,y} = \bar{J}_{external\,x,y} + \bar{J}_{eddy\,x,y} \end{aligned} \tag{4.1.3}$$

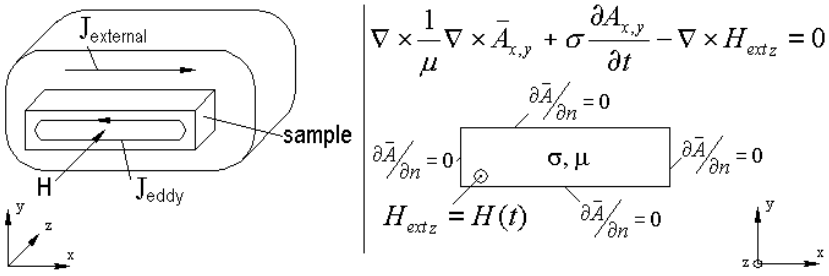

A. B.

Fig. 4.1.2. Numerical problem (A - general description, B – formulation).

According to Faraday's law, the density of the eddy currents, i.e. $\bar{J}_{eddy\,x,y}$, can be rewritten as a function of a vector potential $\bar{A}$ (with $\bar{B} = \nabla \times \bar{A}$). Moreover, taking into account a single-valued magnetization characteristic, the magnetic field in the sample is also a function of that vector potential. Equation (4.1.3) becomes:

$$\nabla \times \left(\frac{1}{\mu} \nabla \times \bar{A}_{x,y}\right) + \sigma \frac{\partial \bar{A}_{x,y}}{\partial t} = \bar{J}_{external\,x,y} \tag{4.1.4}$$

where $\bar{J}_{external\,xy}$ is identical zero in the sample. In order to enforce the field in the sample due to the external current in the excitation winding, see Fig. 4.1.2.A, we

introduce in the 2D FE model of the sample, see Fig. 4.1.2.B, a fictive field $\overline{H}_{ext}$ which on one side is space independent in the sample and on the other side equals zero outside the sample. In this way we enforce on the boundary of the 2D FE domain a predefined current density. According to Ampere's law, the right hand side of (4.1.4) can be replaced by a circulation of the fictive magnetic field $\overline{H}_{ext}$ resulting in:

$$\nabla \times (\frac{1}{\mu} \nabla \times \overline{A}_{x,y}) + \sigma \frac{\partial \overline{A}_{x,y}}{\partial t} = \nabla \times H_{ext\,z} \bar{1}_z \tag{4.1.5}$$

with $\overline{A}_{xy}$ the unknown function and $\overline{H}_{ext}$ the source term.
The natural boundary condition forces the eddy currents to flow parallel to the considered boundary of the domain of interest.

Unlike in the conventional 2D electromagnetic computations, the vector potential is situated in the plane of the domain of interest while the flux density is oriented perpendicularly. Therefore, for this numerical problem the edge elements were used.

The simulation result, using the same mesh (Fig. 4.1.3) but different frequencies, are presented on Fig. 4.1.4-4.1.7. The sample 5 mm x 0.5 mm with μ_r=2000 and σ=2.10^6/Ωm is subjected to the alternating magnetic field. The longest vector on the figures corresponds to the maximum amplitude.

In order to check if the chosen formulation is correct the eddy current losses at each time point *t* were computed in the sample using the formula [Gyselinck2000 ch. 5 p. 20]:

$$p_{cl}(t) = \frac{\int_S \overline{J}_{eddy} \overline{E} dS}{S} = \frac{\frac{1}{\sigma} \int_S \overline{J}_{eddy}^2 \cdot dS}{S} = \frac{\frac{1}{\sigma} \sum_{i=1}^{N} \int_{element_i} \left(\sigma \frac{\partial \overline{A}}{\partial t} \right)^2 dS}{S} \tag{4.1.6}$$

The obtained classical losses $p_{cl}(t)$ (4.1.6) as a function of time for a frequency *f* of 50Hz, are presented in Fig. 4.1.8. The average value P_{cl} equals 2674 W/m^3. This average value also follows from the area enclosed by the $B_{av}H_{surf}$-loop where H_{surf} is the magnetic field at the surface of the sample while B_{av} is given by:

$$B_{av}(t) = \frac{1}{S} \int_S B(x,y,t) ds \tag{4.1.7}$$

The classical losses per time unit can also be obtained analytically from the formula [Gyselinck2000 ch. 5 p. 10]:

$$P_{cl} = \frac{1}{6} \sigma \cdot \pi^2 \cdot d^2 \cdot f^2 \cdot {B_{av,\max}}^2 \cdot F_{sk}(\lambda) \tag{4.1.8},$$

where d equals the thickness of the lamination and

$$\delta = \sqrt{\frac{1}{\pi \cdot f \cdot \sigma \cdot \mu}}, \quad \lambda = \frac{d}{\delta}, \quad F_{sk}(\lambda) = \frac{3}{\lambda} \cdot \frac{\sinh(\lambda) - \sin(\lambda)}{\cosh(\lambda) - \cos(\lambda)} \qquad (4.1.9)$$

$B_{av,max}$ corresponds to the maximum value of the average flux density in the cross-section of the sample, i.e. $B_{max}=\Phi_{max}/S$. In this case $B_{av,max}$=1.7496T, which is slightly smaller than the maximum flux density value due to the small skin effect.
The losses computed from (4.1.8)-(4.1.9) at f=50 Hz are equal to 2940W/m^3.

From the numerical computations we can conclude that:

- At a frequency of 50Hz, the non-uniformity of the flux density in the sample can be neglected;
- It is generally true that reduction of the excitation frequency results in a smaller non-uniformity of the flux density within a cross-section of the sample.

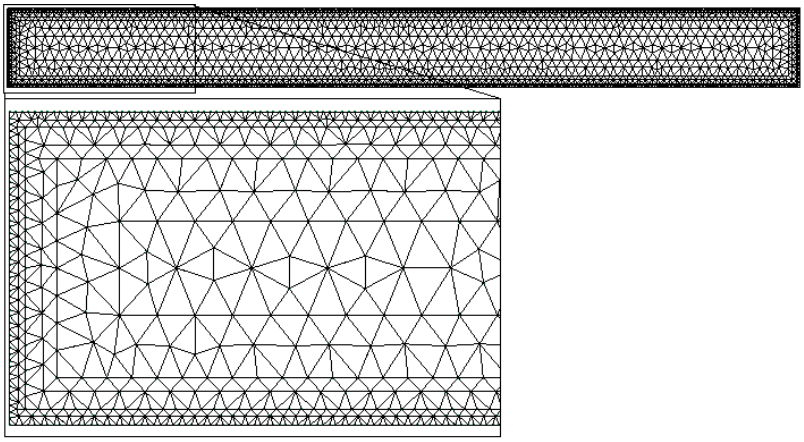

Fig. 4.1.3. The mesh of the problem.

Measurements conducted at high frequencies are needed for the investigation of the properties of the magnetic materials in the real conditions. Here we must distinguish between 'global' magnetic permeability (H_{surf} is the magnetic field at the surface of the material):

$$\mu_{gl} = \frac{B_{av,\max}}{H_{surf}} \qquad (4.1.10)$$

and 'local' magnetic permeability

$$\mu = \left(\frac{B}{H}\right)_{loc} \qquad (4.1.11)$$

The latter gives the relation between the magnetic induction and magnetic field value in each point of the sample.

The global permeability decreases with the frequency as a result of the skin-effect and according reduction of the cross-section of the sample.

There is a good correspondence between the local permeability and the global permeability when the excitation frequency is low. This underlines the importance of the investigation of the magnetic properties at the quasi-static excitations.

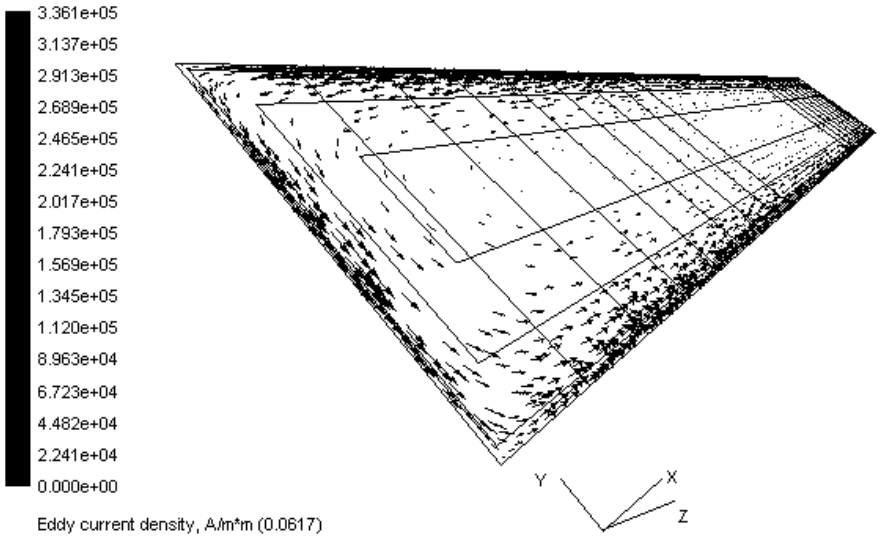

Fig. 4.1.4. Current density distribution at 50Hz frequency (vector output).

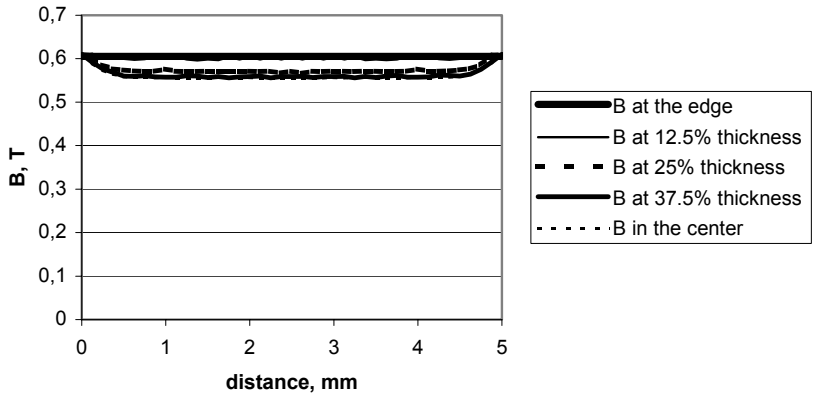

Fig. 4.1.5. Flux density distribution at 50Hz frequency at t=0.0617s.

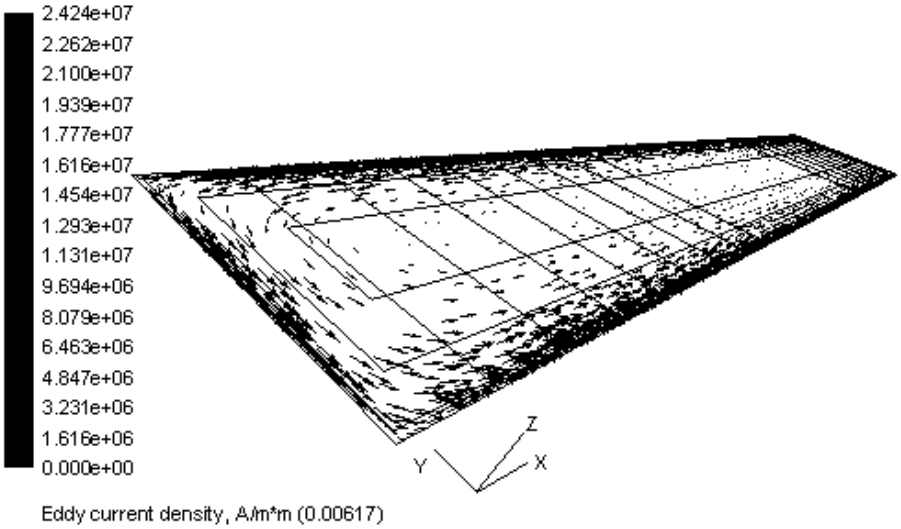

Fig. 4.1.6. Current density distribution at 500Hz frequency.

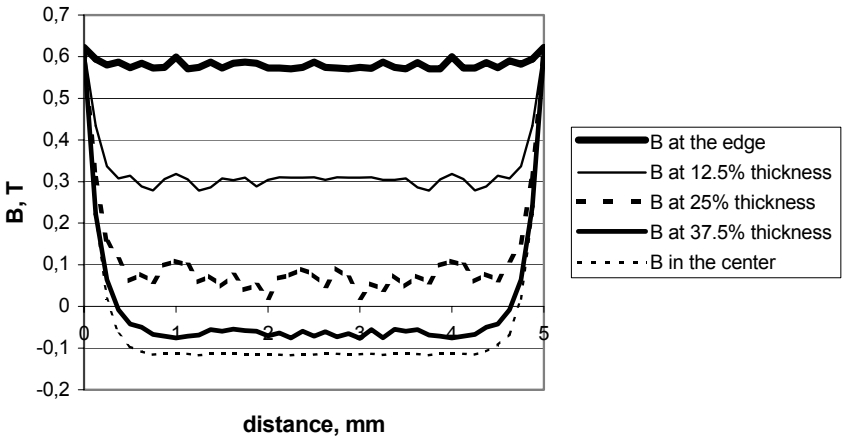

Fig. 4.1.7. Flux density distribution at 500Hz frequency at t=0.00617s.

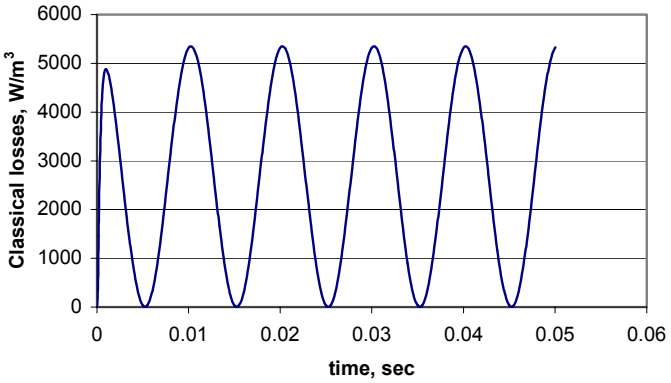

Fig. 4.1.8. Classical losses vs. time (f=50Hz).

4.1.2.2 Needle probes

It is also possible to use the voltage induced in the sample itself in order to measure the magnetic flux. The eddy currents flowing along the surface of the sample are directly defined by the total magnetic flux in the sample and its time variation.
Consider the induced voltage in the sample due to an alternating magnetic excitation. A cross-section of the sample perpendicular to the magnetic excitation is shown in Fig. 4.1.9. The Faraday's law in the integral form for the S_1 area is given by:

$$\oint_{1ba21} \overline{E} \cdot d\bar{l} = -\int_{S_1} \frac{dB}{dt} ds \tag{4.1.12}$$

The circulation of the electrical field can be calculated as follows:

$$\oint_{1ba21} \overline{E} \cdot d\bar{l} = \int_{1}^{b} \overline{E} \cdot d\bar{l} + \int_{b}^{a} \overline{E} \cdot d\bar{l} + \int_{a}^{2} \overline{E} \cdot d\bar{l} + \int_{2}^{1} \overline{E} \cdot d\bar{l} \tag{4.1.13}$$

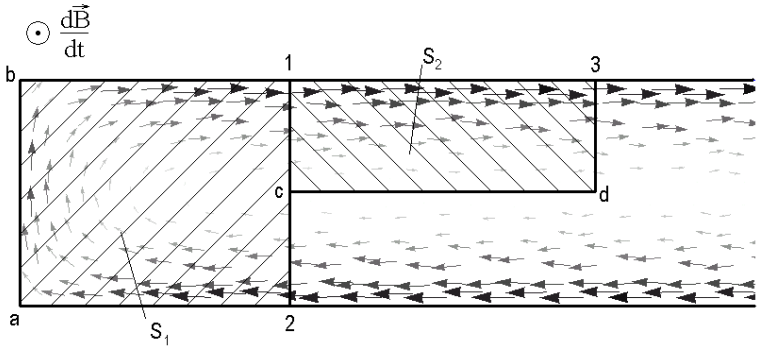

Fig. 4.1.9. Induced voltage in the sample due to the alternating excitation (the distribution of the electrical field is obtained in GetDp software).

If in each point of the straight line connecting the points 1 and 2 the electrical field is oriented horizontally then the last integral in the right hand side of equation (4.1.13) is equal to zero. So the e.m.f e_{12} induced between the points 1 and 2, when following the surface of the material and orthogonal to $\overline{B}$, corresponds to the circulation of the electrical field $\overline{E}$ along the 1ba2c1 closed path. We obtain:

$$e_{12} = \int_{1ba2} \overline{E} \cdot d\bar{l} = -\int_{S_1} \frac{dB}{dt} ds \quad or$$
$$B_{S_1}(t) = -\frac{1}{S_1} \cdot \int_0^t e_{12} dt \tag{4.1.14}$$

This requirement mentioned above can be met if the points 1 and 2 are symmetrically placed with respect to each other and the distance from the edge ab is larger more than 2 times the thickness of the sheet (Fig. 4.1.10). Otherwise a considerable error can appear (Fig. 4.1.10). Analogous results are presented in [DeWulf2002 p. 33].

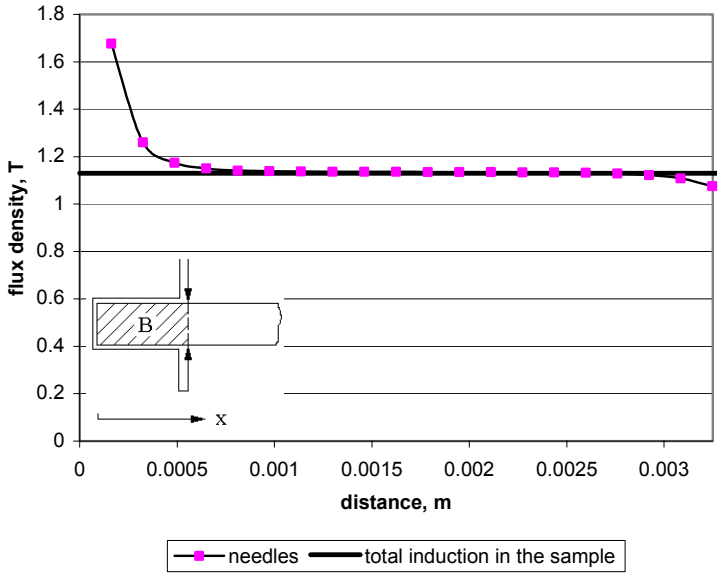

Fig. 4.1.10. Integrated flux density (4.1.14) at f=50Hz at the increasing distance from the edge in a 0.65 x 3.25mm^2 sample, B_{av}=1.13 Tesla.

An analogous investigation can be carried out for the potential difference between the points 1 and 3 situated on the same side of the sample:

$$e_{31} = \int_{S_2} \frac{dB}{dt} ds \tag{4.1.15}$$

Displaced points can also be used in order to measure in a local way the induction level. The area for the integration of the flux density has to be modified accordingly:

$$e_{32} = e_{31} + e_{12} = \int_{S_1+S_2} \frac{dB}{dt} ds \qquad (4.1.16)$$

In this way, it is possible to study the magnetic flux density in specific areas of the sample. Special probes with a built-in spring were used in order to provide the required local pressure (Fig. 4.1.11) and a good electrical contact. The needle probe was installed in the special conducting holder in order to simplify an installation of the probe and soldering of the connection wires.

Fig. 4.1.11. Needle probe of Ingun firm (www.ingun.co.uk) with 30^0 tip (specific information on the dimensions of the probe used in this study can be found at www.ingun.com/de/produkte/kontaktstifte/pdf/15.pdf).

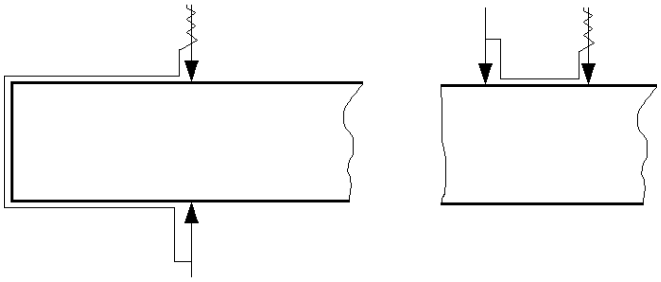

Fig. 4.1.12. Positioning of the needles.

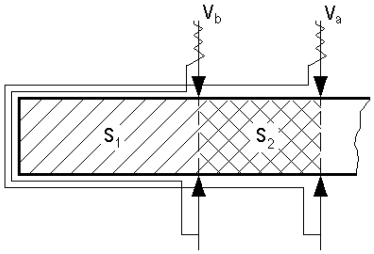

Fig. 4.1.13. Modified needle probe positioning.

The connection wires are placed as close to the surface of the sample as possible in order to minimize coupling with the stray fluxes.

In [Loisos2001] a comparison of the different methods for the local measurement of the flux density is provided. It is shown in that article that if the distance between the needles is exceeding 10 mm, it is possible to use the arrangement shown on the right hand side of Fig. 4.1.12. For smaller distances a better accuracy is provided when positioning the needles as shown in Fig. 4.1.13. The connection wires are placed on the surface of the sample in the same way for both pairs of the needles thereby reducing coupling with a stray flux.

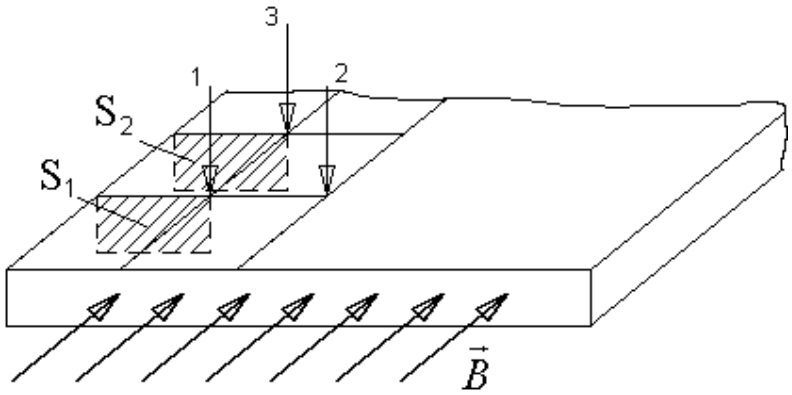

Fig. 4.1.14. Shift of the needles.

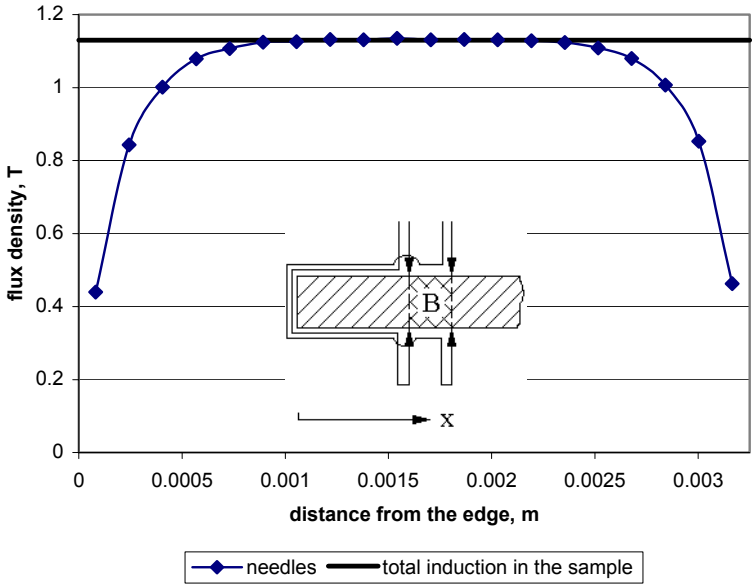

Fig. 4.1.15. Integrated flux density at f=50Hz for increasing distance from the edge for a couple of needles installed at 0.162mm distance between each other in the 0.65 x 3.25mm^2 sample, B_{av}=1.13 Tesla.

If the magnetic properties are sufficiently uniform in the sheet then the corresponding points of the cross-sections (S_1 and S_2 in Fig. 4.1.14) produce equipotential lines. Since the needles 1 and 3 in Fig. 4.1.14 are installed on one of such lines $V_{12}=V_{32}$.
It is worth noting that the distance from the edge should be sufficiently large in order to avoid a considerable error (Fig. 4.1.15) due to non-zero fourth integral in the right hand side of (4.1.13). As in the previous case the suggested limit is 2 times the thickness of the sheet.

The magnetic domain structure present in the sample can impose certain limitations on the application of the needle probe method. If the size of the domains is sufficiently large compared to the spacing between the needles then the movement of the domain walls can result in jumps in the measured signal. It is shown in [Loisos2001] that a considerable scattering of the measurement results can take place if the needle probe method is applied to grain-oriented electrical steels. However this limitation is neglected throughout this work, since only non-oriented electrical steels having small grains are investigated.

In order to avoid confusion between the different measurement approaches we will further refer to the needle probe method as to the local measurement of the flux density. The use of the measurement coil wrapping up the whole sample will further be denoted as a global measurement of the flux density.

4.2. Measurement of the magnetic field.

4.2.1. H measurement via the electric current and magnetic path length.

Consider a coil with *w* windings through which an electrical current *i* flows. Amper's law in the integral form states that the electric current iw through the surface S bounded by the specified contour L induces the magnetomotive force (m.m.f.) in this contour:

$$\oint_l \overline{H} \cdot d\bar{l} = iw \qquad (4.2.1.1),$$

If integration is carried out along a magnetic field line then in the integral of (4.2.1.1), the vector symbols can be dropped. If the excitation system provides a constant field along the specific magnetic path l_{path} and in the rest of magnetic circuit magnetic field is negligible then H can be easily derived from the excitation current *i*:

$$H = \frac{iw}{l_{path}} \qquad (4.2.1.2)$$

Let us consider what is required to keep H constant. It follows from (1.1.4) that the integral of $\overline{B}$ on any closed surface is equal to zero. It is possible to find such a closed surface around the magnetic path that the flux remains the same on every cross-section of the surface normal to the magnetic path. This surface is called a flux tube (Fig. 4.2.1.1).

For the considered flux tube and the magnetic path the following relation can be established:

$$H = \frac{B}{\mu_r \mu_0} = \frac{\Phi}{\mu_r \mu_0 S} \qquad (4.2.1.3)$$

So it is required to keep $\mu_r S$=constant in every point of the magnetic path in order to provide a constant H.

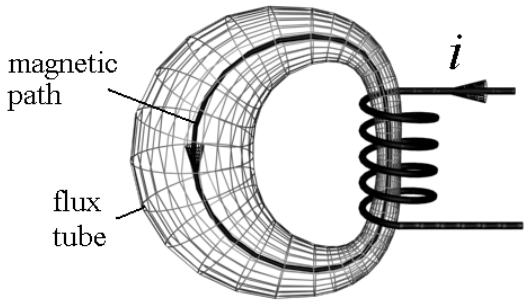

Fig. 4.2.1.1. Flux tube.

In the measurement setups it is usually possible to define a flux tube comprising the sample (or its working part). The magnetic path of the setup is defined by the path associated with this flux tube. The flux tubes, which do not intersect the sample (or its working part), define the leakage flux.

In the conventional measurement setups (Fig. 4.2.1.2) the configuration of the magnetic path can be easily established. In case of a ring as magnetic object, the width of the ring should not exceed 10% of the external diameter according to the ICE norms. It provides sufficient uniformity of the magnetic induction in the cross-section of the ring. So this setting seems to be the most suitable for the investigation of the magnetic properties of isotropic magnetic materials. A disadvantage of this setting is that it requires an installation of a new winding for each new sample. The Epstein frame is a convenient setup in this respect. It also allows to study the magnetic properties of anisotropic materials in the considered direction. A disadvantage of an Epstein frame is that there is a distortion of the magnetic induction uniformity in the corners of the frame. This leads to additional losses as shown in [Gyselinck2000 ch. 3]. However since the dimensions of the frame are standardized the repeatability between the different setups for the same material is known to be very good. Despite the mentioned imperfections, the measurements obtained on the Epstein frame are generally used as a reference.

An alternative set up is a double yoke single-sheet tester (SST) where the sample is clamped between two ferromagnetic yokes (Fig. 4.2.1.3). This system is also widely used in practice. But its accuracy depends on a number of factors:

1) There has to be a good contact between the sample and the yokes. In this way a parasitic air gap is minimized. The importance of this requirement increases with a decrease of the size of the setup.
2) The $\mu_r S$ value in the yokes must be considerably larger than its value in the sample. In that case, the m.m.f. drop on the yokes can be neglected. For instance, if the thickness of the sample is equal to 0.5mm then 15mm thick yokes take a 60 times smaller magnetic field (4.2.1.3) compared to the field in the sample. It is implied in this calculation that the permeability in the yoke is the same as the permeability of the sample. The use of a superior material for the yokes is preferable.
3) There has to be as little displacement of the yokes with respect to each other as possible. This is particularly important in small setups. For example, if the path

length in the sample is equal to 50mm then the longitudinal displacement of the yokes on 0.5mm results in 2% error for the magnetic field.

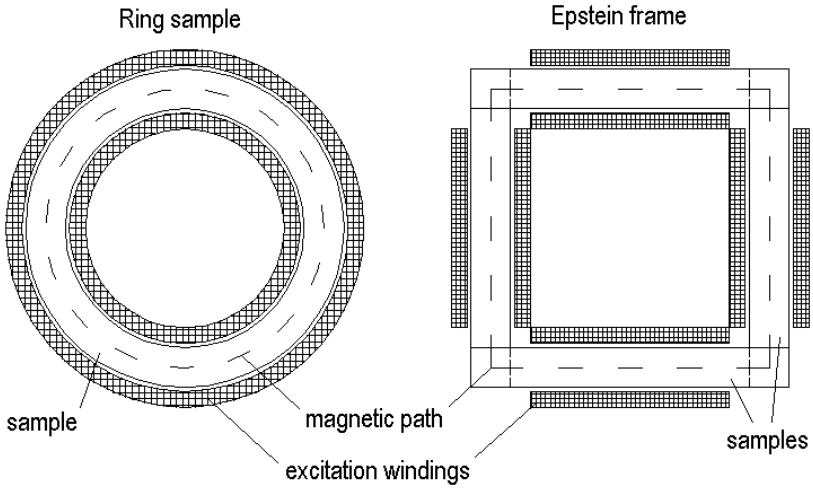

Fig. 4.2.1.2. Conventional measurement systems. The measurement windings not shown here are normally placed inside the excitation windings.

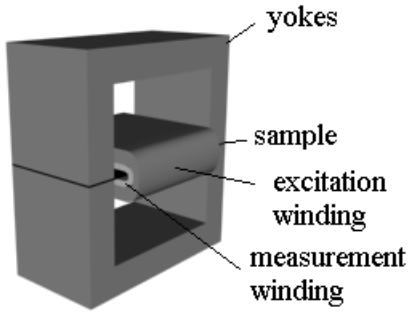

Fig. 4.2.1.3. Basis structure of a double yoke single sheet tester.

The third problem can be avoided by accurate positioning. However the first two problems require more attention. The easiest way to account for these drawbacks is to calibrate the magnetic path length using the results obtained on the Epstein frame as described in [DeWulf2002 p. 55].

4.2.2. H-measurement via local sensors.

In the setups containing air-gaps it is very difficult and sometimes impossible to derive the magnetic field in the sample under study, starting from the current in the excitation coil system. An alternative is to measure the H-field at the surface of the material. It is known that a tangential component of the magnetic field is continuous at the surface of the sample. So the measurement of the magnetic flux density in the air but as near as

possible to the surface of the sample can be used in order to identify the magnetic field at the surface of the sample.
There are quite small Hall and magnetoresistive sensors on the market. The advantage of these sensors is that their output is not dependent on the frequency of the excitation. However at this moment most are designed for the measurement of small or medium (~1000A/m) magnetic fields. During induction control the applied field often exceeds this value. For this reason in the current investigation the measurement of H was carried out by means of self-made H-coils.

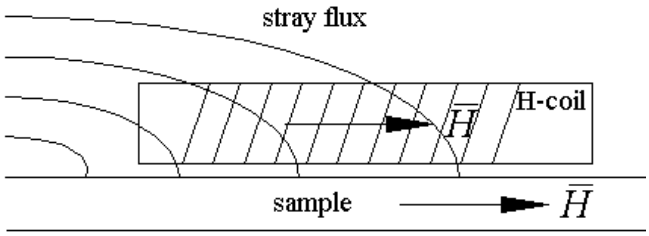

Fig. 4.2.2.1. The influence of the leakage flux on the measurement of the magnetic field.

The accuracy of the measurement of H by means of H-coils depends on a number of factors. The magnetic field decreases with the distance from the sample. Therefore it is important to have a flat sensor placed close to the surface of the sample. The presence of stray flux (as in Fig. 4.2.2.1) affects the measurement of the field since additional voltage is induced in the sensor by this flux. This effect is specific for each magnetic structure. It is considered in more detail in the next section.

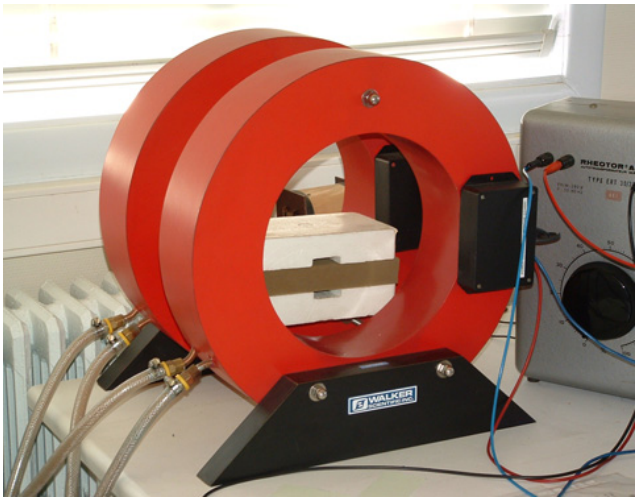

Fig. 4.2.2.2. Helmholtz coils.

Helmholtz coils (Fig. 4.2.2.2) creating a uniform magnetic field were used in order to calibrate the constructed H-coils. The connection wires from the H-coils were twisted in order to avoid coupling with the field created by the Helmholtz coils during the calibration.

It seems convenient to distinguish between a *local* measurement of H conducted using the H-sensors installed at the surface of the sample under study and the identification of the magnetic field H using the excitation current and the magnetic path length (*global* measurement).

4.3. Measurement setups.

Three different setups were used in the current investigation. The setups presented in the subsections 4.3.2 and 4.3.3 are designed to serve the same function. But the first one, being more sophisticated, was finished recently.

In the subsections below, the geometry of the setups, their features and drawbacks are analyzed. It is shown in the section above, that even the structures referred as conventional ones are not perfect. It is not the aim of the designs presented below to address the drawbacks of conventional measurement set-ups. Instead, the purpose is to provide new capabilities related to the subject of this study. Along with the new capabilities new drawbacks inevitably appear. These drawbacks are also addressed in the discussion.

4.3.1. SST for the direct investigation of the effect of punching.

4.3.1.1. Basic construction

This setup is designed for the direct investigation of the effect of the mechanical cutting on the magnetic properties of non-oriented electrical steel. The experimental data collected using this setup are presented in the 8th chapter.

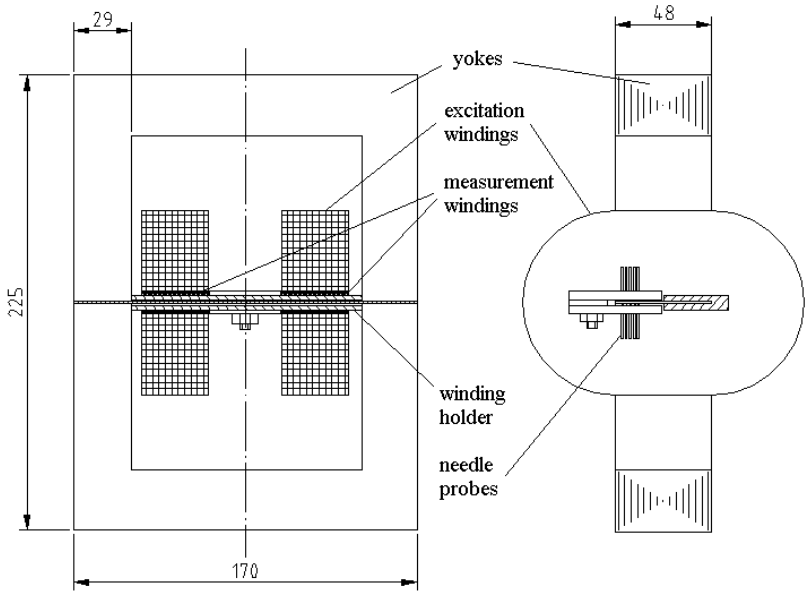

Fig. 4.3.1.1. General structure of the SST for the local magnetic measurements.

The conventional structure of the SST does not provide easy access to the sample, which is required for local magnetic measurements. Therefore in the setup constructed at EELAB, the excitation and the measurement windings are split into 2 parts. The winding holder contains a slot in its central part in order to allow an access to the surface of the sample (Fig. 4.3.1.1).

A. 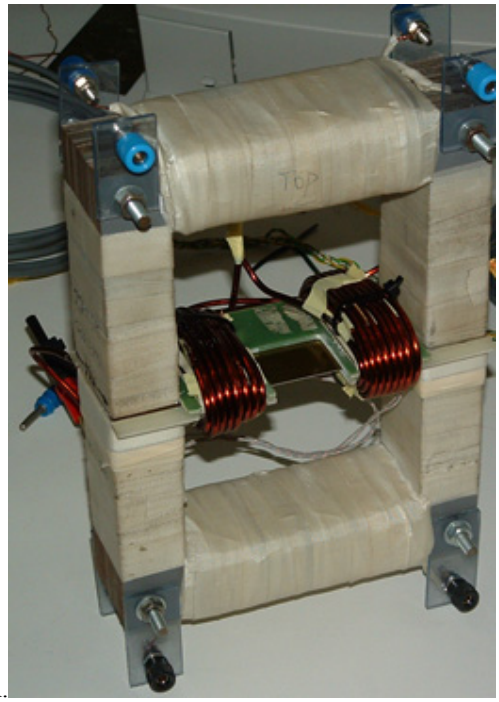

B. 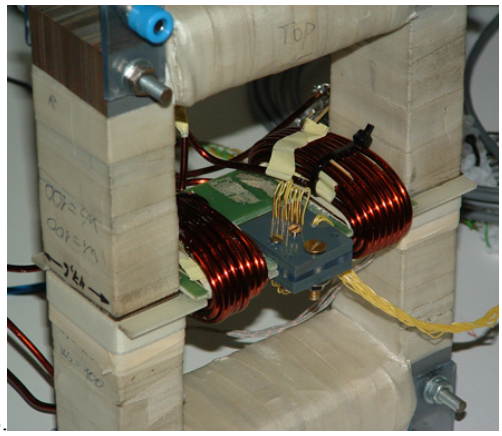

Fig. 4.3.1.2. Photo of the SST (A- without the needles, B - with the needles installed on the sample).

The needle probes are installed in a special plastic holder that is attached to the sample by means of a bolt.

4.3.1.2. Numerical analysis of the setup

The properties of the setup were evaluated by a proper numerical analysis. Using the results of the numerical analysis, we could check whether the material properties assigned to the sample under study for the analysis could be reconstructed using the computed signals of the sensors.
The sample is assumed to be an ideal soft magnetic material that does not show hysteresis effects and that has zero conductivity. In this way, it is sufficient to investigate the quasi-static case only. Since the induction level in the yokes is small, the non-linear magnetic behaviour of the yokes can be neglected.

The finite element formulation is based on the following equations:

$$\begin{cases} \nabla \times \frac{1}{\mu_0} \nabla \times \bar{A} = 0, \quad \textit{in air} \\ \nabla \times \frac{1}{\mu_0} \nabla \times \bar{A} = \bar{J}_{external}, \quad \textit{in winding} \\ \nabla \times \frac{1}{\mu_0 \cdot \mu_{yoke}} \nabla \times \bar{A} = 0, \; \mu_{r,yoke} = 2000 \quad \textit{in yokes} \\ \nabla \times \frac{1}{\mu(\nabla \times \bar{A})} \nabla \times \bar{A} = 0, \quad \textit{in sample} \end{cases} \tag{4.3.1.1}$$

The edge elements were used in the computations. In order to save the memory, the symmetry of the geometry was used. It appears to be sufficient to model only 1/8 of the whole geometry (Fig. 4.3.1.3).

The tetrahedral mesh of the problem was generated using the GMSH software. The mesh consists of 16240 nodes and 94549 elements. The number of finite elements layers along the thickness of the sample is equal to 3.

If the Dirichlet (A=0) boundary condition is applied in the edge element structure, it means that the tangential components of $\bar{A}$ is zero. Consequently, the normal component of the flux density equals zero at the boundary where the Dirichlet condition is used. Therefore boundaries constituting the walls of the flux tube containing the whole flux are assigned Dirichlet boundary conditions (Fig. 4.3.1.4). However one boundary plane (of the 1/8 geometry model) is cutting the flux tube perpendicular to the magnetic path. To this plane a natural (default) boundary condition is assigned.

The sample of the material under investigation is split into 2 parts as shown in Fig. 4.3.1.5. The magnetic properties are evaluated in each part separately.

In order to study the efficiency of the H-sensors, corresponding elements were introduce into the model (Fig. 4.3.1.5).

The investigation in [Fujiwara1995] revealed that the current density has to change smoothly in the corners of the winding in case of using the edge elements. This is required to keep the divergence of the current density as low as possible, approximating the law $\nabla \cdot \overline{J} = 0$. If this requirement is not met then the convergence of the linear problem can be lost. It appears that the $11^0 15'$ step for changing the direction of the current density in the winding is sufficient for avoiding this problem. The discretization of the excitation winding is shown in Fig. 4.3.1.6.

The magnetic field obtained using the edge elements is sufficiently uniform under the excitation winding (Fig. 4.3.1.7). Part 1 of the sample has uniform magnetic flux density (Fig. 4.3.1.8). Part 2 is practically magnetically unloaded.
It can be seen from the numerical results that the part of the sample, below the yoke(s), is not loaded magnetically, i.e. the magnetic flux density in that part of the sample is low. So the magnetic path length corresponds to the distance between the limbs of the yoke. The surface of the limbs was polished in order to improve the contact with the sample.

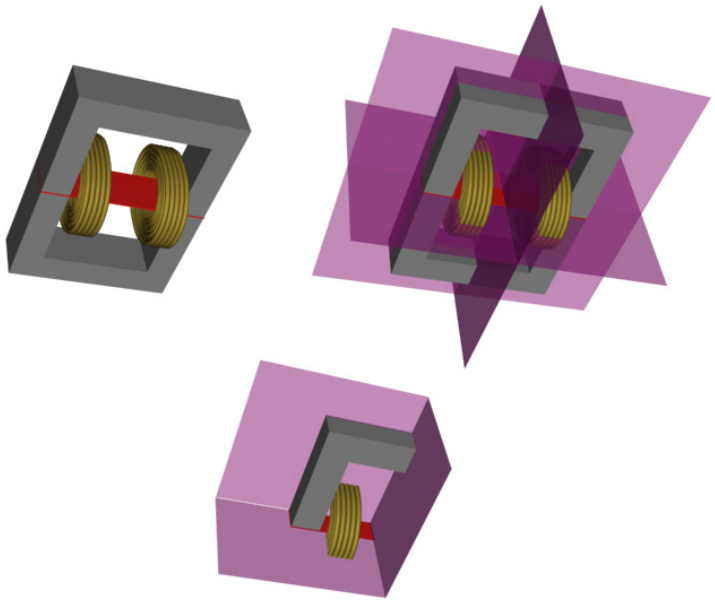

Fig. 4.3.1.3. Using the symmetry planes for reduction of the size of the problem.

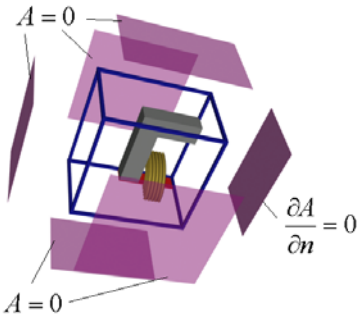

Fig. 4.3.1.4. Definition of the boundary conditions.

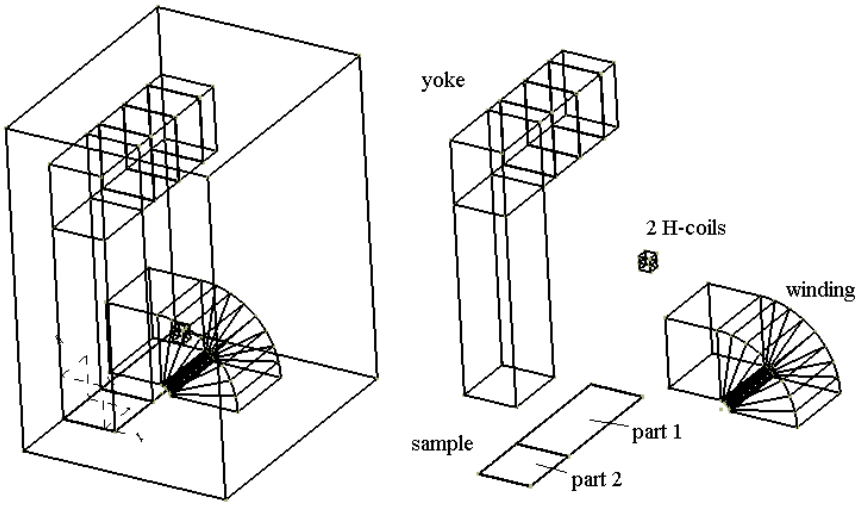

Fig. 4.3.1.5. The discrete construction of the geometry of the 1/8 geometry model.

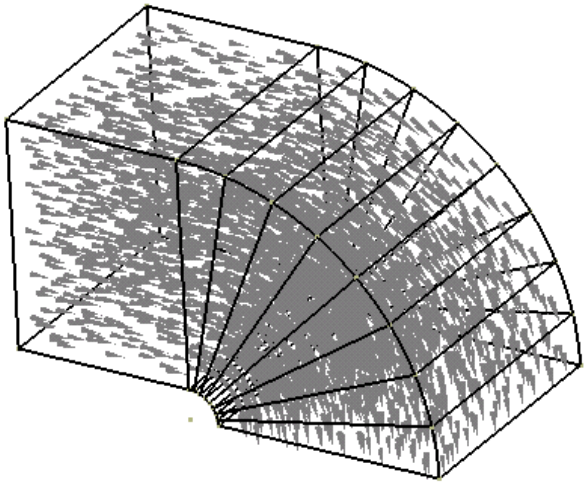

Fig. 4.3.1.6. The assigned current density distribution in the excitation winding.

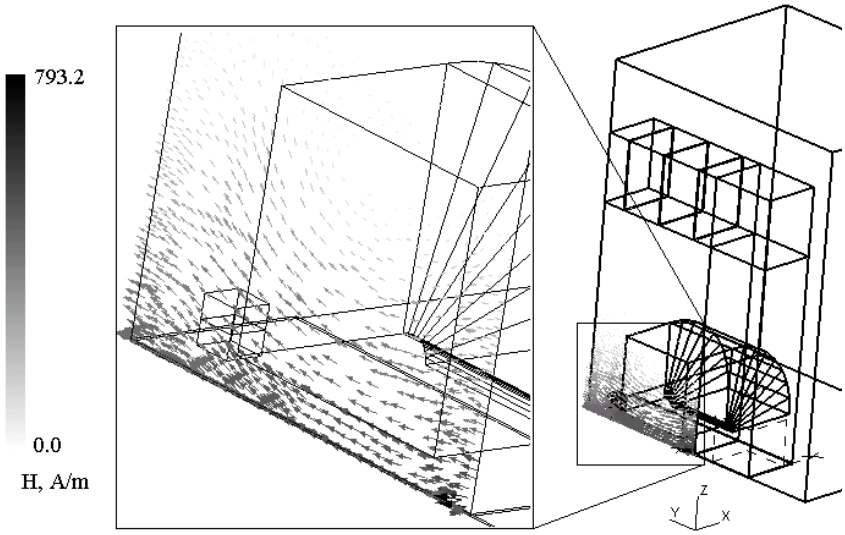

Fig. 4.3.1.7. Distribution of the magnetic field in the cross-section of the space model.

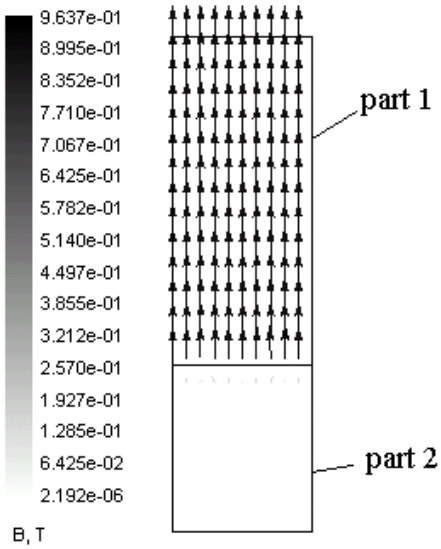

Fig. 4.3.1.8. Distribution of the flux density in the sample.

4.3.1.3. Analysis of B- and H-sensors using the FE computations.

From the definition of the total inductance *L* of the excitation winding with w turns through which a current I flows, we have:

$$LI^2 = \Psi I = w\Phi I \qquad (4.3.1.2)$$

The total physical magnetic flux Φ created by the excitation system can be split into a finite number of flux tubes, each of them corresponding with the fluxes $\Phi_1, \Phi_2, \ldots \Phi_N$ such that $\Phi = \sum_{i=1}^{N} \Phi_i$.

Then

$$LI^2 = w\Phi I = \sum_{i=1}^{N} w\Phi_i I = \sum_{i=1}^{N} L_i I^2 \qquad (4.3.1.3),$$

where L_i is inductance of the corresponding flux tube.
Consider now a finite number of slices of the *i*-flux tube. From Ampere's law we know that

$$wI = \oint_{l_i} H_i dl_i \cong \sum_{j=1}^{M} H_{ij} \Delta l_{ij} . \qquad (4.3.1.4),$$

Let us introduce (4.3.1.4) into (4.3.1.3) taking into account that within the *j*-slice of the *i*-flux tube the local flux can be interpreted as $\Phi_i = B_{ij} S_{ij}$:

$$\sum_{i=1}^{N} w\Phi_i I = \sum_{i=1}^{N} \Phi_i \sum_{j=1}^{M} H_{ij}\Delta l_{ij} = \sum_{i=1}^{N}\sum_{j=1}^{M} B_{ij}H_{ij}S_{ij}\Delta l_{ij} = \sum_{i=1}^{N}\sum_{j=1}^{M} B_{ij}H_{ij}\Delta V_{ij} \quad (4.3.1.5),$$

$B_{ij}H_{ij}\Delta V_{ij}$ is a contribution of the *j*-slice of *i*-flux tube into the total LI^2. This way a contribution of any volume V into the total LI^2 can be considered. It is possible to introduce the inductances L_V related to the volume V:

$$L_V I^2 = \int_V BHdV = \sum_i \int_{element_i} BHdV \quad (4.3.1.6),$$

where the elements considered in the summation are the FE elements lying in the volume V.
The ratio between the corresponding inductances of the different bodies can be found as follows:

$$\frac{L_{V_1}}{L_{total}} = \frac{L_{V_1} I^2}{L_{total} I^2} = \frac{\int_{V_1} BHdV}{\int_{total} BHdV} \quad (4.3.1.7)$$

The proposed approach is used further for the computations of such parameters as leakage factors at different excitations in the considered structure.
For us it is important to know until when the leakage of the setup can be neglected. The magnetization curve assigned for the sample is shown below in Fig. 4.3.1.9.

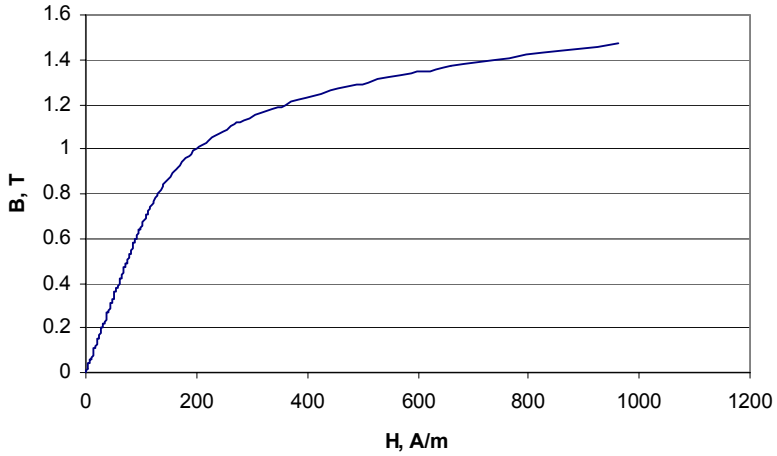

Fig. 4.3.1.9. Magnetization curve assigned in equation (4.3.1.1) to the sample.

If the solution of the FE problem is known, it is also possible to integrate an average field or the flux density in the specific volume. For instance, the average y-component of the magnetic field in the volume V can be computed using the following relation:

$$H_y = \frac{1}{V}\sum_i \int_{element_i} \frac{(\nabla \times \overline{A})_y}{\mu(\nabla \times \overline{A})} dV \qquad (4.3.1.8)$$

The summation is conducted on the elements situated in the volume.
Due to the specific winding and positioning, the H-coil is supposed to have a coupling with the y-component of the field only.

Analogous approach can be used for the definition of the average flux density in the volume V:

$$\overline{B} = \frac{1}{V}\sum_i \int_{element_i} (\nabla \times \overline{A}) dV \qquad (4.3.1.9)$$

In Table 4.3.1.1 it is shown in which part of the measurement set-up the highest magnetic fields are present. Moreover, the table shows the average value of the magnetic field obtained from the numerical computations at the place where the two H-sensors are placed.

Table 4.3.1.1. Results of the magnetic computations

H in the active part of the sample, A/m	B in the active part of the sample, T	H_y in the first H-coil at the sample, A/m	H_y in the second H-coil at the sample, A/m	$\frac{L_{air+windings}}{L_{total}}$	$\frac{L_{active\ part\ of\ the\ sample}}{L_{total}}$
165	0.917	153	142	0.021	0.918
513	1.302	463	432	0.045	0.925
864	1.442	761	713	0.068	0.912

The following conclusions can be drawn from these results:

1. The field H_y defined according to (4.3.1.8) and coupled with the H-coils is smaller than the field in the sample. It is confirmed that for this setup the error increases with distance.
2. The leakage factor (air+windings) increases with the saturation of the sample. But for the considered field range [0, 761A/m] it did not exceed 7%, which is beneficial for the measurement of the flux density. If the measurement winding is not mount right on the sample or if the needles are used for the local measurements there is a little risk that the signal can be distorted by the leakage flux. This conclusion makes this setup suitable for the local magnetic measurements presented in chapter 8.

4.3.2. RSST for the direct investigation of the effect of the mechanical deformation on the magnetic properties of the non-oriented electrical steels.

The aim of the setup discussed in this section is the investigation of the effect of unidirectional mechanical stress on the magnetic properties of non-oriented electrical steels.
The effect of the stress on the magnetic properties depends on the considered magnetization direction in the sample. So the possibility to measure the magnetic properties at different angles with respect to the applied mechanical stress has to be provided.

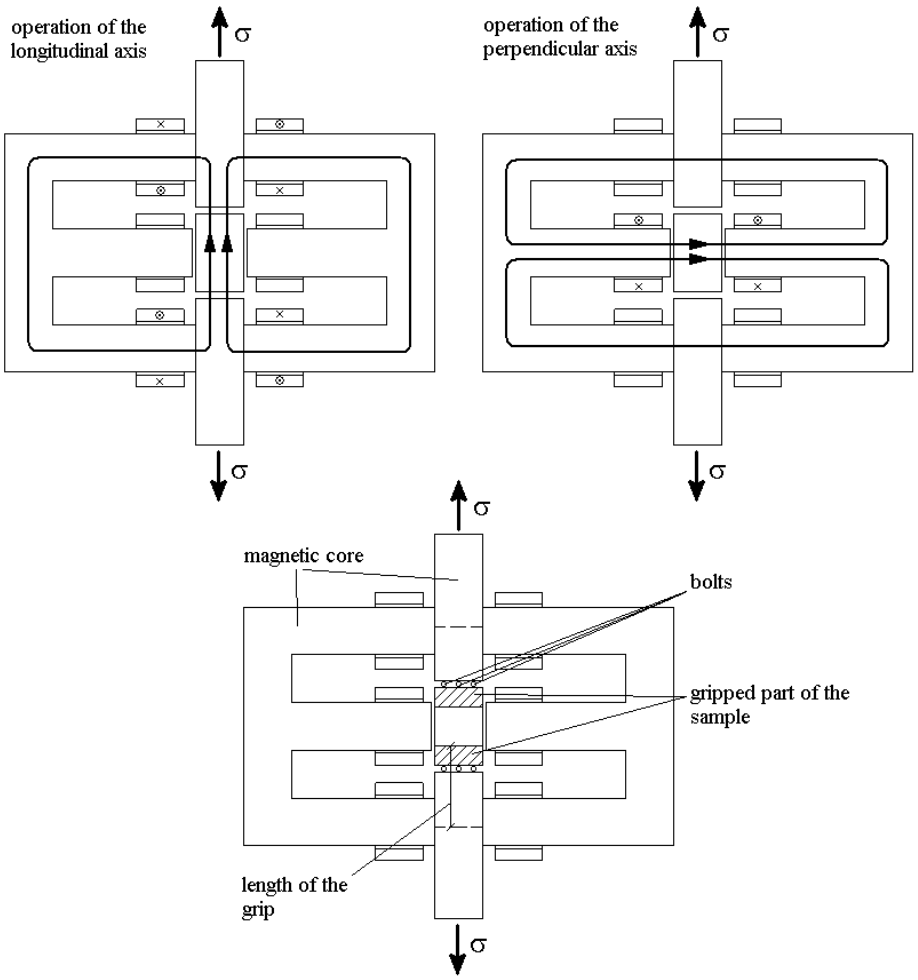

Fig. 4.3.2.1. Structure of the setup.

The research rarely begins from a blank sheet. It is shown in [Dabrowski1989] that the effect of the stress is especially pronounced at the moderate induction levels where the active domain wall motion takes place. As soon as the domain walls are wiped out, the effect of the stress on the magnetic properties appears to be negligible.

The most suitable solution is the rotational single sheet tester (RSST) which allows the identification of vector properties instead of scalar properties. The structure of such system is presented in [Makaveev2003 p. 30]. Its main disadvantage is that it does not allow the accurate measurements of magnetization loops at high induction. Another problem is that there is practically no free space around the sample in order to construct the system for applying mechanical stress.

Therefore a new setup was constructed in such a way that certain elements of the magnetic core were use for the application of the mechanical stress. The limbs of the magnetic core carry the brass grips that allow holding the sample. The maximum width of the sample is 80mm. The length of the sample must be in the range from 110mm to 200mm.
Since the thickness of the core is 20-40 times larger than the thickness of the sample the mechanical stress emerging in the limbs does not exceed 30MPa, which is quite acceptable in terms of mechanical stability of the core. As shown further in this subsection the induction level in the limbs is relatively small. As the measurements are conducted in the central area of the sample the effect of the applied stress on the magnetic properties of the limbs can be neglected.

Three-phase transformer sheets with appropriate dimensions were used for the core of the magnetic circuit of the measurement setup. The arrangement of the sheets is shown in Fig. 4.3.2.1. The assembled setup is shown in Fig. 4.3.2.2.

The preliminary results obtained by 2D electromagnetic computations (XY cross-section) showed that the H and B measurements could be implemented at any angle with respect to the longitudinal axis of the sample. Notice that the longitudinal axis corresponds to the direction of the applied mechanical stress (Fig. 4.3.2.3). 2D simulations performed on the YZ cross-section of the setup indicate the presence of a considerable leakage flux. Since it is difficult to link the computations carried out on the different cross-sections with each other, also a 3D simulation is needed. The corresponding results are presented below.

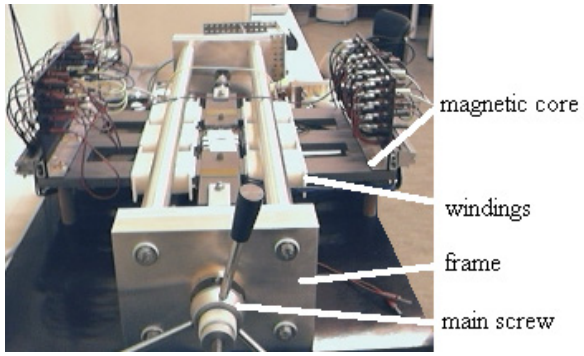

Fig. 4.3.2.2. Assembled setup.

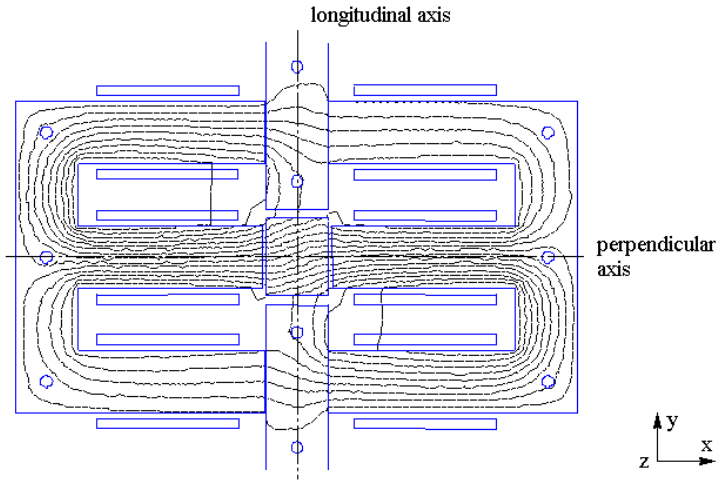

Fig. 4.3.2.3. 2D flux pattern showing the operation of the both magnetic axes (1st – longitudinal axis, 2nd – perpendicular axis).

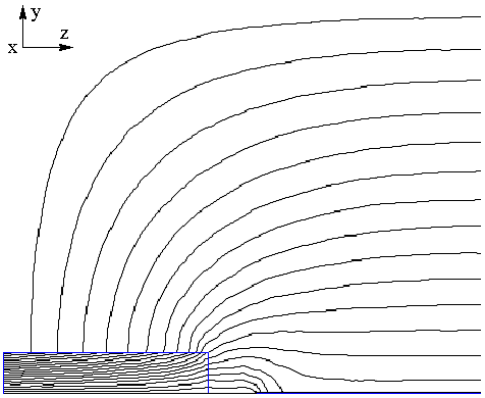

Fig. 4.3.2.4. 2D flux pattern illustrating the stray field above the sample.

4.3.2.1. The mechanical system.

The sample needs to be gripped in order to apply the mechanical stress. The material of the grips has to be non-magnetic. Otherwise the magnetic system would be distorted. Four brass grips carrying the abrasive layers were used in order to hold the sample (Fig. 4.3.2.1.1). The abrasive layer assures a high friction factor between the grips and the sample. We recall that the friction factor is the tangent of the angle between the force and the normal such that when applying a larger angle, sliding of the two contact surfaces occurs. A system of bolts permits the application of compression to the grips.
The grips designed in the laboratory provide both sufficient friction and compression force in order to sustain load force, as large as 49kN.

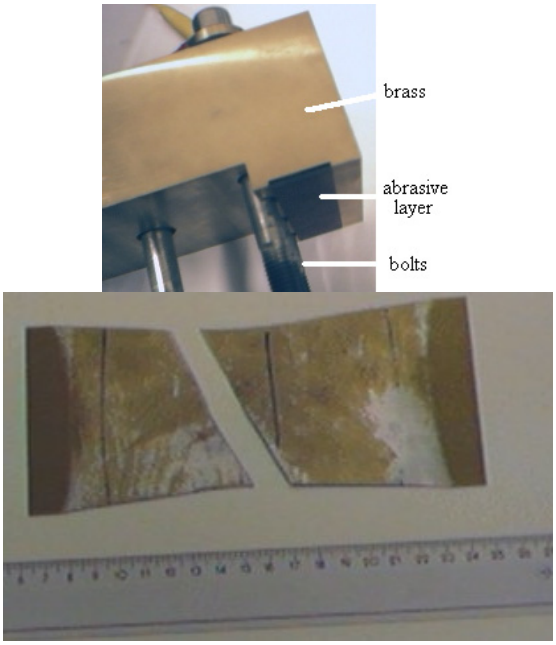

Fig. 4.3.2.1.1. Brass grip and destroyed sample.

The mechanical system allows both application of tension and compression. The applied tension can be high enough to destroy the sample. The level of applied compression is limited by possible bending of the sample. This bending imposes a 50MPa limit on the compression of a 0.65mm thick sample. The general structure of the mechanical part is shown in the figures below.

An aluminum frame provides sufficient rigidity to the setup. The rudder on the right shaft (Fig. 4.3.2.1.2) is used to apply the mechanical load. The left shaft is fixed. The shafts are connected to the ferromagnetic cores. Two couples of the bronze grips are linked to the cores. Each grip has an abrasive layer in order to hold the sample. In order to avoid an unnecessary friction a set of bronze rolls is installed under the grips. Two plastic covers are provided on both sides of the grips. These covers assure the position of the sample when the load is applied, especially for the case of compression.

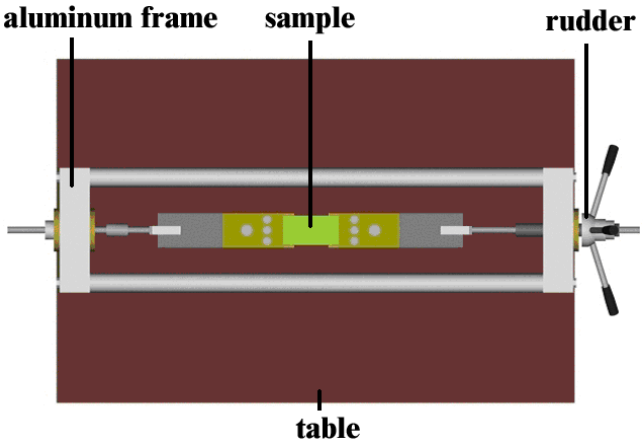

Fig. 4.3.2.1.2. Top view of mechanical part.

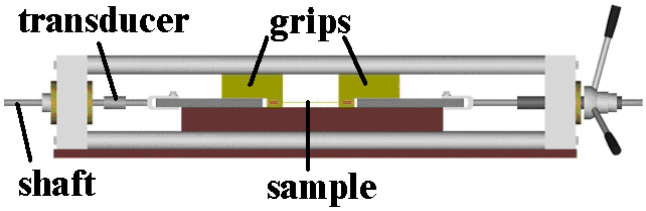

Fig. 4.3.2.1.3. Front view of mechanical part.

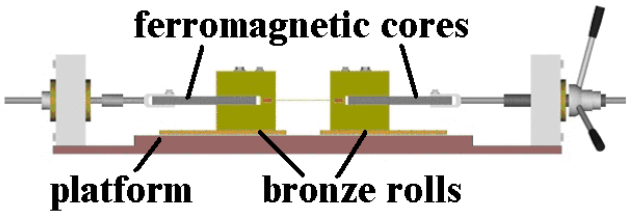

Fig. 4.3.2.1.4. Front view of the mechanical part without horizontal aluminum bars and plastic side covers for the grips.

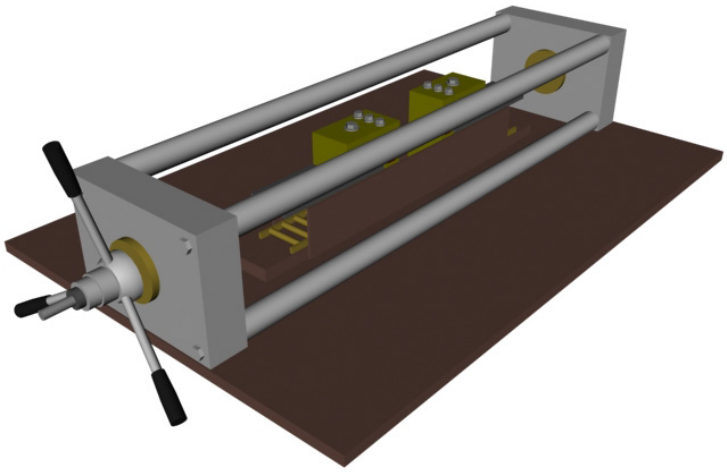

Fig. 4.3.2.1.5. Axonometric view of mechanical part.

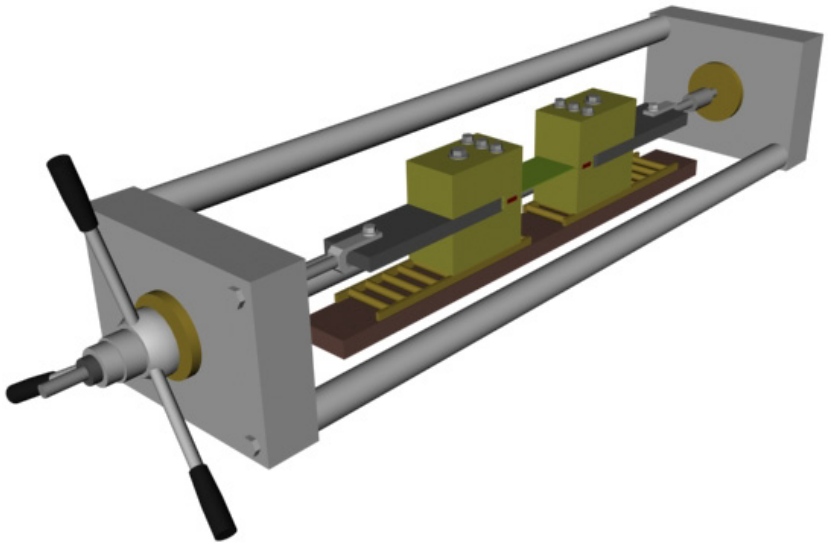

4.3.2.1.6. Axonometric view of the mechanical part without top right aluminum bar and plastic side covers for the grips.

4.3.2.2. The magnetic system.

The magnetic system provides any direction of the field in the plane of the sample. The presence of the grips and bolts requires an increase of the air-gap. The needed rigidity results from the long grips. Therefore, it was impossible to place the excitation windings for the longitudinal axis on the axis of the moving limb. It was decided to put them on the static part of the magnetic core.

It can be seen that the structure of the setup is magnetically asymmetric with respect to the x- and y-axes. Due to the presence of the large air-gaps along the longitudinal direction a non-uniformity of the magnetic field and the flux density in the sample can be anticipated. Therefore the measurements should be conducted in the central part of the sample. The domain where the flux density is sufficiently uniform was preliminary estimated using 2D finite element computations. A correction of the dimensions of the sensors was performed based on the 3D computations (based on edge elements) presented below.
It will be shown later that a much larger field is observed in the air-gap between the sample and the core compared to the field in the sample. So the largest part of the magneto-motive force created by the excitation system is spent on driving the flux through the air-gap.
The numerical analysis of the setup can be reduced to 1/8 of the whole geometry of the problem.
The corresponding current density distributions are shown in Fig. 4.3.2.2.2 and Fig. 4.3.2.2.3. The surfaces for which we use the natural boundary conditions are shown in the figures. For the other surfaces the Dirichlet (A=0) boundary condition is assigned in order to prevent the magnetic induction from crossing them. The corresponding mesh contains 21927 nodes and 94445 elements. The number of layers of the elements in the sample is equal to 4.
The obtained flux density distributions for a magnetic excitation along the longitudinal axis of the setup are shown in Fig. 4.3.2.2.4 and Fig. 4.3.2.2.5. The analogous computations were performed for a magnetic excitation in the perpendicular direction, which is shown in Fig. 4.3.2.2.6 and Fig. 4.3.2.2.7. The flux density in the sample is less uniform when the setup is operating in the perpendicular direction (Fig. 4.3.2.2.6 vs. Fig. 4.3.2.2.4).

Presented field and flux density distributions are suitable for the qualitative analysis of the considered measurement setup. For the quantitative estimation of the properties of the setup some integral parameters were calculated on the specific volumes of the model. We are mostly interested in what the sensors would show. The positioning of the sensors is shown in Fig. 4.3.2.2.8. At the same time it is necessary to know what is actually going on in the sample in the region below the sensor. The average magnetic field was integrated according to (4.3.1.8) both in the part of the sample below the sensor and in the volume of the sensor (H-coil). When the sample was excited in the longitudinal (perpendicular) direction the y-component (x-component) of the field was integrated. The flux density was integrated according to (4.3.1.9) only in the part of the sample below the sensor. In reality the flux density is measured by needle-probes. The BH-curves using first the value for the H in the sample and next the field coupled with the H-sensors, both obtained by the numerical computations are shown in Fig. 4.3.2.2.9 for a longitudinal magnetic excitation and in Fig. 4.3.2.2.10 for a perpendicular magnetic excitation.
Fig. 4.3.2.2.9 and Fig. 4.3.2.2.10 show that a deviation can be observed for both magnetic axes systems. The cause of this deviation is due to the error signal induced in the H-coils by stray fields. This error is definitely larger for the perpendicular axis, and thus the deviation is larger in this direction.
The uniformity of the flux density in the sample is quite good for the longitudinal direction (Fig. 4.3.2.2.4). In order to acquire a sufficient signal the corresponding needles were first positioned at 41mm distance between each other. The perpendicular

direction is worse with respect to the uniformity of the flux density (Fig. 4.3.2.2.6). In order to avoid a systematic error due to the averaging, the measurement of the flux density in the perpendicular direction has to be more local. Therefore the B-needles for this direction are positioned at 10 mm distance between each other.
The magnetic leakage factors for the two main axes of the discussed setup were investigated numerically by considering the contributions to the total inductance by different regions of the magnetic system. The results obtained are presented in Table 4.3.2.2.1 and Table 4.3.2.2.2 for both directions of the setup.

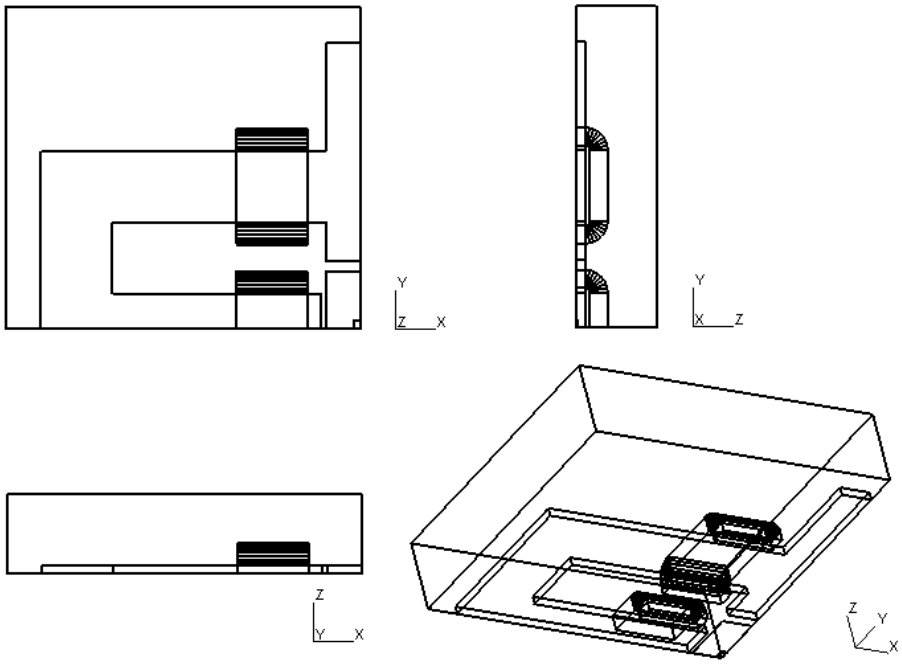

Fig. 4.3.2.2.1. The geometry of the problem.

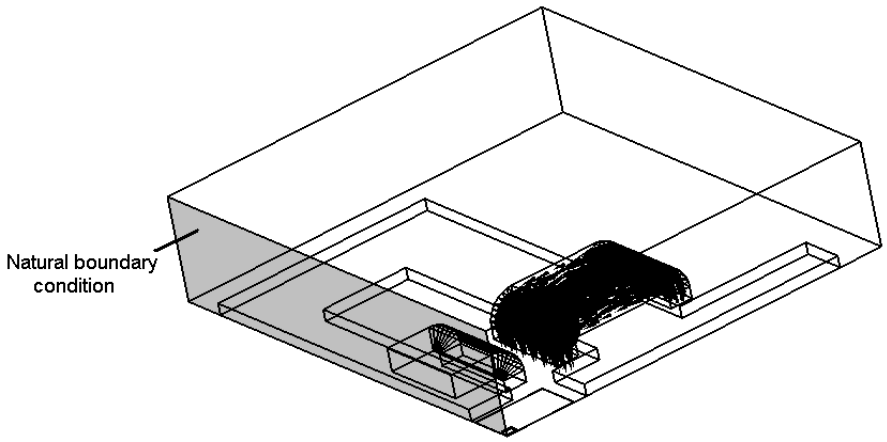

Fig. 4.3.2.2.2. The current density distribution for excitation of the sample in the longitudinal direction.

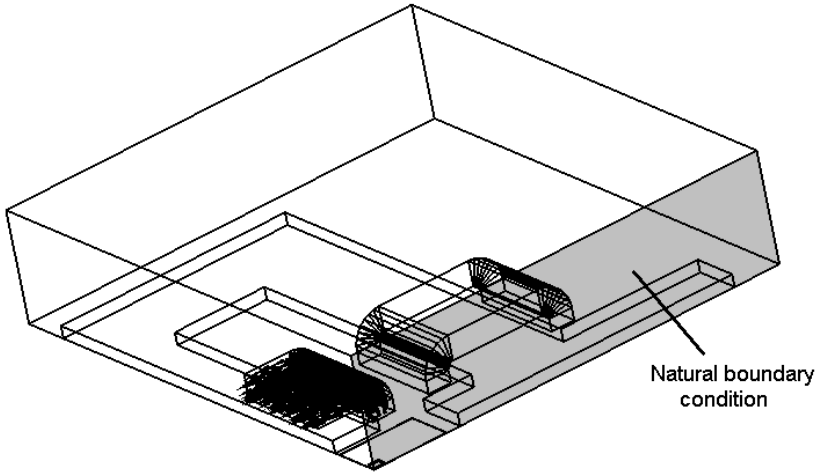

Fig. 4.3.2.2.3. The current density distribution for excitation of the sample in the perpendicular direction.

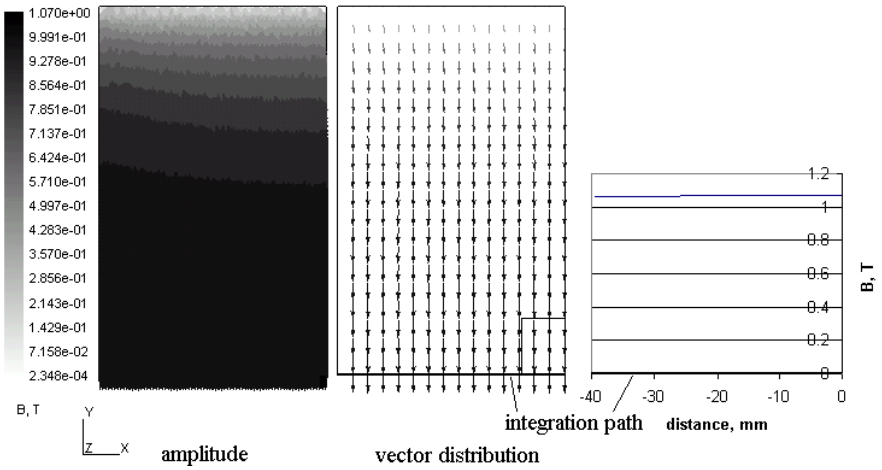

Fig. 4.3.2.2.4. The flux density distribution in the sample for excitation in the longitudinal direction.

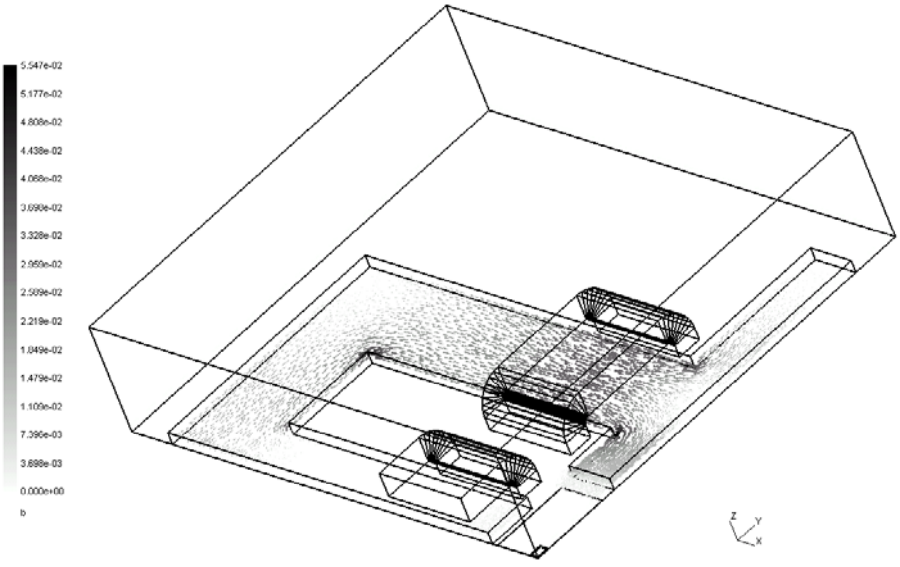

Fig. 4.3.2.2.5. The flux density distribution in the cross-section of the core for excitation in the longitudinal direction.

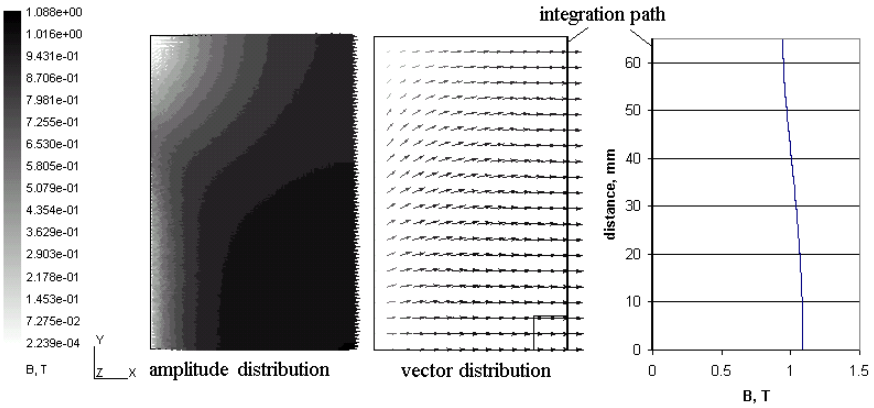

Fig. 4.3.2.2.6. The flux density distribution in the sample for magnetic excitation in the perpendicular direction.

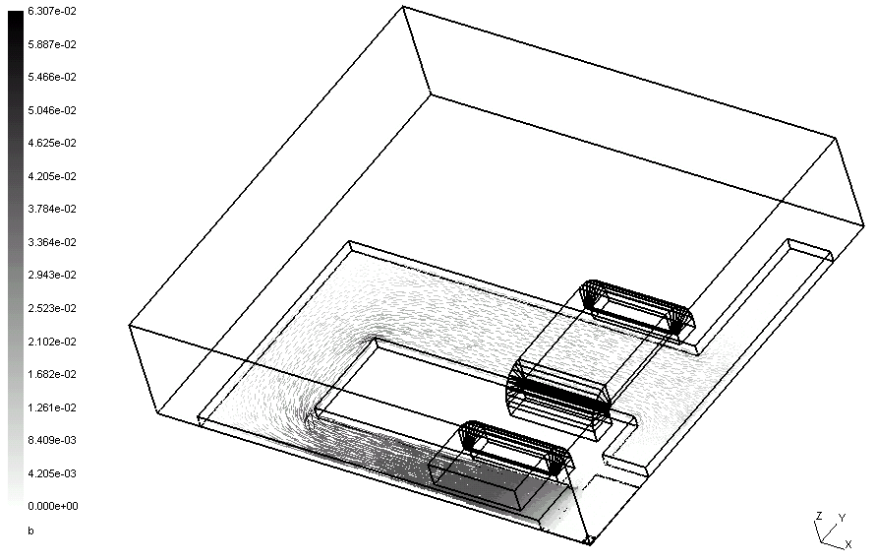

Fig. 4.3.2.2.7. The flux density distribution in the cross-section of the core for magnetic excitation in the perpendicular direction.

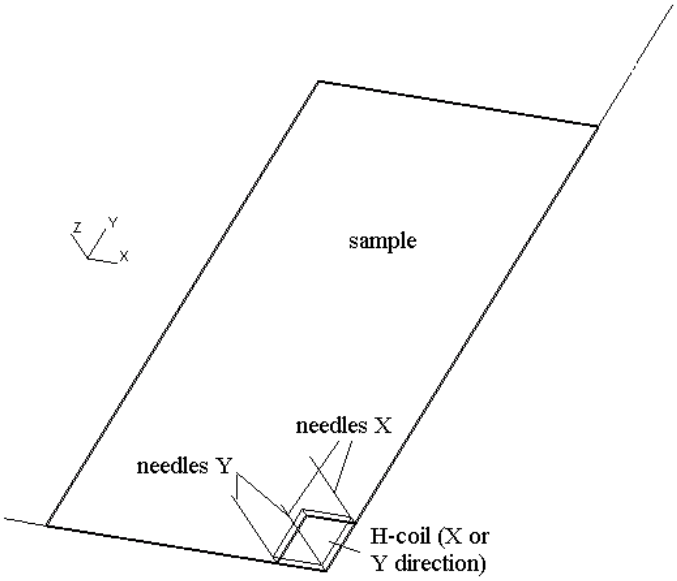

Fig. 4.3.2.2.8. Positioning of sensors - H-coil and B-needles shown on ¼ of the sample.

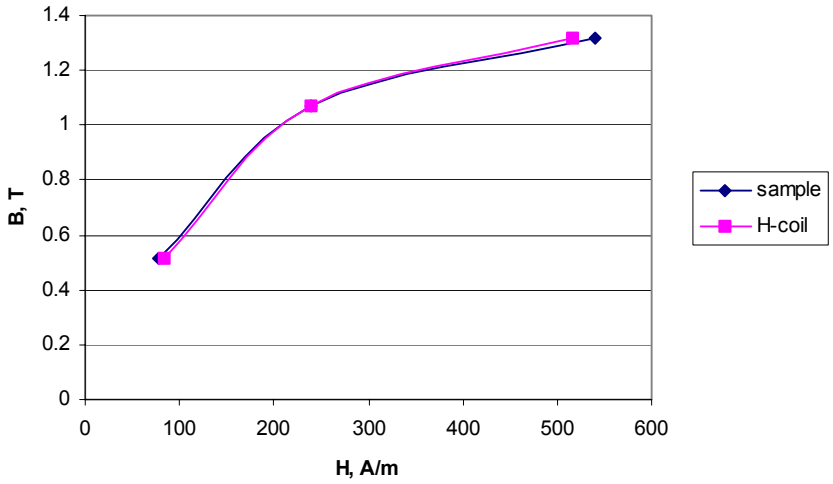

Fig. 4.3.2.2.9. The BH-curves obtained for longitudinal excitation using H in the sample and the field coupled with the H-coil.

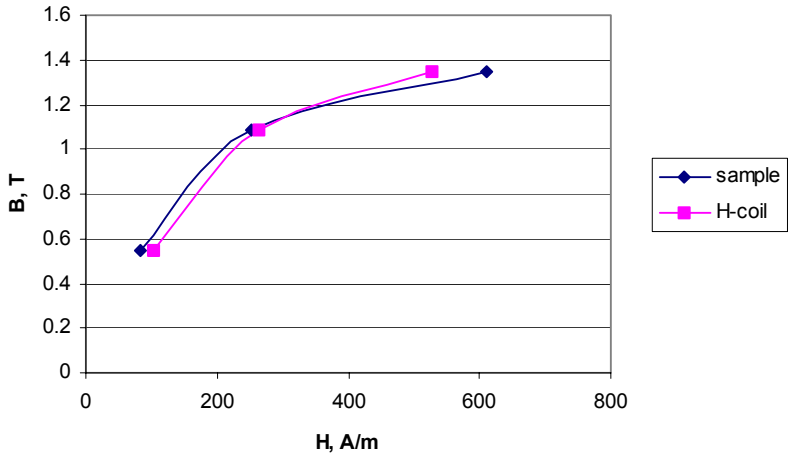

Fig. 4.3.2.2.10. The BH-curves obtained for perpendicular excitation using H in the sample and the field coupled with the H-coil.

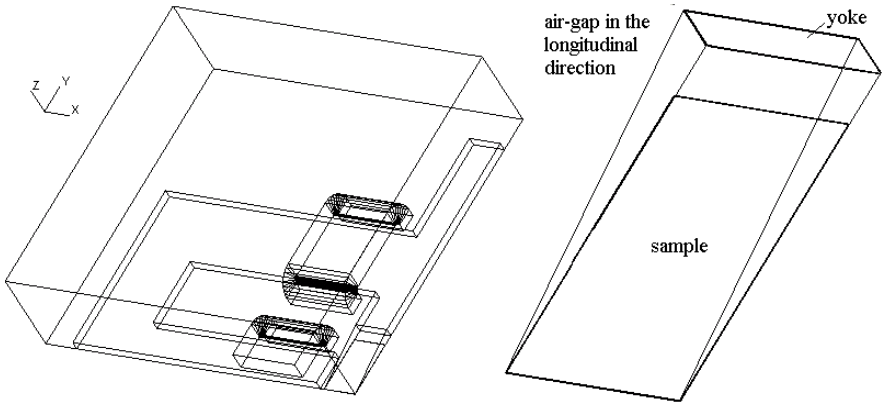

Fig. 4.3.2.2.11. The model that accounts for fringing in the longitudinal direction.

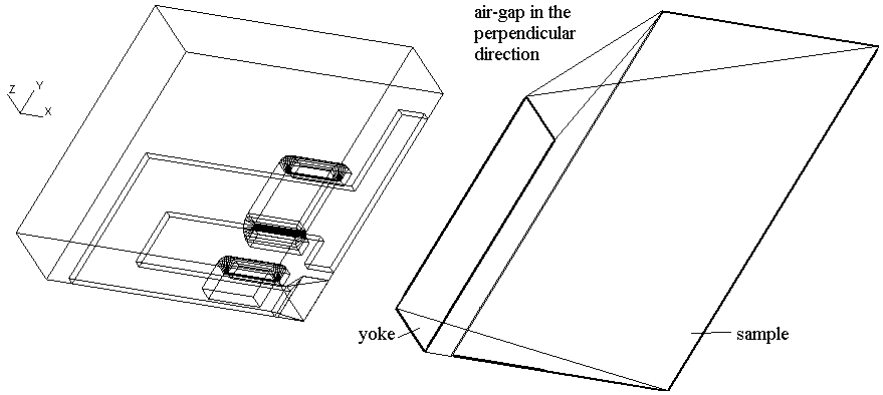

Fig. 4.3.2.2.12. The model that accounts for fringing in the perpendicular direction.

Table 4.3.2.2.1. Computational results for the longitudinal axis of the setup.

H in the sample, A/m	B in the sample, T	$\frac{L_{sample}}{L_{total}}$	$\frac{L_{gap}}{L_{total}}$	$\frac{L_{sample+gap+core}}{L_{total}}$
242	0.986	0.0072	0.0995	0.1225
3290	1.69	0.0047	0.1031	0.1237

Table 4.3.2.2.2. Computational results for the perpendicular axis of the setup.

H in the sample, A/m	B in the sample, T	$\frac{L_{sample}}{L_{total}}$	$\frac{L_{gap}}{L_{total}}$	$\frac{L_{sample+gap+core}}{L_{total}}$
50.8	0.339	0.0111	0.3235	0.3638
215.7	0.967	0.0074	0.3285	0.3654
5045	1.86	0.0577	0.2292	0.3139

The following conclusions can be drawn out of this investigation:

1. The flux in the sample constitutes just a small part of the total flux created by the excitation system.
2. The inductance of the gap remains practically unchanged for the longitudinal axis of the setup. However it is dependent on the saturation of the sample in case of the perpendicular excitation.
3. The setup has a very considerable leakage (relation between flux through the sample and flux coupled with the excitation coil). Therefore attention has to be paid on the twisting of the wires if the needles are used for the local measurement of the magnetic flux density. This is particularly important for the longitudinal axis. An alternative approach for dealing with the H measurement in the presence of the high stray fields is shielding. The details concerning this approach are presented below.

The drawbacks of the setup discovered during the numerical simulation of the operation of the setup were taken into account in order to achieve a good correspondence with other measurement systems, like classical single sheet tester, Epstein frame,…. The dynamic effects such as the eddy current losses are dependent on the geometry of the sample. So it was decided to do the measurements at low frequencies (Fig. 4.3.2.2.13, 4.3.2.2.14).
A good correspondence can be seen, which means that the geometry of the H-sensor and the area for the local flux density measurement are chosen correctly.

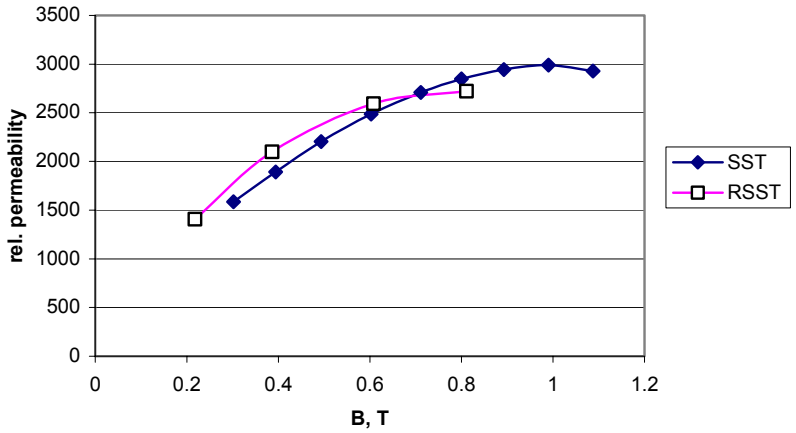

Fig. 4.3.2.2.13. The relative permeability measured on the different setups for RD of V850-65 steel at f=3Hz.

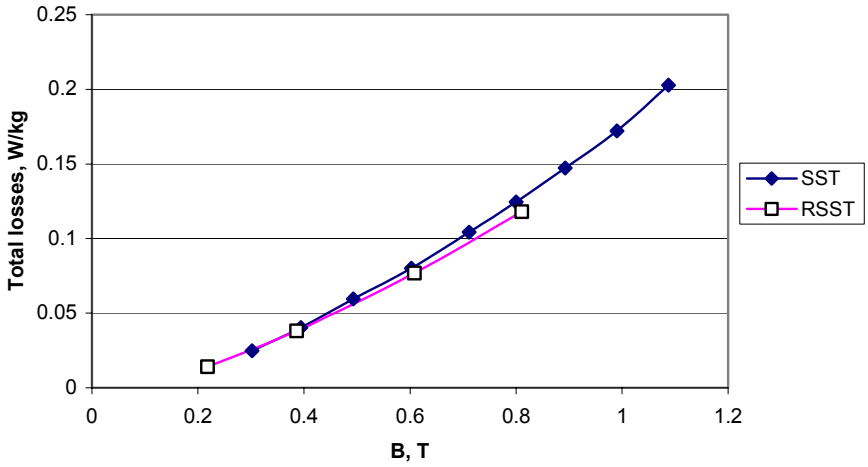

Fig. 4.3.2.2.14. The total magnetic losses obtained on the different setups for RD of V850-65 steel at f=3Hz.

It will be shown in the next chapter that despite having a large leakage this measurement system has some definite merits regarding the shape control of the flux density in the sample.

Notice that the numerical study was conducted assuming that the material of the sample is isotropic, which means that the fundamental error shown in Fig. 4.3.2.2.10 can increase under applied stress due to the anisotropy.

Some special measures should be applied in order to diminish the effect of the stray field and magnetic anisotropy on the magnetic field measurement. Shielding of the H-sensor [Makaveev2003 p. 48] proved to be a suitable solution. When shielding the H-sensors, two samples can be gripped in the setup with a certain space provided between them for the H-coil.

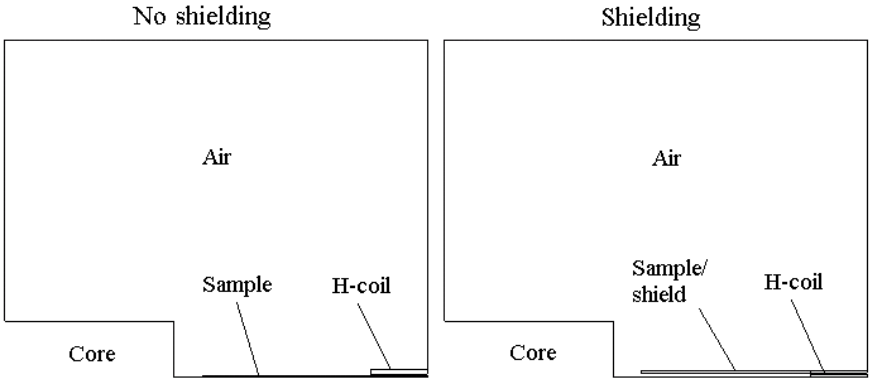

Fig. 4.3.2.2.15. Geometry for the numerical investigation of the effect of shielding.

In order to estimate the effect of shielding for this specific structure, two different geometries (Fig. 4.3.2.2.15) were simulated. The flux patterns presented in Fig. 4.3.2.2.16 and Fig. 4.3.2.2.17 show that in the situation where 2 samples are used, the stray field is not coupled with the H-sensor. The integration of the horizontal component of the field in the area of the H-coil shows a complete correspondence with the field in the corresponding part of the sample. On the other hand, a 20% error was encountered when no shielding is applied.

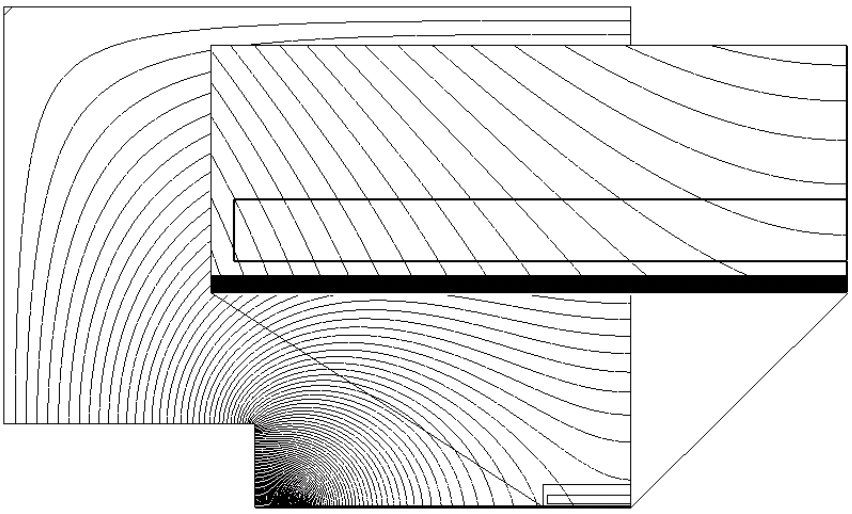

Fig. 4.3.2.2.16. The flux pattern for the case when no shielding is used.

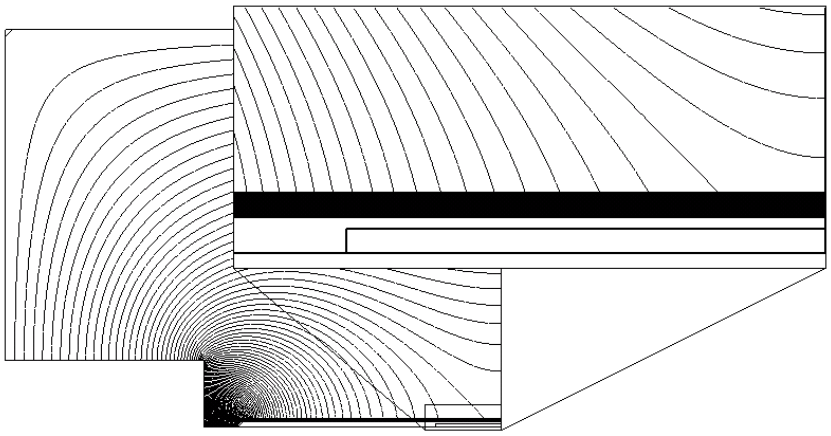

Fig. 4.3.2.2.17. The flux pattern for the case of shielding.

4.3.3. SST with ferrite yokes for the local investigation of the effect of the mechanical deformation on the magnetic properties of the non-oriented electrical steels.

In this subsection an alternative approach for the investigation of the effect of the mechanical stress is proposed. In section 4.3.1 the basic requirements for the size of the sample for the SST were shown. The sample must have the same size as the yokes of the SST in order to avoid additional losses due to the eddy currents as well as distortion of the uniformity of the flux density distribution in the sample. This issue is considered in great detail in [Sievert1990].

A violation of these simple requirements leads to a decrease of the accuracy of the measurements. However we aim at some additional options, such as the investigation of the effect of uniaxial mechanical stress on the magnetic properties of non-oriented electrical steel when this steel is magnetically excited in an arbitrary direction in the plane of the sheet. Notice, that in principle, also the setup discussed in subsection 4.3.2 is suitable for the multidirectional investigation just mentioned. However, due to the complexity of the control of the two axes of the RSST (subsection 4.3.2.), we preferred a modified magnetic excitation based on a classical SST type control.
This setup uses the mechanical system of the setup described in Section 4.3.2 in order to apply a unidirectional stress to the sample. A static but local rotatable double ferrite yoke allows a local magnetic excitation in different directions as shown in Fig. 4.3.3.1. The photos of the setup are shown below in Fig. 4.3.3.2. A top yoke is installed on the bars of the aluminum frame of the mechanical system (Fig. 4.3.2.1.3). The bottom yoke is placed below the sample on the platform. The top yoke is carrying the needles for the local measurement of the flux density in the sample.
A positioning system allows rotation of the yokes so that the magnetic properties under unidirectional magnetic excitation of the material could be tested in the different directions of the sample. In order to assure a good contact with the sample standard ferrite yokes were used for the magnetic system of the setup. For ferrite yokes, [Hug2002] reports that the gap with the sample equals 6 μm.

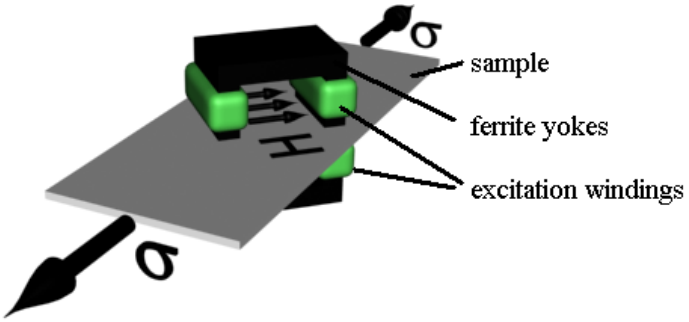

Fig. 4.3.3.1. The general structure of the setup.

As was mentioned before, the maximum width of the sample for the RSST equals 80mm while the length of the sample must be in the range from 110 mm to 200 mm. The sample is rectangular due to the need for gripping. Consequently, the sample is also electromagnetically asymmetric with respect to geometry. The largest difference is clearly between 0^0 (longitudinal direction = direction of the applied mechanical load) and 90^0 orientations (direction perpendicular to the applied mechanical load) of the ferrite yokes. In order to evaluate the properties of the setup, a numerical analysis was carried out for each of these orientations. As before, only 1/8 of the whole geometry was modeled. The mesh corresponding to 0^0 orientation (Fig. 4.3.3.3) contains 7088 nodes and 31373 elements and the mesh corresponding to 90^0 orientation (Fig. 4.3.3.4) has 6952 nodes and 31356 elements.
The flux density distribution in the sample for the two orientations is shown in Fig. 4.3.3.5 and Fig. 4.3.3.6. It can be seen that the part of the sample between the yokes is under a uniform magnetic excitation.

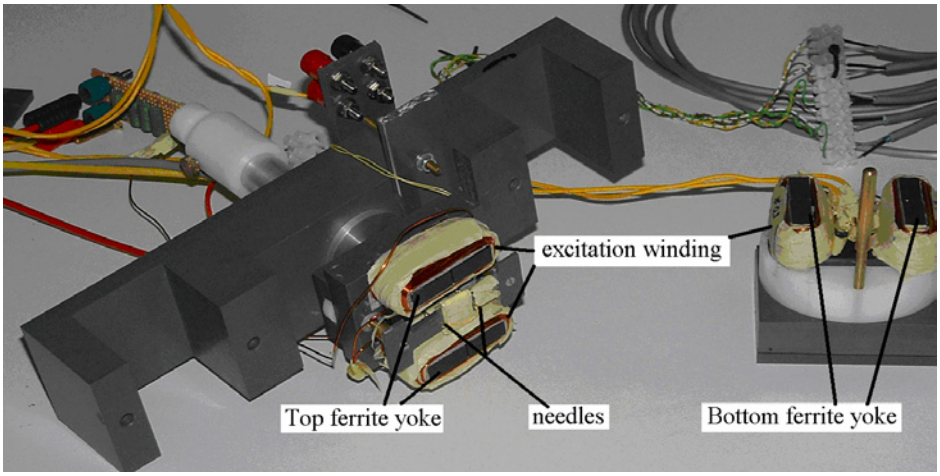

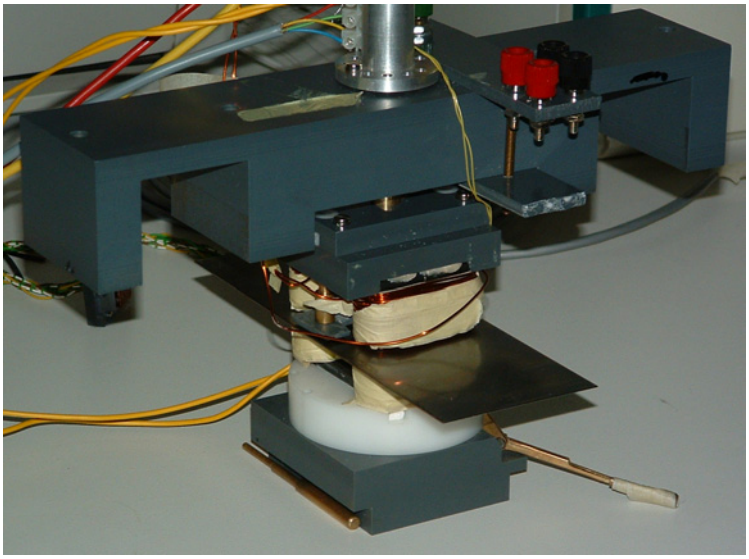

Fig. 4.3.3.2. The view of the setup.

In order to estimate the difference between the axes, the sample was split in 2 parts (Fig. 4.3.3.7). The 1st part of the sample is the part where we would like to have a uniform magnetic flux density. The second part of the sample provides the leakage route. Therefore these two parts are considered separately in Table 4.3.3.1 and Table 4.3.3.2.
It is shown in Table 4.3.3.3 that the flux density in the 1st part of the sample is very similar for the 0^0 and 90^0 orientations if the same currents are supplied to the excitation windings. At low inductions a clear similarity is observed between the calculated inductances of the 1st part of the sample for the 0^0 and 90^0 orientations of the yokes, which means that there is a correspondence in the magnetic field. So we may assume that the field in the 1st part of the sample can be extracted from the current after appropriate calibration of the magnetic path length without taking into account the

orientation of the ferrite yokes. However the measurement of the magnetic flux density should be performed locally. In the actual setup the flux density was measured using the pair of needles installed on the sample.
Since the investigated area is situated in the center of the sample it is not necessary to use a rectangular shape. The shape of the samples used for the setup with the local ferrite yokes is shown in Fig. 4.3.3.8. This shape helps to achieve a better uniformity of the plastic deformation in the sample.
The positioning system together with the ferrite yokes provides a sufficient rigidity to the sample, such that applied compression up to 80MPa is allowed without bending.
In order to estimate if the setup provides correct information on the magnetic anisotropy present in the material the measurements were conducted on V-850-65 steel using the ferrite yokes and the RSST discussed in [Makaveev2003 p. 30]. The results (Fig. 4.3.3.9) show that the difference between the setups is acceptable.
As it was shown in the first chapter of this thesis, the applied elastic stress results in a change of the magnetic anisotropy. Since the purpose of this setup is to study the effect of the stresses it was possible to detect the magnetic anisotropy. The numerical results showed that the systematic error is sufficiently low at moderate and low inductions.

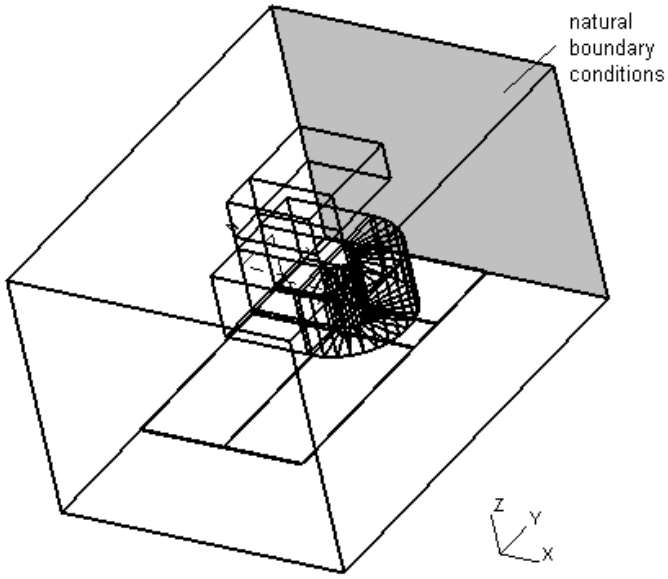

Fig. 4.3.3.3. The 1/8 geometry model for the 0^0 orientation of the yokes. The applied mechanical load is along the y-axis

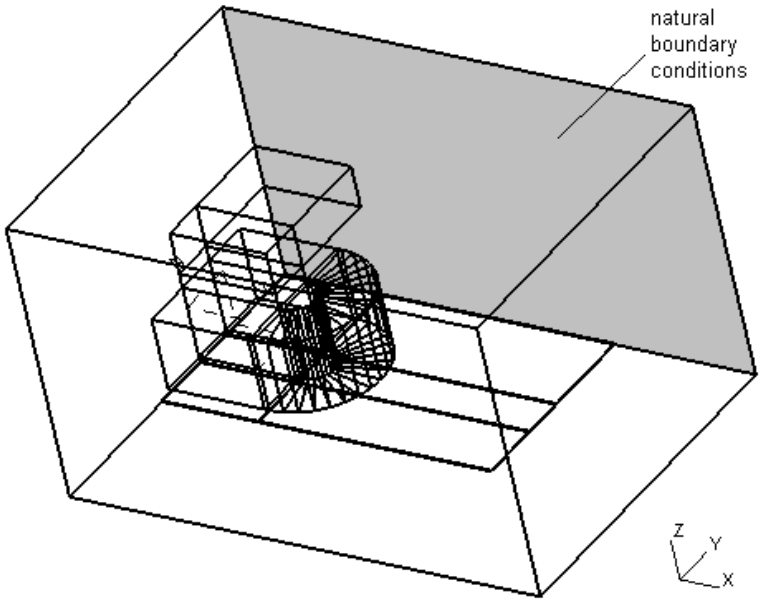

Fig. 4.3.3.4. The 1/8 geometry model for the 90^0 orientation of the yokes. The applied mechanical load is along the x-axis

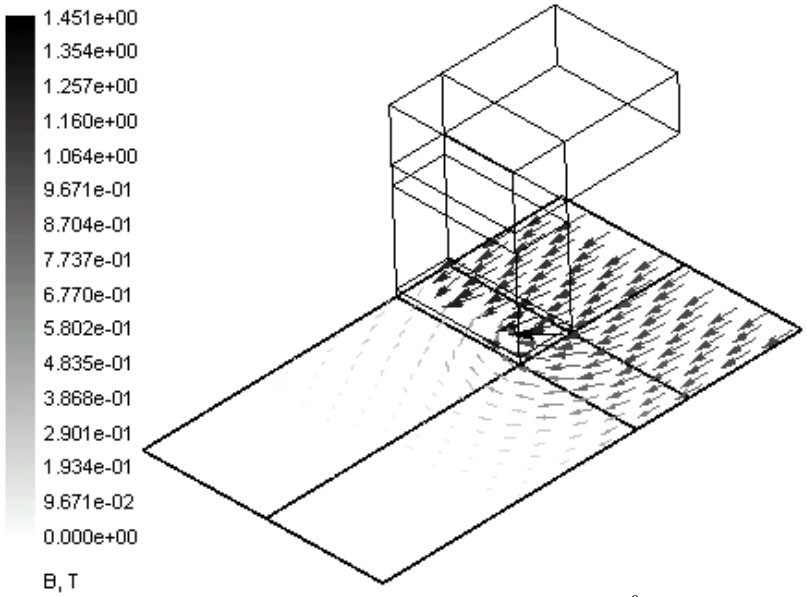

Fig. 4.3.3.5. The flux density distribution in the sample for the 0^0 orientation of the yokes in the 1/8 geometry model.

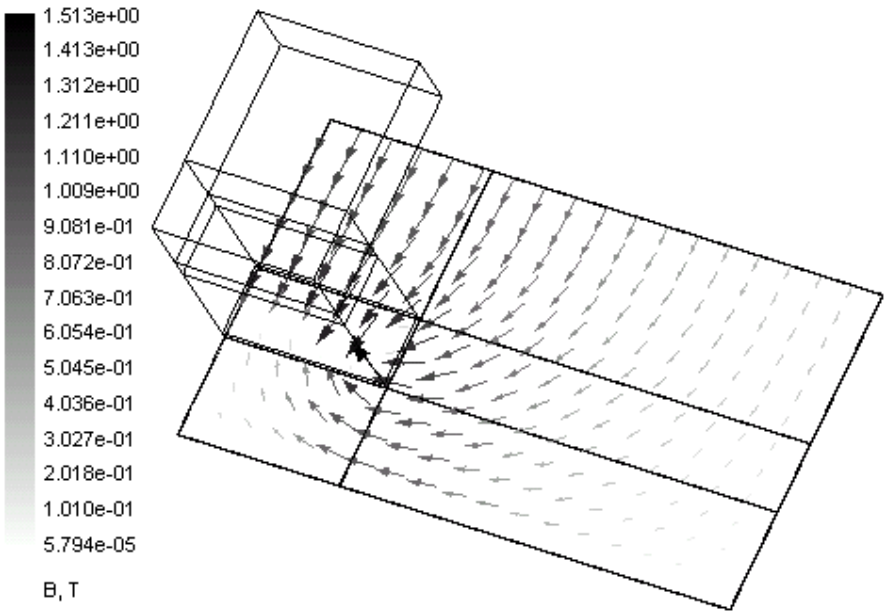

Fig. 4.3.3.6. The flux density distribution in the sample for the 90^0 orientation of the yokes in the 1/8 geometry model.

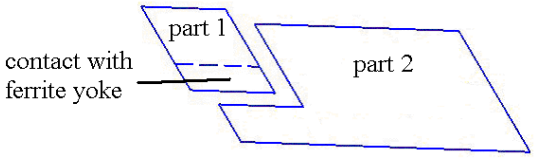

Fig. 4.3.3.7. Splitting up the sample into 2 parts in the 1/8 geometry model.

Table 4.3.3.1. Inductance in the different volumes of geometry for 0^0 orientation of the yokes.

Volume	Excitation I=0.12A	Excitation I=0.36A	Excitation I=1.2A
	$L/L_{\Sigma}*100$	$L/L_{\Sigma}*100$	$L/L_{\Sigma}*100$
part 1 of the sample	**48.211**	**47.947**	**45.884**
part 2 of the sample	28.463	35.240	37.840
air and winding	2.186	3.856	10.850
ferrite core	21.139	12.956	5.426
Total	**100**	**100**	**100**

Table 4.3.3.2. Inductance in the different volumes of the geometry for 90^0 orientation of the yokes.

Volume	Excitation I=0.12A	Excitation I=0.36A	Excitation I=1.2A
	$L/L_\Sigma*100$	$L/L_\Sigma*100$	$L/L_\Sigma*100$
part 1 of the sample	**43.396**	**45.103**	**47.076**
part 2 of the sample	32.051	38.210	40.952
air and winding	1.122	1.951	5.780
ferrite core	23.432	14.736	6.192
Total	**100**	**100**	**100**

Table 4.3.3.3. Average magnetic flux density.

Volume	Average B, T					
	Excitation I=0.12A		Excitation I=0.36A		Excitation I=1.2A	
	0^0	90^0	0^0	90^0	0^0	90^0
part 1 of the sample	0.579	0.578	0.983	0.978	1.296	1.27

Table 4.3.3.4. Comparison of the difference of the inductances in % between 0^0 and 90^0 orientation of the yokes for the different volumes and for the different excitation currents.

Volume	Excitation I=0.12A	Excitation I=0.36A	Excitation I=1.2A
part 1 of the sample	1.78	-5.31	-11.26
Total	-8.39	-10.93	-8.96

Fig. 4.3.3.8. A shape of the samples used for the magnetic measurements.

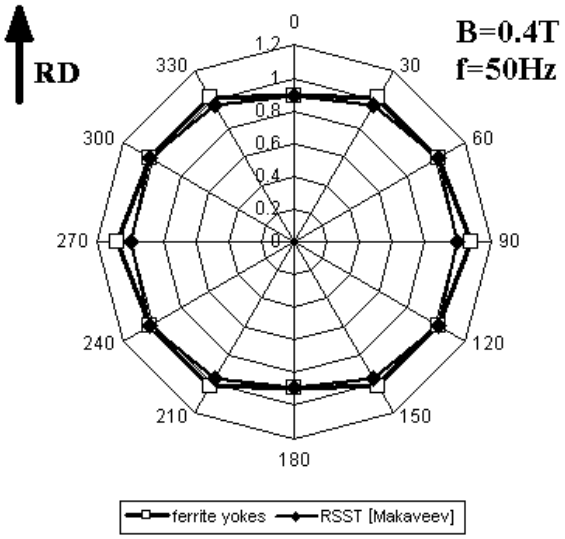

Fig. 4.3.3.9. The total losses distribution obtained on the V850-65 steel using the ferrite yokes and magnetically symmetric RSST setup developed by D. Makaveev.

Conclusions.

In this chapter the basic principles of the magnetic measurements used during the presented research were discussed. The local and the global measurements of the magnetic field and the flux density in the various magnetic structures were considered. The advantages and the drawbacks of the needle probe method were discussed:

- This method is simple and permits very local characterization of the magnetic properties in the sample;
- If applied at the very edge of the sample it can result in a systematic error even if low excitation frequencies are used.
- It leads to much lower signals compared to the B-coil wrapped around the complete sample.

The magnetic structures of 3 constructed measurement setups were presented. The following conclusions can be drawn on each of the setups:

1. The SST (subsection 4.3.1) is clearly the most suitable measurement system for a unidirectional excitation. It provides a sufficiently uniform flux density in the sample. The leakage is low. However it increases with the saturation of the sample.
2. The RSST (subsection 4.3.2) provides sufficient uniformity of the magnetic flux density in the central area of the sample at moderate inductions (below the knee of the magnetization curve), which was shown both by the numerical simulations and by experiments. Due to large air-gaps, this setup has very large stray fields influencing the local H-measurements. The quality of the local H-measurement can be improved by means of shielding.

3. It is confirmed both numerically and experimentally that the SST with the ferrite yokes (subsection 4.3.3) is suitable for the multidirectional magnetic measurements at moderate inductions and applied constant uniaxial stress.

Chapter 5. Flux density shape control.

Introduction.

In magnetic measurements we can either impose the magnetic field H(t) at the surface of the sample or the total magnetic flux $\Phi(t)=B(t)S$, with S the cross-section of the sample. It will be shown in this chapter that in some setups it is relatively easy to manipulate the magnetic field, while in the others it is more comfortable to deal with the magnetic flux density. However it appears that in general the results, e.g. the total magnetic losses and the magnetic permeability, are affected by the choice of the operation quantity (for instance, sinusoidal flux density vs. sinusoidal magnetic field). In order to preserve the correspondence between the measurement results obtained on different setups it was decided to apply a sinusoidal flux density in the working part of the sample on all the setups.

Some special measures must be applied in order to obtain a sinusoidal flux density in the sample. The measurement setups considered in this thesis are to be considered as transformers working in a no-load mode. Indeed, the excitation winding of the setup is equivalent with the primary winding of the transformer while the measurement winding or the needle probes are an analog of the secondary windings in the transformer disconnected from the load. The parameters of a transformer are known to depend strongly on the parameters of the windings. In the present designs of the setups, the efficiency is not a priority. What really matters is the shape of the field quantities and their uniformity in the sample area of interest.
In Section 5.1 it will be considered whether the winding parameters can be used in order to achieve a desired shape of the magnetic flux density or magnetic field.
In Section 5.2 the shape control subroutine developed in [Makaveev2003 p. 53] will be briefly reviewed. Its application to the flux density control in the RSST and other linear magnetic setups is shown.
In Section 5.3 the use of a current supply in order to achieve the desired flux density shape is discussed.

Section 5.1. Winding parameters.

The relation for the inductance of the magnetic system with constant cross-section (Fig. 4.2.1.2) can be found from Ampere's law:

$$iw = H_m l_m = \frac{B_m S_m}{\mu_m S_m} l_m = \frac{\Phi_m}{\mu_m S_m} l_m \qquad (5.1.1)$$

Here, the total magnetic flux Φ due to the current in the excitation winding is split into two parts: the main flux Φ_m and the leakage flux Φ_σ, the former coupled with the excitation winding and flowing throught the sample under investigation while the latter is only coupled with the excitation winding. The component of the voltage in the excitation winding corresponding with the flux Φ_m is given by (supposing a linear behaviour):

$$v_m(t) = L_m \frac{di}{dt} = w\frac{d\Phi_m}{dt} = w\frac{d}{dt}\left(\frac{iw \cdot \mu_m S_m}{l_m}\right) \tag{5.1.2}$$

$$L_m = \frac{w^2 \mu_m S_m}{l_m} \tag{5.1.3}$$

where w is the number of turns in the excitation winding, μ_m is the magnetic permeability of the material of the magnetic circuit, l_m equals the magnetic path length and S_m is the cross-section area of the magnetic system.
The corresponding equivalent circuit is shown in Fig. 5.1.1 below. Here R is the resistance of the excitation winding while L_σ is the leakage inductance corresponding with the flux Φ_σ.

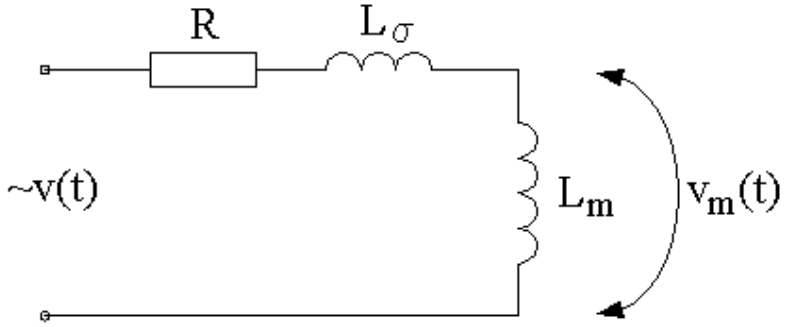

Fig. 5.1.1. The equivalent circuit of the setups shown in Fig. 4.2.1.2.

If the magnetic circuit is SST-like, i.e. it consists of the sample and yokes, then equation (5.1.1.) becomes:

$$iw = \oint_l \overline{H} \cdot d\bar{l} = H_{yoke} l_{yoke} + H_{sample} l_{sample} = \tag{5.1.4`}$$

$$\frac{B_{yoke} S_{yoke}}{\mu_{yoke} S_{yoke}} l_{yoke} + \frac{B_{sample} S_{sample}}{\mu_{sample} S_{sample}} l_{sample} \tag{5.1.4``}$$

Assuming that the same flux is present both in the sample as well as in the yoke:

$$iw = \Phi_m \left(\frac{1}{\mu_{yoke} S_{yoke}} l_{yoke} + \frac{1}{\mu_{sample} S_{sample}} l_{sample}\right) \tag{5.1.5}$$

The voltage $v_m(t)$ corresponding with the main flux Φ_m:

$$v_m(t) = L_m \frac{di}{dt} = \frac{d\Psi_m}{dt} = w\frac{d\Phi_m}{dt} = w\frac{d}{dt}\frac{iw}{\frac{l_{yoke}}{\mu_{yoke}S_{yoke}} + \frac{l_{sample}}{\mu_{sample}S_{sample}}} = \frac{1}{\frac{l_{yoke}}{w^2\mu_{yoke}S_{yoke}} + \frac{l_{sample}}{w^2\mu_{sample}S_{sample}}}\frac{di}{dt} = \frac{1}{\frac{1}{L_{yoke}} + \frac{1}{L_{sample}}}\frac{di}{dt} \quad (5.1.6)$$

Therefore the model should contain two inductances L_{yoke} and L_{sample} connected in parallel. The corresponding equivalent circuit is presented in Fig. 5.1.2 below.

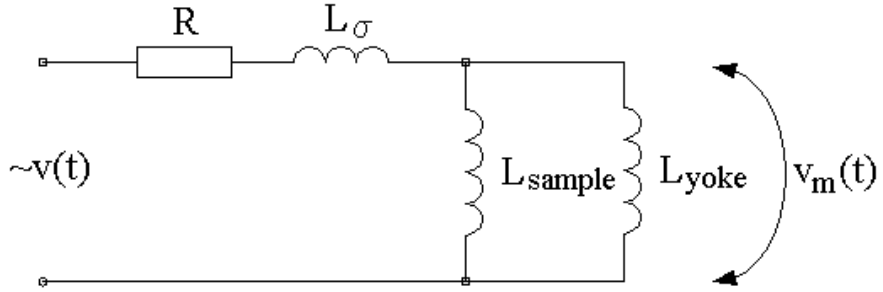

Fig. 5.1.2. Equivalent circuit of the SST-like measurement setups.

Since the cross-section S_{yoke} of the yoke is much larger than the cross-section S_{sample} of the sample and the path length in yoke and sample, i.e. l_{yoke} and l_{sample}, are of the same order, L_{yoke} can be neglected. When the sample is saturated its permeability considerably drops. This results in a further increase of the difference between L_{sample} and L_{yoke}. Therefore L_{yoke} is negligible compared to L_{sample} and, consequently, the equivalent circuit of Fig. 5.1.1 is also applicable to the SST.

In order to take into account the saturation of the sample (in actual situation) we write $L_m(i)$ for the main inductance.

The governing relation for this circuit:

$$v(t) = R \cdot i(t) + \frac{d\Psi_\sigma}{dt} + \frac{d\Psi_m}{dt} = R \cdot i(t) + L_\sigma \frac{di}{dt} + L_m(i)\frac{di}{dt} \quad (5.1.7)$$

The ratio between the leakage flux and the main flux for the SST has been discussed in the previous chapter. It allows us to neglect the second term in (5.1.7). The voltage v(t) over the excitation winding has two terms: a resistive term and a term corresponding to the main flux in the sample. We obtain:

$$v(t) = v_R(t) + v_m(t) \quad (5.1.8)$$

If one wants to provide a certain flux density shape then it is necessary to get a corresponding shape of $v_m(t)$. The basic problem during control is that in the case of a

voltage supply of the excitation winding neither the current defining the field in the sample (5.1.4`) nor the voltage $v_m(t)$ related to the flux density in the sample are directly assigned by the input voltage v(t). Indeed, due to the resistive voltage drop the shape of $v_m(t)$ never completely corresponds to the shape of v(t).

As an example, consider the voltage over the excitation winding for a sinusoidal current with frequency $f=\omega/2\pi$ and assuming a constant permeability of the sample:

$$v(t) = RI_m \sin \omega t + \omega L_m \cdot I_m \cos \omega t \tag{5.1.9}$$

The deviation between the shape of the input voltage v(t) and $v_m(t)$ is largely determined by the ratio $R/\omega L_m$:

$$\frac{R}{\omega L_m} = \frac{\rho \frac{w l_{turn}}{S_{wire}}}{2\pi f \cdot \frac{w^2 \mu S_{sample}}{l_m}} = \frac{\rho \frac{l_{turn}}{S_{wire}}}{2\pi f \cdot \frac{w \mu S_{sample}}{l_m}} = \frac{\rho l_{turn} l_m}{2\pi f \cdot w \mu S_{wire} S_{sample}} \tag{5.1.10}$$

It is obvious that for higher frequencies (e.g. due to harmonics) the ratio is decreasing. The length of one turn l_{turn} is provided by the geometry of the winding holder. The geometry of the sample can also be assumed to be fixed. So the only component that can be manipulated is the cross-section of the winding. The larger wS_{wire}, the smaller the ratio defined in (5.1.10) and, consequently, the smaller the deviation in shape between v(t) and $v_m(t)$. The size of the excitation winding has to be defined during the design of the measurement setup.

The winding of the SST introduced in the previous chapter was designed in such a way that it provides a ratio $R/\omega L_m$ less than 12% at f=10Hz and $\mu=1500\mu_0$. A smaller ratio could not be provided for technical reasons. The measurements conducted on non-oriented electrical steel at 50Hz frequency showed that the form factor of the measured flux density did not change more than 2% compared to the form factor of the sinusoidal input voltage at small and moderate induction levels.
As long as the form factor is close enough to the desired value it is sufficient to operate with an amplitude value of the input voltage in order to provide the required flux density in the sample. Such approach is relatively fast and simple, which in certain cases can be advantageous.
The same approach was applied in the SST with the ferrite yokes, because the setup has a limit on the applied magnetic flux density. Comparison with the measurements carried out on an RSST where a more advanced shape control (see the next section) is provided, showed a good correspondence (Fig. 4.3.3.8).

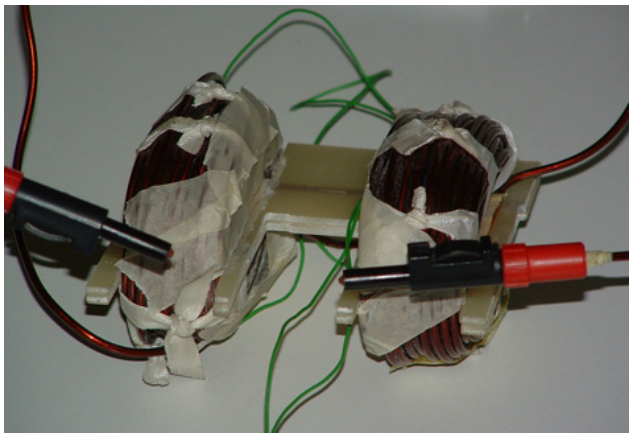

Fig. 5.1.2. Excitation winding with 180 turns of the SST for the voltage supply.

Let us consider the case when the frequency is reduced below the specified limit of $f_\mu=15000\mu_0$. It results in an increase of the ratio $R/\omega L_m$. So the resistive voltage drop cannot be neglected.

Consider the input voltage as a function of the magnetic field and the flux density in the sample. It is shown in the previous chapter that the leakage flux in the present geometry of STT can be neglected. So from (5.1.7) the following can be derived:

$$v(t) = R\frac{H_m l_m}{w} + wS\frac{dB_m}{dt} \tag{5.1.9}$$

It can be seen that the supply voltage is a function of the both field and the magnetic flux density. Taking into account the hysteretic dependence between H and B in the sample, which is unknown in advance, it is difficult to develop a robust shape control subroutine operating with the supply voltage.

In case of voltage supply, it seems to be more efficient to decrease the ratio $R/\omega L_m$ during the design stage of the excitation winding in order to increase the frequency and permeability range. It requires keeping a certain relative height of the winding with respect to the thickness of the sample, see (5.1.10). The length of the sample is less important. Therefore setups with a long and short magnetic path length, but equal height and width, as e.g. shown in Fig. 5.1.4 should have the same shape control properties.

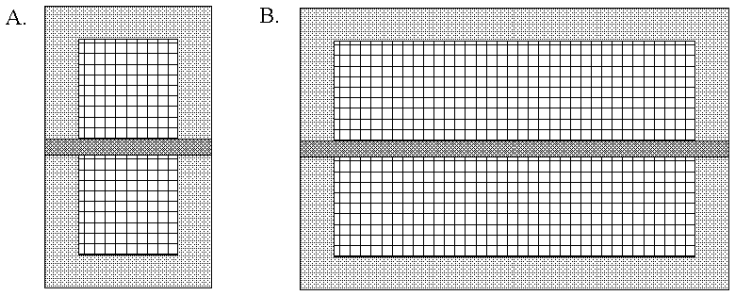

Fig. 5.1.4. The shapes of the setups: A – with a short magnetic path, B – with a large magnetic path.

Section 5.2. The flux density shape control for setups with air-gaps.

5.2.1. Basic principles.

Consider an electromagnetic device constructed out of a coil and an magnetic circuit. It is well known that introducing air-gaps in the magnetic circuit results in a linearization of external characteristics, e.g. the voltage-current relation of the coil of the device. Due to this linearization, we obtain an easier shape control for the magnetic flux in the magnetic circuit of the device.
For this reason air-gaps can be introduced in the magnetic circuit of measurement setups used for the identification of magnetic properties of a material sample under a predefined shape for the magnetic flux density.
An equivalent circuit of the measurement setup containing an air-gap can be drawn as follows:

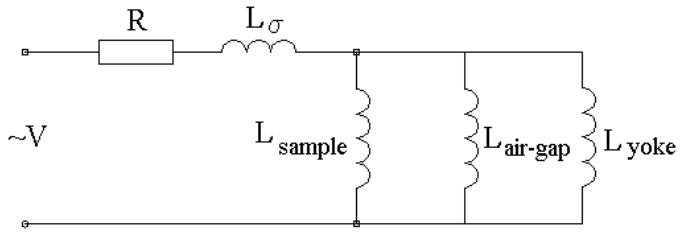

Fig. 5.2.1. Equivalent circuit of the measurement setups with an air gap.

Unless the sample is completely saturated its permeability is in most cases considerably larger than the permeability of the air-gap. Of course, the geometry of the air-gap as well as its relative size with respect to the size of the sample is important. We will suppose that the inductance of the air-gap is much smaller than the inductance of the other elements of the magnetic system.

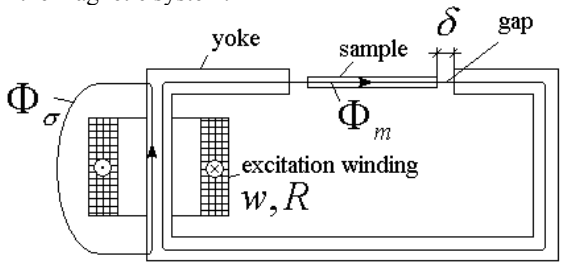

Fig. 5.2.2. Equivalent circuit of the measurement setups with an air-gap.

To fix the ideas, consider the scheme of the measurement setup of Fig. 5.2.2. The voltage over the excitation winding can be written as:

$$v(t) = Ri(t) + \frac{d}{dt}\left(\Psi_\sigma + \Psi_m\right) \qquad (5.2.1),$$

where $\Psi_\sigma = L_\sigma i$ and $\Psi_m = wB_mS_m = wB_{gap}S_{gap} \approx wB_{yoke}S_{yoke}$ or equivalently

$$v(t) = \left(R + L_\sigma \frac{d}{dt} \right) i(t) + \frac{d}{dt}\Psi_m \qquad (5.2.2),$$

From Ampere's law for the circuit shown in Fig. 5.2.2 it follows that

$$wi = H_m l_m + H_{gap} l_{gap} + H_{yoke} l_{yoke} = \frac{B_m}{\mu_0 \mu_m} l_m + \frac{S_m}{S_{gap}} \frac{B_m}{\mu_0} l_{gap} + \frac{S_m}{S_{yoke}} \frac{B_m}{\mu_0 \mu_{yoke}} l_{yoke} \qquad (5.2.3)$$

Since the last term in (5.2.4) is close to zero ($S_m << S_{yoke}$ and μ_{yokes} is high) we will omit it. Equation (5.2.3) reduces to:

$$wi = B_m \left(\frac{l_m}{\mu_0 \mu_m} + \frac{S_m l_{gap}}{S_{gap} \mu_0} \right) \qquad (5.2.4)$$

If the air-gap constitutes 10% of the length of the sample and $S_m = S_{gap}$ then the contribution of the second term in the right hand side in (5.2.4) is $\mu_m/10$ times larger compared to the m.m.f. drop in the sample. If the sample is a non-oriented electrical steel the ratio $\mu_m/10$ exceeds 100 unless the sample is saturated.

Notice that in actual magnetic structures the contribution of the air-gap is less compared to the estimation presented above due to the larger cross-section of the air-gap (fringing effects), which is specific for each setup. However the contribution from the air-gap into the m.m.f. drop in the magnetic circuit remains dominant in most cases.

Consequently, the relation between the excitation current *i* and the flux density B_m in the sample, see (5.2.4.), becomes practically linear after introduction of a sufficient air-gap in the magnetic circuit. The influence of the induction dependent μ_m decreases.

After introducing (5.2.2) into (5.2.4) we can obtain the effect of introduction of the air-gap on a leakage factor. Depending on the structure of the setup the saturation of the sample can influence the whole flux pattern. In these cases the leakage factor is a function of the flux density of the sample.
The magnetic field in the air-gap is much larger for the reason mentioned above. So the component of the magnetic field corresponding to the sample can be neglected:

$$v(t) = R \frac{B_m}{w\mu_0} \frac{S_m}{S_{gap}} l_{gap} + (1 + k_\sigma) w S_{sample} \frac{dB_m}{dt} \qquad (5.2.3)$$

where $k_\sigma = \frac{\Psi - \Psi_m}{\Psi_m}$ is assumed to be constant in time and called the leakage factor of the setup.

Thus the input voltage is dependent on the flux density and its derivative only. It is easier to make a successful control procedure for this formulation than for the formulation presented in (5.1.7).
The corresponding control software is developed in LabView in EELAB and described in [Makaveev2003 p. 57]. A control subroutine was designed for the rotational single sheet tester. Due to the large air-gaps between the sample and the magnetic core, the magnetic reluctance for each of the magnetization axes is almost completely defined by the air-gap. Thereby the axes are assumed to be magnetically independent.

The presence of the air-gap between the sample and the core results in an increase of the leakage, which is strongly dependent on the saturation of the sample. So an increase of the saturation of the sample leads to a distortion of the uniformity of the magnetic flux density in the sample. This disadvantage can be avoided if the air-gaps are built in the yoke.

5.2.2. Constructed SST with distributed air-gaps.

5.2.2.1. Basic dimensions.

In order to demonstrate the applicability of this approach, the air-gaps were introduced in the yokes of the SST measurement setup. An analogous solution is presented in [Bajorek2000] for the RSST. Even though the gap between the sample and the magnetic core is already present an additional element denoted as the regulator of reluctance with the distributed air-gap is introduced into the magnetic system.
The two yokes were constructed with four 0.75mm wide air-gaps in order to decrease fringing (Fig. 5.2.2, 5.2.3). The total width of the air-gap is equal to 3mm. The dimensions of the yokes match the dimensions of the SST without gaps in order to use the same windings and the samples. The measurement of H was carried out using the H-coils positioned on the surface of the sample, while the magnetic induction B was measured using B-pickup coil.

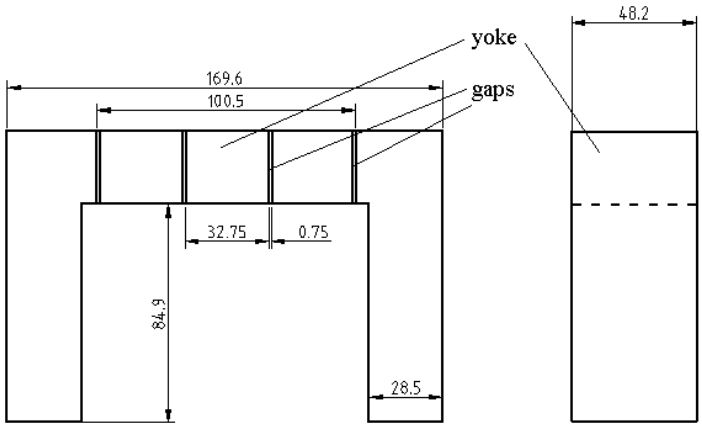

Fig. 5.2.2. Dimensions of the setup. The yokes were constructed with four 0.75 mm wide air-gaps

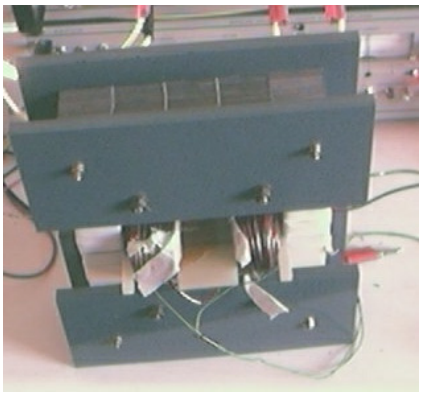

Fig. 5.2.3. Photo of the SST with the air-gaps in the yokes.

5.2.2.2 Numerical evaluation of yokes with distributed air-gaps

In order to evaluate the double yoke system with distributed air gaps, a FE model for the corresponding SST was constructed. The model is shown in Fig. 5.2.4. Table 5.2.1. summarizes the numerical results with respect to the average flux density in the different subregions.

Table 5.2.1. Results of the magnetic computations.

H in the active part of the sample, A/m	B in the active part of the sample, T	H_y in the first H-coil at the sample, A/m	H_y in the second H-coil at the sample, A/m	$\frac{L_{air+windings}^{no\ gaps}}{L_{total}}$	$\frac{L_{active\ part\ of\ the\ sample}}{L_{total}}$
219	1.036	196	175	0.09	0.61
696	1.385	608	559	0.085	0.747

Air-gaps are part of the magnetic circuit. So in order to evaluate the inductance of the rest of the non-magnetic parts of the setup a new value is introduced in Table 5.2.1: $\frac{L_{air+winding}^{no\ gaps}}{L_{total}}$. This value defines the leakage of the setup.

It follows from the computational results presented in Table 5.2.1 that the SST with air-gaps has a somewhat larger leakage $\left(\frac{L_{air+winding}^{no\ gaps}}{L_{total}} = 8.5\%\ at\ B = 1.385T\right)$ compared to the numerical results shown in Table 4.3.1.1 for the SST without air-gaps $\left(\frac{L_{air+winding}}{L_{total}} = 6.8\%\ at\ B = 1.442T\right)$. As it was mentioned in the previous chapter a low leakage is advantageous for the local measurement of the magnetic flux density.

5.2.2.3 Experimental evaluation of the yokes with distributed air-gaps.

With respect to the shape control the developed structure is quite effective. It was confirmed by a large number of measurements. To fix the ideas, one of the worst cases for the control of the SST with the distributed air-gap is presented here. We enforced a high flux density (B=1.75 Tesla) in the V850-65 sample at low frequency (f=5Hz). In Fig. 5.2.5 the flux density shapes are presented before and after the application of the shape control procedure. The flux density curve has initially a clear deviation from the sinusoidal shape. Here a sinusoidal voltage v(t) was applied. A modification of the supply voltage due to the control based on (5.2.3), results in a sinusoidal flux in the sample as shown in Fig. 5.2.6 and Fig. 5.2.7.

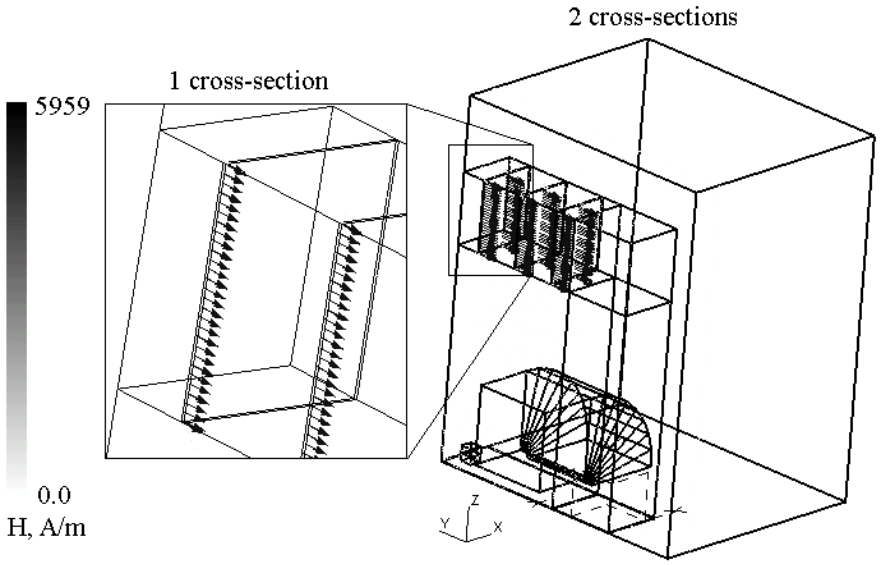

Fig. 5.2.4. Magnetic field distribution corresponding to B=1.3T in the sample.

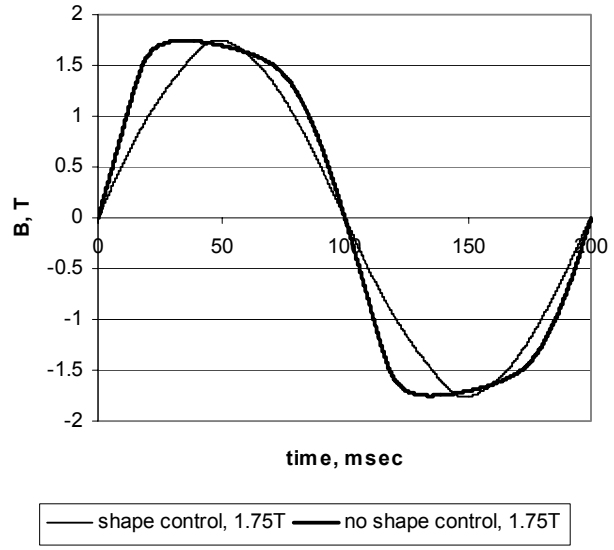

Fig. 5.2.5. Flux density shapes obtained for the V-850-65 steel at f=5Hz.

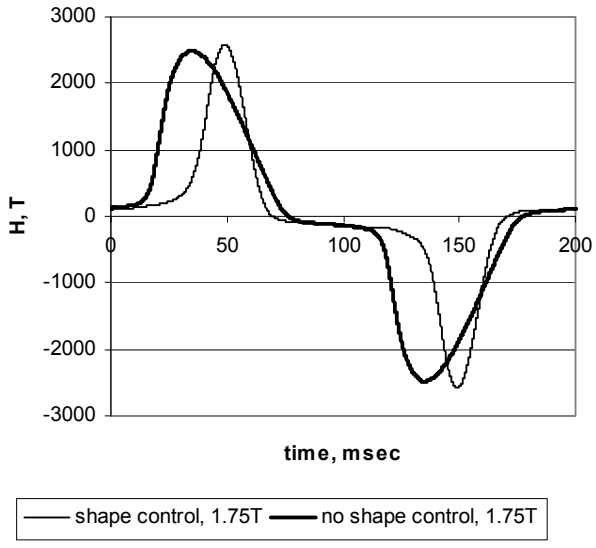

Fig. 5.2.6. Corresponding magnetic field shapes obtained for the V-850-65 steel at f=5Hz.

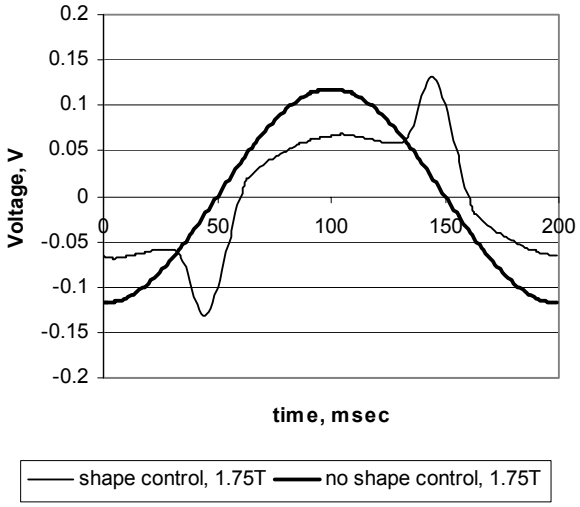

Fig. 5.2.7. Modification of the supply voltage by the B-shape control.

Section 5.3. Flux density shape control using current supply.

Consider a setup with a closed magnetic circuit that does not have air-gaps. For this type of setup there is a direct link between the magnetic field at the surface of the sample and the current in the excitation winding. Therefore, in order to have a flux density shape control using a current controlled supply, it is sufficient to construct the relation between the magnetic field at the surface of the lamination and the total magnetic flux. The hysteresis loop provides the relation between the field and the local flux density and this relation can be used to construct the time variation of the magnetic field (or equivalently the excitation current) in order to achieve the desired flux density shape operating the magnetic field [DeWulf2002 p. 69].
This is an iterative procedure, because the hysteresis loop is generally dependent on the field shape unless a very low frequency is used. So the link between the field and the flux density has to be reestablished every time. It is shown in [DeWulf2002 p.69] that it is sufficient to use only one branch of the loop in order to tune the shape of the field and the supply current. This is illustrated in Figs. 5.3.2-5.3.4.

If the measurement setup is connected to a source with current control, it is necessary to limit the total inductance[1], which is required for the conventional power amplifiers. Reduction of the inductance can be carried out via a decrease of the number of turns of the excitation winding (5.1.3). Since the sample contributes more than 90% in the total inductance of the setup (Table 4.3.1.1) it is also possible to reduce the inductance via the decrease of the width of the sample.

[1] 0.5mH according to Instruction Manual on KEPCO BOP 50-8M bipolar operational power supply, p. 3-30.

In this investigation the geometry of the samples was not modified. Instead, a separate winding with a low number of turns was constructed for the current supply (Fig. 5.3.1 vs. Fig. 5.1.2).

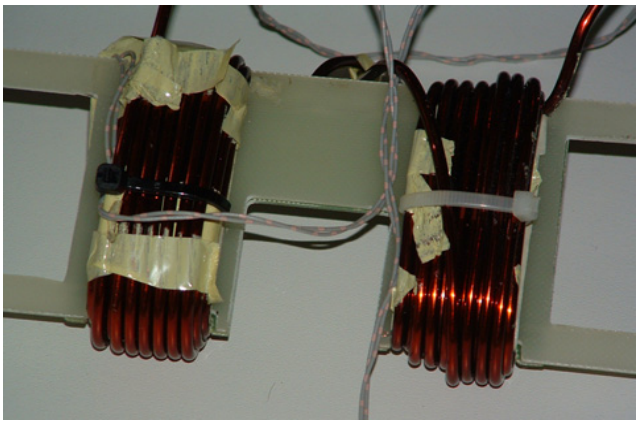

Fig. 5.3.1. Excitation winding with 33 turns of the SST for the current supply.

Unfortunately most of the magnetic structures designed in the frame of the current investigation cannot be supplied from the power amplifier in current mode as the inductance of the setups exceeds the specified limit, mentioned above.

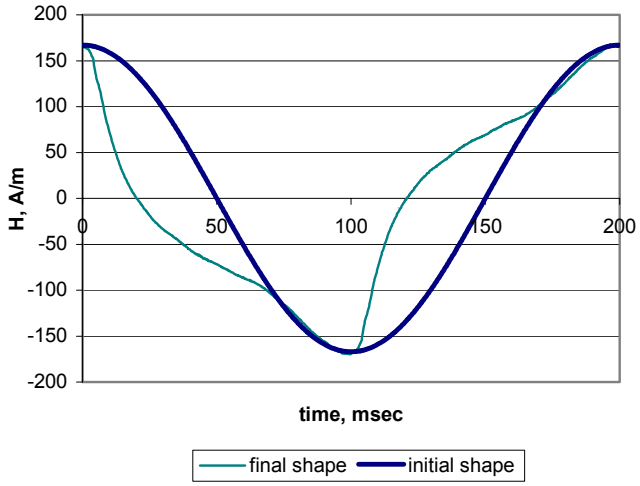

Fig. 5.3.2. The magnetic field at f=5Hz.

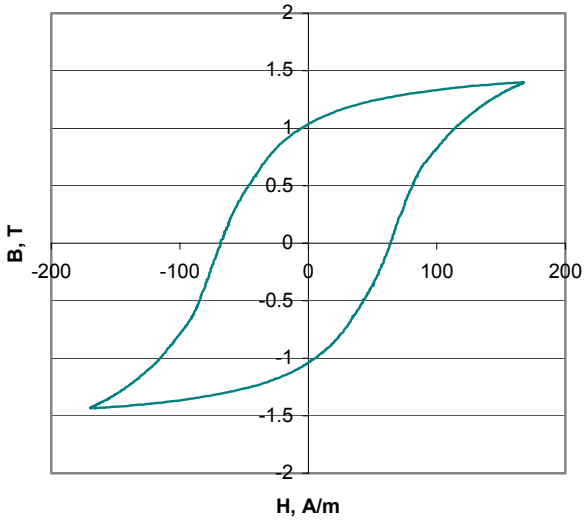

Fig. 5.3.3. The final BH-loop at f=5Hz.

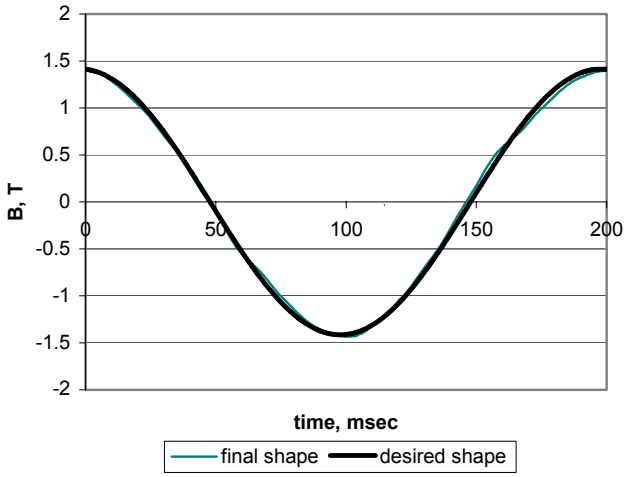

Fig. 5.3.4. The final flux density at f=5Hz.

Conclusions.

Three different approaches were used in the current investigation for the flux density shape control in the sample:

1. The flux density shape can be improved via a modification of the parameters of the excitation winding. A complete correspondence between the desired and the acquired flux density shapes cannot be achieved due to the resistive voltage drop over the excitation winding. But a sufficiently small discrepancy can be provided for a specified range for fμ (f=frequency, μ=permeability).

2. For the measurement setups with large air-gaps in the magnetic circuit the control subroutine developed in [Makaveev2003 p. 57] was successfully employed. It was shown that the leakage of the setup can be kept sufficiently low if the air-gap is introduced in the magnetic core at the certain distance from the sample compared to the case when the air-gap is provided between the sample and the core. This control subroutine is quite stable if the external characteristic of the setup is sufficiently linear and hysteresis effects are minimal.
3. If the measurement setup has a closed magnetic circuit (no air-gaps present) and the structure of the setup provides a linear dependence between the excitation current and the field in the sample, then the current supply together with the acquired BH-loop can be used for the flux density shape control.

Unfortunately, the reality is such that there are no ultimately robust control subroutines. Thus combination of different approaches to the flux density shape control is required in order to provide a sufficiently reliable procedure that can be used in a wide flux density and frequency range.

Chapter 6. Multidirectional experimental investigation of the effect of the mechanical deformation on the magnetic properties of the non-oriented electrical steels.

Introduction.

It was shown in the introductory chapter that the applied elastic stress leads to a change of the magnetic anisotropy of ferromagnetic material. Consequently the multidirectional investigation is necessary for the evaluation of this effect on the magnetic properties of the steel.

The stress mainly affects the magnetic domain wall motion. Therefore the largest effect can be expected at low magnetic induction levels. The measurements were carried out at inductions less than 1T. Additional reasons for using low flux densities are, for instance, the limitations of the SST with the ferrite yokes considered in the 4^{th} chapter.

The effect of the elastic stress depends on the domain structure in the material. The domain structure is dependent on the crystallographic texture. In Section 6.1 and Section 6.2 the effect of different orientation of the rolling direction with respect to the applied mechanical stress is investigated.
As shown in Chapter 2, a lot of changes occur in the material after plastic deformation. In Sections 6.3 and 6.4 it is shown how deformation does change the general sensitivity of the magnetic properties of the electrical steel with respect to the elastic stress. Plastic deformation leads to an increase of the dislocation density in the material, which leads to a deterioration of the magnetic properties. However it also results in the appearance of residual stresses. The investigation of the residual stresses is conducted in Section 6.5.

Section 6.1. The effect of the elastic stress applied along the rolling direction of the sample on the magnetic properties of V850-65 non-oriented electrical steel.

The dependence of the total magnetic losses on the applied mechanical stress is typical for non-oriented electrical steels (Fig. 6.1.1), as is well known. This investigation can be conducted relatively easy if the sample clamped in the SST is subjected to mechanical stress. An alternative procedure is proposed in [Szewczyk] for the investigation of the effect of stress on the properties of amorphous magnetic materials. This measurement setup resembles the setup shown in Fig. 4.2.2. The setup allows application of both tension and compression. However the angle between the stress and the applied magnetic field remains unchanged.
A multidirectional investigation requires more sophisticated equipment. In the current investigation we concentrate on the following 4 directions of the field with respect to the applied mechanical stress: 0^0, 30^0, 60^0 and 90^0. The sample is cut in such a way that the rolling direction is oriented along the stress.
It is shown in Fig. 6.1.1-6.1.8 that the general tendency of change of the magnetic properties remains the same for the considered range of the flux densities. Notice that in the figures, a positive value for the stress always corresponds with tension and a negative value with compression. All the measurements were performed at a frequency

of 50Hz and sinusoidal induction. It can be seen that the change in the total magnetic losses is opposite to the change in the relative permeability. Starting from the unstressed condition, the losses increase in the direction of the applied compression and initially decrease in the direction of applied tension (Fig. 6.1.1 and Fig. 6.1.2), though an increase can be noticed at larger tensile stresses. This tendency decreases as the applied field approaches 45^0 angle with respect to the stress (Fig. 6.1.3 and Fig. 6.1.4). When this angle is exceeded an opposite relation between the magnetic properties and the stress takes place (Fig. 6.1.5 and Fig. 6.1.6), i.e. if compression is applied the total losses generally decrease and in case of tension the losses increase. This effect attains its extreme at 90^0 (Fig. 6.1.7 and Fig. 6.1.8).

Let us now consider one specific induction level and analyze the spatial distribution of the magnetic properties (i.e. the magnetic properties for variable magnetization direction), Fig. 6.1.9-6.1.12.

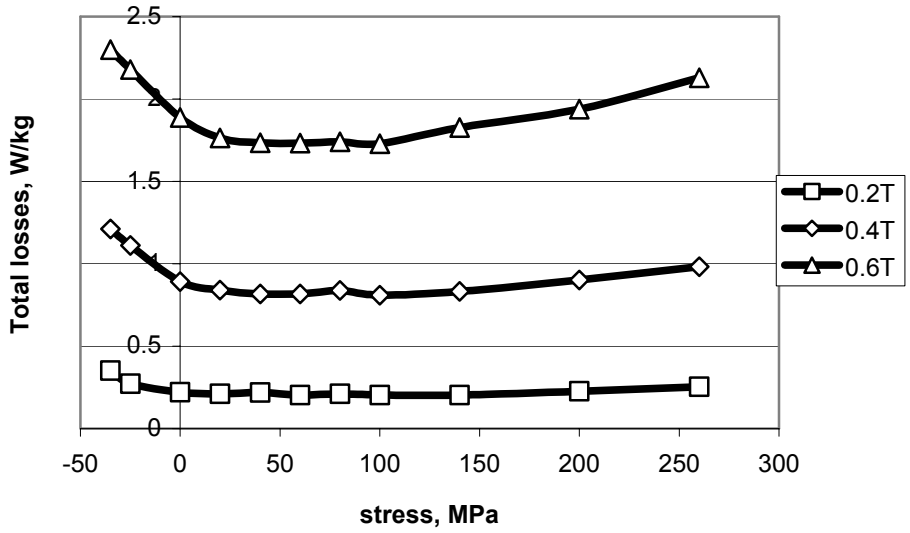

Fig. 6.1.1. The effect of the elastic stress on the total magnetic losses measured in rolling direction along the stress at f=50Hz.

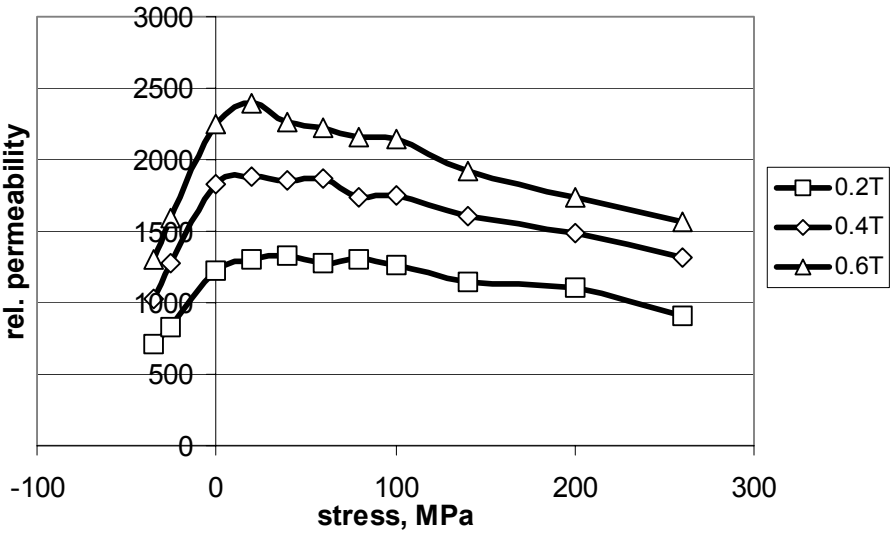

Fig. 6.1.2. The effect of the elastic stress on the relative permeability measured in rolling direction along the stress at f=50Hz.

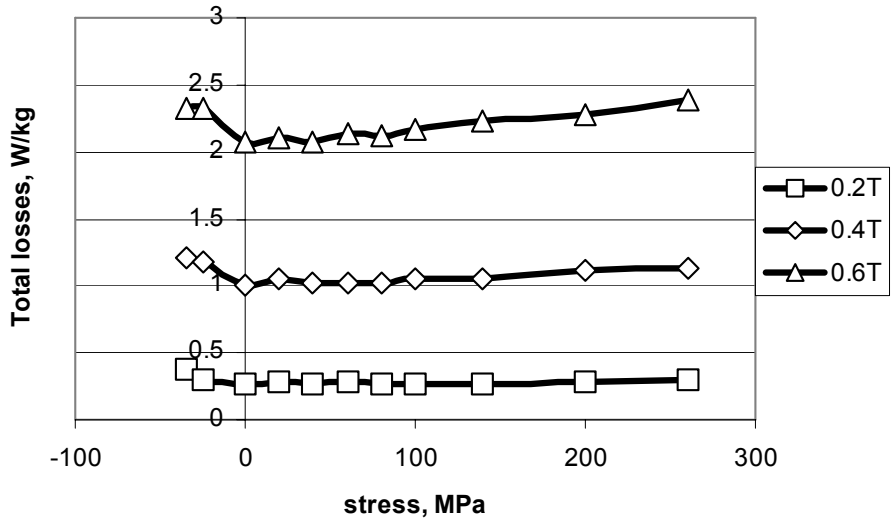

Fig. 6.1.3. The effect of the elastic stress on the total magnetic losses measured at 30^0 with respect to the direction of the stress and rolling direction at f=50Hz.

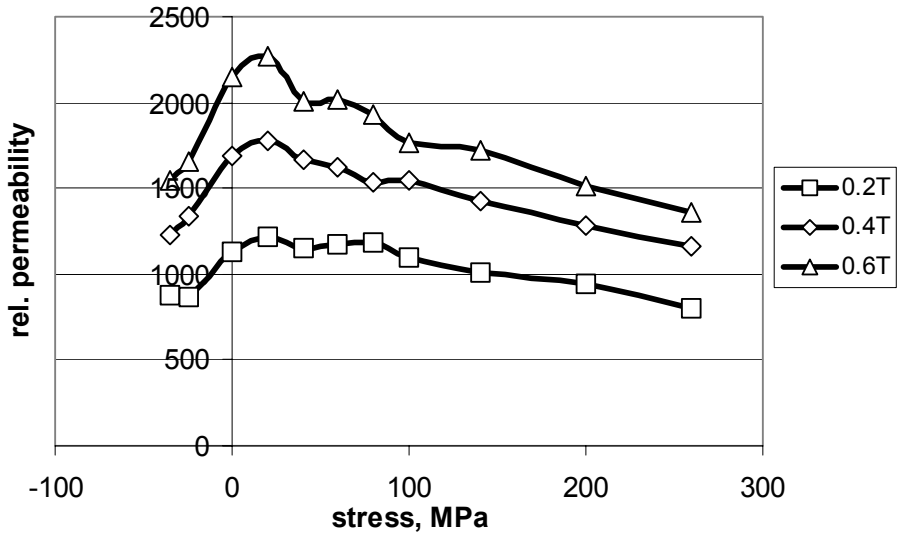

Fig. 6.1.4. The effect of the elastic stress on the relative permeability measured at 30^0 with respect to the direction of the stress and rolling direction at f=50Hz.

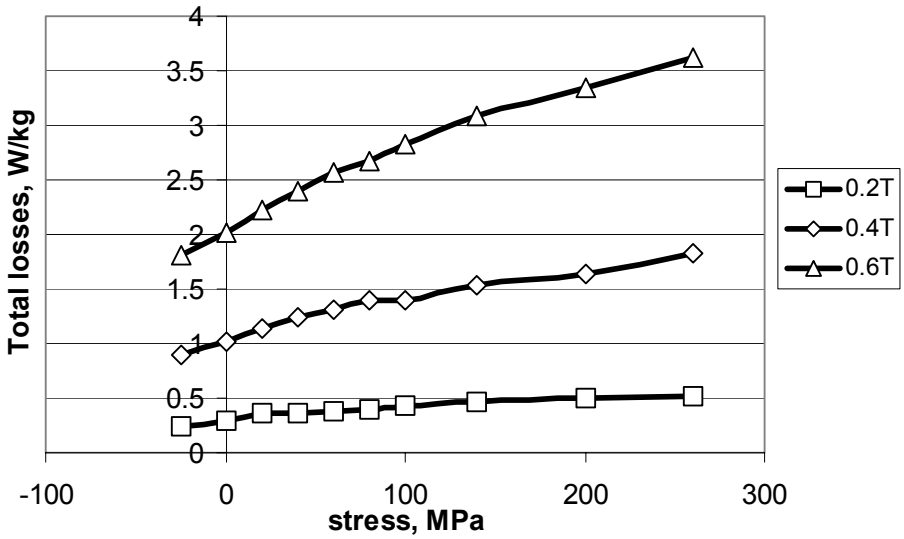

Fig. 6.1.5. The effect of the elastic stress on the total magnetic losses measured at 60^0 with respect to the direction of the stress and rolling direction at f=50Hz.

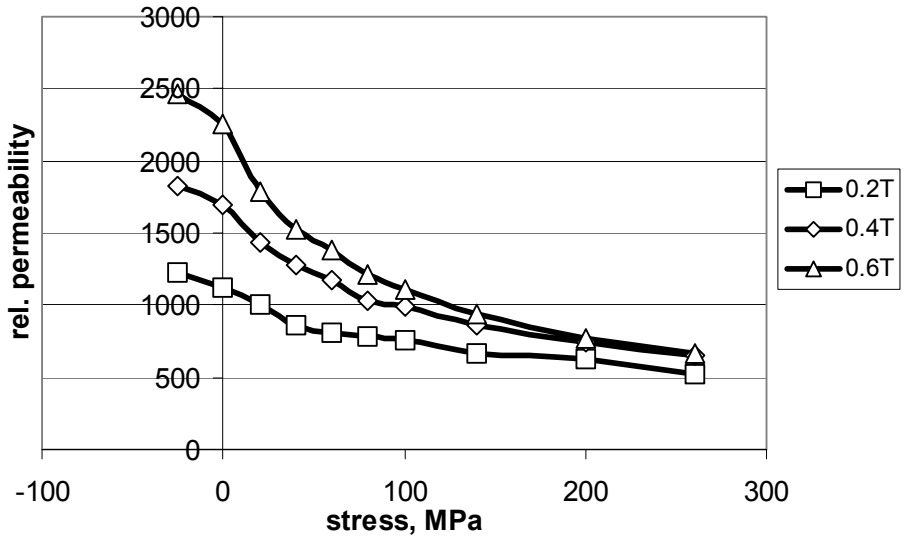

Fig. 6.1.6. The effect of the elastic stress on the relative permeability measured at 60^0 with respect to the direction of the stress and rolling direction at f=50Hz.

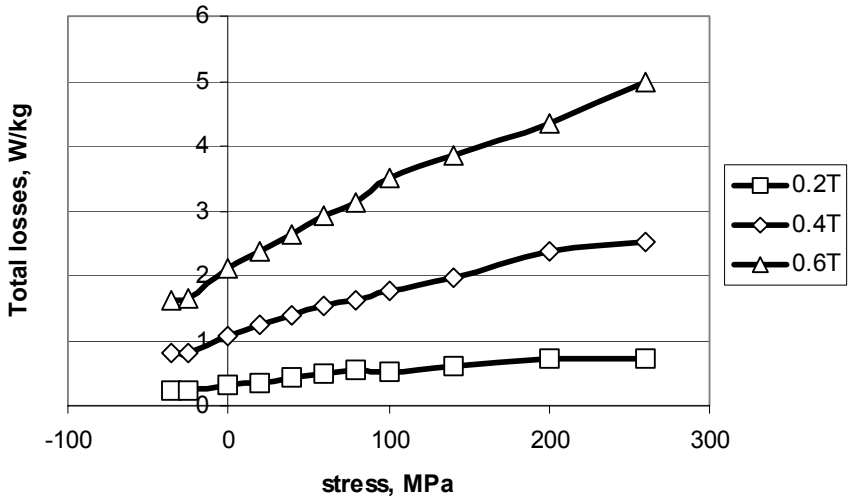

Fig. 6.1.7. The effect of the elastic stress on the total magnetic losses measured at 90^0 with respect to the direction of the stress and rolling direction at f=50Hz.

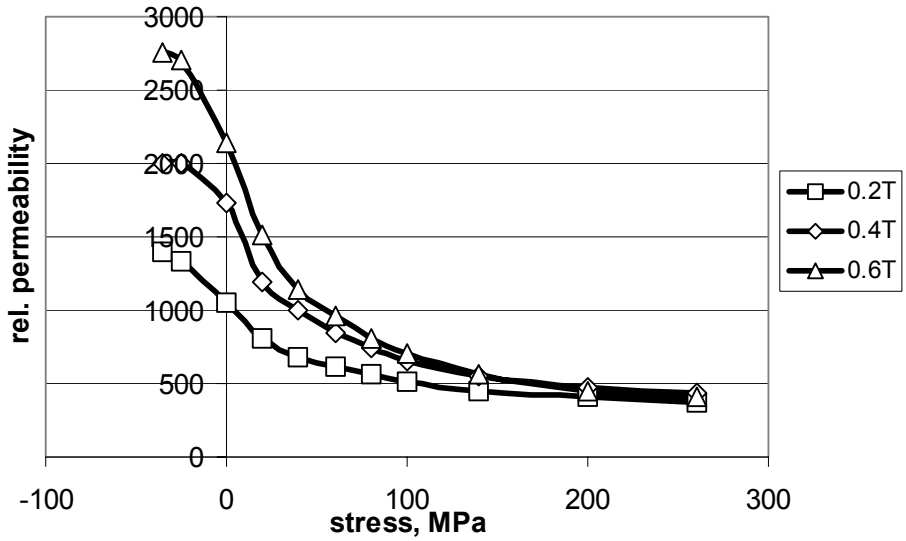

Fig. 6.1.8. The effect of the elastic stress on the relative permeability measured at 90^0 with respect to the direction of the stress and rolling direction at f=50Hz.

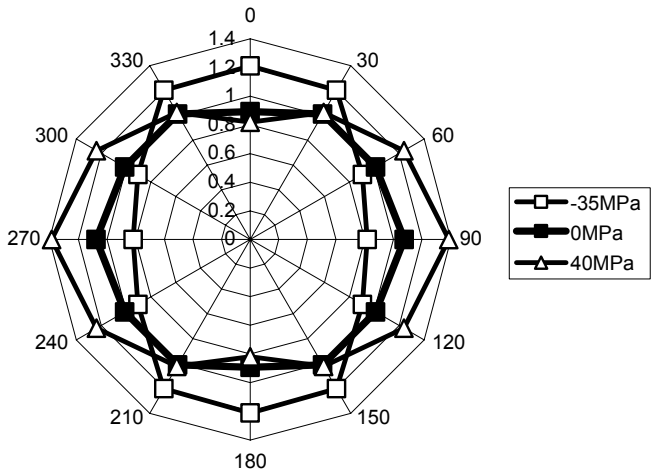

$\uparrow \sigma \uparrow RD$

Fig. 6.1.9. The effect of the small elastic stresses on the distribution of the total magnetic losses (W/kg) measured at B=0.4T and f=50Hz.

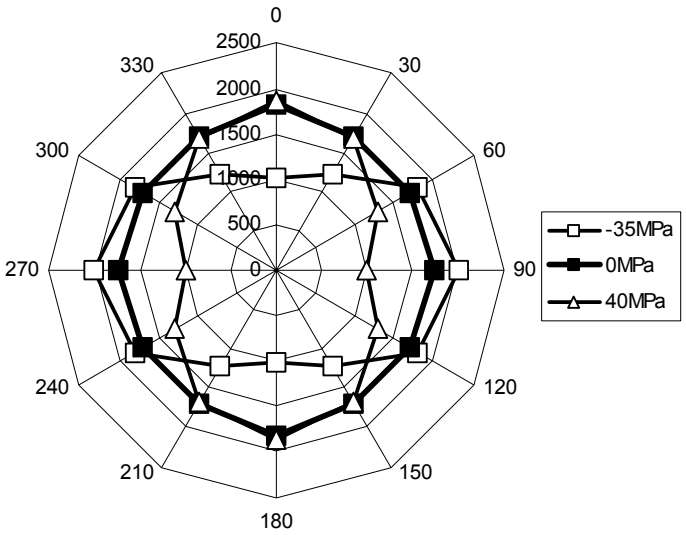

$\uparrow \sigma \uparrow RD$

Fig. 6.1.10. The effect of the small elastic stresses on the distribution of the relative permeability measured at B=0.4T and f=50Hz.

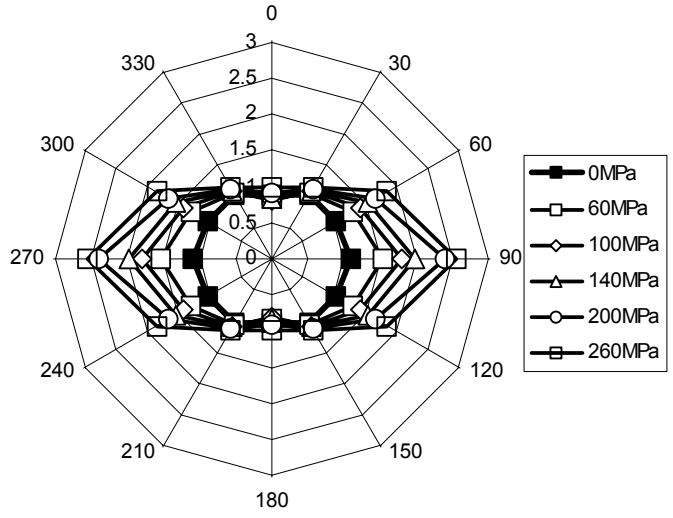

$\uparrow \sigma \uparrow RD$

Fig. 6.1.11. The effect of the large elastic stresses on the distribution of the total magnetic losses (W/kg) measured at B=0.4T and f=50Hz.

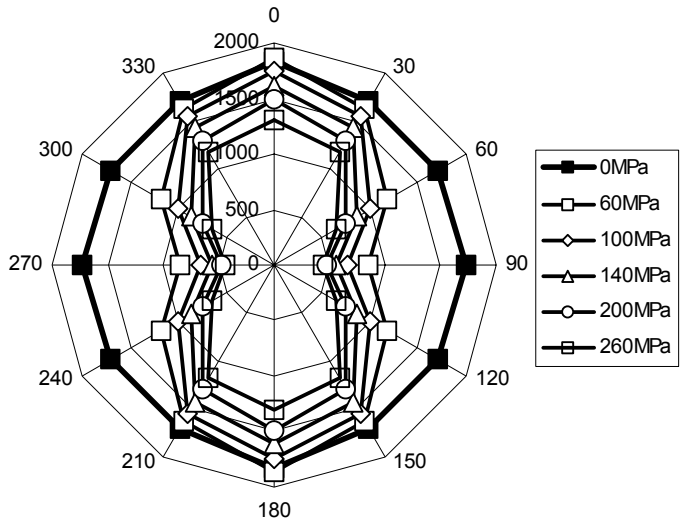

Fig. 6.1.12. The effect of the large elastic stresses on the distribution of the relative permeability measured at B=0.4T and f=50Hz.

It can be seen that the effect of small elastic stresses (Fig. 6.1.9 and Fig. 6.1.10) on the magnetic properties leads to unidirectional anisotropy in the sample. These results correspond with a classical theory presented in the first chapter. However a further increase of the applied stress leads to a more complicated dependence. The losses stop decreasing and then start a slow increase in the direction of the tensile stress (Fig. 6.1.11), which cannot be explained by the classical approach. In the orthogonal direction the properties continue to deteriorate (Fig. 6.1.11 and Fig. 6.1.12).

Section 6.2. The effect of elastic stress applied along the transverse direction on the magnetic properties of V850-65 non-oriented electrical steel.

Let us introduce the new term '*stress sensitivity'* that we will use to denote the dependence of the magnetic properties on the applied stress.

Non-oriented electrical steels are known to have a certain texture, which results in a magnetic anisotropy of the material. In order to evaluate the effect of the texture on the stress sensitivity, the stress should be applied in different directions with respect to the rolling direction. Since the anisotropy of the properties in non-oriented steel is rather weak, it seems sufficient to study the action of the stress only along the rolling and transverse directions.

Moreover, it was shown in the previous section that in the 30^0 and 60^0 orientations the observations are in some way the average of the observations in the 0^0 and 90^0 orientations. So only the extreme orientations will be studied further.

A comparison of the total magnetic losses measured along the stress (Fig. 6.1.1 vs. Fig. 6.2.1) shows that the increase of the total losses at large tensile stresses is smaller. For the considered range of the applied tensile stresses the total losses do not exceed the initial value (Fig. 6.2.1). With respect to the permeability, we observe an improvement

at large tensile stresses compared to the case described in Section 6.1 (Fig. 6.2.2 vs. Fig. 6.1.2).
Some clear changes can be noticed also for the perpendicular direction with respect to the stress. The total magnetic losses grow less steeply with applied tension (Fig. 6.2.3 vs. Fig. 6.1.7).
As to the general magnetic properties the application of tensile stress in the transverse direction is less deteriorative compared to the rolling direction. Though the texture introduces a certain quantitative difference, it does not alter the qualitative dependence of the magnetic properties on the applied mechanical stress. The latter is clearly illustrated in Fig. 6.2.5 and Fig. 6.2.6.

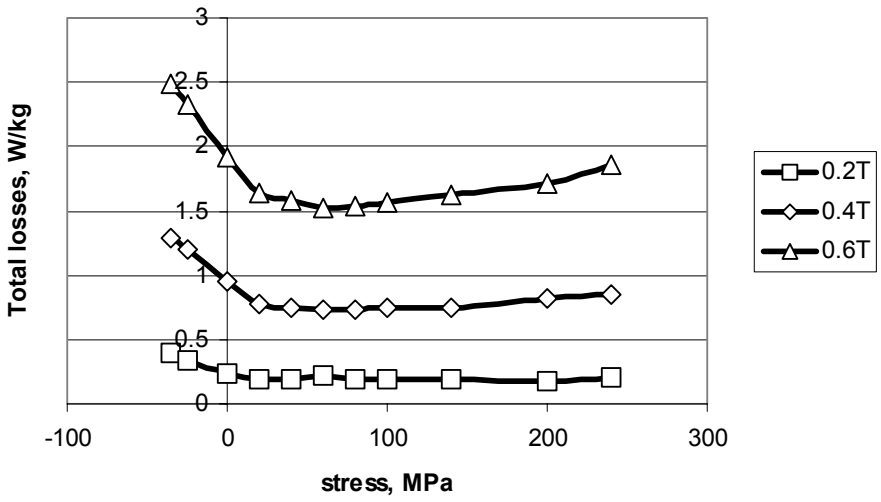

Fig. 6.2.1. The effect of the elastic stress on the total losses measured along the stress with stress in the transverse direction at f=50Hz.

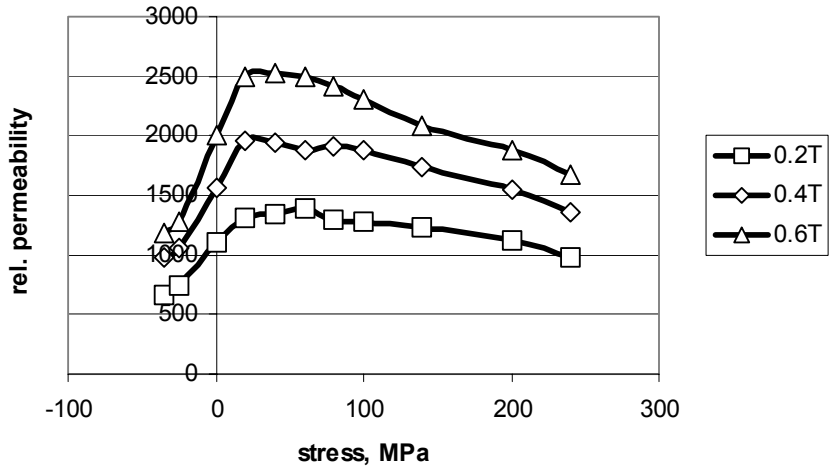

Fig. 6.2.2. The effect of the elastic stress on the relative permeability measured along the stress with stress in the transverse direction at f=50Hz.

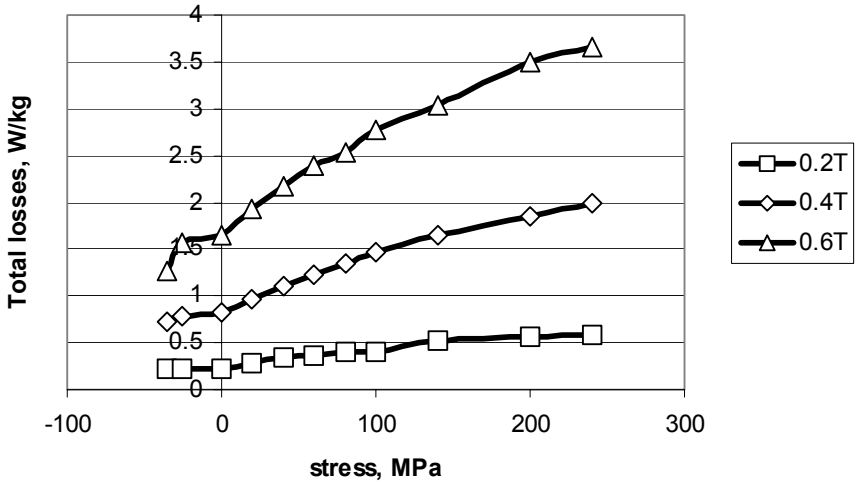

Fig. 6.2.3. The effect of the elastic stress on the total losses measured at 90^0 with respect to the direction of the stress with stress in the transverse direction at f=50Hz.

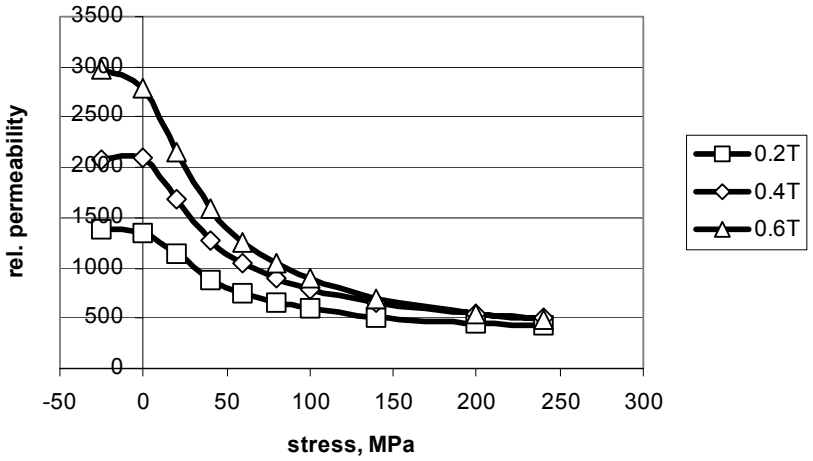

Fig. 6.2.4. The effect of the elastic stress on the relative permeability measured at 90^0 with respect to the direction of the stress with stress in the transverse direction at f=50Hz.

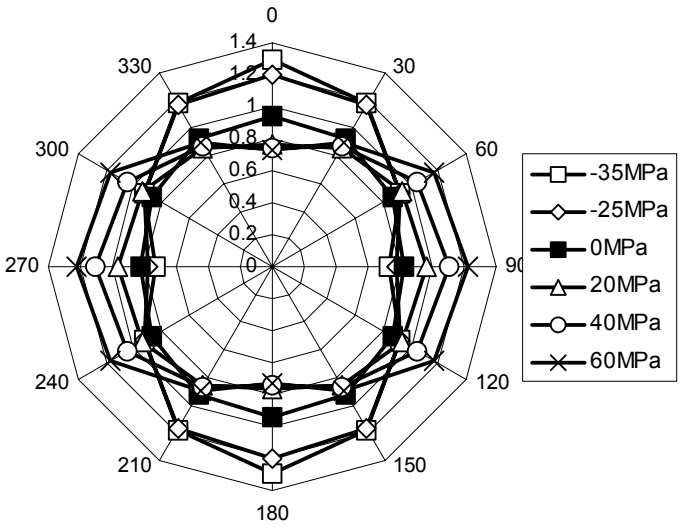

$\uparrow \sigma \rightarrow RD$

Fig. 6.2.5. The effect of the small elastic stresses on the distribution of the total magnetic losses (W/kg) measured at B=0.4T and f=50Hz.

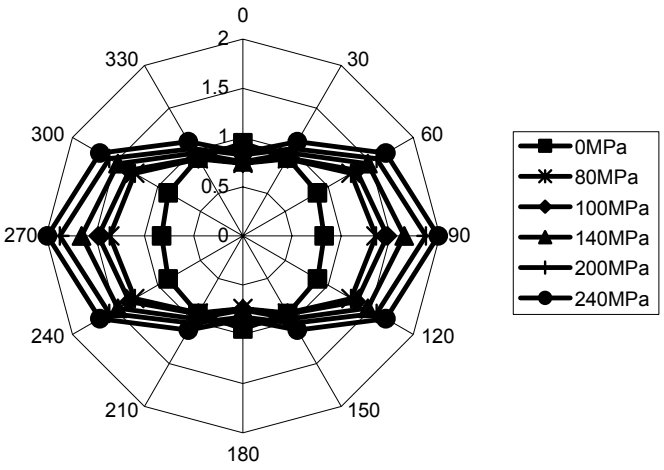

$\uparrow \sigma \rightarrow RD$

Fig. 6.2.6. The effect of the large elastic stresses on the distribution of the total magnetic losses measured at B=0.4T and f=50Hz.

Section 6.3. The effect of elastic stress applied along the rolling direction of the sample on the magnetic properties of V850-65 non-oriented electrical steel after 5.66% tensile plastic deformation applied along the rolling direction.

It is known that there is a likelihood of non-uniformity of the magnetic properties, even in the same sheet of electrical steels. The likelihood increases with a reduction of the size of the sample. Since the region in the samples used for the magnetic measurements is relatively small it was decided to use the same sample as studied in Section 6.1.

Application of plastic deformation results in an increase of the dislocation density in the steel. So the number of pinning sites increases. The domain wall motion requires considerably more energy compared to the undeformed material. It can generally be said that the magnetic state of the deformed material is less sensitive to both the applied magnetic field and the applied mechanical stress. The dissipation of the magnetic energy at the pinning sites results in a general increase of the total magnetic losses (Fig. 6.3.1 vs. Fig. 6.1.1). It also requires a larger magnetic field to magnetize the sample, which corresponds to a reduction of the permeability (Fig. 6.3.2 vs. Fig. 6.1.2).

The RD in the sample after the plastic deformation applied in RD is worse then the TD in terms of the magnetic properties (Fig. 6.3.5). So the direction of the magnetic anisotropy is reversed.

A consequence of the smaller stress sensitivity (Section 6.2) is that the difference in the total magnetic losses between 0^0 and 90^0 orientations, observed at the large tensile stresses, is smaller compared to the undeformed state (Fig. 6.3.6 vs. Fig. 6.1.11).

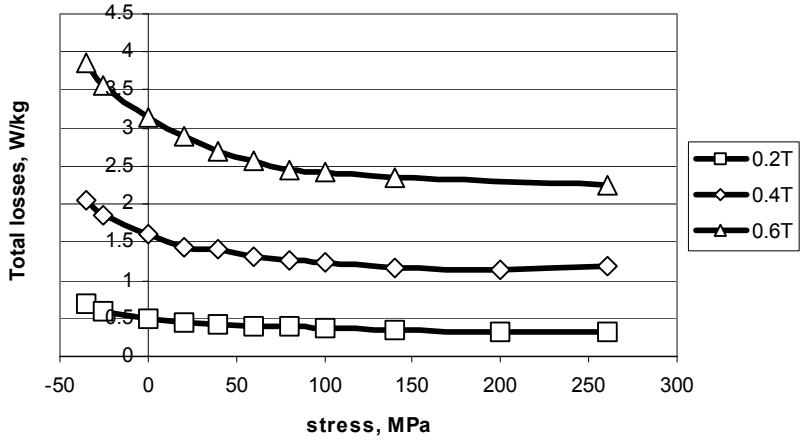

Fig. 6.3.1. The effect of the elastic stress on the total losses measured along the stress with stress in the rolling direction at f=50Hz after 5.66% plastic deformation in RD.

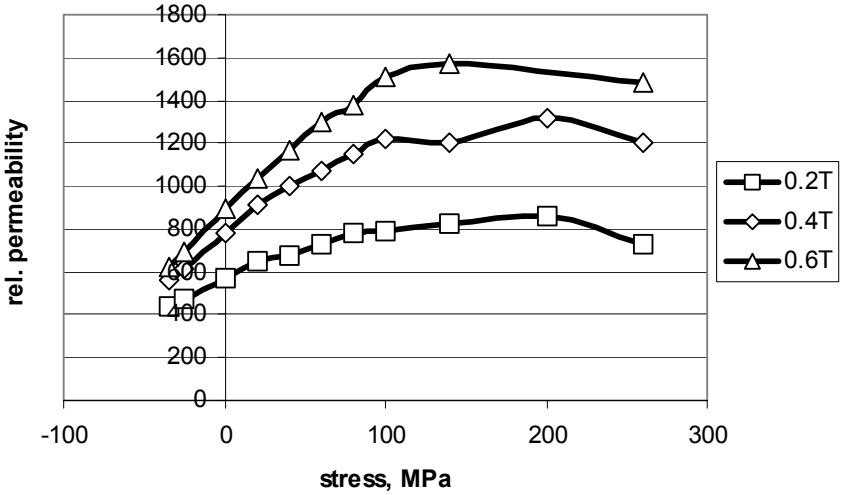

Fig. 6.3.2. The effect of the elastic stress on the relative permeability measured along the stress with stress in the rolling direction at f=50Hz after 5.66% plastic deformation in RD.

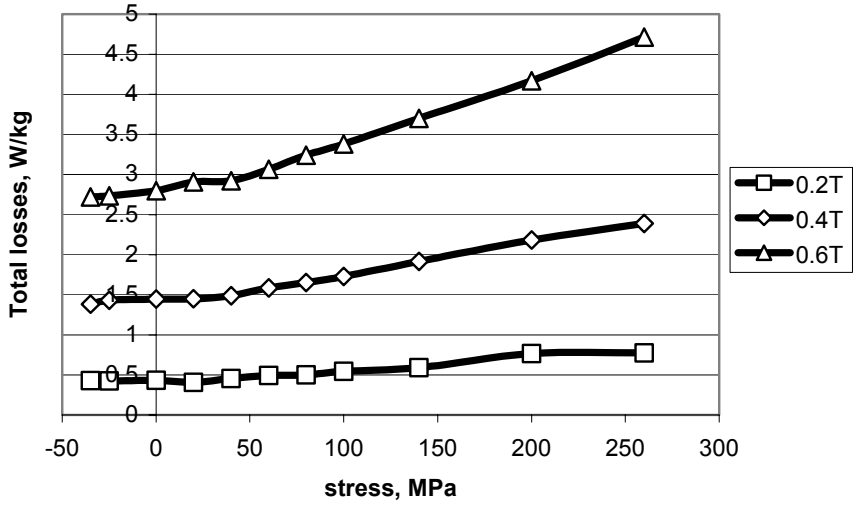

Fig. 6.3.3. The effect of the elastic stress on the total losses measured at 90^0 with respect to the direction of the stress with stress in the rolling direction at f=50Hz after 5.66% plastic deformation in RD.

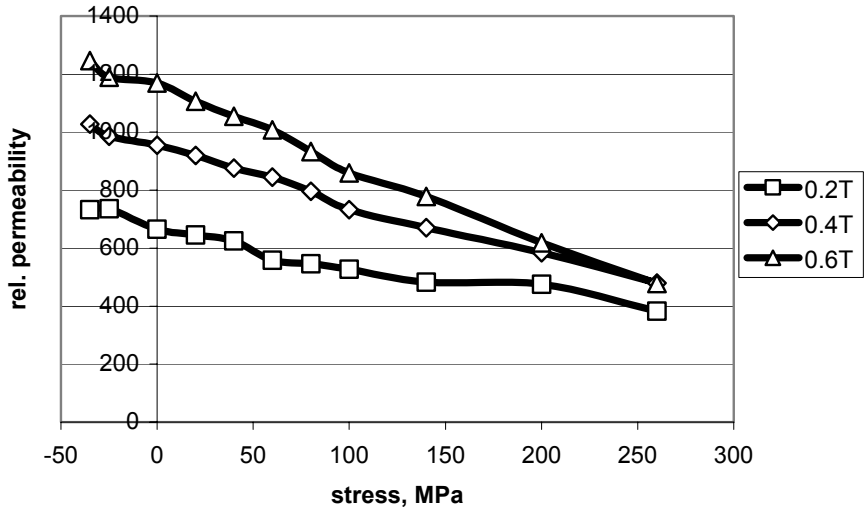

Fig. 6.3.4. The effect of the elastic stress on the relative permeability measured at 90^0 with respect to the direction of the stress with stress in the rolling direction at f=50Hz after 5.66% plastic deformation in RD.

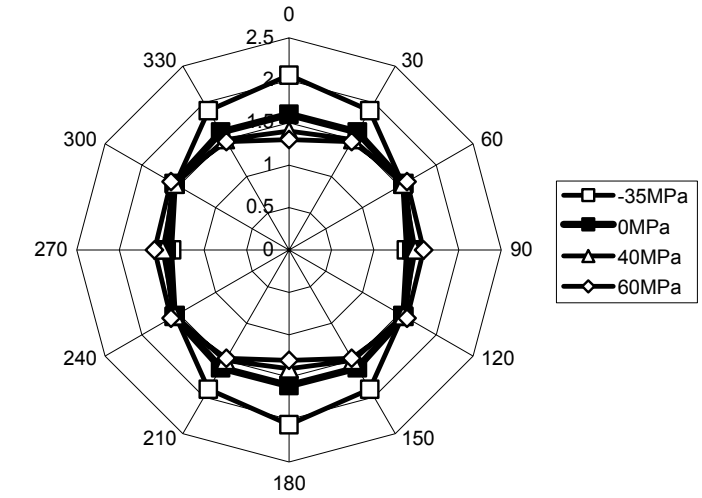

$\uparrow \sigma \uparrow RD$

Fig. 6.3.5. The effect of the small elastic stresses on the distribution of the total losses measured at B=0.4T and f=50Hz after 5.66% plastic deformation in RD.

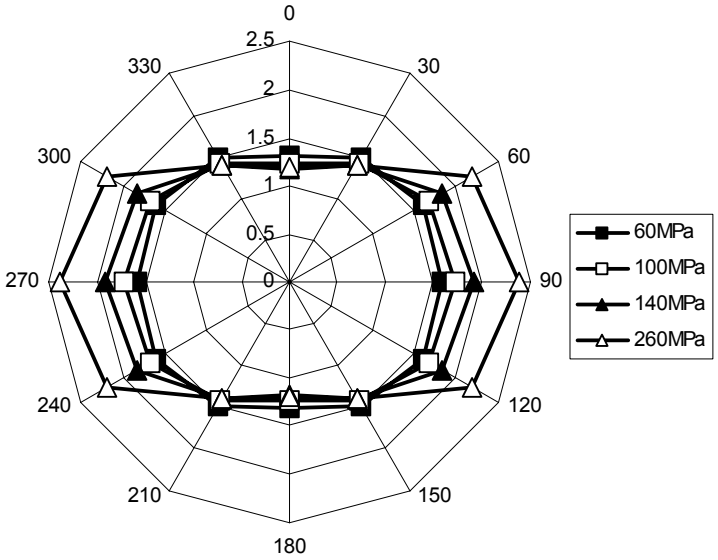

$\uparrow \sigma \uparrow RD$

Fig. 6.3.6. The effect of the large elastic stresses on the distribution of the total losses measured at B=0.4T and f=50Hz after 5.66% plastic deformation in RD.

Section 6.4. The effect of elastic stress applied along the transverse direction of the sample on the magnetic properties of V850-65 non-oriented electrical steel after 4.7% plastic deformation in the transverse direction.

Analogous measurements were conducted for the transverse direction of the material. Like in the previous case (Section 6.3) the dependence of the total losses on the elastic stress is less steep compared to the undeformed material (Section 6.2).
However the difference between RD and TD after plastic deformation applied in TD considerably increases (Fig. 6.4.5).
A comparison of the distributions of the total losses measured at low elastic stresses for the deformed (Fig. 6.4.5) and undeformed states (Fig. 6.2.5) indicates that after plastic deformation in TD there is some sort of compression counteracting the applied tensile stress.
Plastic deformation results in nucleation of new pinning sites, which impede the domain wall movement. As will be shown further this is not the only consequence of the plastic deformation. But with respect to pinning, plastic deformation is similar to an introduction of carbon into the steel as shown in [Makar2000].
Therefore the magnetic behaviour of the plastically deformed non-oriented electrical steels under applied mechanical stress is analogous to the behaviour of undeformed carbon steel.

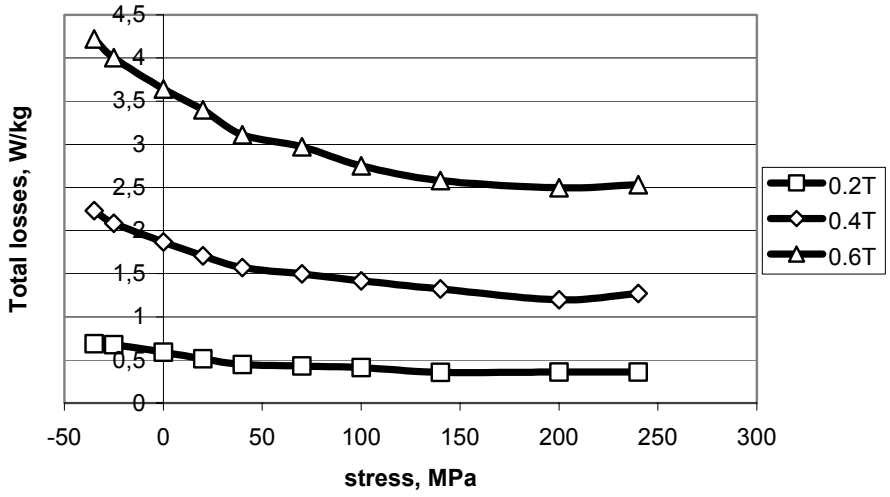

Fig. 6.4.1. The effect of the elastic stress on the total losses measured along the stress with stress in the transverse direction at f=50Hz after 4.7% plastic deformation in TD.

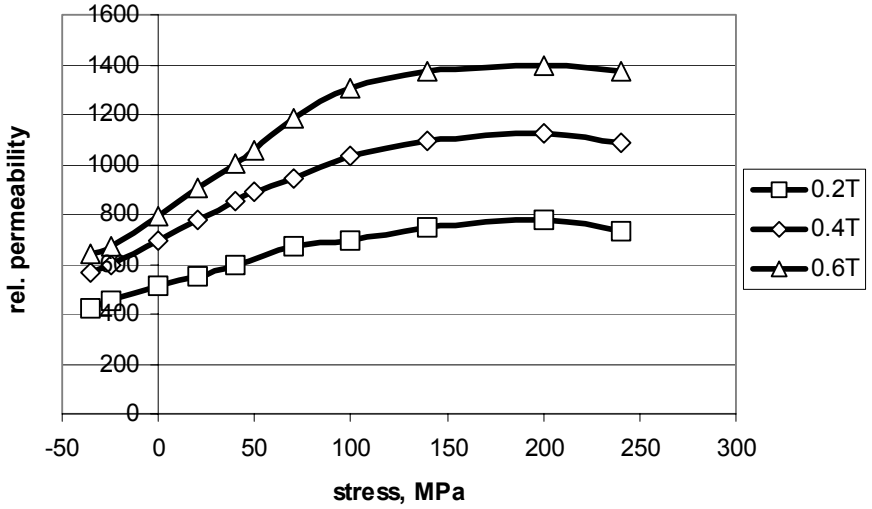

Fig. 6.4.2. The effect of the elastic stress on the relative permeability measured along the stress with stress in the transverse direction at f=50Hz after 4.7% plastic deformation in TD.

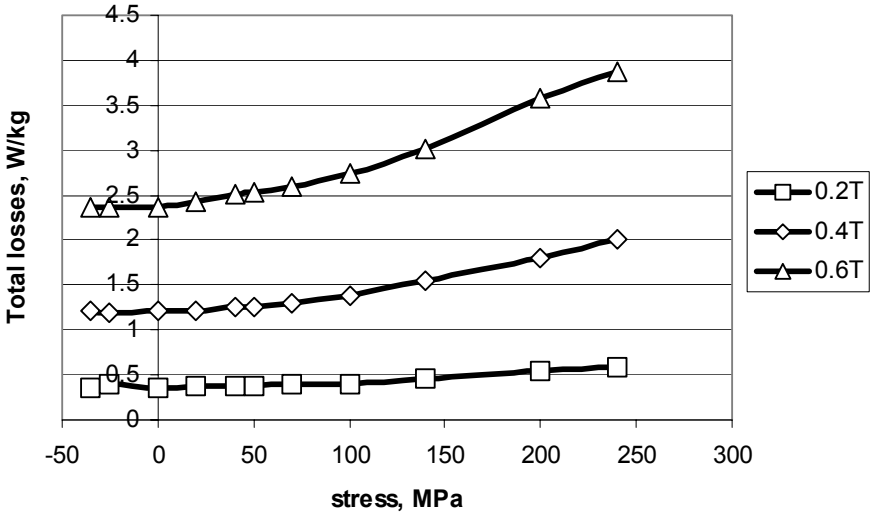

Fig. 6.4.3. The effect of the elastic stress on the total losses measured at 90^0 with respect to the direction of the stress with stress in the transverse direction at f=50Hz after 4.7% plastic deformation in TD.

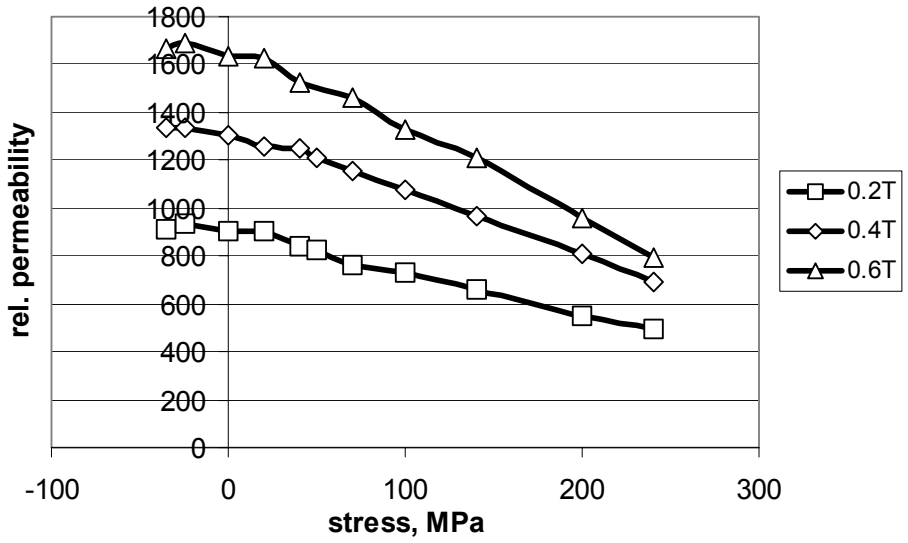

Fig. 6.4.4. The effect of the elastic stress on the relative permeability measured at 90^0 with respect to the direction of the stress with stress in the transverse direction at f=50Hz after 4.7% plastic deformation in TD.

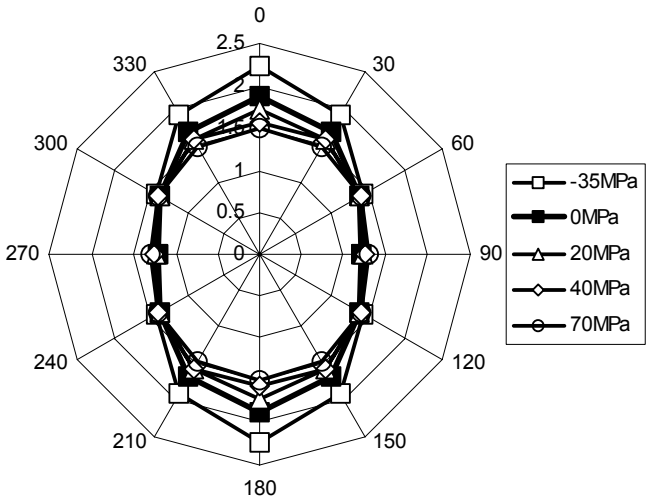

$\uparrow \sigma \rightarrow RD$

Fig. 6.4.5. The effect of the small elastic stresses on the distribution of the total losses measured at B=0.4T and f=50Hz after 4.7% plastic deformation in TD.

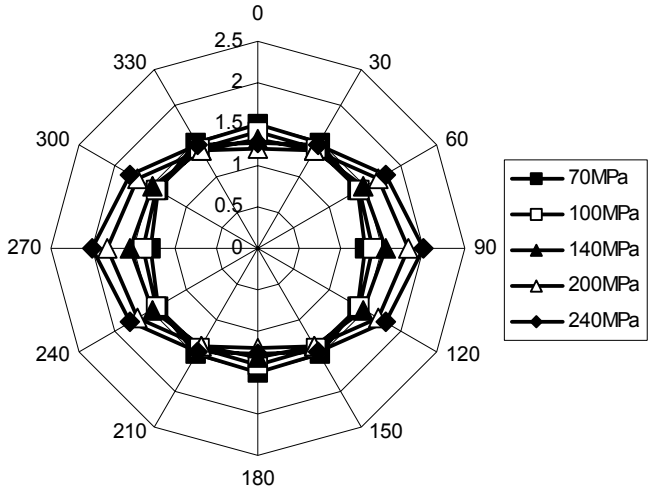

Fig. 6.4.6. The effect of the small elastic stresses on the distribution of the total losses measured at B=0.4T and f=50Hz after 4.7% plastic deformation in TD.

Section 6.5. Investigation of residual stresses due to plastic deformation in non-oriented electrical steels.

6.5.1. Some general information on residual stresses.

So far we considered isotropic and uniformly distributed mechanical properties. Recent results [Hubert2003_2][Hubert2003][Buch1988] show that this is not completely so as far as steels are concerned. The effect of anisotropy on Young's Modulus and Poisson ratio in non-oriented electrical steel is demonstrated in [Hubert2003_2]. This anisotropy is in correspondence with observed crystallographic texture in the considered steel.
The grains also have a different plastic limit, which is confirmed by the fatigue destruction of the steels. There is a low limit stress for fatigue [Buch1988][Rice1988]. Below this limit material can operate infinitely long. Apparently, this limit corresponds to the yield stress of the weakest grains with respect to the applied mechanical load. But any elastic stress above the low limit can result in destruction of material after a specified number of cycles [Buch1988][Rice1988].
It is mentioned in the introductory chapter in [Buch1988] that slip-bands emerge in some grains. This phenomenon is a clear indication of the nucleation of dislocations and plastic deformation of the grain. In fact, slip bands can appear even after a single cycle of elastic stress approaching the yield stress as shown in [Hubert2003].
The plastic deformation is irreversible. So via the weak grains material can accumulate information on the applied mechanical load as shown in Fig.6.5.1.1. below.

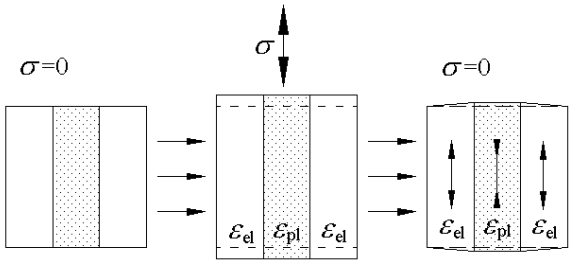

Fig. 6.5.1.1. The nucleation of the residual stresses inside the weak grain and within its vicinity.

In order to provide continuum of the material at the grain boundaries residual stresses emerge. As the amount of the weak grains is small [Buch1988], the residual deformation is normally negligible.

Compressive residual stresses at the surface of material are favourable for constructional applications [Rice1988 p.153] as the residual stresses are summing up with the applied mechanical load. Compressive residual stresses can be introduced by application of sufficiently large tensile stresses as shown in Fig. 6.5.1.1. The latter can be accomplished via special surface treatments [Buch1988 ch. 8].

Our primary concern is, of course, the magnetic properties of the steel, which are affected by the stresses as it was shown in the previous sections. The large residual stresses reported in [Baudouin2002 p. 66] on the laser cut samples are due to the non-uniform thermal treatment at the edge of the sample. The presence of the large residual stresses justifies the observed deterioration of the magnetic properties. The analogous effect can be expected from welding of magnetic cores.

Yet another important source of the residual stresses is a plastic deformation [Hug2002]. As a consequence of the difference between the grains, the dislocation density is non-uniform in the material, which explains the existence of the residual stresses in the plastic region.

Such a plastic deformation also appears at the edge of the sheets due to mechanical cutting. So we will further study the residual stresses due to the plastic deformation only.

6.5.2. Experimental investigation of the residual stresses due to plastic deformation in non-oriented electrical steels.

The aim of this section is to check whether it is possible to use the sensitivity of the magnetic properties of non-oriented electrical steels with respect to applied mechanical stress in order to obtain information on the residual stresses. The mechanical characteristics presented in chapter 3 show a considerable Lüders band that exceeds 5% (Fig. 3.3.1.1). This zone is characterized by a multitude of the local mechanical strains ranging from 0% to the boundary of the Lüders zone. In order to make the state of the sample more certain it was decided to operate with a plastic deformation equal to 5.6%.

Such deformation is insufficient in order to change the texture of non-oriented electrical steel [Djachenko p. 52]. So the same magnetic anisotropy can be expected in the sample. The initial difference between the total losses measured in the different directions of the sample is due to the magnetic crystalline anisotropy:

$$P_{anis} = \frac{P_{TD} - P_{RD}}{2} \qquad (6.5.2.1)$$

The anisotropy energy is related to the texture. If the texture remains unchanged then we should expect no change in P_{anis} (6.5.2.1). For the sample investigated in Section 6.1 (no deformation) P_{anis} = 0.1175W/kg for the sinusoidal flux with frequency f=50Hz and maximum induction level 0.5 T. However the difference between the axes changes sign for the plastically deformed sample in RD: P_{anis} = -0.07732W/kg. This effect is often called 'magnetoplastic anisotropy' [Hug2002]. Apparently, it happens due to the presence of unidirectional residual stresses introducing the additional anisotropy in the sample.

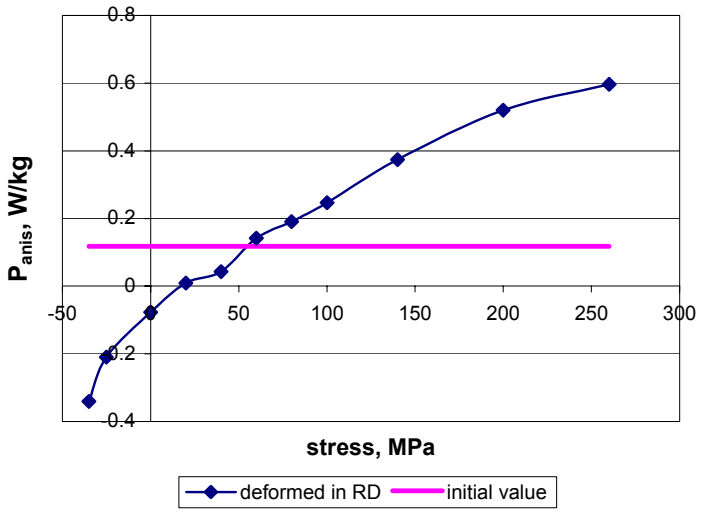

Fig. 6.5.2.1. The dependence of the anisotropy on the applied stress for the sample deformed plastically in the rolling direction.

The action of these stresses can be compensated by external mechanical stress of the opposite sign. The compensation is assumed to be complete when the initial difference between the axes is restored. The global sum of the residual stresses in the material is zero. As it was shown in Sections 6.3 and 6.4 the deteriorating effect of compression on the magnetic properties is much stronger than the improving effect of the tensile stress. Therefore the contribution of the local tensile stresses (Fig. 6.5.1.1) can generally be neglected. Due to arbitrary orientation of the grains, residual stresses along the perpendicular direction with respect to the applied plastic deformation can also be present. However the dominant interaction should be expected along the plastic deformation.

So the applied elastic stress is equal to the compressive unidirectional component of the residual stress distribution present in the material.

Compression is compensated by the external applied tension. From Fig. 6.5.2.1 the tensile stress necessary to restore the initial anisotropy of the sample is equal to 55MPa.

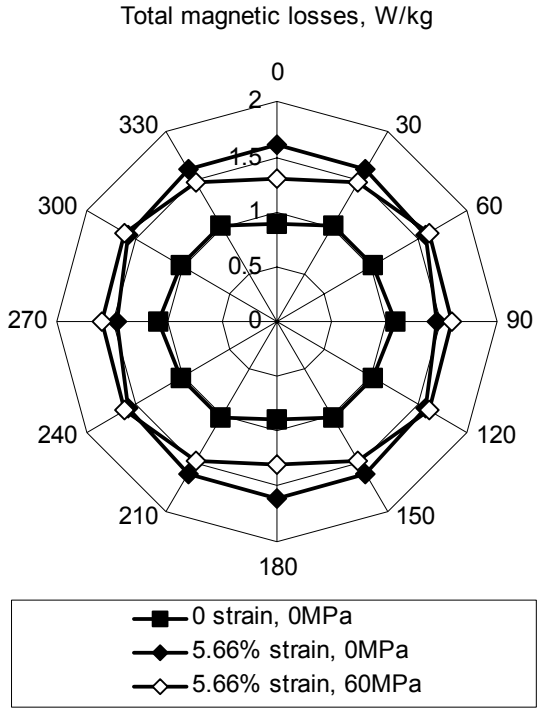

$\uparrow \sigma \uparrow RD$

Fig. 6.5.2.2. Distribution of the total magnetic losses before and after the plastic deformation applied in the rolling direction.

The procedure for the evaluation of the unidirectional compressive residual stresses is defined as follows. At first, the initial distribution of the total losses is measured. Then, the sample is subjected to a plastic deformation and the distribution of the magnetic properties is measured again. A sequence of a tensile elastic stresses is applied in the direction of the plastic tensile deformation. The distribution of the magnetic properties is recorded for each applied elastic stress. Finally the stress is found that provides the recovery of the initial anisotropy of the total losses in the sample. This stress is assumed to be equal to the unidirectional compressive residual stress present in the material.
Analogous measurements were conducted for the sample plastically deformed in the transverse direction (Fig. 6.5.2.3 and Fig. 6.5.2.4). The unidirectional residual stress following the procedure established above is equal to 84MPa.

X-Ray measurements were performed on the sample deformed in TD. The measurements were carried out on both sides of the sample.
The results for the uncoated side are presented below.

a) normal stress parallel to the rolling direction:
$\sigma_{11} = -122\{meas.\,value\}(\pm 25\{accuracy\}) + 28\{correct.\,due\ to\ texture\}(\pm 7\{accuracy\ of\ \ correct.\}) = -94(\pm 32)\ MPa$

b) normal stress parallel to the transverse direction:
$\sigma_{22} = -138\{meas.\ value\}(\pm 25\ \{accuracy\}) + 30\{correct.\ due\ to\ texture\}(\pm 6\{accuracy\ of\ correct.\}) = -108(\pm 31)\ MPa$

c) shear stress in the plane of the rolled plate:
$\sigma_{12} = 61\{meas.\ value\}(\pm 20\{accuracy\}) - 23\{correct.\ due\ to\ texture\}(\pm 6\{accuracy\ of\ correct.\}) = 38(\pm 26)\ MPa$

The term between brackets denotes a possible deviation of the measurement results typical for the X-Ray measurements. The measurements were carried out on the surface of the sample. In the middle of the sheet the opposite stresses can be expected. However it is worth noting that the difference between the principal stresses (62 MPa and 140 MPa) is equal to 78 MPa.

Unfortunately, there was no more precise tool available for an independent evaluation of the residual stresses. However the X-Ray measurements confirm the presence of large compressive stresses in the material after a plastic deformation. Larger stresses operate in the direction of the plastic deformation.

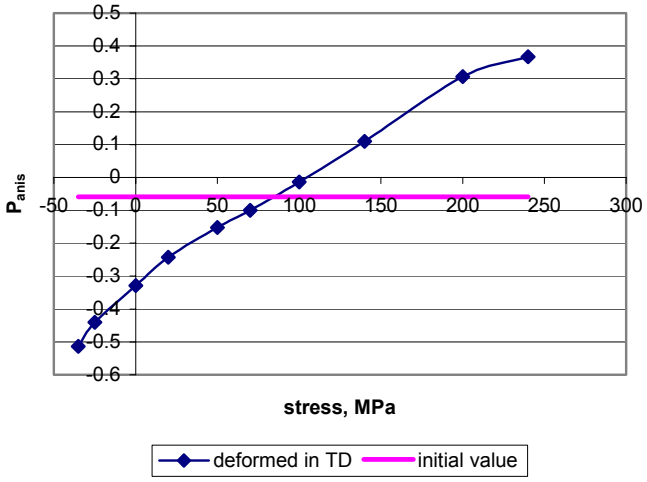

Fig. 6.5.2.3. The dependence of the anisotropy losses on the applied stress for the sample deformed plastically in the transverse direction.

According to [Sablik1995] biaxial compressive stress deteriorates the magnetic properties of carbon steel. The effect of biaxial elastic stress on the magnetic properties in a specific direction is equivalent to the effect of 3 times smaller unidirectional elastic stress applied in the considered direction. Since carbon in the considered steels operates as a pinning site, it makes the magnetic properties of these steels similar to the properties of the plastically deformed electrical steels. Therefore the approach developed in [Sablik1995] for carbon steels can be extended to our case of plastic deformation.

Thus the increase of the total magnetic losses after plastic deformation compared to the undeformed state consists of the following three contributions:

1) dislocation density;
2) biaxial residual stresses;
3) unidirectional compressive residual stresses.

The first two contributions result in an isotropic deterioration of the magnetic properties. The biaxial compressive stresses are probably balanced by the biaxial tensile stresses, which are equivalent to each other with respect to the effect on the magnetic properties [Sablik1995]. Therefore we can assume that the whole volume is affected by this kind of deterioration of magnetic properties. Referring to the X-Ray conducted measurements the impact of the biaxial stress (101MPa) corresponds to the effect of the 33.7MPa(101/3) unidirectional compressive stress [Sablik1995]. The biaxial stress (or equivalent uniaxial stress of 33.7 Mpa) results in a 20% (see Figure 6.4.1.) increase of the total losses in all the directions.

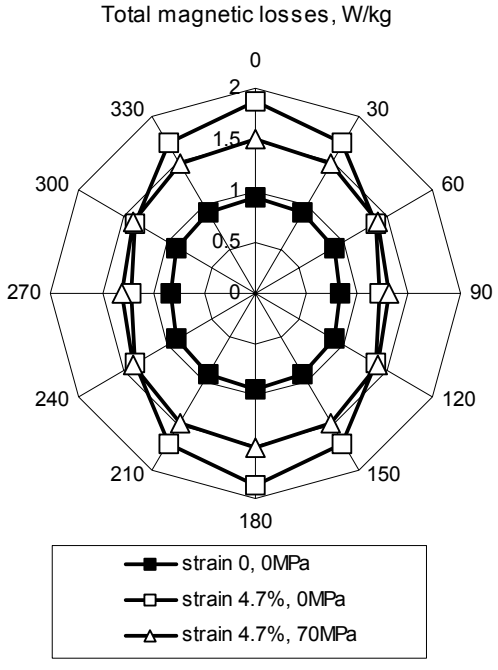

Fig. 6.5.2.4. Distribution of the total magnetic losses before and after plastic deformation applied in the transverse direction.

With respect to the unidirectional compressive residual stresses it is not immediately clear whether they are balanced, i.e. the residual compression can slightly affect the dimensions of the sample as if external load was applied[1]. It explains why the additional magnetic anisotropy is observed after plastic deformation.

[1] The impact of the unbalanced residual stresses on the dimensions of the sample is described in [Rice p. 156].

The investigation of the residual stresses is important for the accurate estimation of the dislocation density. On the other hand, there are methods for the experimental evaluation of the dislocation density. These methods can be used in order to collect information on the considered material and to incorporate it into their hysteresis models like the one presented in [Sablik2001]. When the isotropic deterioration of the magnetic properties due to the dislocations is known the multidirectional magnetic measurements can provide the information not only on the unidirectional component of the residual stress, but also on the biaxial stress. It is worth noting that although the magnetic measurements are not as local as the X-Ray measurements they can provide a better repeatability.

The harmful effect of the residual stresses on the magnetic properties can be reduced if some special measures are applied for the redistribution of the dislocations. The most common procedure is a stress-relief annealing. The forces of the thermal agitation push the dislocations to distribute more evenly in the sample. However it requires a special non-organic coating. As it was mentioned organic coating can lead to the diffusion of carbon into the sample, thereby causing the deterioration of the magnetic properties. However there are alternative treatments [Wu2002]. These include vibrating stress relieving, ultra-sonic methods and a strong magnetic field at low frequency alternating magnetic field treatment. It is shown in [Wu2002] that a strong magnetic field at low frequency (value was not specified) can result in the disappearance of the dislocation tangles, although the dislocation density does not change significantly. The mechanism of this phenomenon is not yet clearly understood, but apparently the dislocations are forced to move by their interaction with the external magnetic field.

According to [Taylor1983] the dislocation tangles are more effective with respect to pinning of the domain walls. It was confirmed experimentally that once the tangles emerge, the domain walls start to accommodate to them, which was not encountered on the single dislocations. So the redistribution of the dislocations can be an effective measure for the reduction of the pinning of the domain walls.

Section 6.6. The effect of applied mechanical stress on the magnetization curves of non-oriented electrical steels.

The unidirectional investigation of the effect of the mechanical stress on the magnetization curves of the investigated electrical steels was carried out using the same magnetic setup. The limitations of the setup defined in Chapter 5 can be considerably reduced if the measurements are conducted on samples with the width matching the width of the ferrite yokes. The measurements were carried out in the direction of applied stress. Since there is no need for a local observation of the flux density in this case a measurement winding was installed on the sample. This setting resembles very much the classical SST setup with the only difference that the excitation windings are installed on the limbs of the yokes rather than around the measurement winding. The investigation in [Hug2002] shows that the present ferrite structure can be used at fields up to 5kA/m.

The results shown in Fig. 6.6.1-6.6.4 demonstrate the effect of the applied elastic stress on the magnetization curve measured in the direction of the applied stress. Analogous results are presented in [Dabrowski1989] on Polish electrical steels, which confirms the general similarity of the magnetomechanical behavior of the non-oriented electrical steels.

As it was noticed earlier in this chapter, the stress affects differently the rolling direction and the transverse direction. It is shown in Fig. 6.6.5 that the tensile stress equal to

25MPa makes the two directions practically equal with only a minor difference in favor of RD. This matter will be discussed in the next chapter.

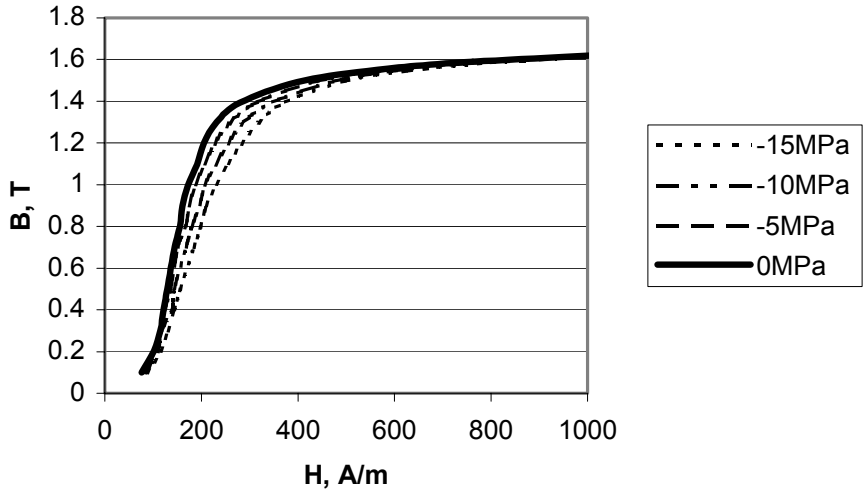

Fig. 6.6.1. The effect of the applied compression on the magnetization curve of V830-65 non-oriented electrical steel measured in RD along the applied stress.

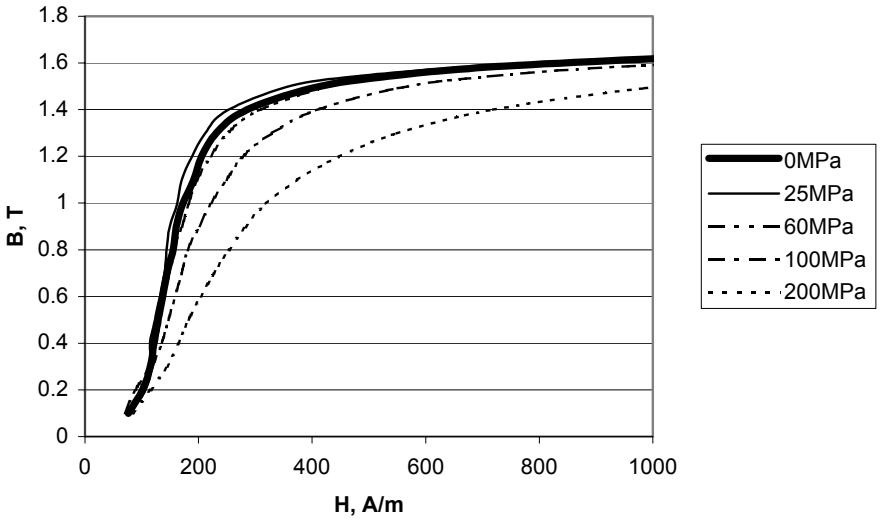

Fig. 6.6.2. The effect of the applied tension on the magnetization curve of V830-65 non-oriented electrical steel measured in RD along the applied stress.

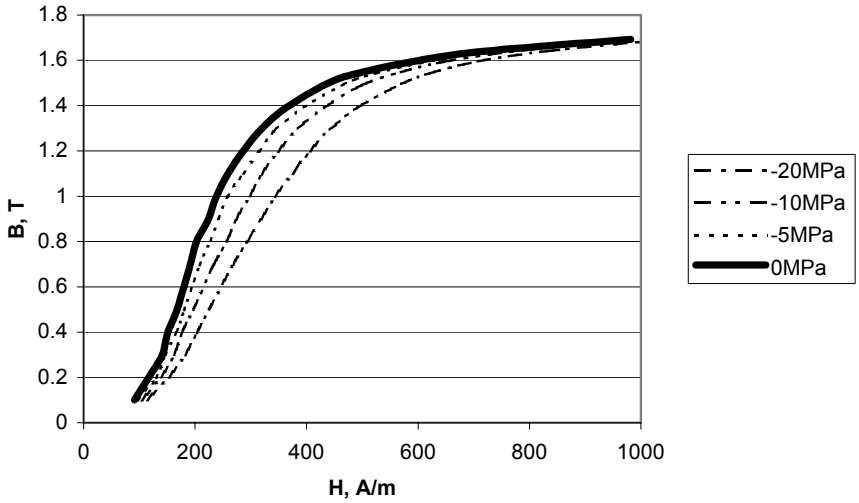

Fig. 6.6.3. The effect of the applied compression on the magnetization curve of V830-65 non-oriented electrical steel measured in TD with the stress applied along the TD

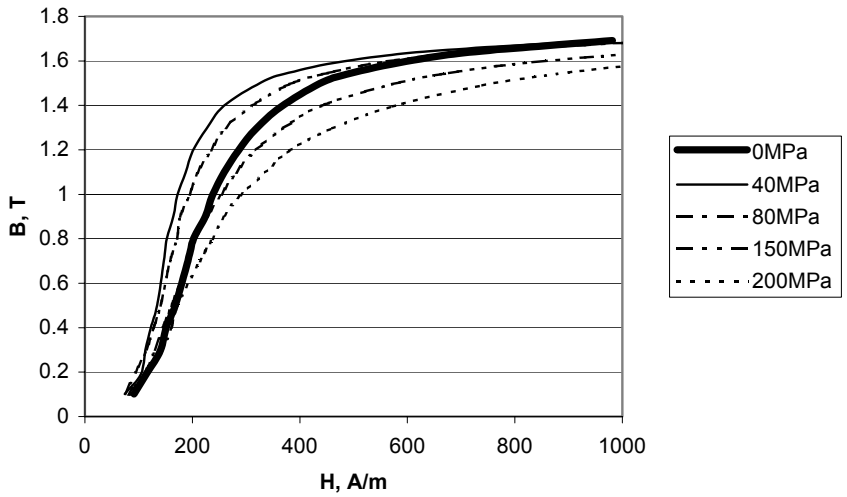

Fig. 6.6.4. The effect of the applied tension on the magnetization curve of V830-65 non-oriented electrical steel measured in TD with the stress applied along the TD.

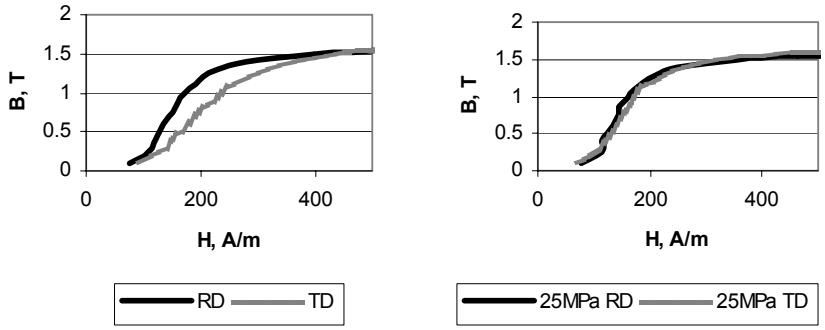

Fig. 6.6.5. The effect of the applied tension on the reduction of the difference between RD and TD of V830-65 non-oriented electrical steel.

The application of the plastic deformation leads to the severe degradation of the magnetic properties (Fig. 6.6.6, Fig. 6.6.7). A particular deterioration apparently occurs at the low strains as it is suggested in [Ossart2000] and [Hubert2003].

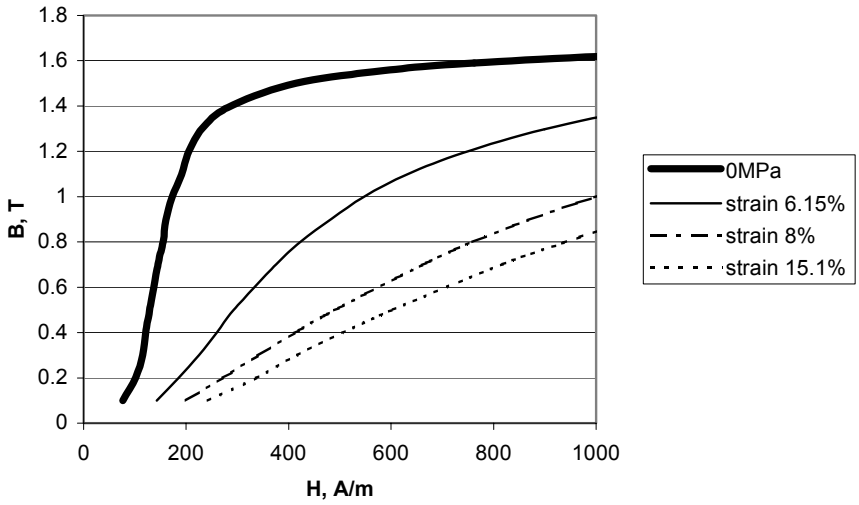

Fig. 6.6.6. The effect of the tensile plastic deformation on the magnetization curve of V830-65 non-oriented electrical steel measured in the RD with the stress applied along the RD.

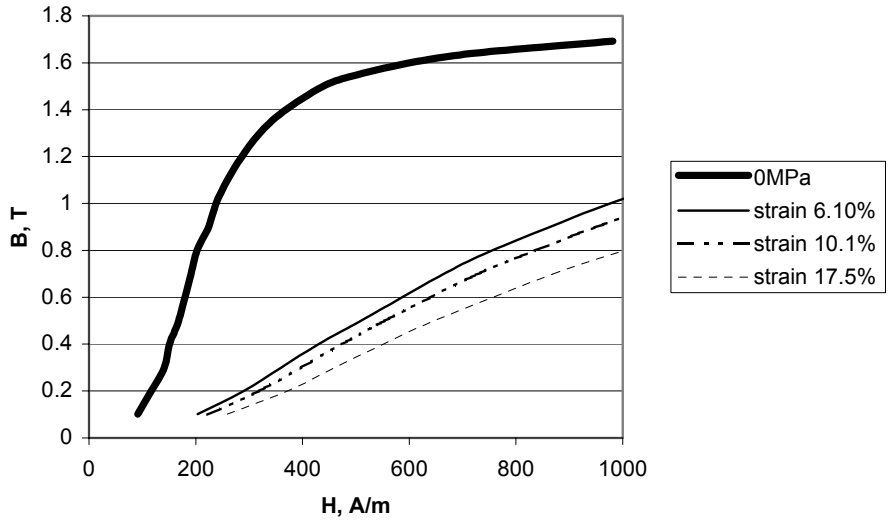

Fig. 6.6.7. The effect of the tensile plastic deformation on the magnetization curve of V830-65 non-oriented electrical steel measured in TD with the stress applied along the TD.

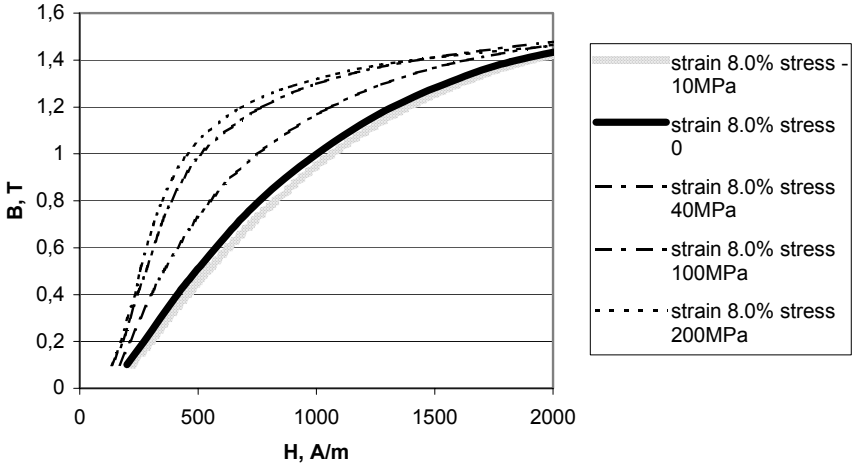

Fig. 6.6.8. The effect of elastic deformation applied to the plastically deformed sample of V830-65 non-oriented electrical steel in RD.

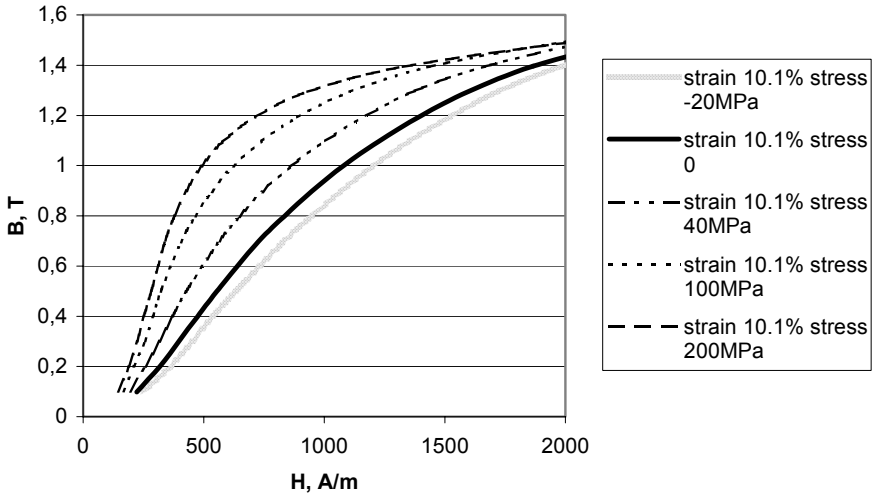

Fig. 6.6.9. The effect of elastic deformation applied to the plastically deformed sample of V830-65 non-oriented electrical steel in TD.

The effect of the elastic stress on the slope of the magnetization curve of the plastically deformed sample is smaller, which is in accordance with the multidirectional observation presented in the previous sections.
It can be concluded that the increase of the induction range does not reveal any new effects compared with the previous sections. So from the fundamental point of view the investigation at low induction levels provides sufficient information on the qualitative effect of punching on the magnetic properties of non-oriented electrical steels.
The experimental results presented in this section will be used further in Chapter 9 for the numerical simulation of the effect of the production stresses.

Discussion and conclusions.

It was experimentally confirmed in this chapter that the elastic stresses applied to non-oriented electrical steels affect the magnetic anisotropy. The effect of the stress depends on the amount of pinning sites in the material. It was clearly shown that the plastically deformed material is less sensitive to applied stress compared to the undeformed state.
Another parameter defining pinning in the steel is the grain size [Sablik2001]. So one can expect that material with larger grains is more sensitive to the applied mechanical stress than material with smaller grains, assuming that other metallurgical parameters are the same. It is shown in [Dabrowski1989] that many types of non-oriented electrical steel have better permeability at 40MPa tensile stress compared to the initial state. But after annealing this optimum shifts to stresses around 10MPa. It clearly indicates that the sensitivity of the magnetic properties to the applied elastic stress is increased by annealing.
Plastic deformation of non-oriented electrical steels leads to a general deterioration of the magnetic properties of non-oriented electrical steels and affects the magnetic anisotropy due to the presence of residual stresses.

The remaining question is why the magnetic properties of the steel start to deteriorate after exceeding a specific tensile stress?

An investigation on this matter is presented in [Jillek1980]. In this paper grain-oriented electrical steel was studied, since this material is more suitable for the direct observation of the magnetic domains. The observed magnetic domain pattern revealed blocking of certain groups of magnetic domains by tensile stress at an induction of $\mu_0 M_s/2$. However the results presented in Section 6.6 show that the saturation magnetization M_s is unaffected by the applied stress. Analogous conclusions can be drawn from the data presented in [Dabrowski1989].

According to [Makar1998_3 p. 123] the deterioration of the magnetic properties at large tensile stresses is due to the multiplication of dislocations. Although this statement is generally in accordance with the data presented in [Hubert2003] it is relevant only for stresses approaching the yield point. The nucleation of the dislocations is normally irreversible. So it does not explain why the deterioration of the magnetic properties is recoverable if the applied tensile loads do not exceed 80% of the yield stress.

There is yet another deformation mechanism discussed in Chapter 2. Due to the presence of the Si atoms serving as the saddle points, the dislocations tend to bend under the application of the stress. It is shown in [Hubert2003] that the dislocation sequences start appearing in the grains preferably oriented with respect to the applied stress. Bending happens prior to the multiplication of the dislocations. So it can be suggested that bending of dislocations also begins in these grains sooner than in others. Thus some grains appear to be more deformed than the neighbors. This non-uniformity leads to the emergence of internal stresses tending to maintain the continuity of the body [Hubert2003]. These stresses are apparently responsible for the changes in the magnetic domain pattern [Jillek1980].

When the load is released the bent stretches of the dislocations straighten as it corresponds to a lower internal energy. So the internal stresses decrease. This explains why the magnetic properties recover after the release of moderate elastic tensile stress.

With respect to the effect of single dislocations on pinning of the domain walls it is shown in [Taylor1983] that this effect is not considerable. It is stated there that the domain configuration is practically unaffected by the dislocation density unless a cellular dislocation structure emerges in the material.

The very presence of the linear defects and grains makes the lattice irregular or uncertain, which brings some uncertainty into the material parameters. It was shown in the first paragraph of Section 6.5 that the very meaning of the yield stress as the maximum elastic stress is not completely correct. Irreversible transformations can occur in the material at lower mechanical stresses, even though the material preserves the original dimensions.

Chapter 7. Magnetomechanical effects.

Introduction.

The results presented in the previous chapter defined the link between the stress and the magnetic properties of non-oriented electrical steels. In this chapter we basically deal with the same subject. However the primary goal here is to define whether the observed magnetomechanical effects can be employed in order to improve certain aspects of the behaviour of non-oriented electrical steels.
In the first section of this chapter an interrelation between tension and compression is determined. It will be shown that compression applied perpendicular to the magnetic field can be used for the improvement of the magnetic properties. In the second section a link with magnetostriction is defined. It will be shown that the conducted measurements can be used for the indirect estimation of magnetostriction. A comparison with conventional measurements is presented. The advantages and drawbacks of the developed approach are analyzed. At the end, actions are proposed that can help to reduce the magnetostriction.

Section. 7.1. The interrelation between tension and compression.

7.1.1. Experimental observations

As in the previous chapters the following two types of commercial non-oriented electrical steels are considered – V850-65 and M330-50. The Orientation Distribution Function (ODF) measurements show the presence of a certain texture in both materials (Fig. 7.1.1).

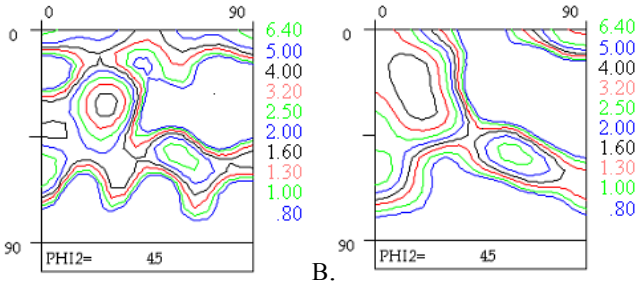

Fig. 7.1.1. Crystallographic texture observed in the investigated materials (A - M330-50, B – V850-65).

The magnetic measurements were carried out under stress, applied successively in the transverse direction (TD) and the rolling direction (RD) of the material. As in chapter 6 both the total magnetic losses and the relative permeability were evaluated at 0.4T sinusoidal induction and 50Hz frequency. The effect of the mechanical stress on the magnetic properties measured in the TD for the V850-65 is shown in Fig. 7.1.2 and Fig. 7.1.3.

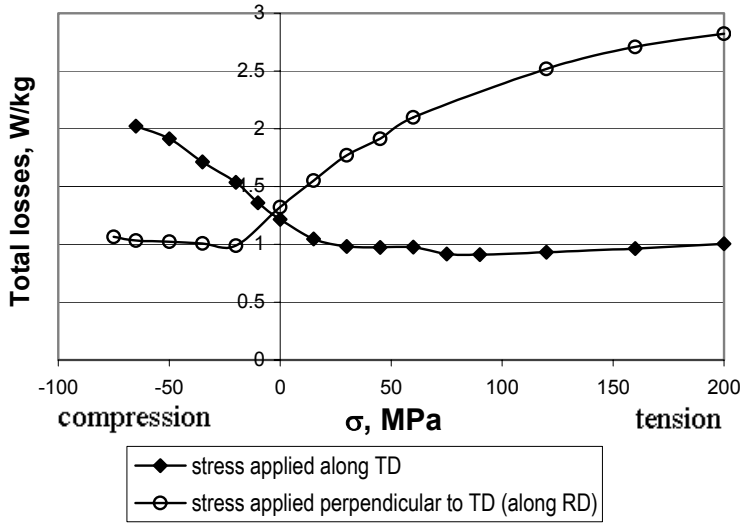

Fig. 7.1.2. The total magnetic losses measured along the TD of the sample of the V850-65 steel, at B=0.4T, f=50Hz.

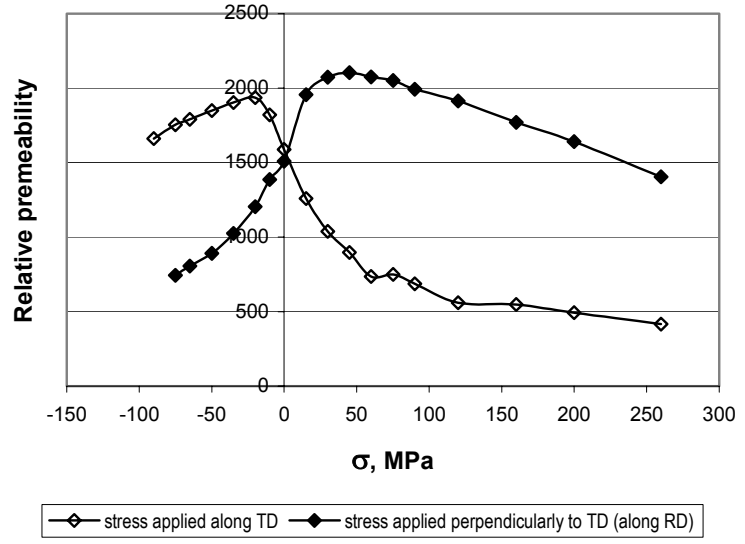

Fig. 7.1.3. The relative permeability measured along the TD of the sample of the V850-65 steel, B=0.4T, f=50Hz.

There is a small deviation in the properties observed at the unloaded state (σ=0MPa) for the samples, which is an artifact of the measurement procedure. However this deviation is definitely smaller than the observed change in the magnetic properties due to the application of the mechanical stress.

It can be seen that the effect of tension on the magnetic properties measured along the stress directions is very similar to the effect of compression on the magnetic properties measured in the direction perpendicular to the stress. Tensile stresses below 30MPa lead to a clear improvement of the magnetic properties in the considered directions. Larger stresses do not introduce any visible effect on the total magnetic losses, but result in a decrease of the permeability. With regard to the magnetic properties measured in the direction of compression or perpendicularly to the tension it can be noticed that the properties considerably deteriorate with the stress.

A comparison of the effect of tension and compression on RD and TD is presented in Fig. 7.1.4. and Fig. 7.1.5
Here the properties were measured perpendicularly to the applied stress. The difference between RD and TD considerably decreases when the applied compression reaches 20MPa. However after this stress the difference in the relative permeability starts to grow, as shown in Fig. 7.1.5

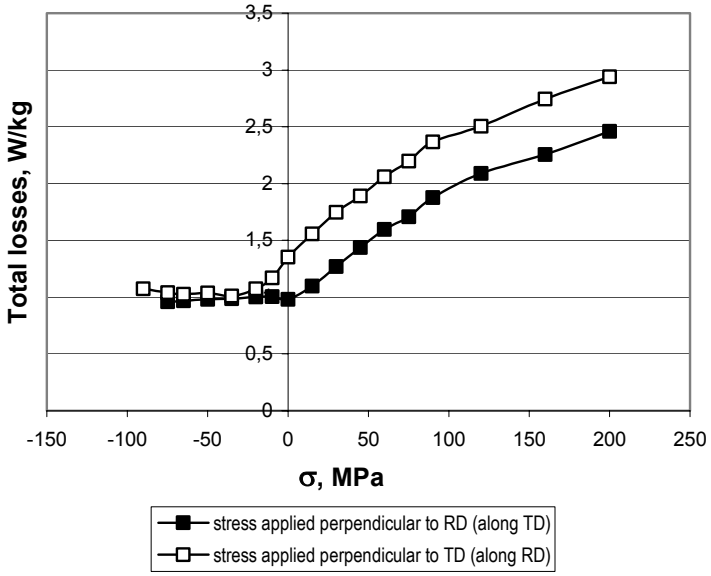

Fig. 7.1.4. The total magnetic losses measured in the direction perpendicular to the applied stress of the sample of the V850-65 steel, at B=0.4T, f=50Hz. Positive values of σ correspond with tensile stresses.

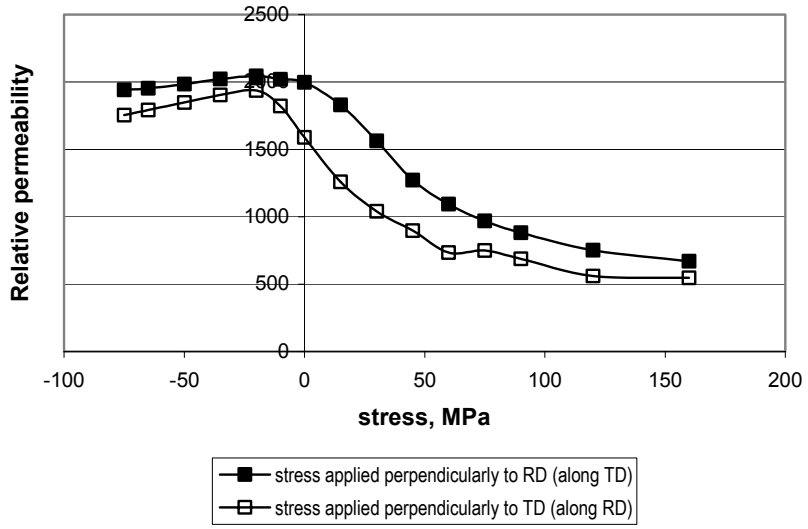

Fig. 7.1.5 The relative permeability measured in the direction perpendicular to the applied stress of the sample of the V850-65 steel, at B=0.4T, f=50Hz. Positive values of σ correspond with tensile stresses.

Analogous measurements were carried for the M330-50 steel (Fig. 7.1.6, 7.1.7, 7.1.8). A similarity with the behaviour of V850-65 material is encountered.

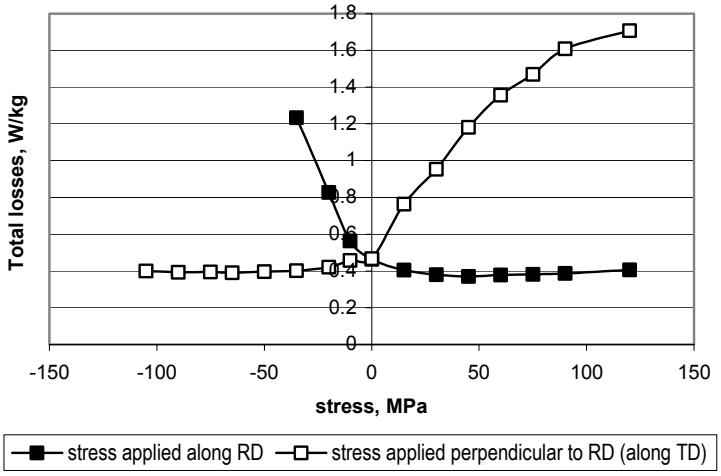

Fig. 7.1.6. The total magnetic losses measured along the RD of the sample of the M330-50 steel at B=0.4T, f=50Hz.

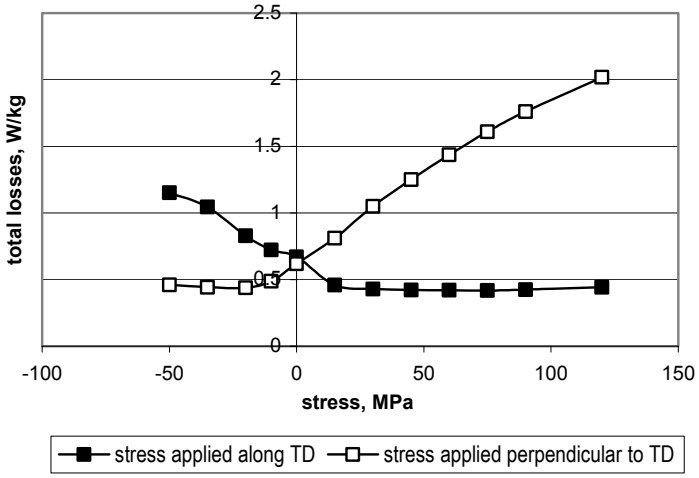

Fig. 7.1.7. The total magnetic losses measured along the TD of the sample of the M330-50 steel at B=0.4T, f=50Hz.

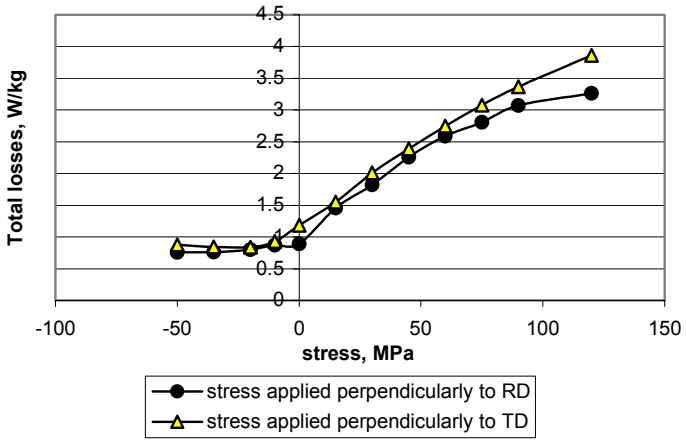

Fig. 7.1.8. The total magnetic losses measured in the direction perpendicular to the applied stress of the sample of the M330-50 steel, at B=0.4T, f=50Hz.

The results on the two materials reveal that the observed variation of the magnetic properties with the applied elastic stress is typical for non-oriented electrical steels. Similar measurement results are obtained at other induction levels.

7.1.2. Microstructural interpretation.

Taking into account the fact that non-oriented electrical steel has a weak texture the stress can occupy any arbitrary orientation with respect to the crystallographic directions in each considered grain. But at low and moderate inductions the magnetization vector

tends to align along the easy magnetic axis. In Chapter 1 it was shown that if the elastic tensile (compressive) stress is oriented along the easy magnetic axis, the direction of the stress (plane perpendicular to the stress) is favoured, which introduces an according change in the domain structure. However if tensile (compressive) stress is oriented along the [110] medium hard magnetic axis it favours the {110} crystallographic plane ([001] crystallographic axis).
So both tension and compression can make either a particular direction or a particular plane favourable with respect to the magnetic properties, as demonstrated in Fig. 7.1.9.

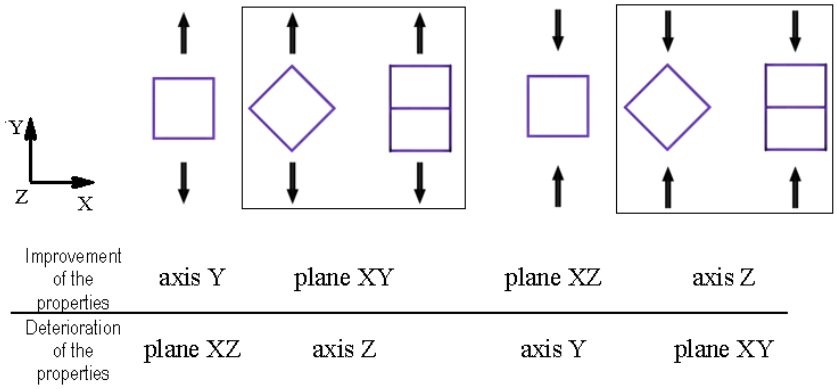

Fig. 7.1.9. The effect of the elastic stress applied in different crystallographic directions on the magnetic properties according to relations defined in Chapter 1 for the magnetoelastic energy in electrical steel.

If the material is perfectly isotropic, i.e. its grains are uniformly distributed between the various space orientations, then the effect of the applied elastic compression on the magnetic properties is equivalent to the effect of the tensile stress of the same value and oriented perpendicularly (Fig. 7.1.10).
The real material has a certain anisotropy, which affects the correspondence between the applied tension and compression. However, it is generally true that the compression, applied in the direction normal to the plane of the sheet, results in an improvement of the magnetic properties at moderate inductions and a decrease of the magnetic anisotropy.
The action of the compression in the direction of the flux should be avoided as it leads to a considerable deterioration of the magnetic properties of non-oriented electrical steel. The same conclusion is valid for the tensile stress acting perpendicularly to the applied magnetic field.

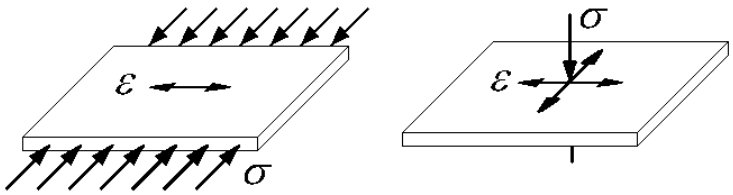

Fig. 7.1.10. The deformation of the electrical steel.

It is worth noting that the magnetic properties, measured along the stress and perpendicularly to it, are changing almost symmetrically with respect to the vertical axis (Fig. 7.1.2, 7.1.3, 7.1.6, 7.1.7).
Due to possible buckling of the sample it is difficult to provide large compressive stresses in the plane of the sheet. Instead, the tensile stress can be used, when accepting the non-perfect symmetry just mentioned.

Section. 7.2. Correlation with magnetostriction.

7.2.1. Internal magnetic forces.

The magnetostriction forces are internal forces due to the presence of a magnetic domain structure. Indeed, the presence of a magnetic domain structure results in an inherent deformation of the ferromagnetic body even in the demagnetized state.
Since λ_{100}, see Chapter 1, is positive for FeSi alloys, the material elongates along the local magnetization M that is initially oriented along one of the easy magnetic axis (Fig. 7.2.1).
The deformation of the material becomes visible only if the domain configuration changes.

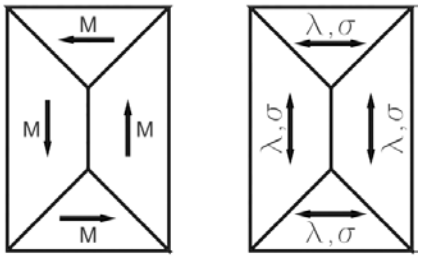

Fig. 7.2.1. Initial distribution of the magnetization and magnetostriction.

If material is placed in an external magnetic field than the domains with a favourable orientation grow at the expense of the neighbours (Fig. 7.2.2). Consequently, the material deforms. The deformation of the material along the axis of the external magnetic excitation in comparison with the demagnetized state is called the magnetostriction. It can be easily seen that the movement of the 90^0 domain walls contribute to the deformation of the material unlike the propagation of the 180^0 domain walls. A contribution of the various magnetization mechanisms into the magnetostriction is considered in detail in [Yu1997].

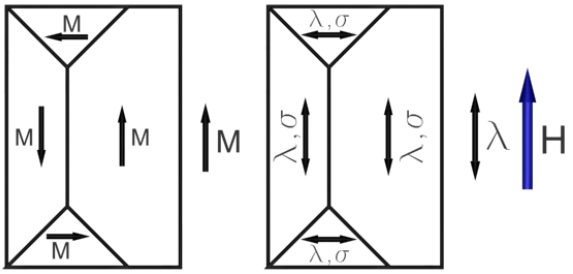

Fig. 7.2.2. Change in magnetostriction due to the application of an external magnetic field.

A change of the domain configuration occurs due to the change of the total energy of the system (see Chapter 1). This change can be provided by elastic deformation of the ferromagnetic material. This deformation results in an introduction of magnetoelastic energy as it was shown in Section 1.6. If tension is applied then the magnetoelastic energy (section 1.6) favours the growth of the magnetic domains aligned along the stress at the expense of the neighbours oriented perpendicularly. This growth leads to an additional deformation of the material due to the internal magnetic forces (Fig. 7.2.3).

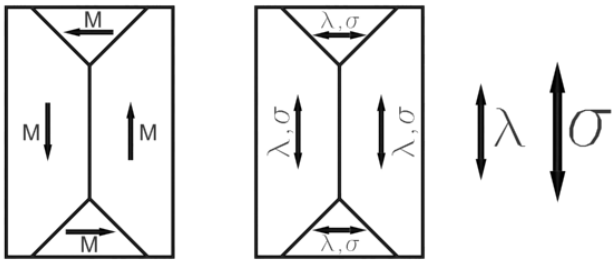

Fig. 7.2.3. Magnetostriction due to the application of the external mechanical stress.

This additional deformation may explain the fact that the Young modulus modifies with applied mechanical stress. This process is also well known as the ΔE effect [Bozorth1993 p. 684][Garshelis1986][Hogston1994][Squire1996].

The experimental observation of the magnetic domain structures [Takezawa2003] in the non-oriented electrical steel shows that magnetic domains in the non-oriented electrical steels have a relatively simple convex shape. So if the volume of the considered domain increases, we may say that its surface also increases.

7.2.2. Effect of 180^o and 90^o domain wall motion on electromagnetic losses and permeability.

Consider a magnetic domain structure and an external applied magnetic field H as shown in Fig. 7.2.4. Under the action of the applied magnetic field H, the motion of the 90^0 domain walls over a distance Δx leads to a 2 times smaller change in the magnetization compared to the motion of a 180^0 domain wall over the same distance if $\alpha=0$. For some particular orientations ($\alpha=\pi/4$ in Fig. 7.2.4) of the magnetic domains the

motion of the 90^0 domain walls is equivalent to the 180^0 domain wall motion in terms of the contribution to the magnetization M_H=Mcosα.

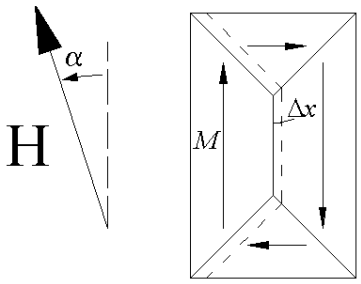

$$\Delta M_H^{180^0}(\alpha, \Delta x) = 2M \sin\alpha \, \Delta x$$
$$\Delta M_H^{90^0}(\alpha, \Delta x) = M(\cos\alpha + \sin\alpha)\Delta x$$

Fig. 7.2.4. Domain wall motion under the action of the applied magnetic field. Modification of the magnetization component along the direction of the applied field due to 180^o and 90^o domain wall motion over a distance Δx.

Assuming uniform distribution of the grains (and, consequently, 90^0 domain walls) among different orientations in space, the average difference between 180^0 and 90^0 domain walls with respect to contribution to the magnetization is equal to 1.41[1]. Consequently, for a fixed variation of magnetization M_H, 1.41 times less movement is necessary when ΔM_H is only due to the 180^0 domain walls movement compared to the case of only 90^0 domain walls moving. In average, when magnetization variation is provided only by the 180^0 domain walls, the magnetization process is at least 1.41 times less subjected to pinning.
Thus the decrease of the area of the 90^0 domain walls due to the application of the tensile stress should lead to a reduction of hysteresis losses and an increase of the permeability, which is confirmed by the experimental data presented in Chapter 6 and Section 7.1.

Additionally we mention two indirect confirmations that the 180^0 domain walls motion has a priority with respect to the motion of the 90^0 domain walls.

1. According to [Makar2000 p. 300-301] the 90^0 domain wall movement wall is dominating at high magnetic fields, while 180^0 domain wall motion is dominant at lower fields. This way the non-linearity of dependence of magnetostriction on the magnetic flux density was interpreted.
2. Another indirect confirmation can be found in [Makaveev2003 p. 84] where a comparison between the rotational and the unidirectional excitation is provided. The rotational magnetization at low and moderate inductions takes place mainly due to the 90^0 domain wall motion. Due to smaller pinning of the 180^0 domain wall motion the losses at low and moderate induction levels and

[1] It can be shown that in grains oriented in the different directions with respect to the applied magnetic field (for instance, in the range $0<\alpha<\pi/4$) the total contribution to the magnetization M_H due to the displacement of all the 180^0 domain walls on Δx distance is 1.41 times larger compared to the contribution due to the analogous displacements of 90^0 domain walls. In reality, the displacement of the domain walls is dependent on their orientation. So the efficiency of a 180^0 domain wall motion compared to a 90^0 domain wall motion can be estimated as a value between 1.41 and 2.

measured under unidirectional magnetization are nearly 2 times smaller compared to the rotational losses.

7.2.3. Relation between magnetostriction and hysteresis losses.

Since the movement of 90^0 domain walls is less efficient due to larger pinning, we can introduce the additional losses $\Delta W_{d.w.}$. These losses reflect the difference in the energy dissipation due to pinning during the motion of the 90^0 domain walls compared to the equivalent movement of the 180^0 domain walls in terms of the contribution to the magnetization M_H: $W^{M_H}_{pinning\ of\ 90^0\ d.w.} = W^{M_H}_{pinning\ of\ 180^0\ d.w.} + \Delta W_{d.w.}$.

The movement of 90^0 domain walls is also responsible for the magnetostriction. After a 90^0 domain wall passes the considered volume of the grain, the orientation of the magnetization and the corresponding deformation λ_{100} switch from one easy magnetization axis to another. Since $\lambda_{100}=\lambda_{010}=\lambda_{001}$, the value of the lattice deformation within a magnetic domain remains constant. Consequently, the total work $½(\varepsilon)^T(\sigma)$ executed by the magnetoelastic forces remains unchanged over the whole volume of the sample as long as the magnetization in the grains is oriented along the easy axes. Therefore until the domain rotation begins (only at higher induction levels) all the domain configurations result in the same work of the internal magnetoelastic forces. During the 90^0 domain wall movement the space rearrangement of the magnetoelastic forces takes place. As a result of that a global deformation of the sample is observed. If the sample is globally deformed there was a global mechanical work performed. So we can say that this work is the energy W_{me} consumed on the rearrangement of the magnetoelastic forces.
This is another dissipation mechanism that accompanies the movement of the 90^0 domain walls. Therefore the total loss of energy due to the movement of 90^0 domain walls can be formulated as a sum of two contributions described above:

$$W_{90^0\ domain\ wall\ motion} = W_{me} + \Delta W_{d.w.} = \Delta W_{total} \qquad (7.2.1)$$

The term $\Delta W_{d.w.}$ in (7.2.1) indicates that the additional energy loss due to the 90^0 domain wall motion is just a fraction of the total energy loss, because 180^0 domain wall motion is also subjected to pinning. So if we manage somehow to wipe out the 90^0 domain walls from the domain structure we will still observe some magnetic losses. But due to the presence of a more efficient magnetic domain structure in the sample these losses will be reduced by ΔW_{total}.
The application of tensile stress affects the domain structure as was shown earlier. The area of the 90^0 domain walls decreases, which improves the magnetic properties (Section 7.1) in the direction of the stress and reduces the magnetostriction. It is shown in [Zentko1980] that under a well defined tension the magnetostriction becomes zero.
A zero magnetostriction indicates that no rearrangement in the internal magnetoelastic forces is present during domain wall motion, which is possible if only 180^0 domain wall movement contribute to the magnetization M_H. Consequently, the 90^0 domain walls are wiped out or not active.

As a result of achieving the domain configuration for zero magnetostriction, an extremum in the magnetic properties has to be encountered, as the 90^o domain walls are

wiped out or not active. It was experimentally observed that both the total magnetic losses and the magnetic permeability have an optimum under the same tensile stress applied in the direction of the magnetic field. We can assume that this optimum corresponds to the zero magnetostriction.

As a first approximation, we may assume that both contributions into the additional energy dissipation (7.2.1) are linearly dependent on the total area of the 90^0 domain walls. So the proportion $W_{me}/\Delta W_{total}$ is rather defined by the density of pinning sites in the material than by the domain configuration. When considering elastic stress, the density of the pinning sites remains the same and consequently $W_{me} \big/ \Delta W_{total} = W_{me}^{\sigma} \big/ \Delta W_{total}^{\sigma}$.

Taking into account a direct link between the magnetoelastic energy W_{me} and the magnetostriction λ we obtain $\lambda^{\sigma=0} \big/ \lambda^{\sigma} = \Delta W_{total}^{\sigma=0} \big/ \Delta W_{total}^{\sigma}$.

This relation allows us to predict the magnetostriction in different stress states as well as in the different directions in the material via an evaluation of the magnetic energy loss of the system.

This approach requires the magnetostriction to be measured in the unloaded condition (σ=0) in order to estimate the contribution of the magnetoelastic energy into the reduction of the total energy of the system. Taking into account the reverse of the sign of the magnetostriction at the large tensile stresses we propose the following formulation:

$$\lambda_{\sigma} = \begin{cases} \dfrac{P_{\sigma} - P_{\min}}{P_{\sigma=0} - P_{\min}} \lambda_{\sigma=0}, \ \sigma < \sigma_{\min} \\ \dfrac{P_{\min} - P_{\sigma}}{P_{\sigma=0} - P_{\min}} \lambda_{\sigma=0}, \sigma > \sigma_{\min} \end{cases} \qquad (7.2.2),$$

where P_{min} is the minimum of the hysteresis losses, σ_{min} is the tensile stress at which the hysteresis losses acquires the minimum.

7.2.4. Experimental evaluation of the indirect identification of the magnetostriction properties starting from electromagnetic loss measurements.

7.2.4.1. Experimental setup for the identification of magnetostriction.

In order to confirm the validity of the approach described in 7.2.3, magnetostriction measurements were carried out under applied tensile stress. The measurements were accomplished on the setup at the Department of Metallurgy and Material Science (Fig. 7.2.5.).

A 6 mm wide sample is excited by means of the excitation winding and the yoke. All the steel sheets used for the magnetostriction measurement were obtained on the milling machine. One part of the sample is fixed. The second part is in contact with the LVDT sensor. A mechanical load is applied to the sample via a cylinder installed in the hole of the sample. Since the magnetic path length in the sample (240mm x 6mm) exceeds 200

mm the effect of the 2 mm hole can be neglected. A specially constructed pivoting mechanism provides the horizontal mechanical force on the sample.
The flux density in te sample is obtained by integration of the voltage induced in the measurement winding. The measurements are conducted at 3Hz.
It is shown in Fig. 7.2.6 for two successive tests that although the general repeatability of the measurements is satisfactory the LVDT sensor introduces quite considerable noise. This noise was properly taking into account for the identification of the peak to peak magnetostriction $\lambda_{p\text{-}p}$. This peak to peak value is defined by the difference between the maximum elongation λ (corresponding with $B=B_{max}$) and the elongation at the time point where λ takes a minimum, see Fig. 7.6.2.

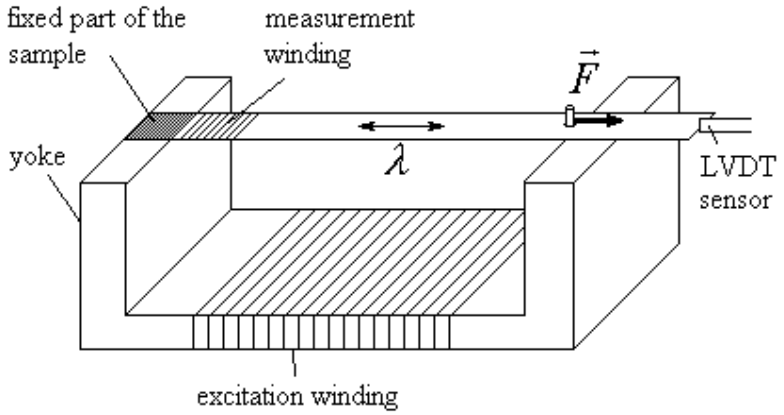

Fig. 7.2.5. A schematic representation of the setup for the measurement of magnetostriction under the applied tensile stress.

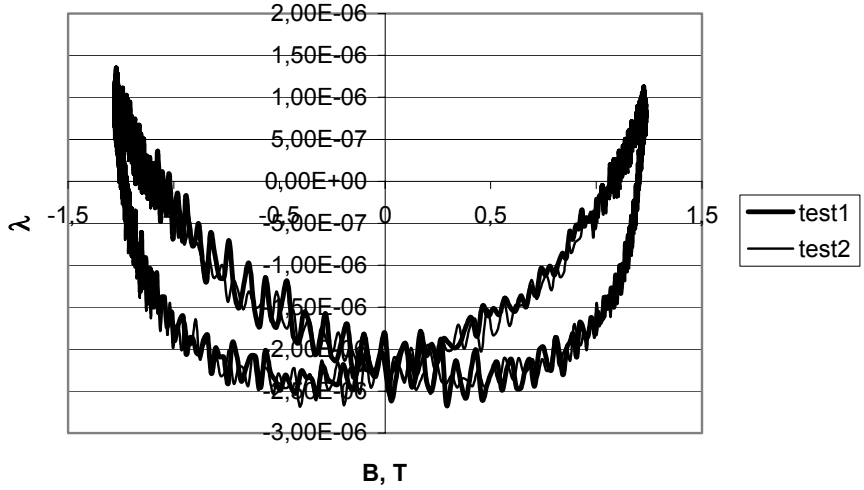

Fig. 7.2.6. The magnetostriction measurements conducted at 2 successive tests on the sample of V850-65 non-oriented electrical steel at σ=0.

7.2.4.2. Measurement results.

The magnetostriction under applied stress is presented in Fig. 7.2.7 and Fig. 7.2.8. It was observed on both materials that the magnetostriction changes sign at a tensile stress between 20 MPa and 25 MPa. A negative value for λ_{p-p} corresponds to a magnetostriction loop where λ at $B=B_{max}$ is negative.

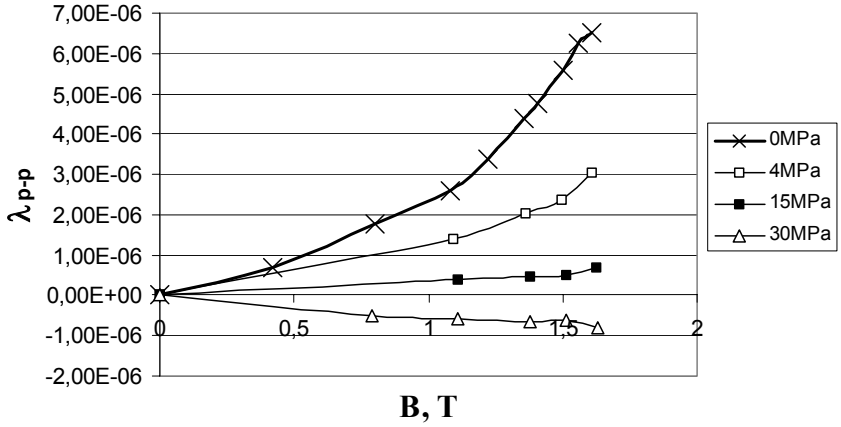

Fig. 7.2.7. Magnetostriction measured on the setup shown in Fig. 7.2.6 under tensile stress on the sample of V850-65 non-oriented electrical steel.

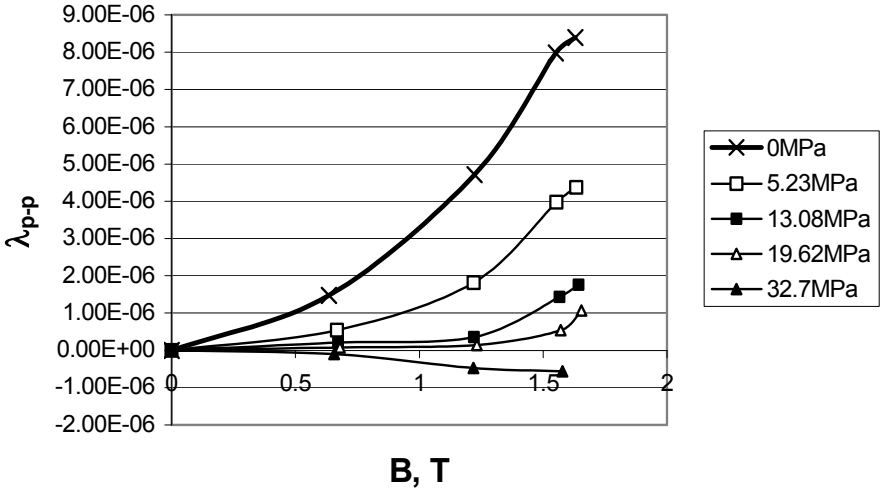

Fig. 7.2.8. Magnetostriction measured on the setup shown in Fig. 7.2.5 under tensile stress on the sample of M330-50 non-oriented electrical steel.

The hysteresis losses were defined as the total losses measured at 5Hz supply frequency.

$$W_h = \frac{P_{total,5Hz}}{f}\rho \qquad (7.2.3),$$

where ρ is the density of the material.

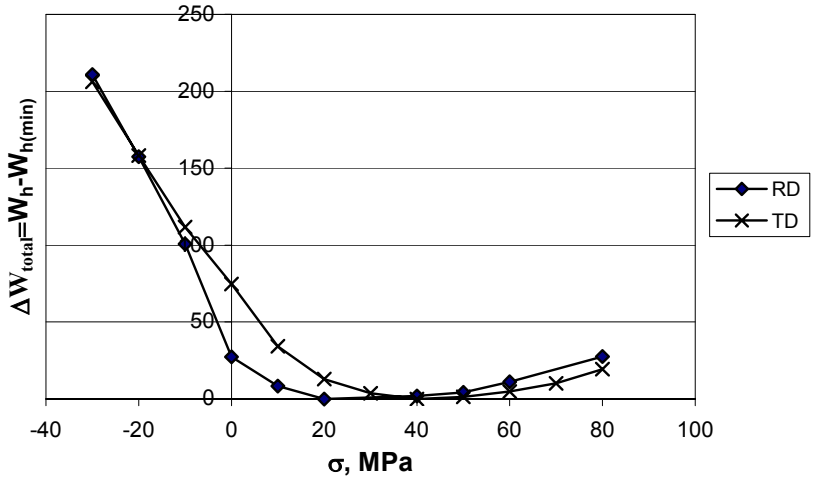

Fig. 7.2.9. Increase of the hysteresis energy (J/m^3) due to the 90^0 domain wall motion at 5Hz under applied stress in the sample of V850-65 steel.

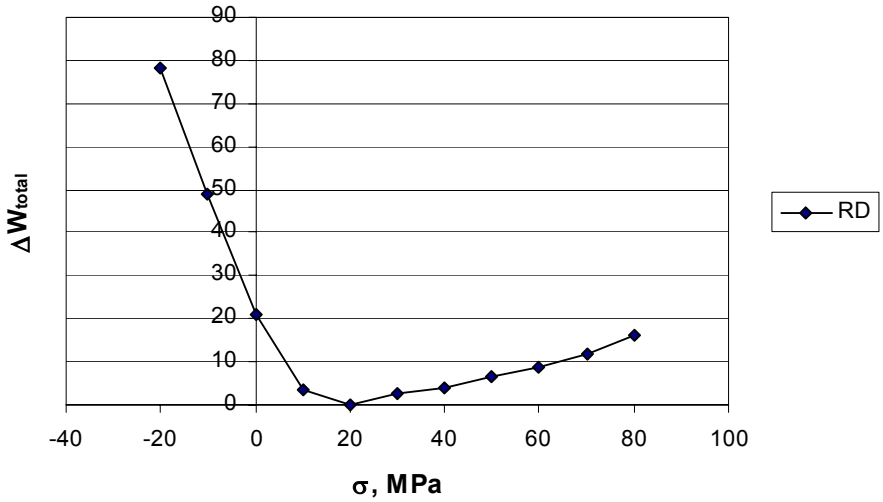

Fig. 7.2.10. Increase of the hysteresis energy (J/m^3) due to the 90^0 domain wall motion measured at 5Hz under applied stress in the sample of M330-50 steel.

7.2.4.3. Experimental evaluation of the indirect magnetostriction evaluation.

The calculated difference of the hysteresis energy is shown in Fig. 7.2.9-7.2.10. According to the approach determined above, the zero magnetostriction should correspond to the minimum of the curves in Fig. 7.2.9-7.2.10, i.e. 20 MPa for the RD. It was experimentally found that the magnetostriction changes its sign between 20 MPa and 25 MPa tensile stress. So the measurement of the total losses under applied stress can at least be used for the determination of the tensile stress at which the magnetostriction becomes zero.
Let us check if we can actually predict the magnetostriction under the stress on the basis of the magnetic measurements. The obtained results are shown in Fig. 7.2.11-7.2.13.

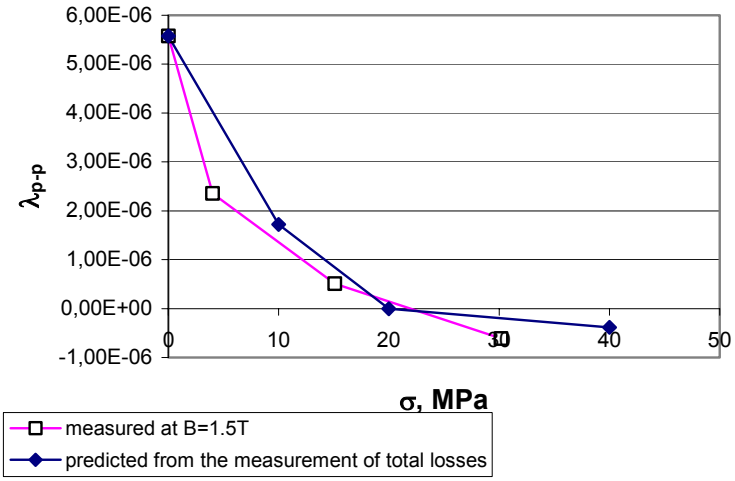

Fig. 7.2.11. Comparison of the measured and predicted dependence of the peak-to-peak magnetostriction on the applied tensile stress on the sample of V850-65 non-oriented electrical steel in RD at B=1.5T.

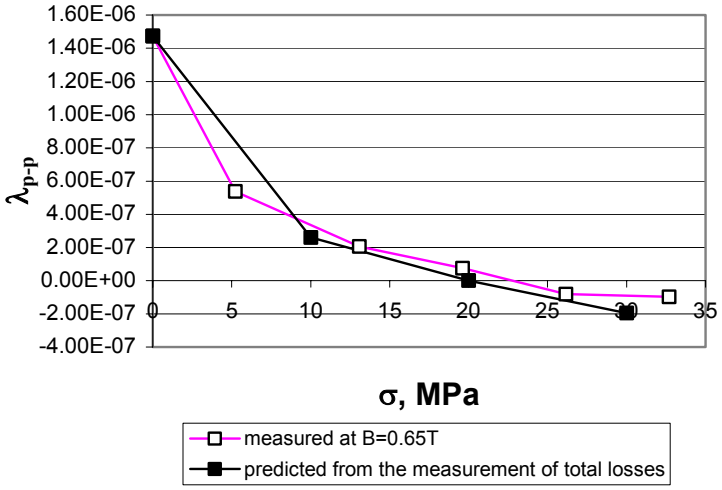

Fig. 7.2.12. Comparison of the measured and predicted dependence of the peak-to-peak magnetostriction on the applied tensile stress on the sample of M330-50 non-oriented electrical steel in RD at B=0.65T.

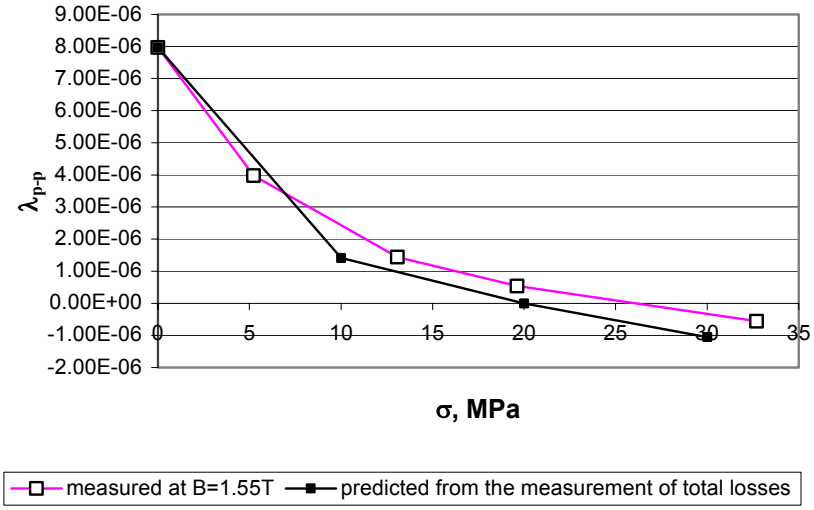

Fig. 7.2.13. Comparison of the measured and predicted dependence of the peak-to-peak magnetostriction on the applied tensile stress on the sample of M330-50 non-oriented electrical steel in RD at B=1.55T.

The difference between the measured and the predicted magnetostriction values is quite low for both investigated materials. It seems that the magnetostriction under the applied stress can be predicted with sufficient accuracy on the basis of conventional magnetic measurements.

Unfortunately it was not possible to do the magnetostriction measurements under compressive stress due to limitations of the measurement setup and excessive bending of the sample. However, having convergence with the predicted magnetostriction values under the tensile stresses, we may assume that there should also be no big discrepancy at the applied compression.

From Fig. 7.2.10 it can be seen that $W_{hyst(\sigma=20MPa)}$-$W_{hyst(\sigma=0)}$=20.808J/m^3 and $W_{hyst(\sigma=20)}$-$W_{hyst(\sigma=-20MPa)}$=78J/m^3. It indicates that a compressive stress of 20 MPa can lead to $\left(W_{hyst\,\sigma=20MPa} - W_{hyst\,\sigma=-20MPa}\right) / \left(W_{hyst\,\sigma=20MPa} - W_{hyst\,\sigma=0}\right) = 3.75$ times increase in magnetostriction if the sample is magnetized in the direction of the stress. According to [Moses2000] the increase of the magnetostriction measured in the direction of the applied 5MPa compressive stress can be up to 80% compared to the unstressed state.
This is important for the analysis of the vibrations of real electromagnetic devices subjected to the production stresses. There may be occasions where the magnetic flux goes along the compressive stress, which is likely to cause additional vibrations and acoustic noise.

In Section 7.1 it was found that the effect of tension applied to the sample is analogous to the effect of the compression applied in the perpendicular direction in the plane of the sample. These effects are summarized in Fig. 7.2.11.

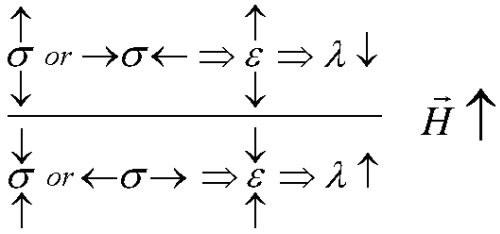

Fig. 7.2.11. A relation between the applied tensile and compressive stresses with respect to magnetostriction.

The effect of the externally applied stress can be summarized as follows:

- If the external applied elastic strain is positive in the direction of the applied magnetic field then there will be a decrease of the magnetostriction compared to the value corresponding to the unstressed state.
- If the external applied elastic strain is negative in the direction of the applied magnetic field then there will be an increase of the magnetostriction compared to the value corresponding to the unstressed state.

These conclusions are made on the basis of the developed approach and the results shown in Section 7.1. The magnetostriction measurements presented here as well as the information published in the literature [Moses2000][Makar1998_1][Yamasaki1996] generally confirm the validity of these conclusions for the case when the mechanical stress and magnetic field are aligned.
It is shown in [Liorzou1999] on a steel cube that compression applied perpendicularly to the magnetic field results in a reduction of magnetostriction. Therefore the statement,

concerning the stress applied perpendicularly to the magnetic field, also appears to be correct.

Due to the restrictions for the geometry of the samples, it was not possible to conduct magnetostriction measurements in the transverse direction. But since the same domain structure is shared between the RD and TD we can extend the developed approach to the evaluation of the anisotropy of magnetostriction in the sample. The following conclusions can be drawn from Fig. 7.2.9:

1. Zero magnetostriction in the TD of the sample of V850-65 non-oriented electrical steel should be expected at σ=40MPa.
2. Since the difference in the hysteresis energy in TD $W_{hyst(\lambda=0,\sigma=40MPa)}$-$W_{hyst(\sigma=0)}$ is 2.74 times larger compared to the RD the analogous difference can be expected in the magnetostriction.

The evaluated magnetostriction anisotropy for M330-50 non-oriented electrical steel equals 1.49. Quite a similar difference with respect to magnetostriction between TD and RD ($\lambda_{TD} / \lambda_{RD} \approx 2$) for non-oriented electrical steel was reported in [Moses2000].
It seems that the anisotropy of the magnetostriction is generally larger compared to the anisotropy of the magnetic properties.

An approach for assembling the sheets in electromagnetic devices consists of the application of compression between 20MPa and 40MPa in the direction normal to the plane of the sheets. From the developed approach it follows that the magnetostriction can be reduced to zero if a specified tension is applied along the magnetic field. This is not immediately clear whether equivalent compression applied perpendicularly to the field will actually result in the same effect. However from the results presented in Fig. 7.1.6-7.1.7 a sufficient reduction of the magnetostriction should be expected.

For the considered materials 30 MPa compression seems to be a good compromise to provide both an improvement of the magnetic properties (Fig. 7.1.3), a reduction of the magnetic anisotropy (Fig. 7.1.4, Fig. 7.1.7) and a decrease of the magnetostriction, which leads to a decrease of the noise of the machine.

Despite clearly positive effects, this approach requires another fixation of the stator core and puts additional pressure on the coating. However, the latter should not be a problem if the laminations are not rotated with respect to each other. This aspect will be discussed in Chapter 9. An axial compression of the stator cores is mostly used in the large power machines.

Conclusions.

The similarity between the effect of elastic tension and compression was considered. It was experimentally illustrated that there is a correspondence between the effect of tension acting along the magnetic field and compression applied perpendicular to the field.

The observed difference in the magnetic properties is due to the impact of the stress on the magnetic domain configuration and particularly on the change of the area of the 90^0 domain walls. This effect can be applied both for the improvement of the permeability

and the reduction of the total losses. If compression is applied perpendicular to the plane of the sheet then a decrease of the magnetic anisotropy can be expected.

The 90^0 domain wall motion is one of the mechanisms defining the magnetostriction of the material during the magnetization. Via the change of the magnetic domain configuration, the external stress can affect the magnetostriction and the magnetic properties of the material. Therefore there has to be a relation between the total loss measurement and the magnetostriction measurement. This leads to a relatively simple approach for predicting magnetostriction under external applied stress. The validity of this approach was confirmed experimentally. The developed approach requires only one magnetostriction measurement at no stress. This data can often be provided by the steel producer. After that, relying on the loss measurements conducted at low frequency, the user can obtain information on the anisotropy of the magnetostriction as well as on the variation of the magnetostriction under the different stress conditions.

Chapter 8. Local magnetic measurements.

Introduction.

Mechanical cutting leads to plastic deformation as it was shown in chapter 3. The consequence of plastic deformation is the nucleation of new pinning sites for the magnetic domain wall motion and the emergence of residual stresses. The multidirectional magnetic measurements together with the X-Ray measurements carried out in Chapter 6 have shown that the plastic deformation results in a compressive stress, which is particularly harmful for the magnetic properties in the direction of plastic deformation. Another confirmation is presented in [Baudouin2002 p. 66]. Here considerable residual stresses were observed at the cut edge of punched samples.
In the area affected by the plastic deformation, the effect of the elastic residual stress is reduced due to the increased pinning. This was clearly demonstrated in Chapter 6. But according to [Hubert2003] even large elastic stresses can lead to irreversible deterioration of the magnetic properties. The presence of a high strain gradient towards the cut edge can lead to additional effects which, unfortunately, cannot be predicted numerically due to the absence of a reliable mathematical procedure.
A discrete approach was used in previous investigations [Ossart2000][Baudouin2002] in order to estimate the effect of the mechanical cutting. The main steps of this approach can be formulated as follows:

Step 1. Measurement of the local microhardness;
Step 2. Relating local microhardness with plastic deformation;
Step 3. Magnetic measurements on a large sample subjected to the uniform plastic deformation;
Step 4. Identifying the local magnetic properties using results from Step 1-3.

Although this approach seems to be applicable to largely deformed zones, it is insufficient for the identification of the general deterioration of the magnetic properties, because it neglects the residual stresses.
This problem can be solved using local magnetic measurements by means of specially constructed sensors presented in Section 8.1.
A numerical investigation on the joint effect of punching and eddy currents is carried out in Section 8.2. The confirmation of the correctness of the measurement procedure is presented.

Section 8.1. The direct local magnetic measurements.

8.1.1. The measurement procedure.

The measurements of the local magnetic induction are carried out using the needle probe method described in detail in Section 4.1. We recall that in order to measure the induction at the edge 2 needles are necessary. For the measurement of the induction in a specific region inside the sample 4 needles can be used. As shown in Fig. 8.1.1.1 the integration (4.1.2) of the voltage V_{2mm} provides at each time point the space average magnetic induction over the area S_1. In order to provide information on the average magnetic induction in the area S_2, the voltage V_{4mm}-V_{2mm} is integrated.

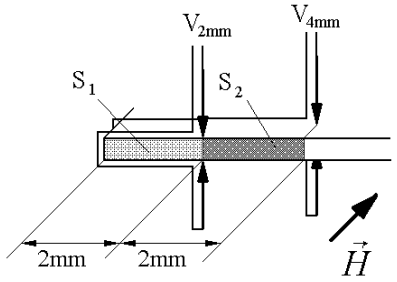

Fig. 8.1.1.1. The principal arrangement of the needles.

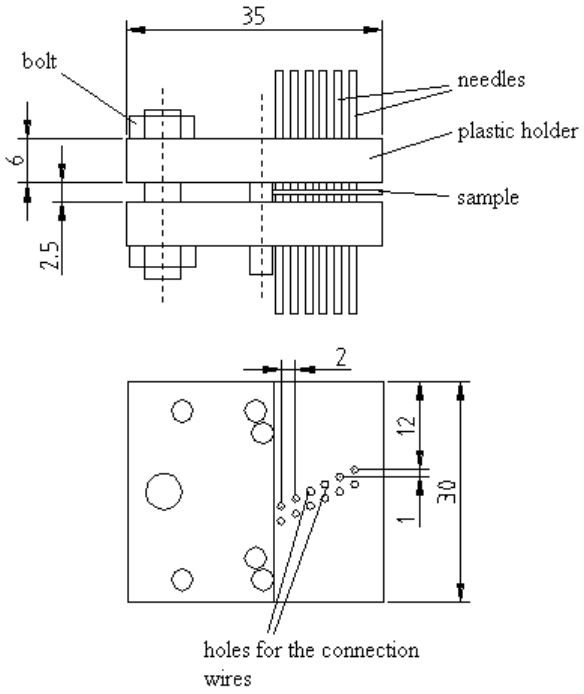

Fig. 8.1.1.2. Side and top view of the needle holder with the needles.

The needle probes are placed in a plastic holder at the top and at the bottom of the sample (Fig. 8.1.1.2, Fig. 8.1.1.3). The top and the bottom parts of the holder are compressed to each other by means of a bolt in order to provide a robust electrical contact between the needles and the sample. Two smaller bolts are used in order to assure the positioning of the holder with respect to the edge of the sample. All the parts of the holder and the needles are made from nonmagnetic material.
During production of the holes the top and bottom parts of the holder were tied together. In this way a symmetric positioning of the needles was provided. The thickness of the holder is 5 mm. This is sufficiently thick in order to avoid a horizontal displacement of the needles. Such thickness also provides a sufficient rigidity of the structure.

The weight of the holder with the needles is just 26 gram. So the effect of stresses in the sample due to the holder can be neglected. The effect of the contact between the needles and the surface of the sample is also negligible as the contact occurs too locally compared to the size of the measurement area. Also, large stress cannot be introduced due to the relative softness of the material of the needle.

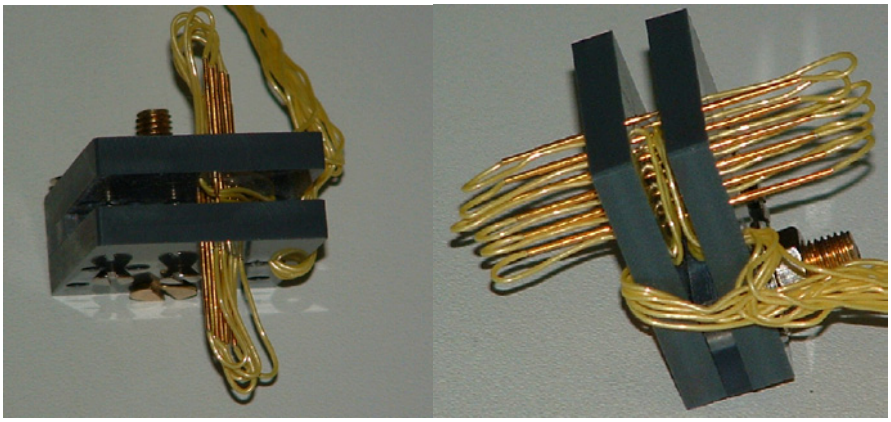

Fig. 8.1.1.3. Photo of the needle holder with the needles.

A single sheet tester (SST) made out of a magnetic circuit without air-gaps and containing an excitation (primary) and a measurement (secondary) winding is used for the magnetic excitation of the sample. This choice was made since this setup has the lowest leakage. Therefore the coupling of the connection wires with a stray field can be assumed to be low compared to the main signal. The connection wires are placed in a similar way with respect to the sample and close to the surface of the sample in order to provide a subtraction of the signal due to the stray field. The connection wires are twisted outside the holder.
In order to keep the magnetic leakage low compared to the main magnetic field, the applied magnetic field does not exceed 400A/m, which is a common field for electrical machinery applications.
An analogous plastic holder was used for the H-coils (Fig. 8.1.1.4).

The eddy currents lead to a distortion of the flux distribution in the sample. Therefore it was decided to use a 3Hz supply frequency.
Consequently, the induced voltage picked up from the needles is very low, which makes it sensitive to noise. Therefore averaging can be used in order to improve the repeatability of the measurements. The noise present in the signal has a zero mean value if infinite number of measurement samples is taken. In practice it is sufficient to achieve a low average value for the noise compared to the measured quantity. Therefore averaging of the signals acquired at the same instant in the period may provide a good approximation for the true value of the unknown variable. In the current investigation the total number of periods used for averaging was varying from 500 to 1000. The latter refers to the smaller values of the measured variables.

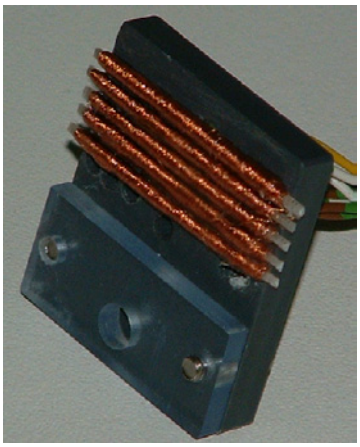

Fig. 8.1.1.4. Photo of the H-coil holder with the H-coils.

If any of the signals acquired from the needles were used for the control of the induction it would have been necessary to apply averaging. However, the control would be too slow. Therefore it was decided to use the voltage induced in the secondary winding around the sample for the control. This signal is more stable and 4 orders stronger. It is practically unaffected by noise.
The excitation winding is supplied from the Kepco power amplifier working in current mode. The corresponding shape control subroutine is described in chapter 5. The signal coming from the output of the acquisition card on the input clams of the amplifier is however not perfectly smooth. This is a sequence of stepwise functions as a result of the digital-to-analog conversion (Fig. 8.1.1.5).

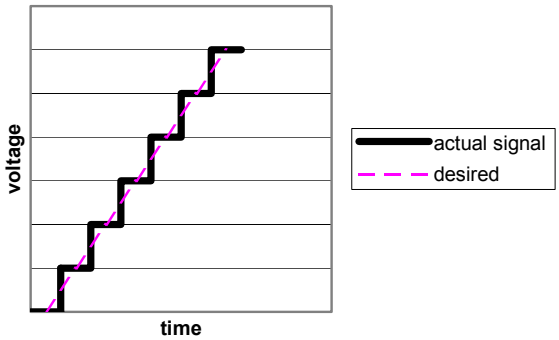

Fig. 8.1.1.5. Comparison of the desired signal and the actual output from the acquisition card.

This problem is not that important if the power amplifier is operating in the voltage mode, because the inductance of the measurement setup suppresses the noise. The filtering capability of the setup increases, of course, with the number of turns of the excitation winding.

When the amplifier is used in the current mode the ripples in the voltage sent from the acquisition card reiterate in the shape of the current. This leads to large voltage ripples defined by $L\frac{di}{dt}$ and eventually to a serious distortion of the induction shape. Moreover, the additional losses due to the noise in the current affect the measurement results. This problem can be solved if a low pass filter is placed at the inputs of the power amplifier [DeWulf2002 p. 77].
A schematic operation of the power amplifier in the voltage and current mode is shown in Fig. 8.1.1.5.

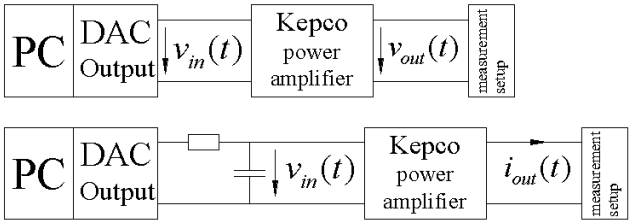

Fig. 8.1.1.5. Operation of the power amplifier in the voltage and current mode.

8.1.2. Experimental results.

8.1.2.1. Experimental results found in literature.

It is worth mentioning what sort of experimental data has been collected by other authors.
In [Nakata1992] conical holes were made on the surface of the sheet of the electrical steel. These holes were filled with conducting paste and twisted wires were attached. The sheet was not subjected neither to mechanical nor to thermal treatment. This makes the measurements truly local. Magnetic measurements were conducted at 50Hz supply frequency. No difference between the local flux density measured from neighboring tips was encountered prior to cutting. This indicates a high accuracy of positioning of the needles. The sheet was then cut using shears for soft steel. He observed a deformation affected zone of more than 10 mm. However, he was not using a blank-holder as the obtained measurement system was probably too delicate to sustain the stresses due to the holder. The quality of the cut was estimated upon the height of the burr, which does not provide enough information on the deformation affected zone.
The size of the deformation affected zone depends on the way the mechanical cutting is carried out. It is shown in [Wisselink2000 p. 98] that the stresses, that are typical for guillotining, can spread to larger areas compared to punching, which indicates an increase of the deformation affected zone. Yet a larger increase can be expected when a blank-holder is positioned far from the sheet or when no blank holder is used at all. An experimental study on this matter is presented in [Pulnikov2003_1]. The data shown there generally correspond to the results obtained in [Nakata1992] for the case when no blank-holder is used. Although an unquestionably good quality and localization of the measurements is achieved in [Nakata1992] it does not provide a complete information on the effect of punching on the magnetic properties of non-oriented electrical steels.

Therefore the purpose of the current investigation is to fill this gap via reproducible non-destructive measurements.

8.1.2.2. Experimental results found at EELAB on a sample shaped by a milling machine.

The measurement system described in the previous subsection clearly provides reproducibility. However the presence of a relocatable holder affects the repeatability of positioning the needles. The shape of the average induction in the cross-section of the sample was controlled using the current supply mode as described in Chapter 5. After adjustment, the current shape is saved in an output file. For the next measurements on the same sample and at the same induction the corresponding output file is loaded. In this way a complete correspondence of the supply is provided.

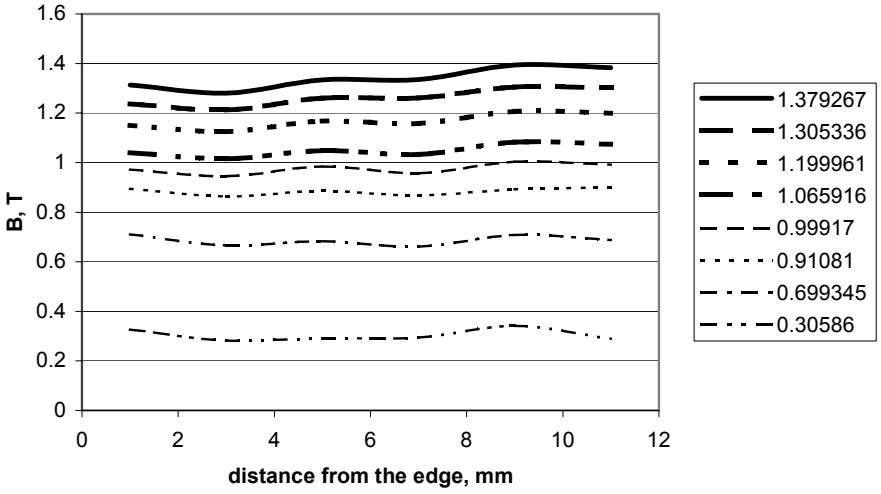

Fig. 8.1.2.1. Local magnetic measurements of the flux density on a sample of V850-65 non-oriented electrical steel cut on the milling machine.

A couple of samples of different electrical steel grades were cut on a milling machine in order to provide the required geometry and at the same time avoid plastic deformation. According to [Rice1988 p. 157] the machining stresses due to milling usually do not extend beyond 0.1mm. Therefore we can expect quite a low effect on the magnetic properties.
The obtained samples were put in the measurement system with an array of needles installed on the surface. The first needle was positioned at 2 mm distance from the edge. The measurement results are shown in Fig. 8.1.2.1 and Fig. 8.1.2.2. The figures corresponding to each line refer to the average induction in the sample. This average induction was measured with the (secondary) measuring winding of the single sheet tester. Whereas straight lines are expected, the figures show small fluctuations, which can be attributed to the slight displacement of the needles (assuming that the magnetic properties are uniform in the sample).

The distributions presented in Fig. 8.1.2.1 and Fig. 8.1.2.2 are quite similar. Thus we may conclude that the measurements reflect the magnetic properties of the sample with 10% accuracy.

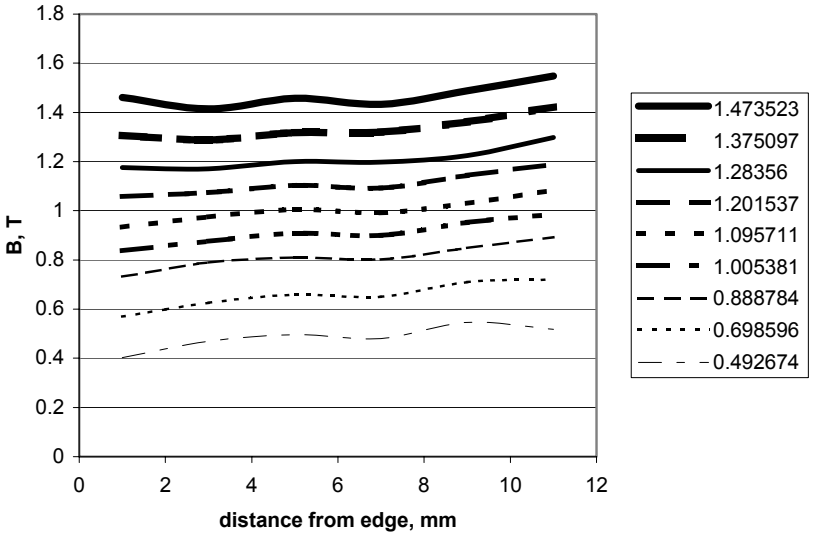

Fig. 8.1.2.2. Local magnetic measurements of the flux density on a sample of V330-50 non-oriented electrical steel cut on the milling machine.

8.1.2.3. Experimental results found at EELAB on a sample shaped by mechanical cutting.

The local measurement of the flux density *B* on a mechanically cut sample of V850-65 non-oriented electrical steel is shown in Fig. 8.1.2.3. The dashed lines in Fig. 8.1.2.3 correspond to the second installation of the sample and the needle probes. This helps to estimate the repeatability of the results.
Very similar results with comparable repeatability were obtained earlier on this material at 50Hz using a different needle holder [Pulnikov2002].
The shape of the integrated local flux densities is shown in Fig. 8.1.2.4. The induction shape differs from the sinusoidal due to the apparent variation of the local magnetic properties.

The local measurements of the magnetic field H, using the pickup coils shown in Fig. 8.1.1.4, revealed practically no deterioration due to punching (Fig. 8.1.2.5). Analogous experimental results were obtained in [Rygal2000].

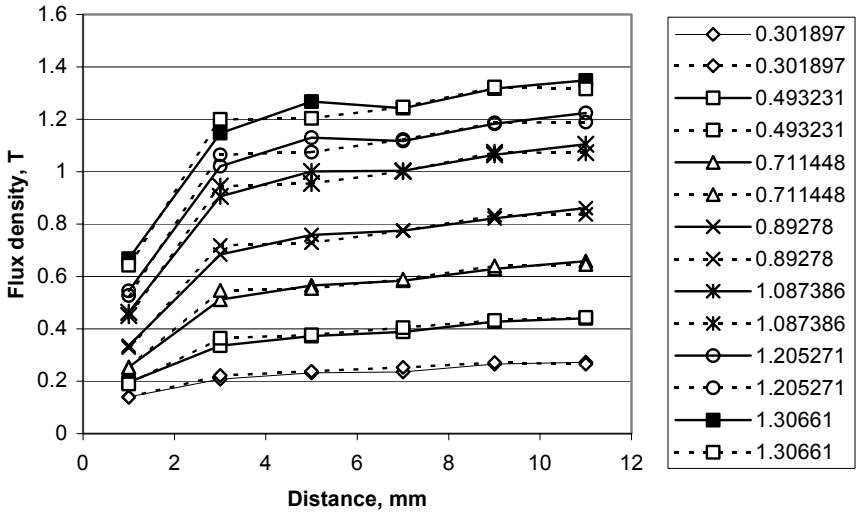

Fig. 8.1.2.3. Local magnetic measurement results on a sample of V850-65 non-oriented electrical steel, mechanically cut.

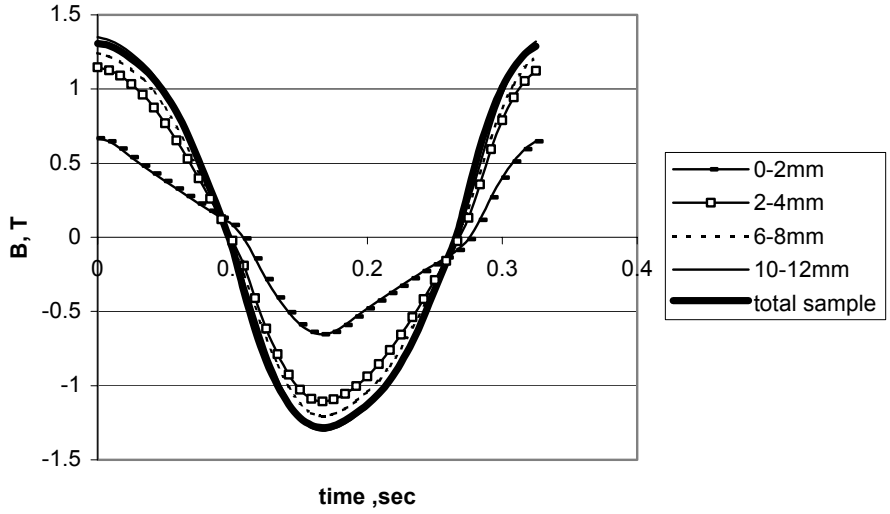

Fig. 8.1.2.4. The local flux density acquired from the different couples of needles at an average induction level of B_{max}=1.308T in the sample at a frequency of 3 Hz.

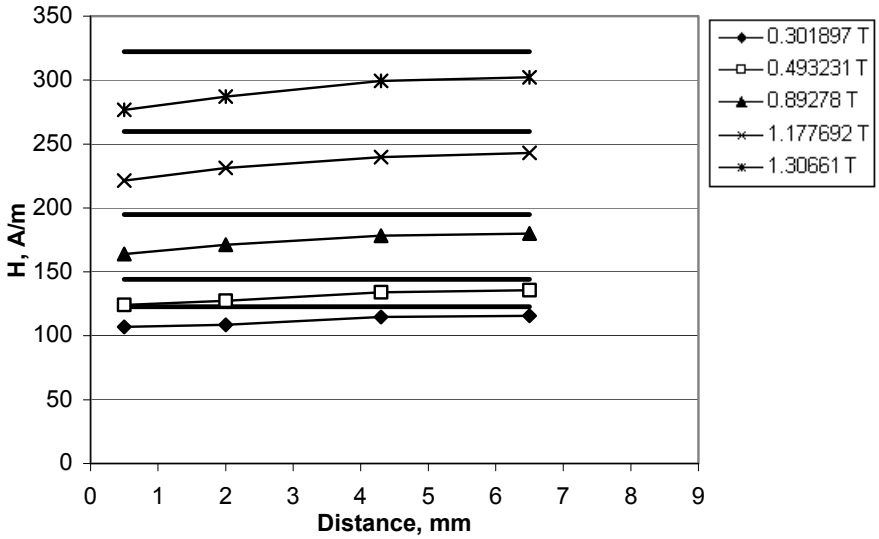

Fig. 8.1.2.5. Local measurements of the magnetic field using H-coils on a sample of V850-65 non-oriented electrical steel (a solid line corresponds to the field value obtained from the excitation current and magnetic path length).

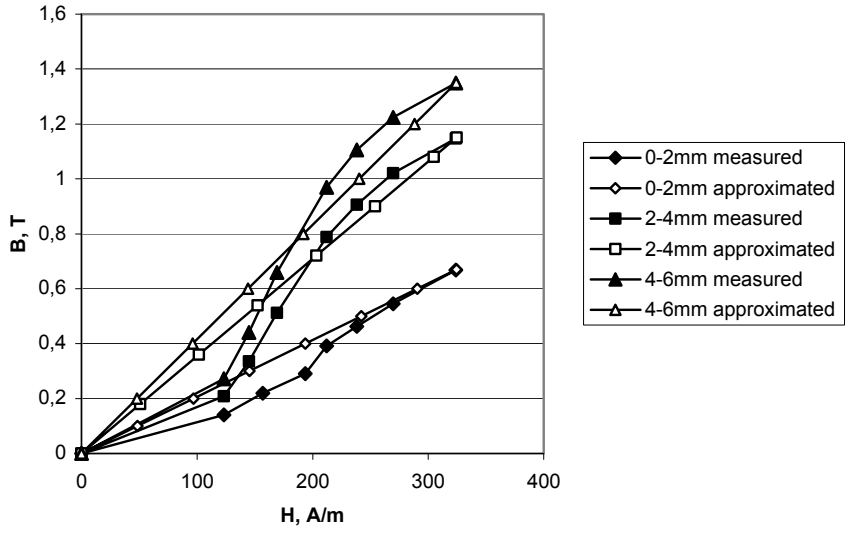

Fig. 8.1.2.6. The magnetization characteristics obtained using the local magnetic measurements.

Direct local measurements using search coils wound through the small holes in the sample were conducted in [Loisos2003_3]. The variation of the flux density observed there was within 5mm.
A lot of indirect investigations on the effect of mechanical cutting were carried out in the last few years [Moses2000_2][Boglietti2001][Schoppa2000_1]. The measurement procedure described in [Moses2000_2][Boglietti2001][Schoppa2000_1] was practically the same. The annealed sample was cut in two halves. Then each of the obtained pieces was cut again and so on. During each stage of material separation the magnetic measurements were performed with all pieces next to each other clamped by the yokes of the single sheet tester. So the total cross-section of the sample remained unchanged. The final width of the pieces in [Moses2000_2] was 12.5mm and 10mm in [Boglietti2001].
According to [Boglietti2001] the increase of the hysteresis losses is proportional to the total cut length. The analogous results are reported in [Moses2000_2]. It is known [Nakata1992] that plastically deformed material is less sensitive to the additional deformation compared to the undeformed state. So overlapping of large affected zones (Fig. 8.1.2.7) would definitely distort the proportionality of the growth of the hysteresis losses. Since it was not observed, the size of the affected zone does not exceed half of the width of the strips obtained after the last cut.
Therefore it can be concluded that the zone where the magnetic properties are deteriorated is within 5mm [Boglietti2001] or 6.13mm [Moses2000_2]. The experimental results presented in this section confirm these results.

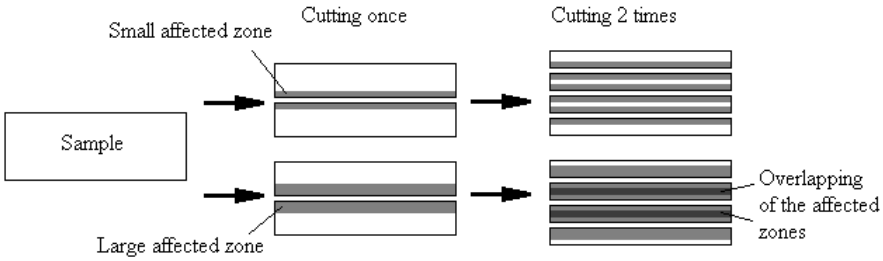

Fig. 8.1.2.7. The effect of multiple cutting.

It is worth noting that there is a clear inconsistency between the zone affected by plastic deformation (Chapter 3) and the zone where the magnetic properties are deteriorated.
The local BH-loops, measured with the needles and the excitation current, at the different induction levels (Fig. 8.1.2.8 and Fig. 8.1.2.9) intersect at one point, which is an indication of the presence of mechanical stresses in the electrical steel [Bulte2002]. If considerable plastic deformation is present such intersection is not observed according to the results presented in [Pulnikov2003_2].
So the dominant effect on the magnetic properties is due to the elastic residual stresses rather than due to the pinning effect of the dislocations.

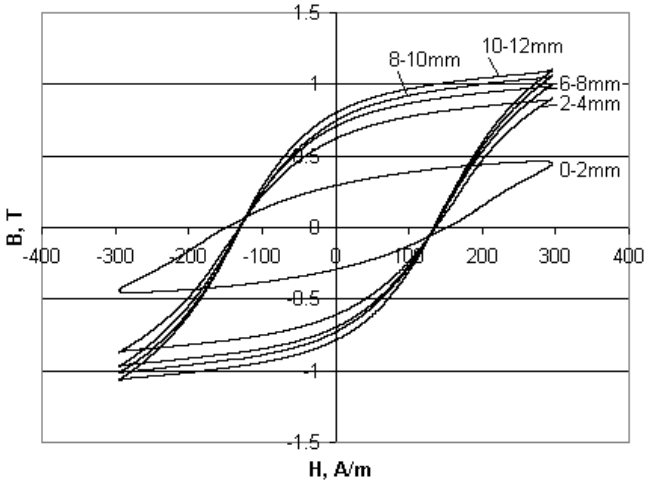

Fig. 8.1.2.8. The local BH-loops acquired at B_{max}=1.087T over the total cross-section of the sample.

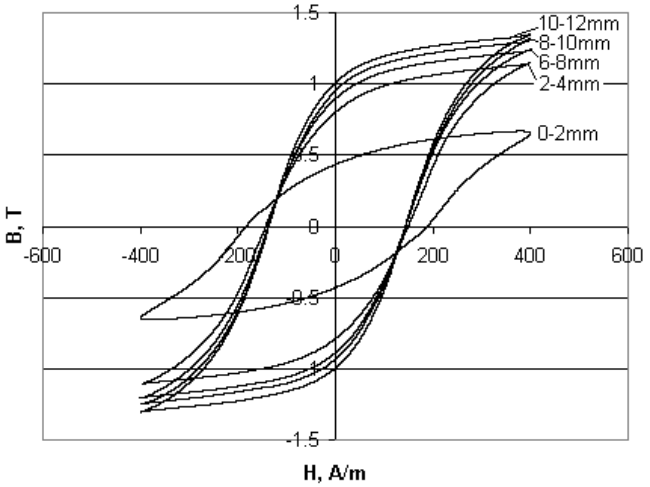

Fig. 8.1.2.9. The local BH-loops acquired at B_{max}=1.306T over the total cross-section of the sample.

8.1.3. Suggestions.

The effect of punching is harmful for the magnetic properties of the sheets. The importance of this effect increases with a decrease of the width of the sample. So if there is no alterative to the mechanical cutting the width of the sample should not be less than 100mm, since it would keep the affected area within some 10% of the total volume of the sample.

Another solution is the application of a stress-relief annealing (at 800^0C) as this reduces the residual stresses and affects the dislocation structure (Chapter 2). Here the

microstructure of the material stays intact, which is important for the investigation of the magnetic properties. Then only a small zone at the edge would likely to remain deteriorated with respect to the magnetic properties due to pinning of the magnetic domain walls. Unfortunately the effect of the stress-relief annealing could not be studied due to the emergence of an oxidation layer that is too strong for the needles. So exact figures concerning the reduction of the affected area by annealing are unknown at the moment. It can be assumed to be equal to the size of the zone affected by the strain exceeding 5%. According to the numerical simulations of punching presented in Chapter 3 this zone is equal to 10% of the thickness.
We may compare these results with the material properties when another means for material separation is used, e.g. milling. In the current investigation a sample was fixed between two 5mm thick steel sheets during milling. The machine should work at a low speed in order to avoid an excessive heating of the sample. According to [Schoppa2003_2] abrasive waterjet cutting also provides practically no effect on the magnetic properties of the sheet. However it requires more complicated equipment.

Section 8.2. The joint effect of punching and eddy currents on the local properties of the sheet of non-oriented electrical steel.

We recall that the edge of the electrical steel sheet is affected by punching as it was experimentally found in Section 8.1. Moreover, due to the electrical conductivity, eddy currents are induced in the electrical steel when enforcing a time dependent magnetic excitation. In this section we want to show by numerical experiments that the local measurement approach of the previous section is applicable for the definition of the affected zone only at low frequencies. Indeed, at high frequencies, due to the presence of high eddy currents, there is an additional non-uniformity of the local flux density through the thickness of the sample, in particular in the affected zone under consideration. This additional non-uniformity due to the eddy currents must be avoided when studying the modifications of the local magnetic properties due to the deformation.

In case that we perform measurements at high frequencies, the obtained ‘local’ magnetic properties refer to an average behaviour of the material between the two or four needles used during identification. This is confirmed by the numerical experiments described in this section.

The presented investigation will be carried out numerically using the FE formulation described in Section 4.1. The boundary conditions as well as the dimensions of the problem are shown in Fig. 8.2.1. The magnetization curves, corresponding with the experimental results of Fig. 8.1.2.6 are assigned to 0-2 mm, 2-4 mm and 4-10 mm regions of the model. The computations take into account the non-linearity of the magnetic properties.

Four point measurements, done at the laboratory, show that electrical conductivity of the sample decreases up to 30% at strain above 20%. This reduction is probably due to increase of amount of lattice defects which impede the electric current. A large strain is observed in a very small area of the cut sheet as shown in Chapter 3. The major deterioration of the magnetic properties at the cut edge is due to the residual stresses,

which do not affect the electrical properties of electrical steel. Therefore we assume that the electrical conductivity is constant in the whole cross-section of the sample.

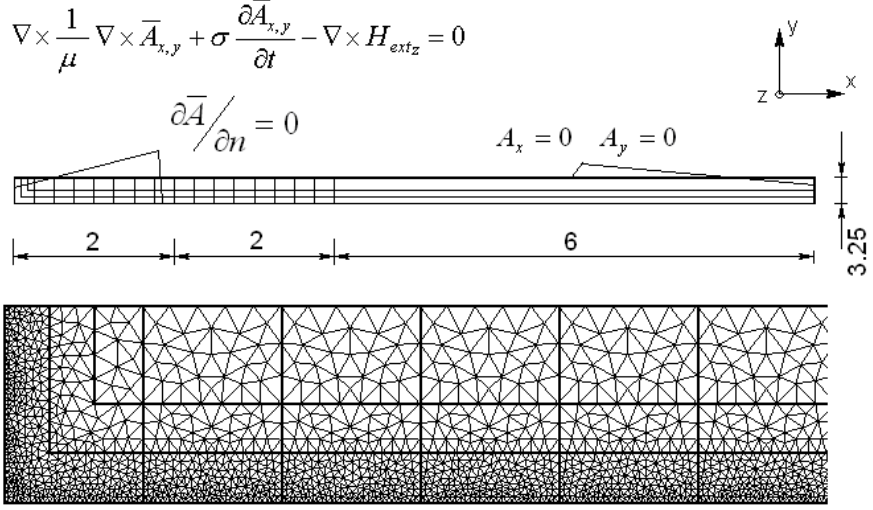

Fig. 8.2.1. The geometry of the problem and the boundary conditions.

The time-step simulation was carried out with the imposed magnetic field varying according to a sinusoidal law: $H_{ext}(x,y,t)=H_{extz}(t)=H_m \sin\omega t$, where H_m=300A/m. The simulation results are shown for the specific time instant where the average flux density reaches its maximum in the second (Fig. 8.2.2) or in the tenth period (Fig. 8.2.4). A larger number of periods was used for the high frequencies in order to reach the steady state as suggested in [Chevalier2000_1]. The distributions of the flux density and magnetic field are shown in Fig. 8.2.2.-8.2.7.
The integration of the flux density over a specified area provides the total flux through that specified area at each time point. When considering the total flux as a function of time, the maximum flux in the sample can be identified. Dividing this maximum value by the cross-section of the sample gives the peak value of the average flux density in the sample, denoted by $B_{av,p}$.

The peak value of the average flux density $B_{av,p}$ in the sample at 50Hz frequency is equal to 1.071T. The analogous values at f=400Hz and f=2000Hz are $B_{av,p}$=0.682T and $B_{av,p}$=0.275T accordingly. The flux density on the surface of the sample is the same in all three cases. But due to the action of the eddy currents, there is a phase shift between the local magnetic induction at the surface of the sample and the local magnetic induction in the center of the sample. They even can point in the opposite direction at certain moments, see e.g. Fig. 8.2.4, 8.2.6.

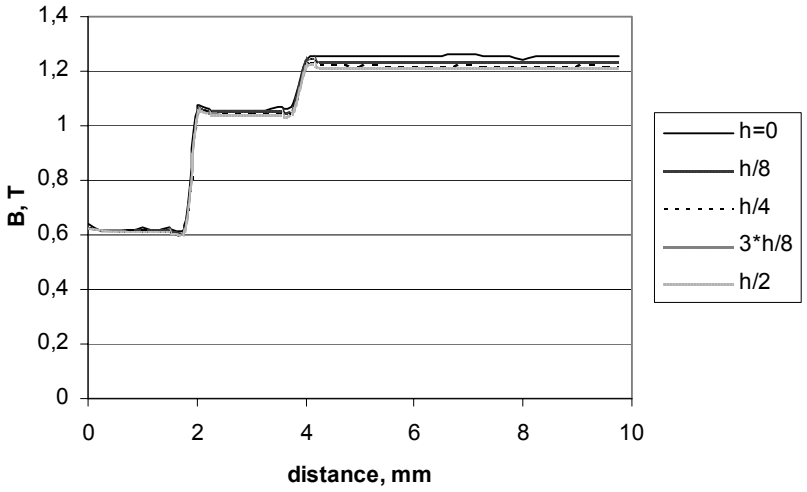

Fig. 8.2.2. The flux density distribution obtained at 50Hz supply frequency at t=0.205sec (time point where the total flux is maximal).

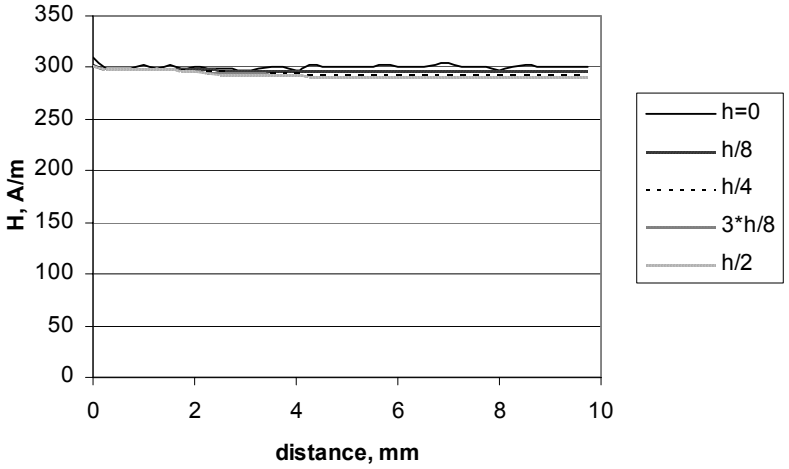

Fig. 8.2.3. The magnetic field distribution obtained at 50 Hz supply frequency at t=0.205sec (time point where the total flux is maximal)

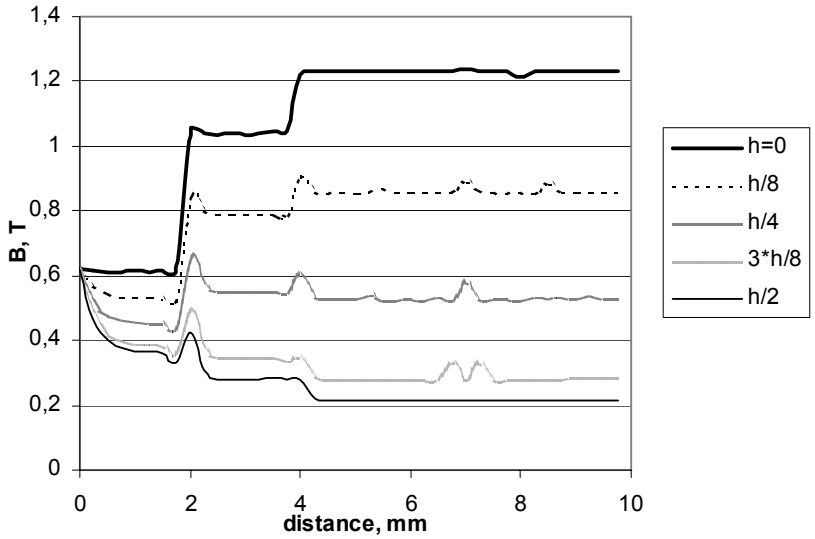

Fig. 8.2.4. The flux density distribution obtained at 400 Hz supply frequency at t=0.0256sec.

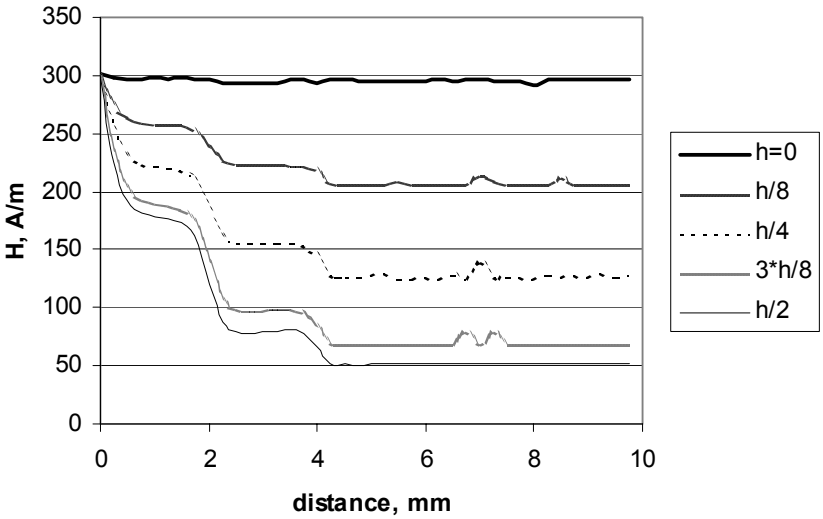

Fig. 8.2.5. The magnetic field distribution obtained at 400 Hz supply frequency at t=0.0256sec.

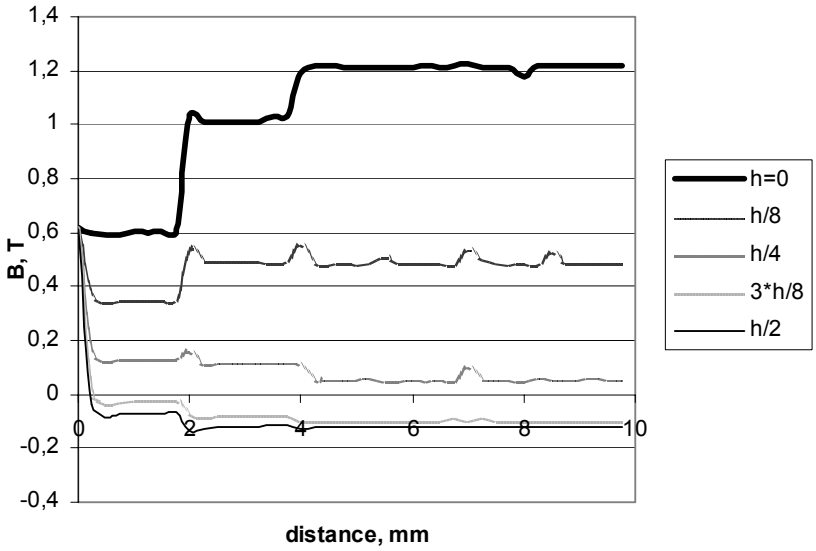

Fig. 8.2.6. The flux density distribution obtained at 2000 Hz supply frequency at t=0.0051sec.

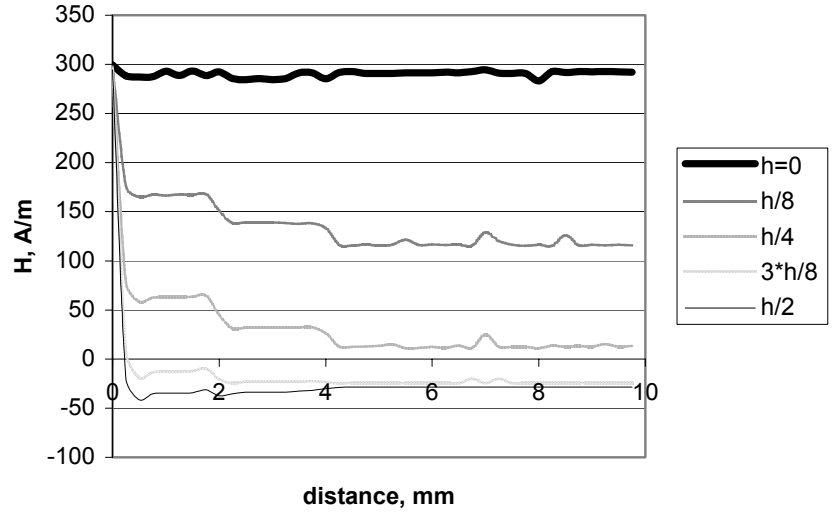

Fig. 8.2.7. The magnetic field distribution obtained at 2000 Hz supply frequency at t=0.0051sec.

These numerical computations allow us to evaluate the accuracy of the local magnetic measurements. From the numerical computations we may evaluate:

- the magnetic flux through the rectangular cross-section defined by the position of the needles using the local B-values obtained numerically;

- the local magnetic flux by carrying out a time integration of the calculated induced voltage on the surface of the sample between fictive needles.

In this way we can reconstruct the local B-measurements numerically and see whether there is a correspondence between the flux density obtained from the needles and the local flux density averaged out over the rectangular cross-section under the needles.

The shape of the 'calculated' induced voltage between the couple of needles (one on top and one below the sample) installed at 0.5 mm distance from the edge is shown in Fig. 8.2.8. It can be seen that the signal is very low. The disturbances in the signal in Fig. 8.2.8. indicate a transient process. However the shape of the induction obtained from integrating the induced signal is sufficiently smooth, see Fig.8.2.9.a. There is a certain discrepancy between the B(t) obtained numerically by the needle probes and the B(t) obtained by averaging at each time point the local B-values within the rectangular cross section defined by the needles. A considerable error appear as the needles are to close to the cut edge. Indeed, in the 0.25 mm region, the eddy currents are not parallel to the surface of the sheet, see e.g. [DeWulf2002 p. 33].

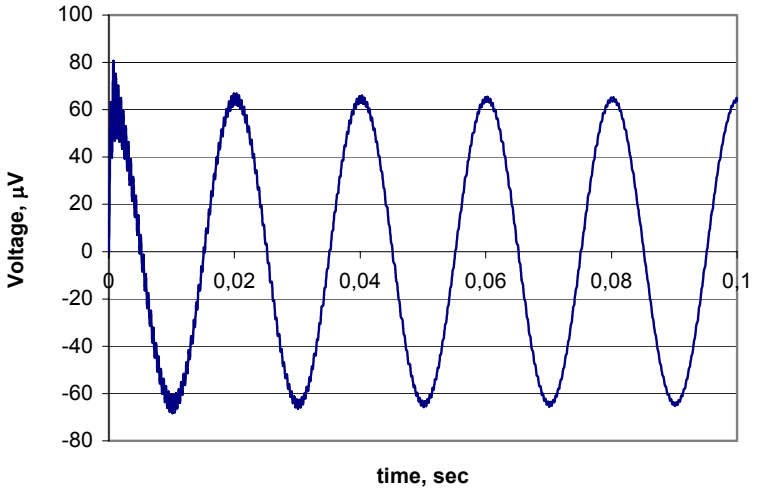

Fig. 8.2.8. The induced voltage on the couple of needles installed at the top and at the bottom of the sample at 0.5mm from the cut edge at f=50Hz, resulting from the numerical computations.

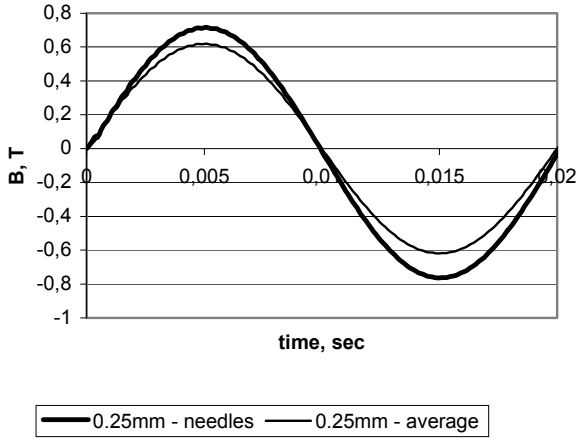

Fig. 8.2.9.a The integrated flux density corresponding to the induced voltage shown in Fig. 8.2.8 assuming a rectangular cross-section.

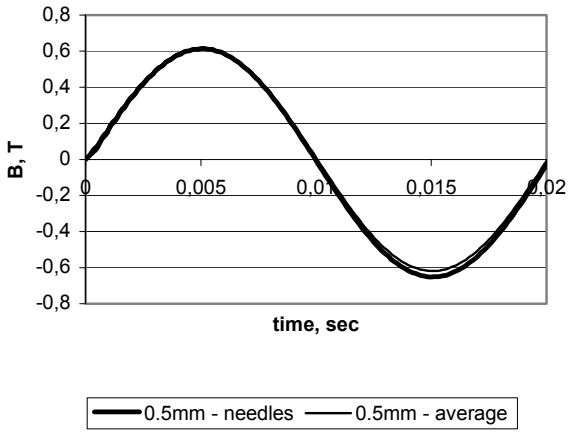

Fig. 8.2.9.b The integrated flux density corresponding to the induced voltage shown in Fig. 8.2.8 assuming a rectangular cross-section.

Similar results are shown in Fig.8.2.9 b when the needles are positioned at 0.5 mm from the cut edge. Now, there is a correspondence between the B(t) obtained by the needle probes and the B(t) obtained by averaging at each time point the local B-values. This numerical result for the 0.5 mm positioning suggests that local magnetic measurements using the needle principle is justified.

If the distance between the couple of needles and the edge increases the variation of the flux density can be obtained. It is shown in Fig. 8.2.10 that after initial decrease a gradual increase of the integrated flux density is observed.
Due to the local deterioration of the magnetic properties a difference can be seen with analogous distribution in the sheet with uniform magnetic properties (Fig. 4.1.10).

However the effect of a local degradation of the magnetic properties is stronger in case of lower frequency.

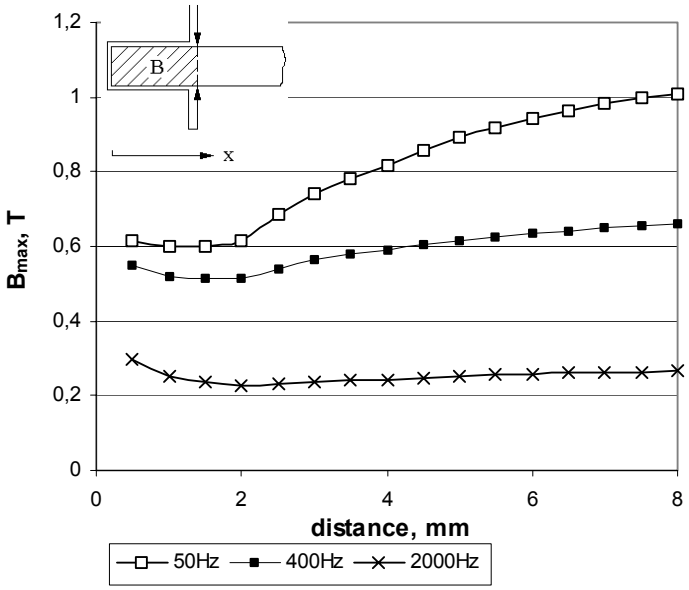

Fig. 8.2.10. The effect of the supply frequency on the measurement with the needles (V_b in Fig. 4.1.13) at the edge of the sheet.

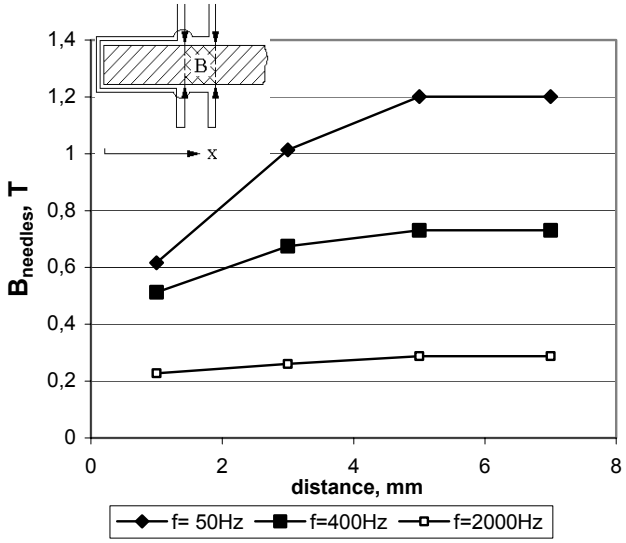

Fig. 8.2.11. The effect of the supply frequency on the measurement with the needles (V_a-V_b in Fig. 4.1.13) at the edge of the sheet.

Let us simulate now the 4-needle measurements. The integrated flux density values are presented in Fig. 8.2.11. Like in case of the real measurements, the calculations were performed with 2mm step. For all the frequencies a complete correspondence was encountered between the flux density integrated from the induced voltage and the flux density integrated directly from the vector potential distribution over the corresponding rectangular areas of the sheet.

This correspondence allows concluding that the eddy currents do not lead to errors in the measurement. However the flux density picked up by the needles equals the average flux density in the corresponding area.

But we must remember that at high frequencies the term "local induction measurement" is inappropriate to the needle-probe method, because averaging of highly non-uniform flux density distribution takes place when the voltage induced in the needles is integrated. So the reduction of the effect of punching shown in Fig. 8.2.11 does not mean that punching becomes less harmful for the magnetic properties. Here we can talk about error averaging that decreases along with a reduction of the frequency. In fact, the apparent reduction of the effect of punching is in correspondence with the experimental observations presented in [Loisos2003_3].
Since even at 50 Hz slight non-uniformity of the flux density is encountered (Fig. 8.2.2), the choice of a 3Hz supply frequency, as in section 8.1, seems to be justified.

Conclusions.

In this chapter the experimental procedure was developed for the direct evaluation of the effect of mechanical cutting on the magnetic properties of non-oriented electrical steels. No deterioration was observed on the samples prepared on the milling machine.
The size of the affected zone in the punched sample can be assumed to be 5 mm. Apparently, the difference between the deformation affected zone defined in Chapter 3 and the zone where the magnetic properties are deteriorated is due to the presence of elastic residual stresses. The existence of the intersection points in the corresponding BH-loops is the indirect confirmation of this conclusion.

The validity of the measurement procedure was confirmed by the numerical analysis. Computations revealed a reduction of the effect of punching with an increase of the supply frequency when applying a sinusoidal magnetic field at the surface of the sheet with the same amplitude. This reduction occurs due to the non-uniform distribution of the flux density in the cross-section of the sample. It is evident that when applying a total sinusoidal magnetic flux, similar results will be obtained. Indeed, when applying a total magnetic flux, the flux will be pushed to the middle of the sample due to the deterioration of the magnetic quality near the cut edge. However the strong eddy currents due to the higher frequency will lead to skin effects, pushing the magnetic flux back to the cut edge.
For this reason, the low frequency local measurements are preferable as they provide a more adequate information on the local magnetic properties of non-oriented electrical steel.

Chapter 9. Effect of punching on the magnetic properties of electromagnetic devices.

Introduction.

It was experimentally confirmed in Chapter 8 that mechanical cutting results in a local deterioration of the magnetic properties of the sheet at the cut edge. But this is not the only consequence of cutting. Indeed, the shape of the cut edge is distorted as was demonstrated in Chapter 3. These imperfections of the profile of the sheets result in some additional effects when the laminations are stacked into the magnetic core. The investigation of these effects supported by numerical simulations is carried out in Section 9.1.

Electrical steels are used in a wide variety of electromagnetic devices. These devices include transformers, rotating machines, actuators and many others. There are also different types in each of the mentioned classes of devices. In order to evaluate the effect of the production stresses on the performance of electromagnetic devices we decided to concentrate on induction motors. This choice was made for two reasons. According to [Hill-Cottingham2003] small induction machines consume about 50% of the generated electricity in the industrialized countries. So even a little improvement in the designs of these machines has a considerable impact. Secondly, the induction machine is very sensitive to the changes of the geometry of the magnetic system (e.g. the air-gap), since it is excited by the primary current. In the design approaches, developed in industry, the empirical knowledge on the general change of the magnetic properties of the core allows to take into account the production effects. However the use of this approach is limited to specified ranges of dimensions and electromagnetic loads, which considerably confines the flexibility of this procedure. As a rule, the empirical method is inapplicable to new structures. Construction of prototypes can secure the designer from mistakes, but it makes the design costly and slow.

In order to account for the complex geometries new numerical methods have been developed in the last few years. These methods are capable of sufficiently accurate prediction of the behaviour of the machine if operating conditions and material properties are properly assigned. However the problem of assigning the proper magnetic properties during numerical computations is not yet completely solved.

The non-uniformity of the magnetic properties within the laminations of electromagnetic devices is usually neglected. As a result, this can lead to a systematic discrepancy between the expected and observed parameters of the machine. On the other hand, the explicit introduction of all these aspects into the design optimization techniques [Liuzzi2003][Nam2003] would considerably retard the whole calculation process.

Therefore the aim of the investigation, described in Section 9.2, is to propose a simple approach that would allow a sufficiently accurate handling of the production stresses during design.

Section 9.1. The effect of mechanical cutting on the magnetic properties of the core.

The effect of the mechanical cutting of the sheet results not only in a deterioration of the magnetic properties at the edge of the sheet. It also distorts the shape of the sheet as was demonstrated in Section 3.3. It is shown in [Nakata1992][Ossart2000] that a stress-relief

annealing sometimes used after punching helps to recover the original magnetic properties of the sheets. But this does not solve the problem of the distortion of the cut edge.

As it was shown in Section 3.3 the distortion of the shape depends on the parameters of the punching, more precisely on the quality of the cutting tools and the clearance. The use of lubricants allows maintaining a good quality of the tools. We recall that the most known problem arising from the shape distortion is the burr. A sharp tip of the bur can damage the insulating coating of the sheet. If the burr penetrates through the insulation then the eddy current losses can increase considerably due to the short circuit effects between the neighboring laminations of the magnetic core of the device. These losses lead to an excessive heating of the core and also have a negative impact on the performance of the electromagnetic device.

A possible positioning of the sheets in the stack is shown in Fig. 9.1.1.

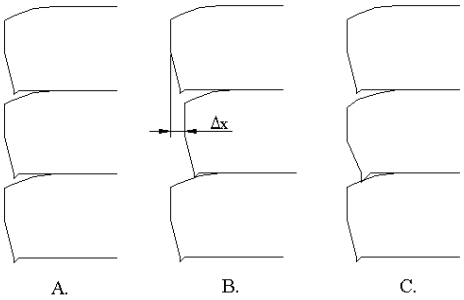

Fig. 9.1.1. Cross-sections of the stack.

If the burr is extensively large then grinding the sheet seems to be the only possibility to maintain the insulation between the laminations. However if the sheets are cut the same way using the same setting of punching device and they are not grinded, then the rollover can secure the coating from the contact with the burr of the neighboring sheet (Fig. 9.1.1A) unless the sheets are stacked inaccurately (Fig. 9.1.1B).

In rotating machines the stator sheets are often rotated with respect to each other. This is done for different reasons depending on the power of the machine. In small motors it is implemented in order to reduce the effect of the magnetic anisotropy of the electrical steel. In large motors, the whole stator sheet cannot be punched, because the external diameter exceeds the width of the sheet of electrical steel. So sectors of the stator laminations are punched. Each next lamination placed in the core is rotated over minimum one tooth with respect to the previous lamination in order to reduce the effect of the joint between neighboring sectors.

Although this procedure has certain benefits, it increases the possibility of a contact between the coating of one sheet and the burr of another sheet (Fig. 9.1.1C). This problem can be avoided via the use of a smaller clearance, as it would reduce the uncertainty of the profile of the sheet.

More radical measures need modification of the punching facility, which was considered in detail in Chapter 3. For instance, the use of fine-blanking is known to allow a complete elimination of the burr. Another alternative is the use of the laser cutting. If the cutting parameters are well defined then a good quality of the cut edge can be obtained [Baudouin2002 ch. 4]. However it also leads to oxidation and a

generally larger affected zone compared to mechanical cutting. Another disadvantage of the fine-blanking and laser cutting is their high cost.

Avoidance of the contact between the coating and the burr allows the decrease of the thickness of the coating. According to the results presented in [Loisos2003_2] the thickness of the coating, required to provide insulation with sufficient safe margin, has to be just 1-5 μm. In fact, there are new types of coatings which have a thickness below 5 μm [Coombs2001]. But it appears that in practice thicker coatings are used. For example, the thickness of the organic coating on the V830-65 non-oriented electrical steel is 45 μm, which is clearly a precaution for the burrs. On the other hand, a reduction of the thickness of the coating can result in a more than 5% increase of the filling factor of the core. It is also worth noting that a thinner coating is also better with respect to the heat transfer in the normal direction with regard to the plane of the sheets in the core. This is beneficial both for the core and for the windings.

In electrical machines the air-gap separates the static and rotating parts. The sheets on both parts are generally punched. The distortion of the profile of the sheets is usually neglected, which results in the underestimation of the actual size of the air-gap.

Consider the most typical profile of the sheet observed after punching with 40% shear zone, 40% ductile fracture zone and 20% roll-over. This profile was obtained after averaging the profiles observed in the literature [Emura2003][Wisselink2000][Brokken1999] and those presented in Section 3.3. Taking into account a possible diversity of the relative positions of the stator and the rotor stacks the following configurations of the air-gaps can be encountered (Fig. 9.1.2).

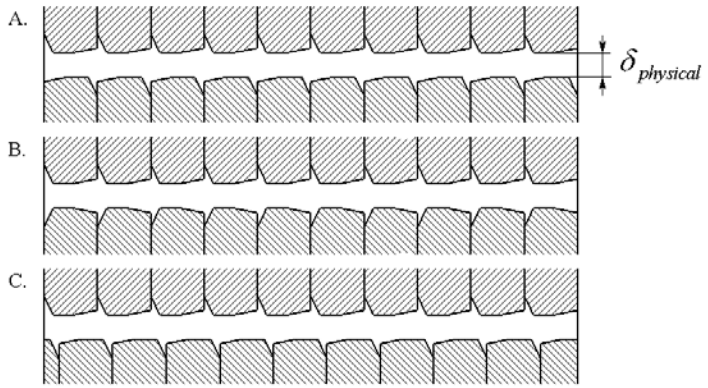

Fig. 9.1.2. Relative positions of the stator and rotor sheets (thickness 0.65mm) in the air-gap (0.3mm) of the electrical machine.

It can be expected that the equivalent air-gap is larger. In order to estimate the difference, FE magnetostatic computations were carried out with the boundary conditions assigned as shown in Fig. 9.1.3. The permeability of the stack is assumed to be infinite.

All the 3 cases, shown in Fig. 9.1.2 were simulated with the same physical air-gap value and the same boundary conditions. A comparison with the rectangular configuration of the air-gap was conducted.

As is shown further the flux lines in any of the cases (Fig. 9.1.2) differ from straight lines. So a solution of the problem either requires the use of the appropriate boundary

conditions [Gyselinck2000] or an increase of the length of the problem such that the number of considered laminations would have been sufficiently large.
A sufficiently large repetition of geometry diminishes the effect of the error arising due to the inappropriate boundaries.

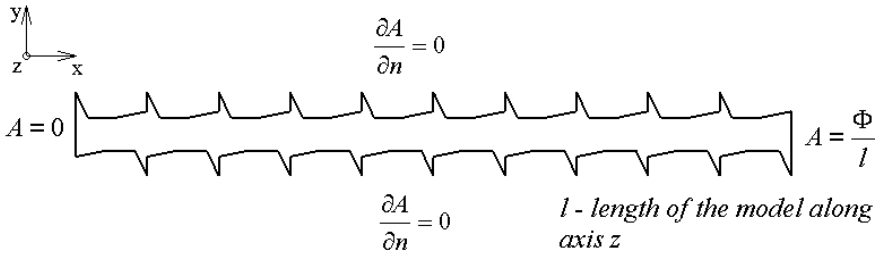

Fig. 9.1.3. Relative positions of the stator and rotor sheets (thickness 0.65mm) in the air-gap (0.3 mm) of the electrical machine (2D nodal FE formulation was used with unknown the amplitude of the magnetic vector potential. Here $\overline{A} = A \cdot \overline{1}_z$.)

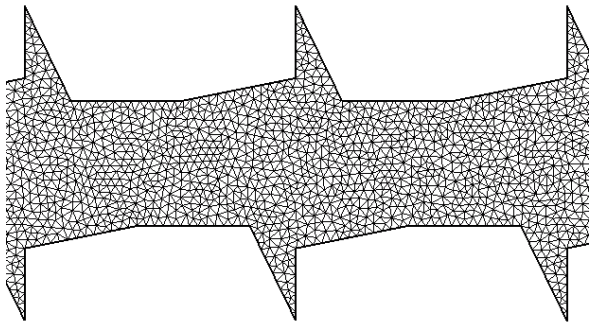

Fig. 9.1.4. Triangular finite element mesh.

In all cases (A, B and C in Fig. 9.1.2) the number of nodes of the triangular mesh exceeded 5400 and the number of elements was larger than 10000 (Fig. 9.1.4).
The equivalent air-gap provides an equivalent inductance. The relation of inductances can be obtained using the approach introduced in Chapter 4.
With respect to the reluctance of the air-gap it can be expected that case B (Fig. 9.1.2) and case C are the most and the least favourable respectively. In case B the most prominent parts of the laminations are situated right across each other, while in case C they are positioned at the maximum distance for the specified physical air-gap value.
The results for the 0.3 mm physical air-gap ($\delta_{physical}$) are shown below:

$$\int_{\text{rect}} BHdS = 0.8328\ {}^{J}\!/_{m},\quad \int_{case\,A} BHdS = 0.9142\ {}^{J}\!/_{m},\quad \int_{case\,B} BHdS = 0.9138\ {}^{J}\!/_{m},$$

$$\int_{caseC} BHdS = 0.9158\ {}^{J}\!/_{m}$$

The computational results confirm the expectations. Indeed, case B leads to the smallest and case C results in the largest magnetic energy.

The inductance of the rectangular air-gap is inversely proportional to the size of the air-gap. So it can be concluded that $\frac{\int_{rect,\delta_{phys}} BHdS}{\delta_{phys}} = \frac{\int_{real} BHdS}{\delta_{equiv}} = const$. Using this relation the equivalent air-gap for the real geometry can be found as:

$$\delta_{equiv} = \frac{\int_{real} BHdS}{\int_{rect,\delta_{phys}} BHdS} \delta_{phys} \tag{9.1.1}$$

A definition of the equivalent air-gaps for different relative positions of the sheets is presented in Table 9.1.1.

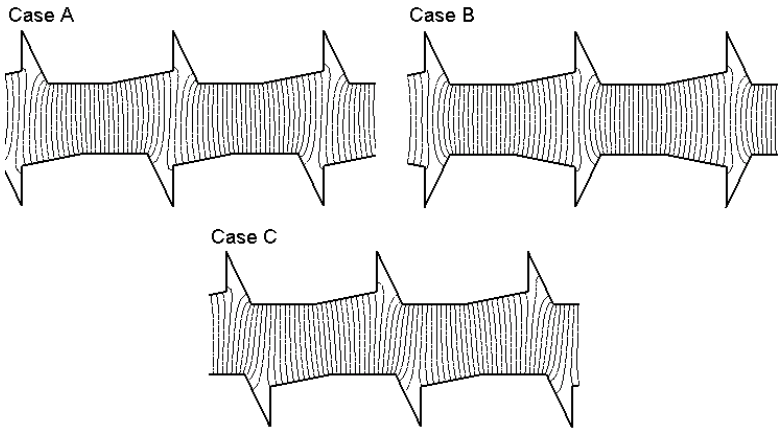

Fig. 9.1.5. Flux lines in the air-gap.

Table 9.1.1. Equivalent air-gaps defined using (9.1.1) versus physical air-gap. All dimensions are in mm.

$\delta_{physical}$	$\delta_{equiv\_case\_A}$	$\delta_{equiv\_case\_B}$	$\delta_{equiv\_case\_C}$
0.15	0.1779	0.1774	0.1809
0.3	0.3293	0.3291	0.3299
0.5	0.5296	0.5295	0.5296
0.75	0.7796	0.7796	0.7795

It can be seen that the results presented in each row in Table 9.1.1 are very close to each other. So the relative orientation of the cores is not that important. An increase of the equivalent air-gap can be assumed to be dependent only on the profile of the edge of the sheets.

In average, the difference between the equivalent air-gap and its physical value is equal to 0.029 mm, which corresponds to 4.6% of the thickness of the sheet. It is obvious that the contribution of the stator and the rotor into the increase of the air-gap is similar. Therefore the equivalent air-gap can be estimated as follows:

$$\delta_{equiv} = \delta_{physical} + 0.023 \cdot thickness_{sheet\ stator} + 0.023 \cdot thickness_{sheet\ rotor} \qquad (9.1.2)$$

The modified air-gap (9.1.2) can further be used in FE simulations. It can be concluded from Table 9.1.1 that the distortion of the shape of the sheets becomes particularly important in low power machines where the air-gap $\delta_{physical}$ is smaller.

It can be added that, generally speaking, the wole geometry of the magnetic sheet in the machine should be modified in order to account for the distortion of the profile of the cut edge, e.g. during numerical analysis of the electromagnetic device. An example of the principal modification of the geometry of the slot of an electrical machine is illustrated in Fig. 9.1.7.

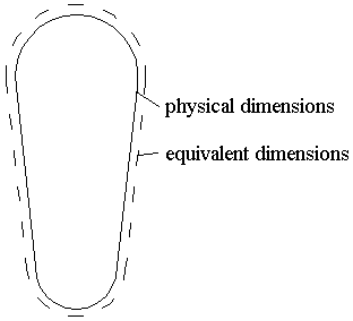

Fig. 9.1.7. Effect of mechanical cutting on the equivalent dimensions of the slot.

For instance, the width of the teeth is slightly smaller if a rectangular cut edge is assumed. However, this correction is of minor importance and we will only concentrate on the modification of the dimensions of the air-gap and the quality of the sheets in this region.

If the quality of the airgap edge of the stator is sufficiently improved this can provide a 10% decrease of the 'magnetic' air-gap in low-power machines with 0.15 mm air-gap (Table 9.1.1). An analogous improvement can be achieved with the rotor sheets. However for low power induction machines the rotor is usually grinded down. So the profile of the cut edge of the rotor sheets is not important and the rotor can be assumed smooth.

It is worth noting that the distortion of the profile of the sheet can be larger, as was demonstrated in Chapter 3. Therefore it seems feasible to use the fine-blanking technique for punching the internal circumference of the stator. The other elements such as slots can be punched using conventional equipment. Certainly, the punching cost would increase, but the positive effect of the air-gap reduction on the no-load current and the general performance of the machine would be unquestionable.

Section 9.2. The numerical simulation of the joint effect of the assembling stresses and mechanical cutting on the parameters of induction machine.

A typical geometry of a low power 4-pole induction motor (Fig. 9.2.1) is investigated in this section. This machine was also discussed in detail in [Gyselinck2000].
It is known that the most important regime with respect to the magnetic state of the induction motor is the no-load mode. At the normal operation and particularly in the short-circuit mode a reduction of the total magnetic flux is observed in the induction machine if it is supplied from the conventional 3-phase power supply with 50 Hz frequency.

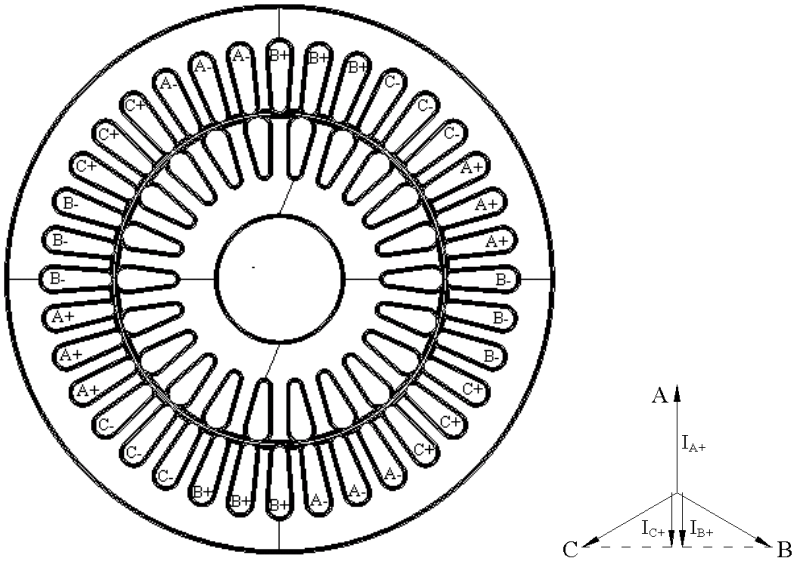

Fig. 9.2.1. The geometry of the low power induction machine considered in this section and an overview of the symmetrical 3 phase currents in the slots: $I_{A+}=-2I_{B+}=-2I_{C+}=2I_{B-}=2I_{C-}=-I_{A-}$.

For the sake of simplicity, we are going to investigate a static mode with a current distribution in the stator as shown in Fig. 9.2.1. The rotor is at a standstill and eddy currents in the rotor cage are assumed to be zero. According to [Gyselinck2000 ch. 9] these simplifications are generally acceptable as long as only the no-load characteristics of the motor have to be defined. Indeed, if the rotor has closed slots, then the eddy currents in the rotor cage considerably decrease in the no-load mode [Gyselinck2000 ch. 9 p. 14]. Besides, it is shown in [Gyselinck2000 ch. 9 p. 12] that the stator currents do not differ much if no-load mode is compared with a standstill rotor without a squirrel cage.

The aim of this investigation is to evaluate the effect of the non-uniformity of the magnetic properties of the magnetic core - due to the machine production - on the parameters of the machine. In the current simulation we choose the geometry with closed slots in the rotor. It allows us neglecting the rotor currents and rotation of the rotor without considerable effect on the accuracy. All the computations are conducted

for the same position of rotor and the same current distribution in the stator winding. So at least for the fixed time point the computations are completely adequate.

As it was experimentally found in Chapter 5 the elastic stresses lead to the introduction of magnetic anisotropy in the sheet of non-oriented electrical steel. At large stresses the effect of the elastic stress is adverse in all the directions. The numerical evaluation of these effects is given in subsection 9.2.1.
The effect of punching leads to an additional deterioration of the magnetic properties, which was clearly demonstrated in Chapter 8. The effect of punching with and without the production elastic stresses present is studied in Subsection 9.2.2. We recall that the production elastic stresses are due to stacking of the magnetic sheets in order to construct the magnetic cores and due to clamping of the magnetic stator core in the house of the machine and of the magnetic rotor core on the shaft.

9.2.1. The effect of the production elastic stresses on the parameters of the induction machine.

In this subsection it is assumed that the stator and the rotor cores are annealed in a special atmosphere. Consequently, the effect left is the elastic deformation of the magnetic core during assembling and fixation. We will begin with the description of the material model used in the computations.

9.2.1.1. Numerical modeling of the effect of the applied stress on the magnetic anisotropy in the non-oriented electrical steels.

9.2.1.1.1. Analytical expression for the magnetization curves.

It was experimentally determined (Chapter 6, 7) that the applied mechanical stress affects the magnetic properties of non-oriented electrical steels. Depending on the applied stress value this can lead to a considerable anisotropy. As hysteresis effects do not affect the shape of the stator current [Gyselinck2000 ch. 9 p. 15] in the induction machine considerably, the hysteretic feature of the magnetic properties can be neglected. So the goal is to develop an anisotropic material model that provides a permeability tensor for any combination of local flux density and mechanical stress.
It is possible to define the magnetization curve in the following analytical way [Gyselinck2000 ch. 3].

$$\mu(B) = \frac{1}{k_1 \cdot e^{k_2 B^2} + k_3} \qquad (9.2.1.1.1.1),$$

where the coefficients k_1, k_2 and k_3 are adjusted in order to obtain a good correspondence with the measured curve.
There are some advantages of using an analytical formulation. Firstly, it limits the amount of experimental information required for the mathematical description of the magnetization curve. Secondly, it assures the smoothness of the magnetization curve, which is beneficial for the numerical simulations (stability aspects).
A comparison of the measured magnetization curves with corresponding analytical interpretations is presented in Fig. 9.2.1.1.1.1 and Fig. 9.2.1.1.1.2.
The disadvantage of an analytical approximation is an inevitable discrepancy between the measurement results and the analytical curve especially at the inductions below 0.5

However, in induction machines the flux density along the main flux path usually exceeds this value. So it can be assumed that the difference between the measured and approximated magnetization curves is acceptable.

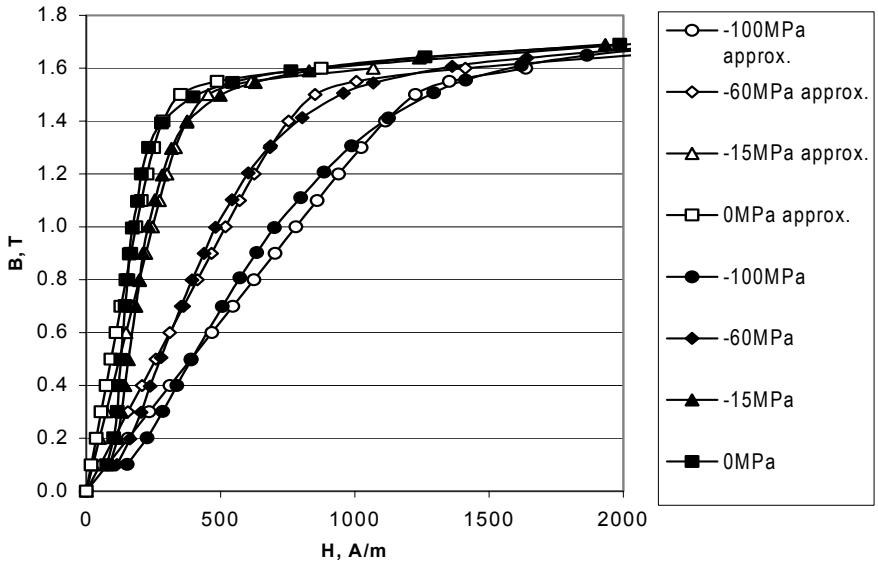

Fig. 9.2.1.1.1.1. The magnetization curves measured under compressive stress and corresponding analytical approximations.

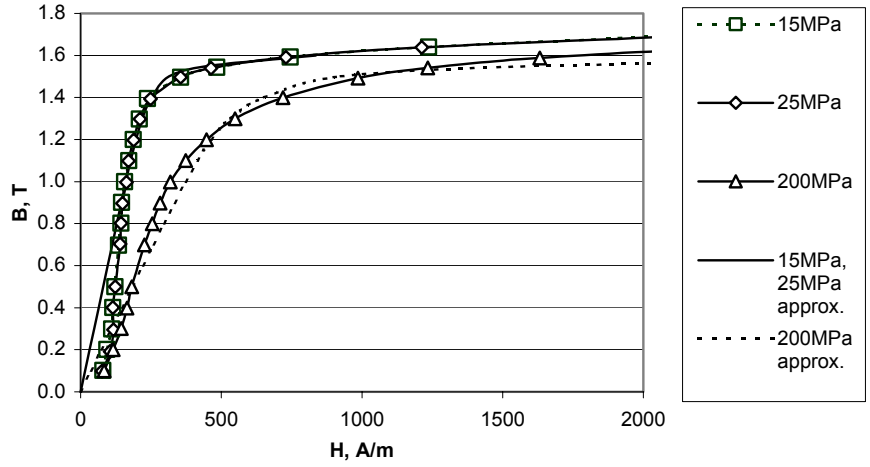

Fig. 9.2.1.1.1.2. The magnetization curves measured under tensile stress and corresponding analytical approximations.

Table 9.2.1.1.1.1. The coefficients of the analytical formulations.

σ, MPa	-100	-60	-15	0	15	25	100	200
k_1	0.0492	0.0492	0.0492	0.0469	0.0469	0.0492	0.0492	0.1788
k_2	2.9434	3.0835	3.1340	3.0975	3.0975	3.0975	3.1571	3.2167
k_3	779.87	517.18	245.66	184.25	159.68	159.68	245.66	368.49

The corresponding values of the coefficients for the analytical formulation are given in Table 9.2.1.1.1.1. It can be seen that the largest variation is experienced by the third coefficient, which together with the first coefficient mainly affects the initial slope of the magnetization curve. Since the applied stress results in a monotonous variation of the magnetic properties it can be assumed that the magnetization curves for intermediate stresses can be obtained using a linear interpolation of the corresponding coefficient values from Table 9.2.1.1.1.1.

The equation (9.2.1.1.1.1) can be transformed as follows:

$$\mu(\sigma, B) = \frac{1}{k_1(\sigma) \cdot e^{k_2(\sigma)B^2} + k_3(\sigma)} \qquad (9.2.1.1.1.2)$$

9.2.1.1.2. Equivalent stress ratio.

It was shown in Chapter 3 that for the real stress state in the application, both principal stresses, σ_1 and σ_2, are usually nonzero. Therefore some additional treatment is needed in order to adopt the experimentally collected material data (under uniaxial conditions: $\sigma_1=0$ or $\sigma_2=0$) to the actual stress state.

This subject is relatively new. However there are some models developed elsewhere [Sablik1994], [Sablik1995] on this matter. The model of Sablik was developed primarily for the biaxial stress states in carbon steels. As it was introduced in Chapter 6, the biaxial stress state is encountered when tension (or compression) is applied to the sample in two perpendicular directions. In fact, we have already used this model in Chapter 6 for the operation with residual stresses. Due to the presence of biaxial stress and a considerable number of pinning sites in the material, the use of the model of Sablik was acceptable.

In the present case, the pure biaxial stress is not encountered (see Chapter 3) as far as the assembling stresses are concerned. So some additional analysis has to be done in order to check the applicability of this model.

According to the model of Sablik the effect of biaxial stress on the magnetic properties along the first principal stress is equivalent to uniaxial stress computed as follows:

$$\sigma_{eq1} = \begin{cases} \frac{1}{3}\left[\left(\sigma_1 - \sigma_2\right) + \sigma_1\right], & \sigma_1 < 0 \\ \frac{1}{3}\left[\left(\sigma_1 - \sigma_2\right) - \sigma_2\right], & \sigma_1 > 0 \end{cases} \qquad (9.2.1.1.2.1)$$

Analogous computations can be conducted along the second principal stress:

$$\sigma_{eq2} = \begin{cases} \frac{1}{3}\left[\left(\sigma_2 - \sigma_1\right) + \sigma_2\right], & \sigma_2 < 0 \\ \frac{1}{3}\left[\left(\sigma_2 - \sigma_1\right) - \sigma_1\right], & \sigma_2 > 0 \end{cases} \qquad (9.2.1.1.2.2)$$

The equivalent stress values computed for various combinations of the principal stresses are given in Table 9.2.1.1.2.1.

Table 9.2.1.1.2.1. The equivalent stresses computed in the relative units via the model of Sablik.

	σ_1					
σ_2		-1	-0.5	0	0.5	1.0
	-1	(-0.333, -0.333)	(0, -0.5)	(0.333, -0.667)	(0.833, -0.833)	(1, -1)
	-0.5	(-0.5, 0)	(-0.167, -0.167)	(0.167, -0.333)	(0.5, -0.5)	(0.667, -0.667)
	0	(-0.667, 0.333)	(-0.333, 0.167)	(0, 0)	(0.167, -0.167)	(0.333, -0.333)
	0.5	(-0.833, 0.833)	(-0.5, 0.5)	(-0.167, 0.167)	(-0.167, -0.167)	(0, -0.5)
	1.0	(-1, 1)	(-0.667, 0.667)	(-0.333, 0.333)	(-0.5, 0)	(-0.333, -0.333)

It can be seen from Table 9.2.1.1.2.1 that in the model of Sablik the effect of the uniaxial stress (for instance: $\sigma_1=1$, $\sigma_2=0$) is underestimated ($\sigma_{eq1}=0.333$, while $\sigma_{eq1}=1$ should be expected). If tension is applied along the first principal axis and compression is applied along the second principal axis ($\sigma_1=1$, $\sigma_2=-1$), the model of Sablik again provides a clear underestimation ($\sigma_{eq1}=1$, $\sigma_{eq2}=-1$) as if the applied stresses are acting independently.

An alternative approach can be used:

$$\sigma_{eq1} = \sigma_1 - \sigma_2$$
$$\sigma_{eq2} = \sigma_2 - \sigma_1 \qquad (9.2.1.1.2.3)$$

This approach is not applicable to pure biaxial stress states. But it looks more adequate with respect to the stress states encountered due to the assembling stresses.

9.2.1.1.3. Permeability tensor for the numerical simulations.

The next step is to determine the mathematical apparatus for handling the anisotropy during the magnetic computations. There are different procedures developed on this matter.

The easiest way is to consider the anisotropy axes magnetically independent. So if one axis is saturated the other axis may have a high permeability. This is as if the axes have two independent sets of magnetic domains, which does not reflect the reality.

In real material when the domain walls are wiped out (saturation in one direction) the permeability reduces in any direction. This feature can be reflected if the magnetic permeability in each anisotropy direction is altered according to the total flux density:

$$\mu_x = \mu_x(|\overline{B}|), \quad \mu_y = \mu_y(|\overline{B}|), \quad B^2 = B_x^2 + B_y^2 \qquad (9.2.1.1.3.1)$$

Let us check if this model is adequate to the experimental results presented in Chapter 6. Consider the applied flux density B=0.4T for which the orientation gradually changes in the plane of the sheet. The corresponding magnetic field can be found as follows:

$$H_x = \frac{B_x}{\mu_x(|B|)}, \quad H_y = \frac{B_y}{\mu_y(|B|)} \tag{9.2.1.1.3.2}$$

As a result of the anisotropy, the flux density $\overline{B}$ and the corresponding magnetic field $\overline{H}$ can occupy different directions in space. So in order to simulate the measurements the projection of the flux density on the applied magnetic field has to be found.

$$B_{pr} = B_x \cdot \frac{H_x}{|\overline{H}|} + B_y \cdot \frac{H_y}{|\overline{H}|} = \frac{\frac{B_x^{\,2}}{\mu_x(|\overline{B}|)} + \frac{B_y^{\,2}}{\mu_y(|\overline{B}|)}}{\sqrt{\frac{B_x^{\,2}}{\mu_x^{\,2}(|\overline{B}|)} + \frac{B_y^{\,2}}{\mu_y^{\,2}(|\overline{B}|)}}} \tag{9.2.1.1.3.3}$$

Since hysteresis is neglected, $B_{pr} \geq 0$. The permeability in the direction of the magnetic field can be found as:

$$\mu = \frac{B_{pr}}{H} = \frac{\frac{B_x^{\,2}}{\mu_x(|\overline{B}|)} + \frac{B_y^{\,2}}{\mu_y(|\overline{B}|)}}{\frac{B_x^{\,2}}{\mu_x^{\,2}(|\overline{B}|)} + \frac{B_y^{\,2}}{\mu_y^{\,2}(|\overline{B}|)}} \tag{9.2.1.1.3.4}$$

A comparison between the model[1] and the measurement results is presented in Fig. 9.2.1.1.3.1. A small difference can be seen. However the model appears to be generally adequate.

[1] In experiments we directly measure the projection of the magnetic induction on the applied magnetic field. But in the computations we were assigning the total magnetic induction rather than its projection, which is smaller. However the simulations conducted for σ=40MPa show that due to the relatively small angle between the induction and the field the difference between the total induction and its projection on the applied field is quite small $|B_{total}-B_{pr}|/B_{total}<0.05$. This 5% difference should be added to the observed discrepancy between the measured and calculated permeabilities.

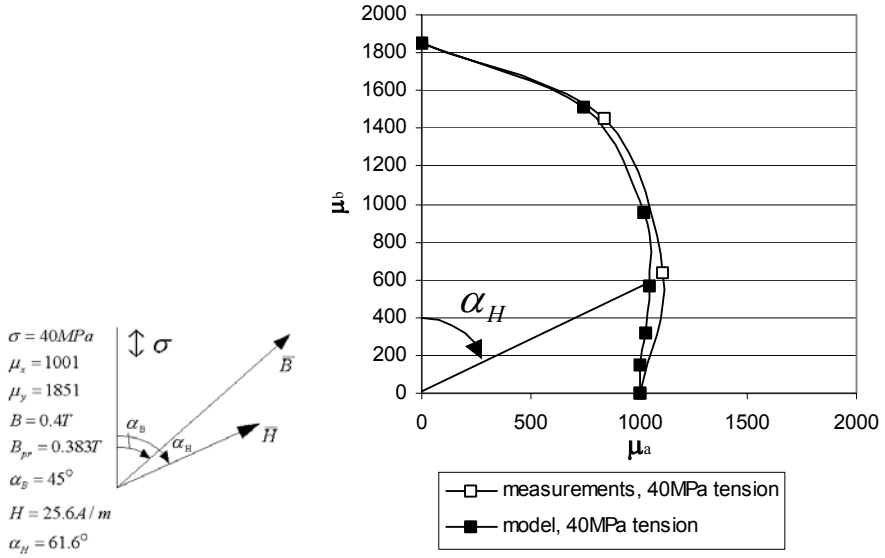

A. B.

Fig. 9.2.1.1.3.1. A comparison of the measurement results and the model (A: the computed orientations of the magnetic induction and magnetic field at $\alpha_B=45^0$ and σ=40MPa; B: the loci of the relative permeability obtained for the different orientations of the flux density B=0,4T, $\mu^2=\mu_a^2+\mu_b^2$ with $\mu=B_{pr}/H$ when we consider H along the direction defined by α_H. The vertical axis corresponds with the direction of applied stress).

The anisotropy axes have to be adapted to the orientation of the principal stress axes in the considered part of material. This can be accomplished using the rotation matrix:

$$\overline{\overline{\nu(B)}} = \overline{\overline{r(\alpha)}}^{T} \cdot \begin{bmatrix} 1/\mu_{along\ \sigma_{eq1}}(\sigma_{eq1}) & 0 \\ 0 & 1/\mu_{along\ \sigma_{eq2}}(\sigma_{eq2}) \end{bmatrix} \cdot \overline{\overline{r(\alpha)}} \qquad (9.2.1.1.3.5)$$

$$\overline{\overline{r(\alpha)}} = \begin{bmatrix} \cos(\alpha) & \sin(\alpha) \\ -\sin(\alpha) & \cos(\alpha) \end{bmatrix}$$

where the angle α is defined from the stress tensor:

$$\alpha = 0.5 \cdot arctg \frac{2\sigma_{12}}{\sigma_{11} - \sigma_{22}} \qquad (9.2.1.1.3.6)$$

9.2.1.1.4. Numerical example.

Consider the simple example of a rectangular core surrounding a current carrying conductor (Fig. 9.2.1.1.4.1). The material model assigned to the core was described above. At first, the problem was solved without any stress applied. The corresponding flux density distribution is shown in Fig. 9.2.1.1.4.2A. In the second computation a 100 MPa compression was applied in the horizontal direction to each of the elements of the mesh (this is certainly an unrealistic example; its only purpose is to demonstrate the capability of the developed model).
The effect of the applied compression on the flux density pattern is presented in Fig. 9.2.1.1.4.2B. A clear difference from the undeformed case can be seen. Compression leads to the deterioration of the magnetic properties. So a higher field is required in order to force the flux in the direction of compression (Fig. 9.2.1.1.4.3B).

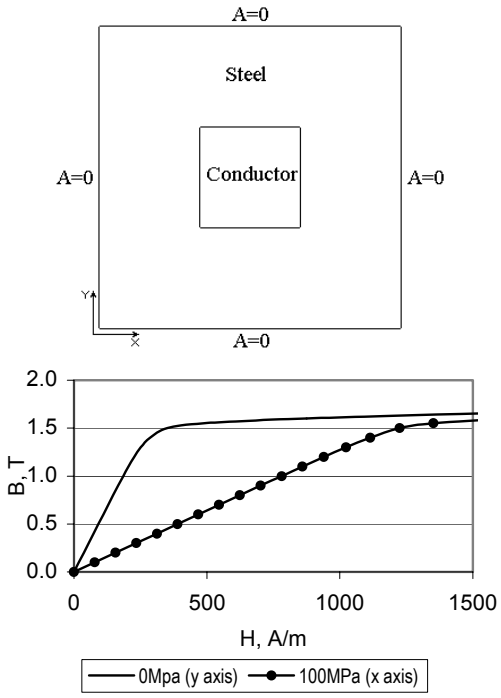

Fig. 9.2.1.1.4.1. Geometry of the problem and assigned material characteristics.

As a consequence of the magnetic anisotropy the vectors of the magnetic flux density B and the magnetic field H are not parallel at the corners of the magnetic core (Fig. 9.2.1.1.4.4B) unlike in the no stress state (Fig. 9.2.1.1.4.4A).

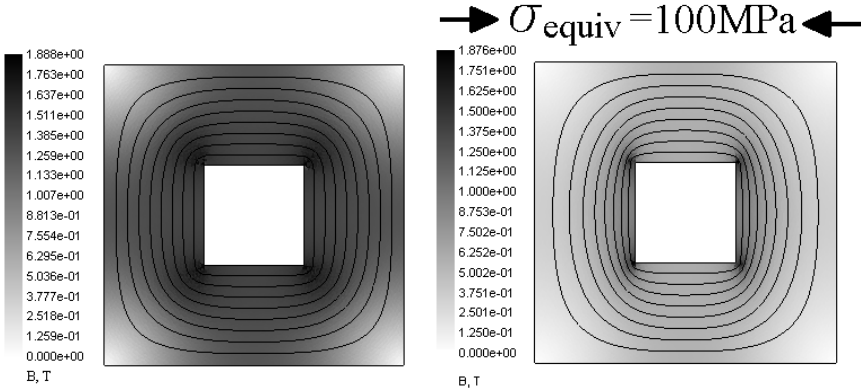

A. B.

Fig. 9.2.1.1.4.2. The magnetic flux pattern computed without stress (A) and with the uniformly compressed magnetic core (B).

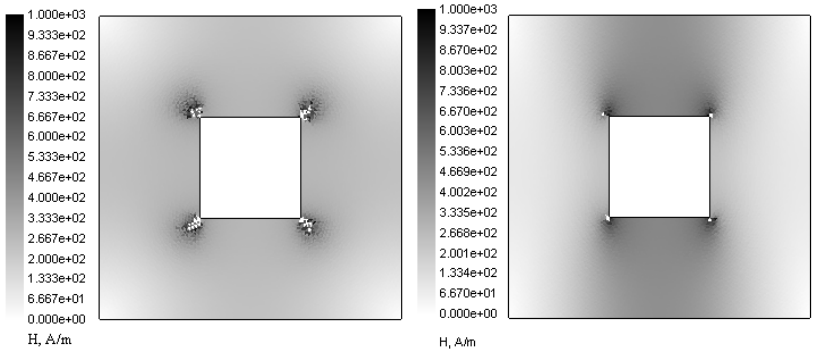

A. B.

Fig. 9.2.1.1.4.3. The magnetic field pattern computed in the core without stress (A) and with the uniformly compressed magnetic core (B).

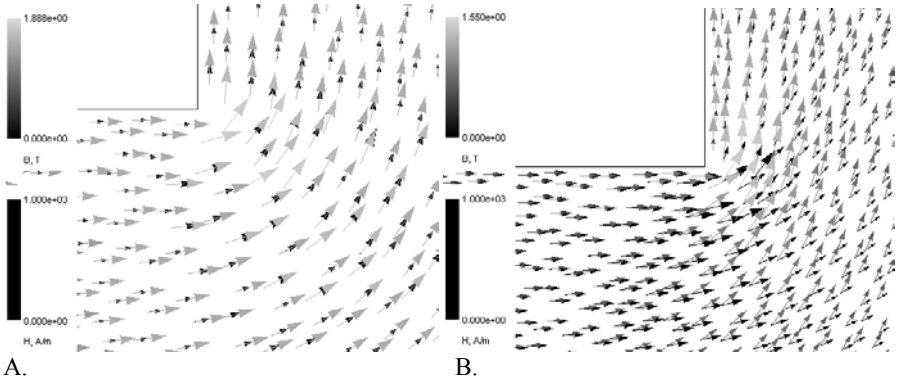

A. B.

Fig. 9.2.1.1.4.4. The local vectors of B and H in the core without stress (A) and with the uniformly compressed magnetic core (B).

9.2.1.2. The application of the developed model to the simulation of the effect of the applied assembling stress on the magnetic anisotropy in non-oriented electrical steels.

Unfortunately the machine constructors in Europe are reluctant to release specific information regarding their production process. Therefore the data used in this chapter is derived from Russian series of induction motors matching the analogous series of European companies.
Usually there is a close correspondence between the tolerances used during production in Europe and in Russia. Therefore the results obtained here are also relevant to other machines with analogous construction.
A four-pole induction machine with an external diameter of the stator core of 89 mm and an internal diameter of the rotor core of 20.5 mm is considered. According to the Russian norms the average deformation of the stator core due to compression into the frame is equal to 30 microns. The analogous deformation of the rotor core is equal to 18 microns. These displacements were used in the numerical computations.
It is worth noting that the displacement of the cores takes place towards the air-gap (Fig. 9.2.1.2.1, 9.2.1.2.2). So the size of the air-gap is clearly affected. The displacement of the stator core is almost equal to the tolerance during the assembling. The displacement of the rotor is approximately 30% smaller than the deformation applied from the shaft. The total stress distribution is presented in Fig. 9.2.1.2.3.
The layers in the model along the edge of the lamination do not play any role here. They are present in order to provide the same mesh in the magnetic cores of the machine and facilitate the evaluation of the effect of the investigated technological procedures.

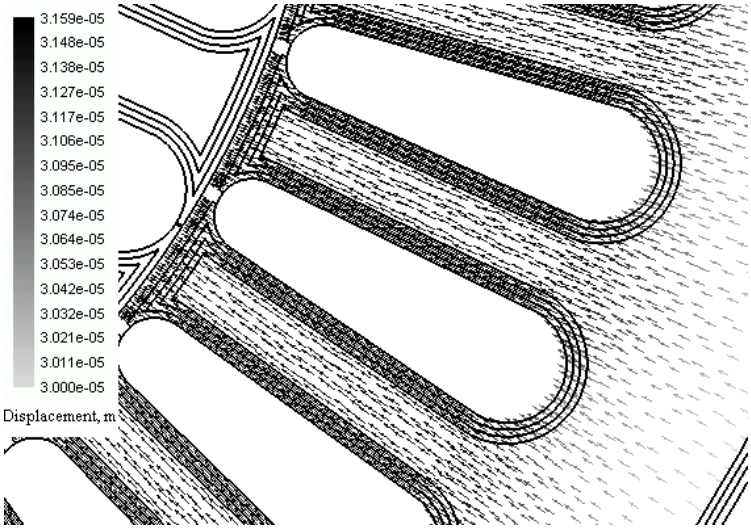

Fig. 9.2.1.2.1. Displacements in the stator due to the action of assembling stresses discussed in Chapter 3.

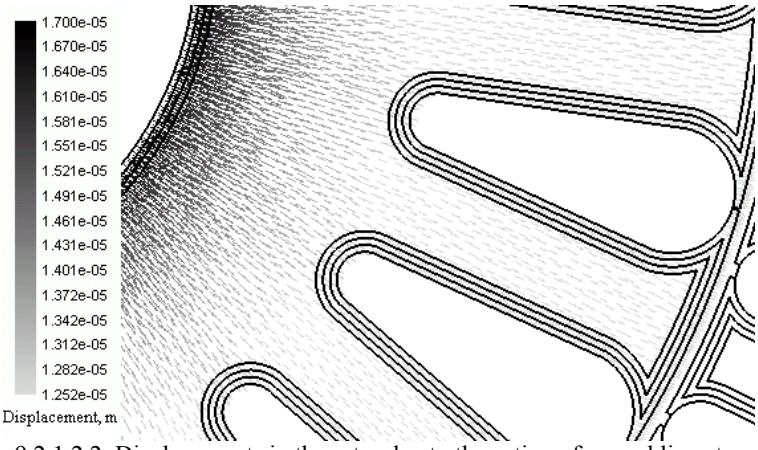

Fig. 9.2.1.2.2. Displacements in the rotor due to the action of assembling stresses.

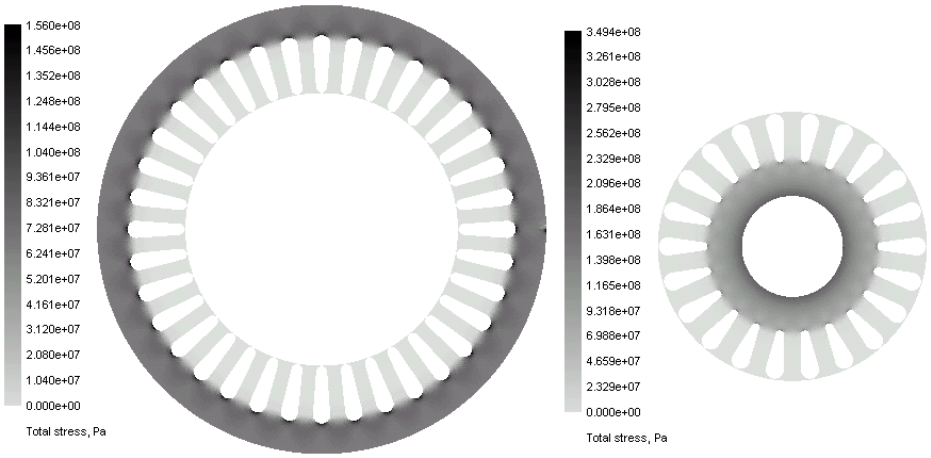

Fig. 9.2.1.2.3. The total stress distribution defined in the stator and rotor cores.

The corresponding principal stress distributions were considered in Chapter 3. The equivalent stresses in terms of the magnetic properties are computed separately in the stator (Fig. 9.2.1.2.4) and in the rotor (Fig. 9.2.1.2.5) cores using the model considered earlier, see eqn. (9.2.1.1.2.3).

The assembling stresses affect the size of the air-gap. So in the electromagnetic computations, the comparison of the stressed and the unstressed states is carried out taking into account the modification of the air-gap. The air-gap corresponding to the stressed state is equal to 0.35mm. For the unstressed state the air-gap value is larger and equals 0.35+0.0125{*displacement of the rotor core, Fig. 9.2.1.2.2*}+0.0315{*displacement of the stator core, Fig. 9.2.1.2.1*}=0.394 mm.

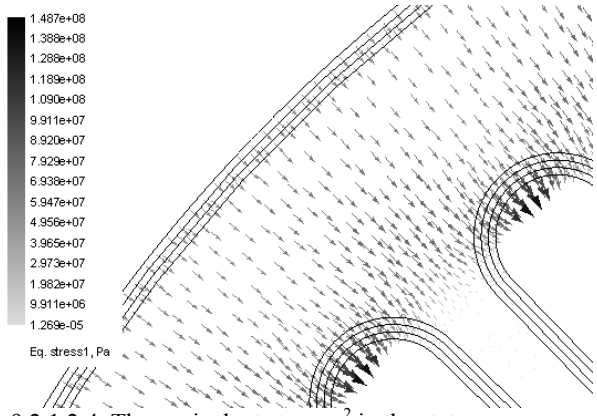

Fig. 9.2.1.2.4. The equivalent stresses[2] in the stator core computed according to eqn. (9.2.1.1.2.3).

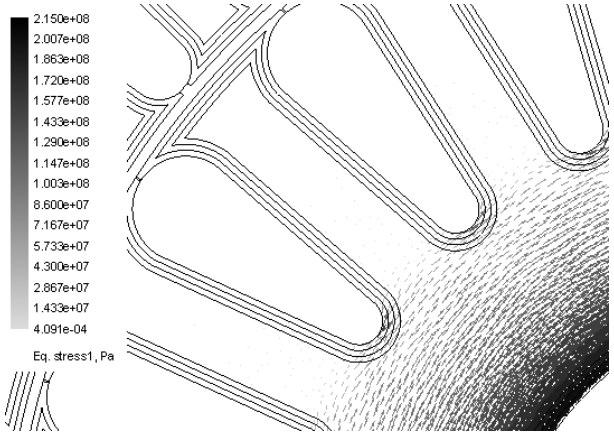

Fig. 9.2.1.2.5. The equivalent stresses in the rotor core computed according to eqn. (9.2.1.1.2.3).

If the rotor is grinded down after assembling then the final radius does not depend on whether or not the stresses are applied to the rotor core. So in the machine with a grinded rotor the size of the air-gap is affected only by the deformation of the stator, i.e. the reduction of the air-gap due to the assembling stresses is smaller and equals 0.394{*air-gap in the unstressed state*}-0.0315{*displacement of the stator core, Fig. 9.2.1.2.1*}=0.3625 mm.

The decreased air-gap (0.35 mm instead of 0.3625 mm) explains a higher induction value in Fig. 9.2.1.2.6B (B_{max}=1.834 T) compared to Fig. 9.2.1.2.6C (B_{max}=1.827 T). Further, due to the action of the compression in the circumferential direction (Chapter 3) a magnetic anisotropy emerges as is shown in Fig. 9.2.1.2.7B and 9.2.1.2.8B via the

[2] The distribution of the principal stresses is shown in Chapter 3 both in the stator and in the rotor. Only one of equivalent stresses (σ_1) is presented here. The other equivalent stress (σ_2) is oriented perpendicularly, has the same amplitude and opposite sign.

permeability tensor. The permeability in the stator yoke in the circumferential direction is much lower compared to the radial direction. So the magnetic flux tends to bypass the yoke through the teeth, since they are not affected by the compression. This apparently leads to an increase of the area of the core affected by rotational magnetization. Also, the areas where the magnetic flux is traveling along the compression are likely to experience higher vibrations due to the increase in the magnetostriction (Chapter 7). A general increase of the total magnetic losses in the stator core can also be expected in these regions. This issue is important as far as the heat distribution in the machine is concerned.

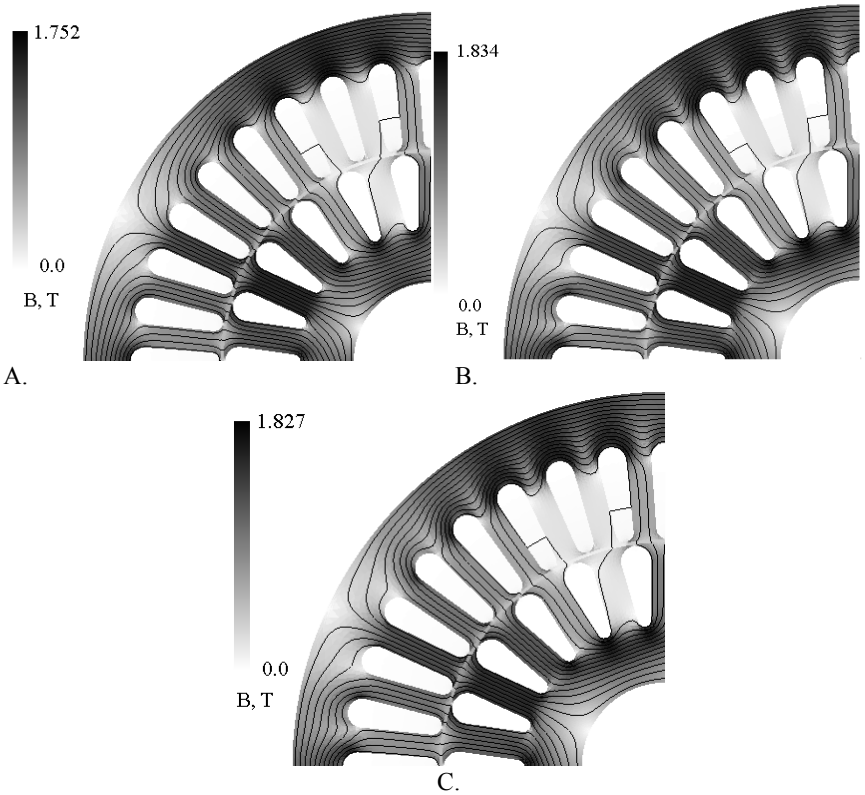

Fig. 9.2.1.2.6. The flux density pattern at J_{A+}=2.625A/mm^2 (A – no deformation is applied; air-gap=0.394 mm , B – assembling stresses are applied; air-gap=0.35 mm, C – assembling stresses are applied and rotor is grinded; air-gap=0.3625 mm).

Unlike the stator, the rotor of the induction motor is affected by a compression in the radial direction (Chapter 3). This leads to a visible flux density gradient in the radial direction in the yoke. A smaller deviation of the flux in the yoke from the circumferential direction can also be pointed out.

In order to provide a quantitative evaluation of the effect of the assembling stresses the ratios of the inductances, as defined in Chapter 4, were computed for the specified regions of the domain of interest.

The effect of assembling stresses consists of two contributions:

1) The displacement of magnetic cores towards the air-gap. Corresponding results are presented in Table 9.2.1.2.1 below. The total inductance of the motor and inductance of the air-gap increases by nearly 11%, which occurs due to a 0.394/0.35=1.126 decrease of the air-gap value. We can conclude that the total inductance of the motor as well as the air-gap inductance depend almost linearly on the air-gap value. The stator leakage remains almost constant.
2) The effect of the elastic stresses on the magnetic properties (Table 9.2.1.2.2). The air-gap is the same. However its inductance decreases, which indicates that a smaller magnetic flux is crossing the air-gap: the total inductance becomes smaller due to the action of the assembling stresses. So the total flux created by the stator winding decreases. The cause is that the stator core is affected by the circumferential compression, which leads to a considerable m.m.f. drop in the stator and a more than 200% increase of its contribution to the total inductance. The rotor core is affected by radial compression, which appears to be less deteriorative with respect to the magnetic properties. Also the stator leakage becomes somewhat smaller.

Numerical results on the joint effect of the displacement of the magnetic cores and the deterioration of the magnetic properties due to the action of assembling stresses are given in Table 9.2.1.2.3.

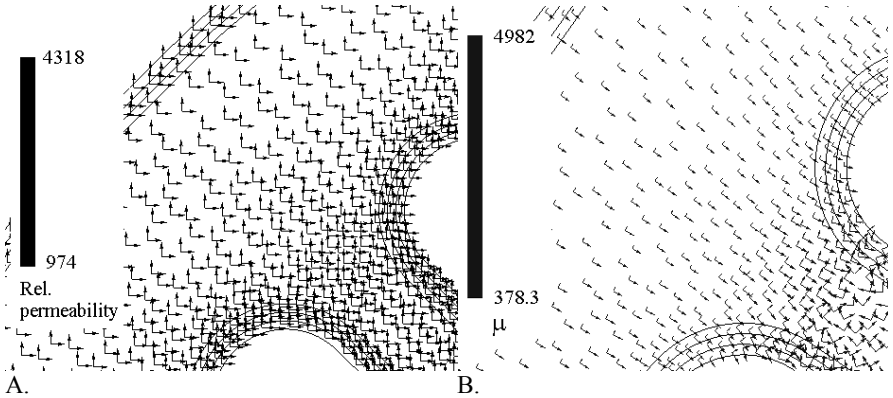

Fig. 9.2.1.2.7. The relative permeability in the stator along the principal stresses at J_{A+}=2.625A/mm^2. (A – no deformation is applied, B – the equivalent stress is computed according to (9.2.1.1.5)).

The total inductance increases by 5% (Table 9.2.1.2.3), which means that the total flux of the motor also increases. The contribution of the air-gap to the inductance in the induction machine subjected to the assembling stresses reduces by more than 2%. So the magnetic flux in this part of the problem decreases. The obvious reason of this effect is the drop of the average permeability of the stator and rotor cores.

The induction motor is usually connected to the voltage supply rather than to a source of current. From Faraday's law $v_m(t)=d\Phi_{total}(t)/dt=L_{total}di/dt$ it follows that in case of voltage supply the total flux in the motor is almost defined, assuming that the voltage drop over the resistance of the stator winding is constant.

The last row in Table 9.2.1.2.3 shows an increase of the total flux due to the assembling stresses, which was obtained at a constant current in the stator windings. In order to account for the voltage supply there has to be a correspondence in the total flux, so all the values in the columns must be divided by 1.05. As a result the flux in the air-gap will decrease even more (Table 9.2.1.2.3): 0.98/1.05=0.933.

Table 9.2.1.2.1. The ratio of the inductances computed in the machine subjected to assembling stresses (only displacement of the stator and rotor is included) and machine with undeformed magnetic cores.

$L_{\delta=0.35mm} / L_{\delta=0.394mm}$	Current density in the stator slots, J_{A+}, A/mm^2			
	0.875	1.75	2.625	3.5
Stator slots	0.998	0.998	0.983	0.888
Air gap	1.109	1.108	1.088	0.964
Rotor core	1.244	1.248	1.392	1.331
Stator core	1.238	1.243	1.386	1.633
Total	1.113	1.113	1.103	1.033

Table 9.2.1.2.2. The ratio of the inductances computed in the machine subjected to assembling stresses (displacement of the stator and rotor is not included) and the machine with undeformed magnetic cores.

$L_{\sigma,\delta=0.394mm} / L_{\delta=0.394mm}$	Current density in the stator slots, J_{A+}, A/mm^2			
	0.875	1.75	2.625	3.5
Stator slots	0.896	0.896	0.898	0.948
Air gap	0.897	0.896	0.895	0.943
Rotor core	1.272	1.292	1.313	1.022
Stator core	2.118	2.112	2.022	1.193
Total	0.946	0.946	0.945	0.967

Table 9.2.1.2.3. The ratio of the inductances computed in the machine, subjected to joint effect of the assembling stresses (model described in 9.2.1.1.3) and a reduction of the air-gap, and machine with undeformed magnetic cores.

$L_{\sigma,\delta=0.35mm} / L_{\delta=0.394mm}$	Current density in the stator slots, J_{A+}, A/mm^2			
	0.875	1.75	2.625	3.5
Stator slots	0,88	0,88	0,88	0,86
Air gap	0,98	0,98	0,97	0,93
Rotor core	1,56	1,60	1,71	1,43
Stator core	2,59	2,59	2,52	1,74
Total	1,05	1,05	1,04	1,01

This short discussion is intended to demonstrate the meaning of the variation of the total inductance. In the low power machines the resistive voltage drop is not negligible, so the assumption about the total flux being constant is not that strict.
We recall that the motor has to provide a specified mechanical torque. So the magnetic flux in the air-gap has to be sufficiently high, while the current density must remain acceptable in order to avoid excessive heating of the stator winding.

Therefore we are going to concentrate further on the inductance of the air-gap calculated at a specified current density. Indeed, this procedure allows us to evaluate whether the imposed requirements on the stator current and the flux in the air-gap can be satisfied.
Since the air-gap is the most important element of the magnetic system and its relative permeability equals 1, the correspondence to the undeformed machine with respect to the magnetic flux in the air-gap can be recovered via an equivalent increase of the size of the air-gap. The equivalent size of the air-gap of the undeformed machine can be found as 0.394*{air-gap value in the unstressed state}*/0.975*{averaged reduction of inductance of the air-gap}*=0.404mm.
Analogous calculations can be conducted on the machine with a grinded rotor. The inductance of the air-gap in such machine decreases by 5% due to the application of the assembling stresses (Table 9.2.1.2.4). So the equivalent air-gap of the undeformed machine can be found as 0.394/0.95=0.415mm.

Table 9.2.1.2.4. The ratio of the inductances computed in the machine subjected to the assembling stresses (model (9.2.1.1.5)) and machine with undeformed magnetic cores. The rotor is grinded.

$L_{\sigma,\delta=0.3625mm} \Big/ L_{\delta=0.394mm}$	Current density in the stator slots, J_{A+}, A/mm^2			
	0.875	1.75	2.625	3.5
Stator slots	0,89	0,89	0,89	0,89
Air gap	0,96	0,95	0,95	0,94
Rotor core	1,47	1,50	1,57	1,30
Stator core	2,44	2,43	2,36	1,56
Total	1,02	1,02	1,01	1,00

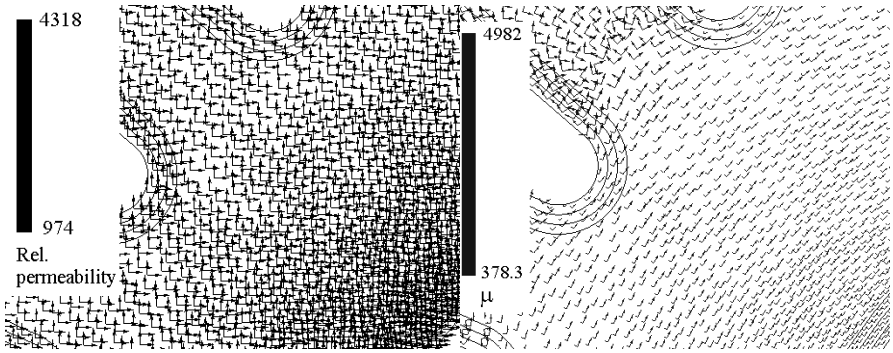

Fig. 9.2.1.2.8. The relative permeability in the stator along the principal stresses at J_{A+}=2.625A/mm^2. (A – no deformation is applied, B – the equivalent stress is computed according to (9.2.1.1.5)).

9.2.2. Analysis of the effect of mechanical punching on the parameters of the induction machine.

9.2.2.1. Introduction.

The experimental information on the effect of punching in Chapter 8 was collected in assumption that the magnetic field is uniform in the sample. For that geometry it was valid and, indeed, there are zones in any electromagnetic device where a similar situation is present.
In the induction machine, such situation can be encountered in the top part of the teeth (Fig. 9.2.2.1.1, regions 1, 2 and 3). Here, the different regions 1, 2 and 3 are in parallel with respect to the total flux Φ. In this parallel scheme the total flux is split into parts favouring the regions with higher permeability.
However the magnetic flux must also enter the tooth through the area defined by the regions 4, 5 and 6 near the air-gap. The tooth tip (regions 4,5 and 6) is also deformed and redistribution of the flux in favour of higher permeability cannot take place. Here, the different regions 4, 5 and 6 are in series with respect to the total flux Φ. So in this area it is more appropriate to suppose a constant magnetic flux density B as it is demonstrated in Fig. 9.2.2.1.2.

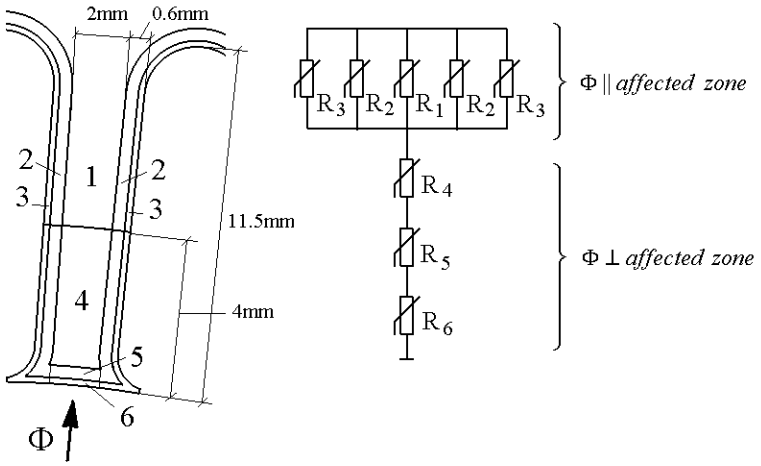

Fig. 9.2.2.1.1. The equivalent magnetic circuit corresponding to the case when magnetic flux is oriented along or perpendicular to the cut edge.

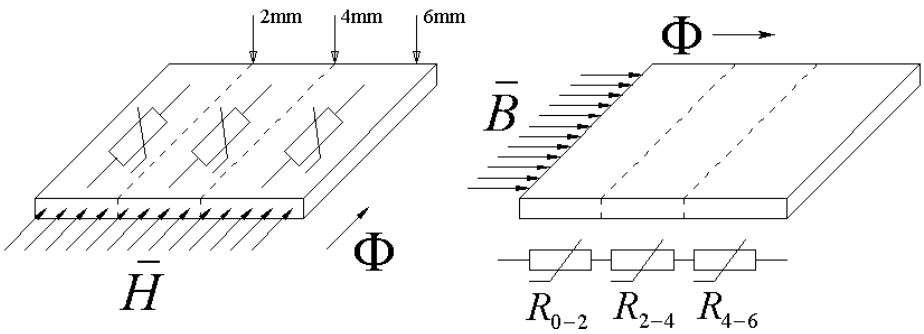

A. B.

Fig. 9.2.2.1.2. Definition of the equivalent circuit for the zone affected by punching in the vicinity of the air-gap of the induction machine
(A: orientation of the deformation affected zone with respect to the applied magnetic field in the local magnetic measurements; Situation A describes cut edge near the slot. B: orientation of the deformation affected zone with respect to the magnetic flux entering the tooth from the air-gap; Situation B describes cut edge near the air-gap).

As was determined in Chapter 8 the deformation affected zone exceeds 4 mm, which is comparable with the width of the tooth. If the cut sheet has a width equal to 3.2 mm (width of the tooth in the considered geometry), then there will certainly be an interaction of the neighbouring deformation affected zones. There are however some complications here.
First of all, the local magnetic measurements do not provide the complete information on the residual stresses. They may only indicate their presence. However in order to deal with the interaction between the different residual stress zones, full information on the stress tensors is required. Secondly, a simulation of the interacting fields of the residual stresses is required. At the moment this is not possible as there are no successful mathematical approaches developed on this matter. Conventional FE computations are dealing with continuous functions. They imply the continuity of the material properties in the considered volume. However the nature of the residual stresses is in the non-uniformity of the mechanical properties of material on a microscopic scale and the non-uniformity of the applied mechanical deformation [Buch1988][Rice1988].
In order to avoid simulation of interaction between the neighboring residual stress domains we will introduce equivalent layers with a size smaller than that of the deformation affected zone. The correspondence with the experimental data for the case, when B is constant, can be provided relatively easy.

9.2.2.2. Modeling of affected zone of the teeth near the air-gap.

In measurements described in chapter 8, the deformation affected zone was investigated with a 2 mm step. According to these measurements, the effect of punching vanishes within 4-6 mm. Taking into account the dimensions of the tooth region, see Fig. 9.2.2.1.1, and the dimensions of the affected zone due to punching, there is a clear overlap of affected zones corresponding to neighbouring edges. As no experimental magnetic information is available for overlapping affected zones, we would like to introduce in the numerical model of the induction machine equivalent layers, such that,

firstly, no overlapping is present due to neighbouring cutting edges and, secondly, a good correspondence is obtained between the numerical model of the machine and the real situation with respect to m.m.f. drops.

Since in the air-gap the magnetic flux successively passes the affected zones, the magnetic reluctance can be computed as a sum of the reluctances defined for each region considered in chapter 8:

$$R_{\Sigma}(B) = R_{0-2mm}(B) + R_{2-4mm}(B) \qquad (9.2.2.2.1)$$

$$R_{\Sigma}(B) = \frac{\Delta l}{\mu_{0-2mm}(B) \cdot d \cdot b} + \frac{\Delta l}{\mu_{2-4mm}(B) \cdot d \cdot b} \qquad (9.2.2.2.2),$$

where

Δl = 2mm – length of each zone,
d = 0.65mm – thickness of the sheet,
b = arbitrary value. We choose the value equal to 2 mm, the width of the unaffected area of the stator tooth (in the model) (Fig. 9.2.2.3.2).

Let us introduce the *equivalent* layers 0-0.2mm-0.6mm-4mm with the available magnetic properties shown in Fig. 9.2.2.2.1. These equivalent layers will be used later in the numerical magnetic simulations. The total reluctance of these layers can be computed as:

$$R_{\Sigma}^{eq}(B) = K \cdot \left[\frac{\Delta l_{eq1}}{\mu_{\varepsilon=9.5\%}(B) \cdot d \cdot b} + \frac{\Delta l_{eq2}}{\mu_{\varepsilon=6\%}(B) \cdot d \cdot b} \right] + \frac{\Delta l_{eq3}}{\mu_{\varepsilon=0}(B) \cdot d \cdot b} \qquad (9.2.2.2.3),$$

where

Δl_{eq1}=0.2mm – the length of the 1st equivalent layer;
Δl_{eq2}=0.4mm – the length of the 2nd equivalent layer;
Δl_{eq3}=3.4mm – the length of the 3rd equivalent layer;
l_{total}=4mm – total length of the equivalent zone,
K=3 – correction factor required in order to achieve a correspondence with (9.2.2.2.2).

The choice of ε=9.5% and ε=6% is arbitrary. Once the choice is made, the correction factor K is fitted in order to adjust the equivalent reluctance (9.2.2.2.3) to the total reluctance (9.2.2.2.2). We obtained the value K=3. The choice of the magnetization curves was justified by the fact that the sheet actually experiences a plastic deformation at the edge. As demonstrated in [Loisos2003_3][Nakata1992] and in Chapter 8 the non-linearity of the magnetic properties at the edge is quite weak. This is favourable for the adjustment of the equivalent reluctance to the reluctance computed according to (9.2.2.2.2).

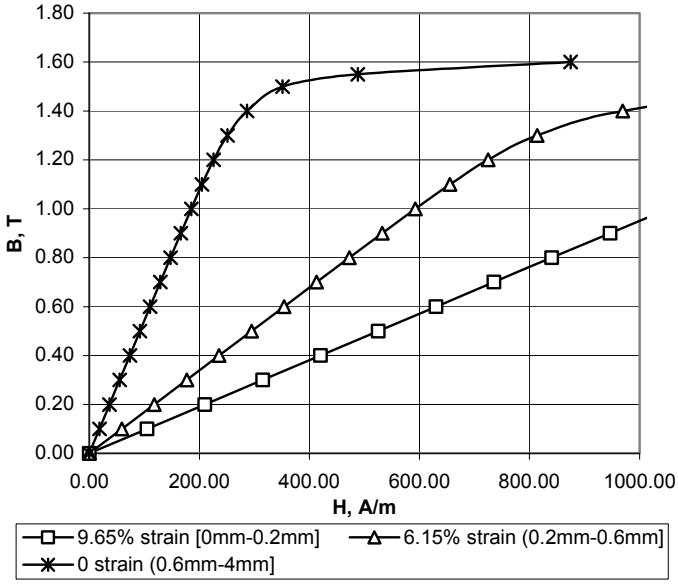

Fig. 9.2.2.2.1. The analytical interpretation of the magnetization curves measured at various plastic deformations.

So the following permeability can be introduced into the FE simulations:
$\mu_{0\text{-}0.2mm}(B)= 1/K\{$*correction factor from (9.2.2.2.3)*$\}*\mu_{\varepsilon=9.5\%}(B)= 1/3*\mu_{\varepsilon=9.5\%}(B)$,
$\mu_{0.2\text{-}0.6mm}(B)=1/3*\mu_{\varepsilon=6.15\%}(B)$.

It is demonstrated in Fig. 9.2.2.3.1 that the difference between the measured and equivalent magnetic reluctances is sufficiently small at moderate inductions. In the Rayleigh zone the equivalent reluctance is underestimated compared to the measured one. The opposite can be seen for high inductions.
In case of induction machines the width of the tooth tip is usually larger than the width of the tooth. Therefore the flux density in the tooth tip part is smaller and does not exceed 1.5T, which will be shown further (Fig. 9.2.2.3.3). Under these circumstances the discrepancy observed in Fig. 9.2.2.3.1 is admissible.
In fact, if the only domain of interest was the tooth tip, it would have been possible just to introduce a single layer with equivalent reluctance.

9.2.2.3. Modeling of affected zone of the teeth near the winding slots.

Similarly to section 9.2.2.2, we want to introduce in the numerical model of the induction machine equivalent layers for the cut edge near the slots. Now, the flux Φ is parallel to the cut edge.
As it was shown experimentally the flux tends to displace in favour of the least affected area of the sheet. Using the approach described above we virtually decrease the cross-section of the tooth.

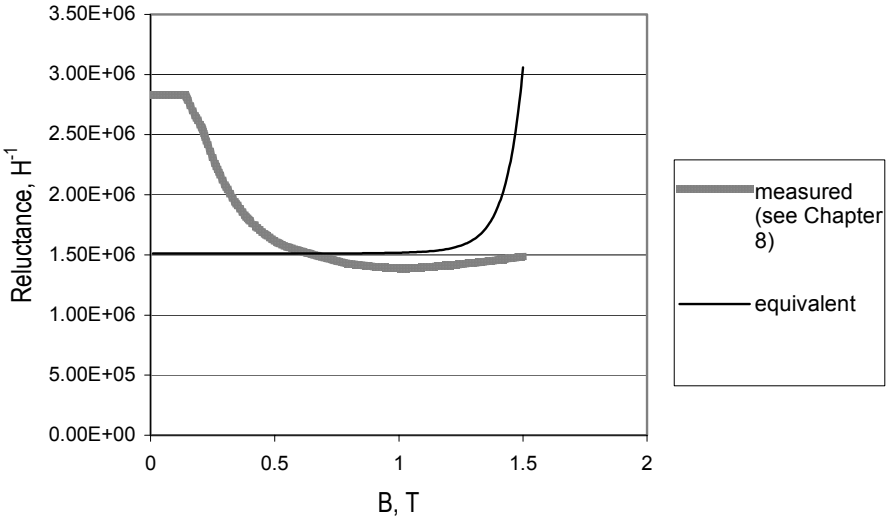

Fig. 9.2.2.3.1. A comparison between the measured (9.2.2.2) and the equivalent (9.2.2.3) reluctances.

The results obtained experimentally in [Kedous2003] show that the central area of the tooth of small dimensions is affected by punching.
The total height of the teeth of the stator in the considered geometry is equal to 11.5 mm. When magnetic flux is going through the stator teeth into the air-gap it passes the equivalent layer that accounts for the 4 mm long deformation affected zone. So the remaining part of the teeth (zone 2) can be the source of underestimation of the effect of punching on the magnetic properties of the teeth. The flux density distribution in the equivalent layers is shown in Fig. 9.2.2.5B.

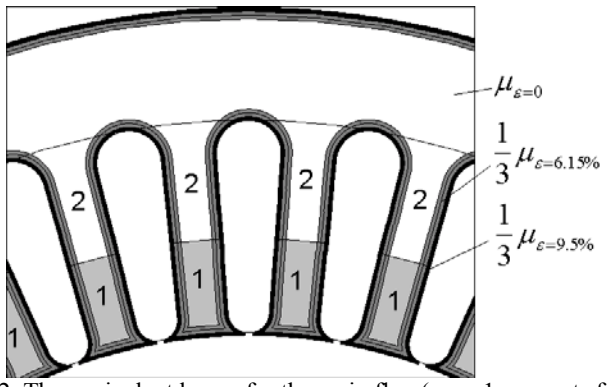

Fig. 9.2.2.3.2. The equivalent layers for the main flux (zone 1 accounts for the m.m.f. drop when flux is entering the tooth through the tooth tip, zone 2 is the rest of the tooth).

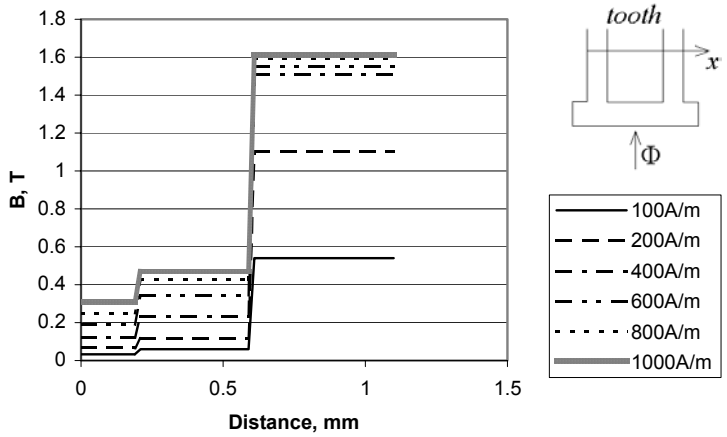

Fig. 9.2.2.3.3. The flux density distribution near the edge of the lamination at a constant field H in the equivalent layers 0-0.2mm-0.6m-4mm

In order to evaluate the error the equivalent reluctance was computed for the parallel connection of the reluctances of the equivalent layers 0-0.2mm-0.6m-4mm:

$$R_{\Sigma}^{eq,\|}(H)=\frac{1}{\frac{1}{\frac{\Delta l_{eq1}}{\mu_{0-0.2mm}(H)\cdot d\cdot l_1}}+\frac{1}{\frac{\Delta l_{eq2}}{\mu_{0.2-0.6mm}(H)\cdot d\cdot l_1}}+\frac{1}{\frac{\Delta l_{eq3}}{\mu_{0.6-4mm}(H)\cdot d\cdot l_1}}} \quad (9.2.2.3.1),$$

where

l_1=11.5-4mm – the length of zone 2 (Fig. 9.2.2.3.1);
d=0.65mm – thickness of the sheet;
Δl_{eq1}=0.2mm – the length of the 1st equivalent layer;
Δl_{eq2}=0.4mm – the length of the 2nd equivalent layer;
Δl_{eq3}=3.4mm – the length of the 3rd equivalent layer;
l_{total}=4mm – total length of the equivalent zone.

The reluctance based on the measurements can be computed using an analogous relation.

A comparison between the equivalent and measured (0-2mm-4mm) reluctances is presented in Fig. 9.2.2.3.3.

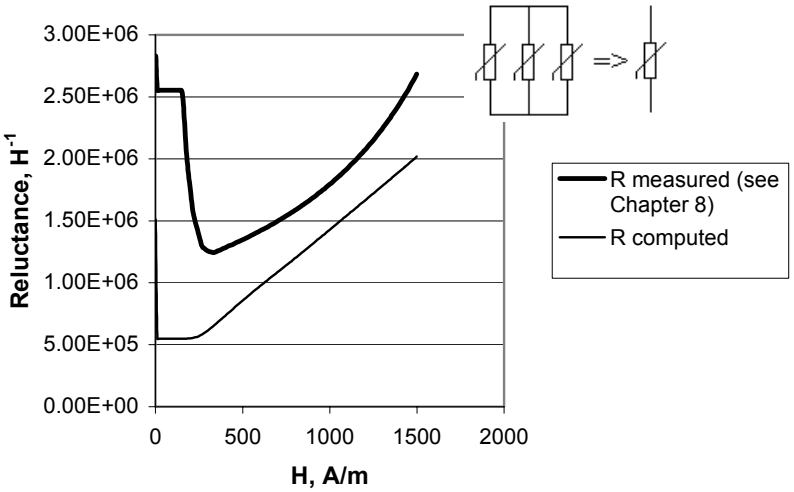

Fig. 9.2.2.3.4. A comparison between the measured R and approximated R_{num} reluctances.

The whole equivalent layer is shorter compared to the actual size of the affected zone. Since a reluctance of the equivalent layers was adjusted with for the tooth tip, in case when the magnetic flux flows parallel to the cut edge the equivalent layer shows in average some 30% underestimation. Taking into account that the total reluctance is the sum of reluctances of zones 1 and 2, the total underestimation of the effect of punching is less than 15%. The overlapping of the affected zones does not lead to a proportional deterioration of the magnetic properties [Nakata1992]. This means that the actual error can be smaller.
The developed approach is applicable for small and short teeth. If the tooth height and tooth width increase, the contribution of zone 2 into the total reluctance increases and the total underestimation of the effect of mechanical cutting on the magnetic properties of the tooth approaches 30%.

9.2.2.4. A numerical simulation of the joint effect of mechanical cutting and assembling stresses on the parameters of induction motor.

The numerical simulation results are presented in Fig. 9.2.2.4.1 below.

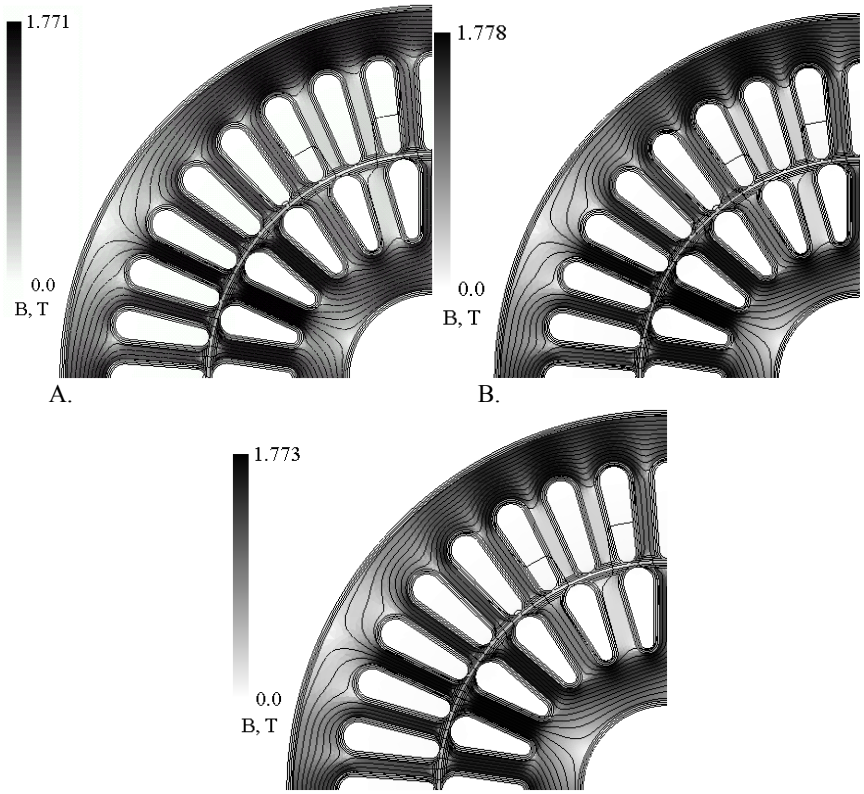

Fig. 9.2.2.4.1. The flux density pattern at J_{A+}=2.625A/mm^2 (A – effect of punching, B – joint effect of punching and assembling stresses, C – joint effect of punching and assembling stresses with grinded rotor).

The main flux passes the tooth tip that is not affected by the applied assembling stresses but by punching. The rest of the flux path in the stator core is going along the zone affected by mechanical cutting.

As experimentally confirmed in Chapter 6 the effect of the applied elastic assembling stresses (stresses due to stacking and clamping of the magnetic core) decreases with increased pinning of the domain walls. Indeed, the pressure imposed by the applied stress on the domain walls can be insufficient in order to alter considerably the domain structure. So the equivalent layers are assumed to be unaffected with respect to the magnetic properties by the applied elastic assembling stresses.

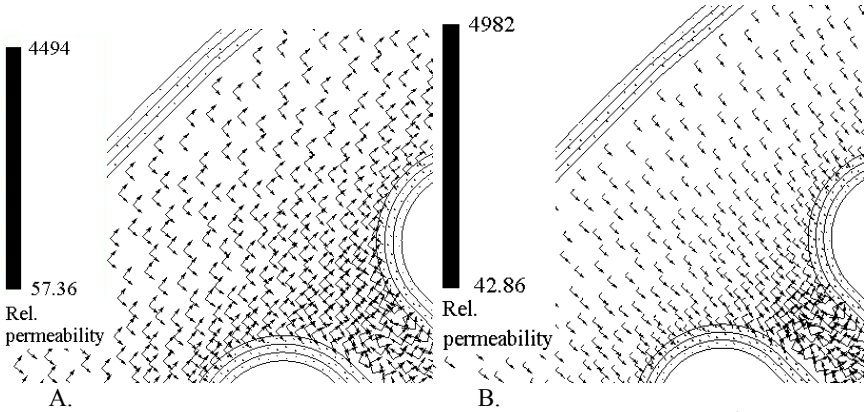

Fig. 9.2.2.4.2. The relative permeability in the stator at J_{A+}=2.625A/mm^2 (A – effect of punching, B – joint effect of punching and assembling stresses).

In some cases a conventional winding is placed in the rotor core. But most of the time cheaper techniques[3] are used for the rotor production, i.e. the slots are filled with melted aluminum rather than with wires. The forms installed at the sides of the rotor permit production of the end rings at the same installation. Among other advantages 100% filling of the slots is reached via this approach. But for us it is important that the rotor core is subjected to heating. So we should estimate the consequences.

The melting temperature of aluminum is 660°C. It is shown in [Yanez2002] that a reduction of the temperature leads to a considerable decrease of the velocity of the material transformations. The apparent reason is the reduction of the thermal agitation forces. Unfortunately there is no information available on the exact timing of aluminum casting. However judging upon the available description of the procedure the melted aluminum is cast and no additional heating is used. So we can assume that the temperature of the rotor core is increasing fast to 660°C and then decreases gradually to the ambient temperature. Since this temperature is sufficiently low and heat treatment is active only for a short period of time (we assume a few minutes), the stress-relief annealing effect (Chapter 2) of aluminum casting can be neglected.

Since production of the rotor is carried out in normal atmosphere some oxidation inevitably occurs on the external surface of the rotor core. The oxidation layer is removed by grinding. However the annealing performed by some producers afterwards[4] leads to reemergence of oxidation.

For some reasons[5] the rotor squirrel cage can be made from copper rather than from the aluminum. According to [Pieters2002] the use of copper is preferable with respect to the efficiency of the motor. However it also leads to some complications due to the high melting temperature of copper (1083°C). Therefore this technique is not yet that common as aluminum casting.

As we aim at the most general consideration we are going to concentrate our attention on the following three cases:

[3] http://www.ramcorotors.com/capabilities/default.htm
[4] http://www.ramcorotors.com/capabilities/rotorA.html
[5] http://www.joliet-equipment.com/rotor_construction.htm

A) Mechanically cut laminations with an ideal fixation of the cores, i.e. without introduction of the assembling stresses.
B) Both cores are subjected to punching and assembling stresses. A decrease of the air-gap is included due to assembling stresses.
C) Both cores are subjected to punching and assembling stresses. The rotor is grinded down. The according decrease of the air-gap is included.

In order to see the joint effect of punching and the assembling stresses on the parameters of electrical machines a comparison was made with the ideal motor that is not subjected to any of these effects. Classically, the modification (due to punching and the assembling stresses) of the magnetic properties of the material in the laminated core is neglected during the numerical analysis, i.e. designers usually deal with an idealized motor.

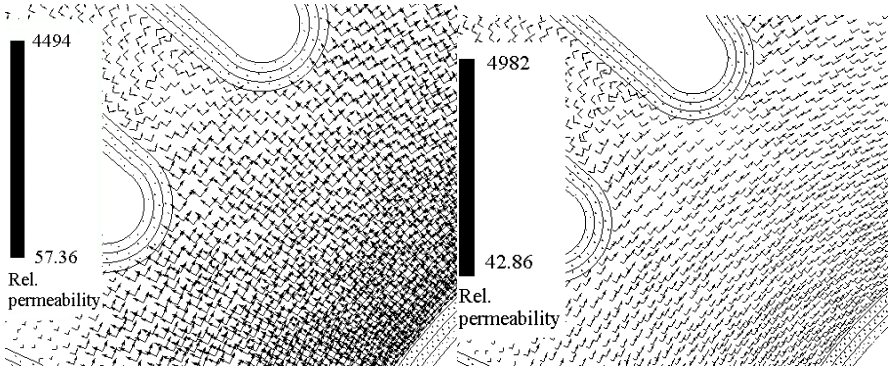

Fig. 9.2.2.4.3. The relative permeability in the rotor at J_{A+}=2.625A/mm^2 (A – effect of punching, B – joint effect of punching and assembling stresses).

It is shown in Table 9.2.2.4.1 that the inductance of the air-gap decreases by more than 8% compared to the machine unaffected by punching.

As it was mentioned earlier there might be some intermediate cases. For instance, one of the cores (usually the stator core) is annealed. In this case the observed increase of the equivalent air-gap has to decrease by 50%. This will provide a rough estimation, because the actual effect on the air-gap inductance can be somewhat stronger taking into account the possible oxidation at the edge of the laminations.

Table 9.2.2.4.1. The ratio of the inductances computed in the machine subjected to punching and the inductances computed in the ideal machine.

$L_{\varepsilon,\delta=0.394mm} / L_{\delta=0.394mm}$	Current density in the stator slots, J_{A+}, A/mm^2		
	0.875	1.75	2.625
Stator slots	0,96	0,96	0,93
Air gap	0,92	0,92	0,87
Rotor core	1,84	1,86	2,41
Stator core	1,53	1,53	1,71
Total	0,96	0,96	0,94

Assembling stresses lead to an additional deterioration of the magnetic properties and an according reduction of the contribution of the air-gap into the total inductance. We recall that the ratios presented in tables correspond to the ratios of the magnetic fluxes in the corresponding volumes. It is demonstrated in Table 9.2.2.4.2 that the equivalent increase of the air-gap is around 12% and increases with saturation of the cores. A grinded down rotor on the other hand (Table 9.2.2.4.3) leads to a 14% increase of the size of the equivalent air-gap compared to the machine unaffected by production.

Table 9.2.2.4.2. The ratio of the inductances, computed in the machine subjected to the assembling stresses (model described in 9.2.1.1.2.3) and punching, and the inductances computed in the ideal machine.

$L_{\varepsilon,\sigma,\delta=0.35mm} / L_{\delta=0.394mm}$	Current density in the stator slots, J_{A+}, A/mm^2		
	0.875	1.75	2.625
Stator slots	0,84	0,83	0,81
Air gap	0,89	0,88	0,83
Rotor core	2,50	2,55	3,22
Stator core	1,40	3,17	3,14
Total	1,00	0,99	0,96

Table 9.2.2.4.3. The ratio of the inductances computed in the machine subjected to the assembling stresses (model described in 9.2.1.1.2.3) and punching with a grinded rotor and the inductances computed in the ideal machine.

$L_{\varepsilon,\sigma,\delta=0.3625mm} / L_{\delta=0.394mm}$	Current density in the stator slots, J_{A+}, A/mm^2		
	0.875	1.75	2.625
Stator slots	0,84	0,84	0,82
Air gap	0,87	0,86	0,82
Rotor core	2,36	2,40	2,95
Stator core	3,00	2,99	2,94
Total	0,97	0,97	0,94

In this thesis we deal with a relatively simple way of fixation of the stator core. However there are different technological solutions which help to avoid the radial compression of the stator core. We cannot study all the possible combinations of the assembling stresses. But we can investigate the limits. Let us assume that the stator is fixed somehow and no elastic stresses are introduced in the core. Meanwhile the rotor is deformed. The results on the investigation of this combination of factors are presented in Table 9.2.2.4.4. Due to the reduction of the physical air-gap the air-gap inductance is generally larger compared to the undeformed rotor (Table 9.2.2.4.1). However it can be shown that if the physical air-gap is maintained constant via grinding of the rotor there will be a slight decrease of the air-gap inductance.

In general, the opposite situation, when the stator is deformed and rotor remains intact, is also possible. The corresponding results are shown in Table 9.2.2.4.5. It can be seen that the reduction of the inductance of the air-gap is practically the same as in the case that both cores are deformed in the machine. It means that the contribution due to the stator deformation is much larger compared to the rotor deformation.

The contribution of the different effects was computed in relation to a specific air-gap value. In Table 9.2.2.4.6 the contribution of each of these effects is determined. Using this data we can define the importance of the different effects with respect to the

machine parameters. For the sake of simplicity we assume that the thickness of all the laminations is equal to 0.5 mm.

Let us demonstrate how these values can be used. Consider the induction machine with 0.39 mm air-gap described in detail in [Gyselinck2000]. The stator is annealed. The rotor is pressed on the shaft and grinded down. The equivalent air-gap can be found as follows:

$$\delta_{eq} = 0.39 + 0.013\{distortion\ of\ the\ stator\ profile\} + 0.0008\{compression\ of\ the\ rotor\} +$$
$$0.01454\{compression\ of\ the\ stator\} + 0.01575\{effect\ of\ punching\ of\ the\ rotor\ sheets\} = 0.434mm$$

According to [Gyselinck2000] the equivalent air-gap value is equal to 0.44mm. This value was obtained by a trial and error procedure in order to achieve correspondence between the measured and calculated magnetization reactance of the machine. The difference of 0.006 mm (0.44 mm - 0.434 mm) can be due to the following reasons:

1) The clearance during cutting exceeded 10%, which resulted in a larger distortion of the profile;
2) The stresses due to production could be larger as the applied deformation is unknown;
3) The annealing of the stator leads to the oxidation, which adversely affects the magnetic properties.

According to [Kedous2003] the effect of punching leads to 5-10% increase of the air-gap in induction machines. The value obtained above (0.4233/0.39=1.11) is very close to this range.

Table 9.2.2.4.4. The ratio of the inductances computed in the machine subjected to punching and the assembling stresses in rotor (model (9.2.1.1.2.3)) and the inductances computed in the ideal machine.

$L_{\varepsilon,\sigma,\delta=0.379mm} / L_{\delta=0.394mm}$	Current density in the stator slots, J_{A+}, A/mm^2		
	0.875	1.75	2.625
Stator slots	0,96	0,96	0,91
Air gap	0,95	0,95	0,88
Rotor core	2,04	2,08	2,73
Stator core	1,63	1,64	1,89
Total	1,00	1,00	0,96

Table 9.2.2.4.5. The ratio of the inductances computed in the machine subjected to punching and the assembling stresses in stator (model (9.2.1.1.2.3)) and the inductances computed in the ideal machine.

$L_{\varepsilon,\sigma,\delta=0.3625mm} / L_{\delta=0.394mm}$	Current density in the stator slots, J_{A+}, A/mm^2		
	0.875	1.75	2.625
Stator slots	0.839	0.838	0.813
Air gap	0.883	0.881	0.832
Rotor core	1.895	1.927	2.559
Stator core	3.063	3.056	3.017
Total	0.978	0.977	0.949

A closer investigation is obviously needed for each structure in order to provide a more specific answer, because it is not possible to develop an ultimately universal approach. For instance, if the number of poles in the electrical machine increases the width of the

yoke decreases compared to the height of the teeth. It means that the evaluation provided in Table 9.2.2.4.4 regarding the assembling stresses cannot be applied straightforwardly.

Table 9.2.2.4.6. Physical contribution of the various production effects into the increase of the air-gap value.

Effect	Increase of the air-gap, mm
Distortion of the profile of the edge due to mechanical cutting (1 side)	0.013
Assembling stresses due to the compression of the stator core in the machine frame	0.01454
Assembling stresses due to the compression of the rotor core on the shaft	0.0008
Deterioration of the magnetic properties due to punching (1 side)	0.01575

The data regarding the effect of punching is more general. However it was collected for a sufficiently good quality of punching. So these data can lead to an underestimation if the quality of cutting is worse.

Conclusions.

In this chapter the contribution of the different production aspects to the deterioration of the magnetic properties was studied. The following reasons of the deterioration of the parameters of the rotating electrical machines can be indicated:

1) The distortion of the profile of the cut edge of the laminations. This effect is very much dependent on the parameters of cutting (Chapter 3). It has to be taken into account at the air-gap.
2) The assembling stresses due to assembling and fixation of the magnetic cores. This item is relevant for low power machines and its importance is defined both by the geometry of the machine and by the precision used during assembling. Each structure has to be analyzed specifically. With respect to induction machines, it is much more important to avoid deformation of the stator than deformation of the rotor.
3) The deterioration of the magnetic properties at the edge of the sheet due to punching (Chapter 8). In low power machines having a small zone 2 (Fig. 9.2.2.4.) the effect of punching remains practically constant and can be assumed to be independent of the geometry. Large machines were not studied in this chapter. However due to the increase of the size of zone 2 the effect of punching becomes dependent on the exact geometry of the electrical machine.

Superposition of these effects is adequate only if the machine is not saturated. Fortunately this condition is practically always satisfied in micro-motors due to the relatively large air-gap. Low power machines are usually operating at moderate magnetic fields in the core (700 A/m or less). Thus, a direct summation of the different contributions is also applicable.

Chapter 10. General conclusions.

In this chapter the new results, described in this thesis, are summarized.

1. The production elastic stresses due to the assembling of the magnetic core of electromagnetic devices were investigated numerically using FE techniques. The mechanical cutting was studied using both numerical computations and microhardness analysis. It was shown that the cutting parameters affect stronger the height of the burr than the size of the deformation affected zone.
2. The investigation of the effect of mechanical deformation on the magnetic properties of non oriented electrical steel was carried out on specially constructed measurement setups. These setups have some new features, but also certain limitations compared to the conventional measurement setups. The limitations of the constructed setups were investigated using FE computations.
3. The multidirectional magnetic investigation carried out under the applied unidirectional mechanical stress reveals nucleation of the additional magnetic anisotropy in the non-oriented electrical steel. A correspondence between the effect of tension and compression in non-oriented electrical steels was demonstrated experimentally. A link between the quasi-static magnetic losses and magnetostriction was defined, which provides a flexible tool for the investigation of magnetostriction under different external stress conditions. The anisotropy of the magnetic properties and the magnetostrictive behaviour in stacked laminations of non-oriented electrical steel can be diminished if an appropriate compression is applied in the direction normal to the plane of the laminations.
4. Plastic deformation of non-oriented electrical steels results in considerable residual stresses.
5. Low frequency local magnetic measurements were carried out in order to evaluate the effect of mechanical cutting on the magnetic properties of non-oriented electrical steel. The affected zone is approximately 5mm wide. The BH-loops observed experimentally in different subregions of the sample intersect in one point. This feature indicates that the residual stresses at the edge have a dominant effect on the deterioration of the magnetic properties of the non-oriented electrical steel. So even a short term (stress-relief) annealing could probably provide sufficient benefit with respect to the recovery of the original magnetic properties.
6. A suitable mathematical model was developed in order to introduce the effect of elastic stress into magnetic FE computations. This model allows an easy coupling of the mechanical and magnetic computations.
7. A typical geometry of a low power induction motor was used for the investigation of the effect of production stresses and the effect of punching on the parameters of the induction motor. These effects can be accounted for during magnetic numerical computations, using the unaffected magnetic material properties, via an appropriate modification of the air-gap .

References.

[AK1] AK Steel Corporation, “Selection of electrical steels for magnetic cores”, Product Data Bulletin, www.aksteel.com.

[AK2] AK Steel Corporation, “Nonoriented electrical steels”, Product Data Bulletin, www.aksteel.com.

[Anayi2003] F. Anayi, A. J. Moses, K. Jenkins, “Effect of aluminium diffusion into electrical steel on power loss under flux distortion conditions”, JMMM, vol. 254-255, January 2003, pp. 36-38.

[Augustyniak1995] B. Augustyniak, J. Degauque, “New approach to hysteresis process investigation using mechanical and magnetic Barkhausen effects”, JMMM, vol. 140-144, February 1995, pp. 1837-1838.

[Ban1989] G. Ban, G. Bertotti, “Frequency and peak induction dependence of eddy current losses in AlSiFe magnetic laminations”, IEEE Trans. on Magn., vol. 25, No. 5, September 1989, pp. 3967-3969.

[Ban2003] G. Ban, P.E. Di Nunzio, “Minimum force model. Effect of crystallographic texture on the magnetostrction and loss characteristics of non-oriented electrical steels”, JMMM, vol. 254-255, January 2003, pp. 265-268.

[Baudouin2002] P. Baudouin, “Effect of Laser and Mechanical Cutting on the Magnetic Properties of Non-Oriented Electrical Steels”, PhD thesis, 2002.

[Bajorek2000] R. Bajorek, J, Bajorek, R. Rygal, S. Zurek, M. Soinski, W. Pluta, “A compact SST for investigation of both alternating and rotational magnetization”, 1&2-Dimensional Magnetic Measurement and Testing, Bad Gastein, 2000, Paper I-10, pp. 80-86.

[Basak1990] A. Basak, A.J. Moses, R. Al-Bir, “Effect of clamping stress on power loss in powercore strip and Si-Fe transformer cores”, IEEE Trans. on Magn., Vol. 26, No. 5, September 1990, pp. 1999-2001.

[Beckley1999] P. Beckley, “Modern steels for transformers and machines”, Power Engineering Journal, August 1999, pp. 190-200.

[Bertotti1998] G. Bertotti, “Hysteresis in Magnetism”, Academic Press, 1998.

[Bertotti1988] G. Bertotti, “General properties of power losses in soft ferromagnetic materials”, IEEE Transactions on Magn., vol. 24, January 1988, pp. 621 –630.

[Bulte2002] D.P. Bulte, R.A. Langman, “Origins of the magnetomechanical effect”, JMMM, vol. 251, October 2002, pp. 229-243.

[Binesti1996] D. Binesti, J.P. Ducreux, “Core losses and efficiency of electrical motors using new magnetic materials”, IEEE Trans. on Magn., vol. 32, No. 5, September 1996, pp. 4887-4889.

[Boglietti2001] A. Boglietti, A. Cavagnino, M. Lazzari, M. Pastorelli, "Effects of punch processes on the magnetic and energetic properties of soft magnetic materials," in Proc. IEMDC 2001 Int. Electric Machines and Drives Conference, Cambridge, MA: Massachusetts Inst. Technol., June 17-20, 2001.

[Bozorth1993] R. Bozorth, “Ferromagnetism”, IEEE Press, 1993.

[Brokken1999] D. Brokken, “Numerical modeling of ductile fracture in blanking”, PhD thesis, University of Eindhoven, 1999.

[Buch1988] A. Buch, “Fatigue strength calculation”, Trans. tech publications, 1988.

[Buiron1999] N. Buiron, L. Hirsinger, R. Billardon, “A micro-macro model for magnetostriction and stress effect on magnetization”, JMMM, vol. 196-197, 1999, pp. 868-870.

[Cahn1987] R.W. Cahn, P. Haasen, “Physical metallurgy”, translated to Russian, vol. 3, “Металлургия”, Moscow, 1987.

[Campos2001] M. F. de Campos, F. J. G. Landgraf, A. P. Tschiptschin, “A method to estimate magnetic induction from texture in non-oriented electrical steels”, JMMM, vol. 226-230, Part 2, May 2001, pp. 1536-1538.

[Carlberg1971] P.M.Carlberg, “The cutting of electrical steel sheets”, Translation of presentation at the Kernkontoret Punching Conference, Stockholm, November 1971.

[Caroni1973] C.A. Caroni, E. Manghi, N.W.W. De Reca, “Influence of Dislocation on Magnetic Domains in Plastically Deformed 3% Si-Fe”, IEEE Trans. on Magn., vol. MAG-9, No. 4, December 1973, pp. 647-650.

[Chang1998] S.K. Chang, J.S. Woo, S.Y. Cha, I.B. Chudakov, “Stabilization and destabilization of domain wall posotion in Fe-Si polycrystals using magnetic annealing effects”, JMMM, vol. 177-181, January 1998, pp. 217-219.

[Chari2000] M.V.K. Chari, S.J. Salon, “Numerical methods in electromagnetics”, Academic Press, 2000.

[Chevalier2000_1] T. Chevalier, A. Kedous-Lebouc, B. Cornut, “A method to evaluate effects of eccentricity and anisotropy on iron losses of electrical machines. Application to an induction motor”, JMMM, vol. 215-216, June 2000, pp. 604-606.

[Chevalier2000_2] T. Chevalier, A. Kedous-Lebouc, B. Cornut, “Influence of electrical sheet width on dynamic magnetic properties”, JMMM, vol. 215-216, June 2000, pp. 623-625.

[Coombs2001] A. Coombs, M. Lindenmo, D. Snell, D. Power, “Review of the Types, Properties, Advantages, and Lastest Developments in Insulating Coatings on Nonoriented Electrical Steels”, IEEE Trans. on Magn., vol. 37, No. 1, January 2001, pp. 544-557.

[Cornut1996] B. Cornut, A. Kedous-Lebouc, Th. Waeckerlé, “From metallurgy to modelling of electrical steels: A multiple approach to their behaviour and use based on physics and experimental investigations”, JMMM, vol. 160, July 1996, pp. 102-108.

[Dabrowski1989] M.Dabrowski, T.Zgodzinski, “Some Effects of Unidirectional Stress in Si-Fe Sheets”, Physica Scripta, vol. 40, 1989, pp. 514-517.

[Degauque1982] J. Degauque, B. Astie, J.L. Porteseil, R. Vergne, “Influence of the grain size on the magnetic and magnetomechanical properties of high-purity iron”, JMMM vol. 26, March 1982, pp. 261-263.

[Denma2000] H. Denma, Y. Ishihara, T. Todaka, M. Doi, “Effect of grain diameter on iron loss properties of non-oriented silicon steel sheets”, JMMM vol. 215-216, June 2000, pp. 106-109.

[Desvaux2003] S. Desvaux, M. Duquennoy, J. Gualandri, M. Ourak, "The evaluation of surface residual stress in aeronautic bearings using Barkhausen noise effect", accepted for publication in *NDT&E International*, 2003.

[Devine1996] M.K. Devine, D.C. Jiles, "Composition Dependence of the Magnetomechanical Effect and Magnetostriction", IEEE Trans. on Magn., vol. 32, No. 5, September 1996, pp. 4740-4742.

[DeWulf2002] M. De Wulf, "Karakterisering en energieverlieszen onder unidirectionele magnetisatie in relatie tot de microstructuur van zacht magnetische materialen", PhD thesis, University of Ghent, 2002.

[Dhar2001] A. Dhar, L. Clapham, D. L. Atherton, "Influence of uniaxial plastic deformation on magnetic Barkhausen noise in steel", NDT & E International, vol. 34, Issue 8, Dec 2001, pp. 507-514.

[Djachenko1982] S.S. Djachenko, V.B. Rabuhin, "Physical principles of the metal hardness", in Russian, Kharkov, «Вища школа», 1982.

[Duan1996] X. Duan, H. Huneus, T. Kochmann, K. Leuridan, R. Kaczmarek, F. Protat, "Effect of annealing temperature and heating rate on the magnetic and mechanical properties of electrical steel", JMMM, vol. 160, July 1996, pp. 133-135.

[Dupre2003] L. Dupré, M. De Wulf, D, Makaveev, J. Melkebeek, "Indirect Identification of Magnetostriction of SiFe alloys", IEEE Trans. on Magn., vol. 39, No. 5, September 2003, pp. 3432-3434.

[Duquennoy2001] M. Duquennoy, M. Ouaftouh, M.L. Qian, F. Jenot, M. Ourak, "Ultrasonic characterization of residual stresses in steel rods using a laser line source and piezoelectric transducers", *NDT&E International*, vol. 34, July 2001, pp. 355-362.

[Emura2001] M. Emura, M.F. de Campos, F.J.G. Landgraf, J.C. Teixeira, "Angular dependence of ,agnetic properties of 2% silicon electrical steel", JMMM, vol. 226-230, May 2001, pp. 1524-1526.

[Emura2003] M. Emura, F.J.G. Landgraf, W. Ross, J.R. Baretta, "The influence of cutting technique on the magnetic properties of electrical steels", JMMM vol. 254-255, 2003, pp. 358-360.

[Endo2001] H.Endo, S.Hayano, Y.Saito, M.Fujikura, C.Kaido, "Magnetization Curve Plotting from the Magnetic Domain Images", IEEE Trans. on Magn., vol. 37, No. 4, July 2001, pp. 2727-2730.

[Endo2003] H. Endo, S. Hayano, H. Mogi, M. Fujikura, C. Kaido, Y. Saito, "Estimation of iron loss distribution by image Helmholtz equation method", IEEE Trans. on Magn., vol. 39, No. 3, May 2003, pp. 1377-1380.

[Fanni2003] A. Fanni, A. Montisci, "A neural inverse problem approach for optimal design", IEEE Trans. on Magn., vol. 39, No. 3, May 2003, pp. 1305-1308.

[Fiorillo1980] F.Fiorillo, P. Mazzetti, G. Montalenti, G.P. Soardo, "Loss anomaly in plastically deformed 3% SiFe laminations", JMMM 19 (1980) pp. 371-373.

[Foot1981] G.E. Foot, K.J. Overshott, "The effect of tensile stress on the domain wall motion and wall bowing in 3% grain-oriented silicon-iron", IEEE Trans. on Magn., vol. MAG-17, No. 6, November 1981, pp. 2869-2871.

[Fujimura2003] H. Fujimura, H. Yashiki, H. Kojima, T. Nakayama, "Effect of stress due to stamping and interlocking on magnetic properties of non-oriented electrical steel sheet", presented at SMM16 Conference in Düsseldorf, 2003.

[Fujiwara1995] K. Fujiwara, T. Nakata, N. Takahashi and H. Ohashi, "On the Continuity of the Magnetizing Current Density in 3-D Magnetic Field Analysis with Edge Element", IEEE Trans. on Magn., vol. 31, No. 3, May 1995, pp. 1364-1367.

[Garshelis1986] I.J. Garshelis, W.S. Fiegel, "Recovery of magnetostriction values from the stress dependence of Young's modulus", IEEE Trans. on Magn., vol. 22, No. 5, Sept. 1986, pp. 436-438.

[Garshelis1994] I.J. Garshelis, "Hysteresis and other relationships between technical magnetostriction and magnetization", J. Appl. Phys. 75 (10), 15 May 1994, pp. 5670-5672.

[Gauthier1998] J. Gauthier, T.W. Krause, D.L. Atherton, "Measurement of residual stress in steel using the magnetic Barkhausen noise technique", *NDT&E International*, vol. 31, No. 1, 1998, pp. 23-31.

[Godec1977] Z. Godec, "Influence of slitting on core losses and magnetization curve of grain-oriented electrical steels", IEEE Trans. on Magn., vol. 13, No. 4, July 1977, pp. 1053-1057.

[Grimm1978] W. Grimm, W. Jillek, A. Hubert, "Measurement and consequences of the stresses induced by coating layers onto oriented transformer steel", JMMM, vol. 9, October-November 1978, pp. 225-228.

[Gyselinck2000] J. Gyselinck, "Twee-Dimesionale Dynamische Eindige-Elementenmodellering van Statische en Roterende Elektromagnetische Energieomzetters", PhD thesis, University of Ghent, 2000.

[Hall2003] J.P. Hall, A.J. Moses, T. Irons, D. Snell, "Novel magnetic method for the detection of residual curvature in electrical steel", JMMM, vol. 254-255, January 2003, pp. 64-66.

[Hashi1996] S. Hashi, K. Ishiyama, K.I. Arai, M. Kawasaki, Y. Yamashiro, "Study on the deformation of 3% Si-Fe Crystal with Magnetic Filed Being Deviated from [001]", IEEE Trans. on Magn., vol. 32, No. 5, September 1996, pp. 4848-4850.

[Hauser1992] H. Houser, P. Fulmek, "The Effect of Mechanical Stress on the Magnetization Curves of Ni- and FeSi-Single Crystals at Strong Fields", IEEE Trans. On Magn., vol. 28, No. 3, May 1992, pp. 1815-1825.

[Hill-Cottingham2003] R.J. Hill-Cottingham, P.C. Coles, D. Rodger, H.C. Lai, "Numerical models of an induction machine", IEEE Trans. on Magn., vol. 39, No. 3, May 2003, pp. 1551-1553.

[Hirano2003] M. Hirano, Y. Ishihara, K. Harada, T. Todaka, "A study on measurement of magnetostriction of silicon steel sheet by laser displacement meter", JMMM, vol. 254-255, January 2003, pp. 43-46.

[Hogston1994] S.N. Hogston, P.T. Squire, D. Atkinson, "Domain Structure Studies by Means of High-Resolution ΔE measurements", IEEE Trans. on Magn., vol. 30, No. 6, November 1994, pp. 4803-4805.

[Holt1969] C. Holt, J.A. Robey, "The AC Magnetostriction of 3.25% Grain-Oriented Silicon Iron under Combined Longitudinal and Normal Compressive Stresses", IEEE Trans. on Magn., vol. MAG-5, No. 3, September 1969, pp. 384-388.

[Hou1994] C.K. Hou, S. Lee, "Effect of Rolling Strain on the Loss Separation and Permeability of Lamination Steels", IEEE Trans. on Magn., vol. 30, No. 2, March 1994, pp. 212-216.

[Hubert1999] O. Hubert, L. Hirsinger, E. Hug, "Experimental influence of internal stresses on the anhysteretic curve of 3% SiFe nonoriented alloys", JMMM, vol. 196-197, May 1999, pp. 322-324.

[Hubert2003] O. Hubert, N. Jendly, L. Daniel, "Modelling of the influence of micro-plasticity on the magnetic behaviour of ferromagnetic polycrystals through a multiscale approach", presented at SMM16 Conference in Düsseldorf, 2003.

[Hubert2003_2] O. Hubert, L. Daniel, R. Billardon, "Experimental analysis of the magnetoelastic anisotropy of a non-oriented silicon iron alloy", JMMM, vol. 254-255, January 2003, pp. 352-354.

[Hug2002] E. Hug, O. Hubert, J.J. Van Houtte, "Effect of internal stresses on the magnetic properties of non-oriented Fe–3wt.% Si and (Fe,Co)–2wt.% V alloys", Materials Science and Engineering, vol. A332, July 2002, pp. 193–202.

[Iordache2003] V.E. Iordache, F. Ossart, E. Hug, "Magnetic characterization of elastically and plastically tensile strained non-oriented Fe-3.2%Si steel", JMMM, vol. 254-255, January 2003, pp. 57-59.

[Jagadish1990] C. Jagadish, L. Clapham, D.L. Atherton, "Influence of uniaxial elastic stress on power spectrum and pulse height distribution of surface barkhausen noise in pipeline steel", IEEE Trans. on Magn., vol. 26, No. 3, May 1990, pp. 1160-1163.

[Jillek1980] W. Jillek and A. Hubert, "The influence of mechanical stresses on losses and domains of oriented transformer steel", JMMM, vol. 19, April 1980, pp. 365-368.

[Jiraskova2000] Y. Jiraskova, O. Schneeweiss, T. Van Hoecke, D. Segers, Ch. Dauwe, "Investigation of defects and stresses in SiFe steel surfaces", JMMM, vol. 215-216, June 2000, pp. 118-120.

[Johansson1999] J. Johansson, M. Oden, X.-H. Zeng, "Evolution of the residual stress state in a duplex stainless steel during loading", Acta Metallurgica, vol. 47, No. 9, 1999, pp. 2669-2684.

[Kawase2003] Y. Kawase, T. Yamaguchi, S. Sano, M. Igata, K. Ida, A. Yamagiwa, "3-D eddy current analysis in a silicon steel sheet of an permanent magnet motor", IEEE Trans. on Magn., vol. 39, No. 3, May 2003, pp. 1448-1451.

[Kedous2003] A. Kedous-Lebouc, B. Cornut, J.C. Perrier, Ph. Manfé and Th. Chevalier, "Punching influence on magnetic properties of the stator teeth of an induction motor", JMMM, vol. 254-255, January 2003, pp. 124-126.

[Kuroda2003] M. Kuroda, S. Yamanaka, Y. Isobe, "Detection of plastic deformation and estimation of maximum value of residual stress in low carbon steel by X-ray stress analysis using statistical techniques", *NDT&E International*, vol. 36, October 2003, pp. 497-502.

[Landgraf2000] F.J.G. Landgraf, M. Emura, J.C. Teixeira, M.F. de Campos, "Effect of grain size, deformation, aging and anisotropy on hysteresis loss of electrical steels", JMMM, vol. 215-216, June 2000, pp. 97-99.

[Landgraf2003] F.J.G. Landgraf, T. Yonamine, M. Emura, M.A. Cunha, "Modelling the angular dependence of magnetic properties of a fully processed non-oriented electrical steel", JMMM, vol. 254-255, January 2003, pp. 328-330.

[Langman1985] R. Langman, "The effect of stress on the magnetization of the mild steel at moderate field strengths", IEEE Trans. on Magn., vol. 21, No. 4, July 1985, pp. 1314-1320.

[Langman1990] R. Langman, "Magnetic Properties of Mild Steel under Conditions of Biaxial Stress", IEEE Trans. on Magn., vol. 26, No. 4, July 1990, pp. 1246-1251.

[Lenz1990] J.E. Lenz, "A Review of Magnetic Sensors", Proceedings of the IEEE, vol. 78, No. 6, 1990, pp. 973-989.

[Lindenmo2000] M. Lindenmo, A. Coombs and D. Snell, "Advantages, properties and types of coatings on non-oriented electrical steels", JMMM, vol. 215-216, June 2000, pp. 79-82.

[Liorzou1999] F. Liorzou, D.L. Atherton, "Effects of compressive stress on a steel cube using tensor magnetization and magnetostriction analysis", JMMM, vol. 195, April 1999, pp. 174-181.

[Liu1994] J. Liu. A. Basak, A.J. Moses, G.H. Shirkoohi, "A method of anisotropic steel modeling using finite element method with confirmation by experimental results", IEEE Trans. on Magn., vol. 30, No. 5, September 1994, pp. 3391-3394.

[Liuzzi2003] G. Liuzzi, S. Lucidi, F. Parasiliti, M. Villani, "Multiobjective optimization techniques for the design of induction motors", IEEE Trans. on Magn., vol. 39, No. 3, May 2003, pp. 1261-1264.

[LoBue1999] M. LoBue, V. Basso, F. Fiorillo and G. Bertotti, "Effect of tensile and compressive stress on dynamic loop shapes and power losses of Fe-Si electrical steels", JMMM, vol. 196-197, May 1999, pp. 372-374.

[LoBue2000] M. LoBue, C. Sasso, V. Basso, F. Fiorillo and G. Bertotti, "Power losses and magnetization process in Fe–Si non-oriented steels under tensile and compressive stress", JMMM, vol. 215-216, June 2000, pp. 124-126.

[Loisos2001] G. Loisos, A.J. Moses, "Critical Evaluation and Limitations of Localized Flux Density Measurements in Electrical Steel", IEEE Trans. on Magn., vol. 37, No. 4, July 2001, pp. 2755-2757.

[Loisos2003_1] G. Loisos, A.J. Moses, "Demonstration of a new method for magnetic flux measurement in the interior of a magnetic material", Sensors and Actuators A: Physical, vol. 106, September 2003, pp. 104-107.

[Loisos2003_2] G. Loisos, A.J. Moses, P. Beckley, "Electrical stress on electrical steel coatings", JMMM, vol. 254-255, January 2003, pp. 340-342.

[Loisos2003_3] G. Loisos, A.J. Moses, "Variation of magnetic flux density with distance from the cut edge of non-oriented electrical steel", presented at SMM16 Conference in Düsseldorf, 2003.

[Lu1998] A.L. Lu, F. Tang, X.J. Luo, J.F. Mei, H.Z. Fang, "Research on residual-stress reduction by strong pulsed magnetic treatment", Journal of Materials Processing Technology, vol. 74 (1998) pp. 259-262.

[Luciano1997] B.A. Luciano, C.S. Kiminami, "An amorphous core transformer: design and experimental performance", Material Science and Engineering, vol. A226-228, June 1997, pp. 1079-1082.

[Lukas2001] D. Lukas, I. Kopriva, "Shape Optimization of Homogeneous Electromagnets and their Application for Measurement of Magneto-optical Effects", presented at the 13th COMPUMAG Conference, Evian France, July 2, 2001.

[Luming2003] L. Luming, H. Songling, W. Viaoeng, S. Keren, W. Su, "Magnetic field abnormality caused by welding residual stresses", JMMM, vol. 261, May 2003, pp. 385-391.

[Maeda1996] H. Maeda, K. Harada, Y. Ishihara, T. Todaka, "Performance of the magnetostriction of a silicon steel sheet with a bias field", JMMM, vol. 160, July 1996, pp. 149-150.

[Makar1998_1] J.M. Makar, B.K. Tanner, "The in situ measurement of the effect of plastic deformation on the magnetic properties of steel Part I – hysteresis loops and magnetostriction", JMMM, vol. 184, April 1998, pp. 193-208.

[Makar1998_2] J.M. Makar, B.K. Tanner, "The in situ measurement of the effect of plastic deformation on the magnetic properties of steel Part II – permeability curves", JMMM, vol. 187, September 1998, pp. 353-365.

[Makar1998_3] J.M. Makar, B.K. Tanner, "The effect of stresses approaching and exceeding the yield point on the magnetic properties of high strength pearlitic steels", *NDT&E International*, vol. 31, No. 2, 1998, pp. 117-127.

[Makar2000] J.M. Makar, B.K. Tanner, "The effect of plastic deformation and residual stress on the permeability and magnetostriction of steels", JMMM, vol. 222, December 2000, pp. 291-304.

[Makaveev2003] D. Makaveev, "Karakteriseren en neuraal-netwerkgebaseerd medelleren van rotationele magnetisatie in niet-georienteerd elektrisch staal", proefschrift, Universiteit Gent, 2003.

[Makaveev2000] D. Makaveev, M. von Rauch, M. De Wulf, J. Melkebeek, "Accurate field strength measurement in rotational single sheet testers", JMMM, vol. 215-216, June 2000, pp. 673-676.

[Mao2001] W.Mao and D.L.Atherton, "Effect of tensile stress on the 3D reversible and irreversible differential magnetic susceptibilities", J. of Applied Physics, vol. 89, num. 11, June 2001, pp. 7251-7253.

[Maylin1993] M.G. Maylin, P.T. Squire, "The effects of stress on induction, differential permeability and Barkhausen count in a ferromagnet", IEEE Trans. on Magn., vol. 29, No. 6, November 1993, pp. 3499-3501.

[Morgan1981] J.V.S. Morgan, S. Hill, K.J. Overshott, "Domain wall angles in silicon-iron with (110) surface", IEEE Trans. on Magn., vol. MAG-17, No. 6, November 1981, pp. 2875-2877.

[Moses1974] A.J. Moses, "Measurement of Magnetostriction and Vibration with Regard to Transformer Noise", IEEE Trans. on Magn., vol. MAG-10, No. 2, June 1974, pp. 154-156.

[Moses1980] A.J. Moses, D. Davies, "Influence of Compressive Stress on Magnetic Properties of Commercial (110)[001] Oriented Silicon-Iron", IEEE Trans. on Magn., vol. MAG-16, No. 2, March 1980, pp. 454-460.

[Moses1981] A.J. Moses, "Effects of stress on the magnetic properties of grain-oriented silicon iron magnetized in various directions", IEEE Trans. on Magn., vol. 25, No. 5, September 1989, pp. 4003-4005.

[Moses1989] A.J. Moses, H. Rahmatizadeh, "Effects of stress on iron loss and flux distribution of an induction motor stator core", IEEE Trans. on Magn., vol. 25, No. 5, September 1989, pp. 4003-4005.

[Moses1994] A.J. Moses, M. Yasin, M. Soinski, "Evaluation of novel transformer cores", JMMM, vol. 133, May 1994, pp. 637-639.

[Moses1995] A.J. Moses, T. Meydan, H.F. Lau, "Domain structures in silicon-iron in the stress transition stage", IEEE Trans. on Magn., vol. 31, No. 6, November 1995, pp. 4166-4168.

[Moses1998] A.J. Moses, "Comparison of the transformer loss prediction from computed and measured flux density distribution", IEEE Trans. on Magn., vol. 34, No. 4, July 1998, pp. 1186-1188.

[Moses2000_1] A.J. Moses, A. Ntatsis, T. Kochmann, J, Schneider, "Magnetostriction in non-oriented electrical steels: general trends", JMMM, vol. 215-216, June 2000, pp. 669-672.

[Moses2000_2] A.J. Moses, N. Derebasi, G. Loisos and A. Schoppa, "Aspects of the cut-edge effect stress on the power loss and flux density distribution in electrical steel sheets", JMMM, vol. 215-216, June 2000, pp. 690-692.

[Moses2000_3] A.J. Moses, N. Derebasi, G. Loisos, A. Schoppa, "Aspects of the cut-edge effect stress on the power loss and flux density distribution in electrical steel sheets", JMMM, vol. 215-216, June 2000, pp. 690-692.

[Moses2000_4] A.J. Moses, G. Loisos, "Comparison of localized flux density measurement methods in electrical steels", 1&2-Dimensional Magnetic Measurement and Testing, Bad Gastein, 2000, pp. 293-296.

[Moses2003_1] A. J. Moses, J. Leicht, P. Anderson, "Characterising electrical steels under complex magnetising conditions", JMMM, vol. 254-255, January 2003, pp. 54-56.

[Moses2003_2] A.J. Moses, "Prediction of core losses of three phase transformers from estimation of the components contributing to the building factor", JMMM, vol. 254-255, January 2003, pp. 615-617.

[Nakase1998] T. Nakase, M. Nakano, K. Fujiwara, N. Takahashi, "Measuring System for Magnetostriction of Silicon Steel Sheet under AC Excitation Using Optical Methods", IEEE Trans. on Magn., vol. 34, No. 4, July 1998, pp. 2072-2074.

[Nakase1999] T. Nakase, M. Nakano, K. Fujiwara, N. Takahashi, "Single Sheet Tester Having Open Magnetic Path for Measurement of Magnetostriction of Electrical Steel Sheet", IEEE Trans. on Magn., vol. 35, No. 5, September 1999, pp. 3956-3958.

[Nakata1987] T. Nakata, Y. Kawasem, M. Nakano, "Improvement of measuring accuracy of magnetic field strength in single sheet testers by using two H coils", IEEE Trans. on Magn., vol. 23, No. 5, September 1987, pp. 2596-2598.

[Nakata1990] T. Nakata, N. Takahashi, K. Fujiwara, "Effects of eddy currents in the specimen in a single sheet tester on measurement errors", IEEE Trans. on Magn., vol. 26, No. 5, September 1990, pp. 1641-1643.

[Nakata1992] T. Nakata, M. Nakano, K. Kawahara, "Effects of stress due to cutting on magnetic characteristics of silicon steel", IEEE Trans. on Magn., vol. 7, No. 6, June 1992, pp. 453-457.

[Nam2003] H. Nam, K.H. Ha, J.J. Lee, J.P. Hong, G.H. Kang, "A study on iron loss analysis method considering the harmonics of the flux density waveform using iron loss curves tested on Epstein samples", IEEE Trans. on Magn., vol. 39, No. 3, May 2003, pp. 1472-1475.

[Ng1996] H.T. Ng, C.C. Yu, D.H.L. Ng, "Domain nucleation and annihilation in a steel bar subjected to an increasing tensile load", IEEE Trans. on Magn., vol. 32, No. 5, September 1996, pp. 4851-4853.

[Nyenhuis2000] E. te Nyenhuis, R. Girgis, "Effect of slitting electrical core steel on measured iron loss", JMMM, vol. 215-216, 2000, pp. 110-111.

[Nozawa1996] T. Nozawa, M. Mizogami, H. Mogi, Y. Matsuo, "Magnetic properties and dynamic domain behavior in grain-oriented 3% Si-Fe", IEEE Trans. on Magn., vol. 32, No. 2, March 1996, pp. 572-589.

[Ossart1999] F. Ossart, L. Hirsinger, R. Billardon, "Computation of electromagnetic losses including stress dependence of magnetic hysteresis", JMMM, vol. 196-197, May 1999, pp. 924-926.

[Ossart2000] F. Ossart, E. Hug, O. Hubert, C. Buvat, R. Billardon, "Effect of punching on electrical steels: experimental model and numerical coupled analysis", IEEE Trans. on Magn., vol. 36, No. 5, September 2000, pp. 3137-3140.

[Pearson2000] J. Pearson, P.T. Squire, M.G. Maylin, J.G. Gore, "Biaxial stress effects on the magnetic properties of pure iron", IEEE Trans. on Magn., vol. 36, No. 5, September 2000, pp. 3251-3253.

[Peters2002] D.T. Peters, D.J. Van Son, J.G. Cowie, E.F. Brush, "Improved Motor Energy Efficiency and Performance through the Die-Cast Copper Rotor", presented at ICEM Conference, Brugges, Belgium, 2002.

[Phillips1974] R. Phillips, K.J. Overshott, "Domain Configuration Under Rotational Flux and Applied Stress Conditions in Silicon-Iron", IEEE Trans. on Magn., vol. MAG-10, No. 2, June 1974, pp. 168-169.

[Pitman1990] K.C. Pitman, "The influence of stress on ferromagnetic hysteresis", IEEE Trans. on Magn., vol. 26, No. 5, September 1990, pp. 1978-1980.

[Ponnaluri2001] S.V. Ponnaluri, R. Cherukuri and P. A. Molian, "Core loss reduction in grain-oriented silicon steels by excimer laser scribing: Part I: experimental work", Journal of Materials Processing Technology, vol. 112, May 2001, pp. 199-204.

[PremKumar2003] R. PremKumar, I. Samajdar, N.N. Viswanathan, V. Singal, V. Seshadri, "Relative effect(s) of texture and grain size on magnetic properties in a low silicon non-grain oriented electrical steel", JMMM, vol. 264, 2003, pp. 75-85.

[Pulnikov2002] A. Pulnikov, P. Baudouin, L. Dupré, M. De Wulf, Y. Houbaert, J. Melkebeek, "Investigation of Local Magnetic Effects in Rotating Electrical Machines", Proc. 7e Conf. ELECTRIMACS, Montréal, 18-21 August, 2002, ISBN 2-921145-31-6.

[Pulnikov2003_1] A. Pulnikov, P. Baudouin, J. Melkebeek, "Induced stresses due to the mechanical cutting of non-oriented electrical steels**",** JMMM, vol. 254-255, January 2003, pp. 355-357.

[Pulnikov2003_2] A. Pulnikov, V. Permiakov, M. De Wulf, J. Melkebeek, "Measuring setup for the investigation of the influence of mechanical stresses on magnetic properties of electrical steel", JMMM, vol. 254-255, January 2003, pp. 47-49.

[Rice1988] R.C. Rice, B.N. Leis, D.V. Nelson, H.D. Berns, D. Lingenfelser, M.R. Mitchell, "Fatigue design handbook", Society of Automotive Engineers, 1988.

[Roychowdhury2002] S. Roychowdhury, Y.D.A. Roy and R.H. Dodds, "Ductile tearing in thin aluminum panels: experiments and analyses using large-displacement, 3-D surface cohesive elements", Engineering Fracture Mechanics, vol. 69, May 2002, pp. 983-1002.

[Rygal2000] R. Rygal, A.J. Moses, N. Derebasi, J. Schneider and A. Schoppa, "Influence of cutting stress on magnetic field and flux density distribution in non-oriented electrical steels", JMMM, vol. 215-216, June 2000, pp. 687-689.

[Ryu2000] K.S. Ryu, J.S. Park, C.G. Kim, D. Son, "Calculation of Saturation Magnetostriction from Measured Second Harmonics in 3% Silicon Steel", IEEE Trans. on Magn., vol. 36, No. 5, September 2000, pp. 3232-3234.

[Sablik1993] M.J. Sablik, D.C. Jiles, "Coupled Magnetoelastic Theory of Magnetic and Magnetostrictive Hysteresis", IEEE Trans. on Magn., vol. 29, No. 3, July 1993, pp. 2113-2123.

[Sablik1994] M.J. Sablik, L.A. Riley, G.L. Burkhardt, H. Kwun, P.Y. Cannell, K.T.Watts, R.A.Langman, "Micromagnetic model for the influence of biaxial stress on hysteretic magnetic properties", J. Appl. Phys. Vol. 75(10), May 1994, pp. 5673-5675.

[Sablik1995] M.J. Sablik, H. Kwun, G.L. Burkhardt, "Biaxial stress effects on magnetization perpendicular to the stress plane", IEEE Trans. on Magn., vol. 31, No. 6, November 1995, pp. 3665-3661.

[Sablik1997] M.J. Sablik, "A model for asymmetry in magnetic property behaviour under tensile and compressive stress in steel", IEEE Trans. on Magn., vol. 33, No. 5, September 1997, pp. 3958-3960.

[Sablik2001] M.J. Sablik, "Modeling the effect of grain size and dislocation density on hysteretic magnetic properties in steels", J. Appl. Phys., vol. 89(10), May 2001, pp. 5610-5613.

[Saito2000] A. Saito, T. Yamamoto, H. Iwasaki, "Magnetization properties and domain structures of grain-oriented silicon steel sheets due to bending stress", IEEE Trans. on Magn., vol. 36, No. 5, September 2000, pp. 3078-3080.

[Salon1995] S.J. Salon, "Finite element analysis of electrical machines", Kluwer Academic Publishers, 1995.

[Sasaki1987] T. Sasaki, S. Takada, F. Ishibashi, I. Suzuki, S. Noda, M. Imamura, "Magnetostrictive vibration of electrical steel sheets under a non-sinusoidal magnetizing condition", IEEE Trans. on Magn., vol. 23, No. 5, September 1987, pp. 3077-3079.

[Schneeweiss2000] O. Schneeweiss, N. Pizurova, Y. Jiraskova, T. Zak, B. Cornut, "Fe_3Si surface coating on SiFe steel", JMMM, vol. 215-216, 2000, pp. 115-117.

[Schoppa2000_1] A. Schoppa, J. Schneider and C. -D. Wuppermann, "Influence of the manufacturing process on the magnetic properties of non-oriented electrical steels", JMMM, vol. 215-216, June 2000, pp. 74-78.

[Schoppa2000_2] A. Schoppa, J. Schneider and J. -O. Roth, "Influence of the cutting process on the magnetic properties of non-oriented electrical steels", JMMM, vol. 215-216, 2 June 2000, pp. 100-102.

[Schoppa2003_1] A. Schoppa, J. Schneider, C. -D. Wuppermann and T. Bakon, "Influence of welding and sticking of laminations on the magnetic properties of non-oriented electrical steels", JMMM, vol. 254-255, January 2003, pp. 367-369

[Schoppa2003_2] A. Schoppa, H. Louis, F. Pude and Ch. von Rad, "Influence of abrasive waterjet cutting on the magnetic properties of non-oriented electrical steels", JMMM, vol. 254-255, January 2003, pp. 370-372.

[Senda2000] K. Senda, M. Kurosawa, M. Ishida, M. Komatsubara and T. Yamaguchi, "Local magnetic properties in grain-oriented electrical steel measured by the modified needle probe method", JMMM vol. 215-216, June 2000, pp. 136-139.

[Shilling1974] J.W. Shilling, G.L. Houze Jr., "Magnetic Properties and Domain Structure in Grain-Oriented 3% Si-Fe", IEEE Trans. on Magn., vol. MAG-10, No. 2, June 1974, pp. 195-223.

[Shimazu1990] T. Shimazu, M. Shiozaki, "Effects of grain size and frequency on eddy current loss in Si-Fe sheets", IEEE Trans. on Magn., vol. 26, No. 5, September 1990, pp. 1972-1974.

[Shirkoohi1994] G.H. Shirkoohi, A.M. Yahya, "Localised flux and iron loss in the tooth tip region of a three-phase induction machine stator core", JMMM, vol. 133, May 1994, pp. 644-646.

[Shirkoohi1996] G.H. Shirkoohi, "Anisotropic dependence of magnetostriction in electrical steels under applied linear stress", JMMM, vol. 157-158, May 1996, pp. 516-518.

[Sieradzki1998] S. Sieradzki, R. Rygal, M. Soinski, "Apparent core losses and core losses in five-limb amorphous transformer of 160kVA", IEEE Trans. on Magn., vol. 34, No. 4, July 1998, pp. 1189-1191.

[Sievert1990] J. Sievert, "Recent advances in the one- and two-dimensional magnetic measurement technique for electrical steel sheet", IEEE Trans. on Magn., vol. 26, No. 5, September 1990, pp. 2553-2558.

[Squire1996] P.T. Squire, S.N. Hogsdon, H. Hauser, "Domain processes in grain-oriented silicon steel studied by means of ΔE effect", JMMM, vol. 157-158, May 1996, pp. 527-528.

[Stephenson1986] E.T. Stephenson, A.R. Marder, "The Effect of Grain Size on the Core Loss and Permeability of Motor Lamination Steel", IEEE Trans. on Magn., vol. 22, No. 2, March 1986, pp. 101-106.

[Stevens2000] K.H. Stevens, "Stress dependence of ferromagnetic hysteresis loops for two grades of steel", *NDT&E International*, vol. 33, 2000, pp. 111-121.

[Szewczyk] R. Szewczyk, A. Bienkowski, "Application of the energy-based model in the field of magnetoelastic properties of amorphous alloys", to be published in JMMM.

[Taguchi1974] S. Taguchi, T. Yamamoto, A. Sakakura, "New Grain-Oriented Silicon Steel with High Permeability "ORIENTCORE HI-B"", IEEE Trans. on Magn., vol. MAG-10, No. 2, June 1974, pp. 123-127.

[Takezawa2003] M. Takezawa, J. Yamasaki, T. Honda, C. Kaido, "Domain structure of chemically thinned non-oriented electrical sheet", JMMM, vol. 254-255, January 2003, pp. 167-169.

[Tang1998] F. Tang, A.L. Lu, H.Z. Fang, J.F. Mei, "Effect of magnetic treatment on magnetostrctive behaviour of HT70 steel", Materials Science and Engineering, vol. A248, 1998, pp. 98-100.

[Taylor1983] R. A. Taylor, J. P. Jakubovics, B. Astié and J. Degauque, "Direct observation of the interaction between magnetic domain walls and dislocations in iron", JMMM, vol. 31-34, part 2, February 1983, pp. 970-972.

[Tutkin2003] N. Tutkun and A. J. Moses, "Measurements of power loss distribution in a typical stator core under PWM voltage excitation", JMMM, vol. 262, June 2003, pp. 230-234.

[Vandevelde2003] L. Vandevelde, J.A.A. Melkebeek, "Magnetic forces and magnetostriction in electrical machines and transformer cores", IEEE Trans. on Magn., vol. 39, No. 3, May 2003, pp. 1618-1621.

[VanKeer1996] R. Van Keer, L.R. Dupre, J.A.A. Melkebeek, "On a numerical method for 2D magnetic field computations in a lamination with enforced total flux", Journal of Computational and Applied Mathematics, vol. 72, 1996, pp. 179-191.

[Weidenfeller1996] B. Weidenfeller, W. Riehemann, "Frequency dependence of loss-improvement of grain oriented silicon steels by laser scribing", JMMM, vol. 160, 1996, pp. 136-138.

[Williams2003] P.I. Williams, A.J. Moses, T. Meydan, R.J.D. Tilley, "Amorphization of bulk magnetic materials by an arc melting technique", JMMM, vol. 254-255, January 2003, pp. 17-19.

[Wisselink2000] H. Wisselink, "Analysis of guillotining and slitting, finite element simulations", PhD thesis, http://www.ub.utwente.nl/webdocs/wb/1/t0000015.pdf, University of Twente, 2000.

[Wu2002] S. Wu, A. Lu, H. Zhao, H. Fang, F. Tang, "Micromechanism of residual stress reduction by low frequency alternating magnetic field treatment", Materials Science and Engineering A, vol. 328, May 2002, pp. 133-136.

[Yamaguchi1989] T. Yamaguchi, K. Takeda, "Effects of [001] axis deflection on magnetic properties of (110)[001] Si-Fe with various thicknesses", Physica Scripta, vol. 40, 1989, pp. 574-576.

[Yamaguchi1998] T. Yamaguchi, K. Senda, M. Ishida, K. Sato, A. Honda, T. Yamomoto, "Theoretical analysis of localized magnetic flux measurement by needle probe", J. Phys. IV France, vol. 8, 1998, pp. 717-719.

[Yamasaki1996] T. Yamasaki, S. Yamamoto, M. Hirao, "Effect of applied stresses on magnetostriction of low carbon steel", *NDT&E International*, vol. 29, No. 5, 1996, pp. 263-268.

[Yamaura2001] S. Yamaura, Y. Furuya, T. Watanabe, "The effect of grain boundary microstructure on Barkhausen noise in ferromagnetic materials", Acta mater., vol. 49, 2001, pp. 3019-3027.

[Yanez2002] T. Yanez, "Innovative production methods for high silicon-steel", PhD thesis, Universiteit Gent, 2002.

[Yu1997] Y. Yu, L. Clapham, D.L. Atherton, T.W. Krause, "Tensor magnetostriction loops for a steel cube", JMMM, vol. 171, July 1997, pp. 94-102.

[Zentko1980] A. Zentko, L. Potocky, T. Tima, T. Svec, R. Mlynek and D. Cech, "Influence of tensile stress on permeability of grain oriented transformer sheets", JMMM, vol. 19, April 1980, pp. 25-26.

[Zueco1999] E. Zueco, W. Rave, R. Schäfer, M. Mertig and L. Schultz, "Observations of Fe surfaces with magnetic force and Kerr microscopy", JMMM, vol. 196-197, May 1999, pp. 115-117.